University of Exeter, Camborne School of Mines

Determination of an Ultimate Pit Limit Utilising Fractal Modelling to Optimise NPV

Submitted by Amir Bijan Yasrebi, to the University of Exeter

as a thesis for the degree of Doctor of

Philosophy in Earth Resources

November 2014

Abstract

The speed and complexity of globalisation and reduction of natural resources on the one hand, and interests of large multinational corporations on the other, necessitates proper management of mineral resources and consumption. The need for scientific research and application of new methodologies and approaches to maximise Net Present Value (NPV) within mining operations is essential.

In some cases, drill core logging in the field may result in an inadequate level of information and subsequent poor diagnosis of geological phenomenon which may undermine the delineation or separation of mineralised zones. This is because the interpretation of individual loggers is subjective. However, modelling based on logging data is absolutely essential to determine the architecture of an orebody including ore distribution and geomechanical features. For instance, ore grades, density and RQD values are not included in conventional geological models whilst variations in a mineral deposit are an obvious and salient feature. Given the problems mentioned above, a series of new mathematical methods have been developed, based on fractal modelling, which provide a more objective approach. These have been established and tested in a case study of the Kahang Cu-Mo porphyry deposit, central Iran.

Recognition of different types of mineralised zone in an ore deposit is important for mine planning. As a result, it is felt that the most important outcome of this thesis is the development of an innovative approach to the delineation of major mineralised (supergene and hypogene) zones from 'barren' host rock. This is based on subsurface

data and the utilisation of the Concentration-Volume (C-V) fractal model, proposed by Afzal et al. (2011), to optimise a Cu-Mo block model for better determination of an ultimate pit limit. Drawing on this, new approaches, referred to Density–Volume (D–V) and RQD-Volume (RQD-V) fractal modelling, have been developed and used to delineate rock characteristics in terms of density and RQD within the Kahang deposit (Yasrebi et al., 2013b; Yasrebi et al., 2014). From the results of this modelling, the density and RQD populations of rock types from the studied deposit showed a relationship between density and rock quality based on RQD values, which can be used to predict final pit slope. Finally, the study introduces a Present Value-Volume (PV-V) fractal model in order to identify an accurate excavation orientation with respect to economic principals and ore grades of all determined voxels within the obtained ultimate pit limit in order to achieve an earlier pay-back period.

Acknowledgments

Table of Contents

List of Figures

List of Tables

List of Appendices

List of Abbreviations

NPV: Net Present Value

C-V: Concentration-Volume

D-V: Density-Volume

RQD: Rock Quality Designation

RQD-V: RQD-Volume

PV-V: Present Value-Volume

NICICO: National Iranian Copper Industries Co

XRD: X-ray Diffraction

EPMA: Electron Probe Micro Analyser

SEM: Scanning Electron Microscopy

PIMA: Portable Infrared Mineral Analyser

PV: Present Values

IDW: Inverse distance weighted

S-A: Spectrum-Area

C-A: Concentration–Area

C-D: Concentration-Distance

PS: Positive strong

PW: Positive weak

MW: Minus weak

OES: Optimal extraction sequences

IP: Induced polarization

RS: Resistivity sounding

Py: Pyrite

Ccp: Chalcopyrite

Mol: Molybdenite

Py I: Early pyrite

Py II: Late pyrite

VPR: Volcano-plutonic rocks

Bt: Biotite

S-Bt: Secondary biotite

Qtz: Quartz

Plg: Plagioclase

Op: Opaque minerals

Kf: K-feldspar

Jar: Jarosite

Epi: Epidote

ICP-MS: Inductively coupled plasma mass spectrometry

OK: Ordinary kriging

MAD: Median Absolute Deviation

SD: Standard deviation

IDWAM: Inverse Distance Weighted Anisotropic method

SK: Simple Kriging

G-T: Grade-Tonnage

T1E: Type I error

T2E: Type II error

OA: Overall accuracy

IBSD: In-situ block size distribution

V. RQD: Volumetric Rock Quality Designation

PQD: Porphyric quartz diorite

COG: Cut-off grade

UPL: Ultimate Pit Limit

BESR: Break-Even Stripping Ration

ODBC: Open Database Connectivity

CAF: Cost Adjustment Factor

CBI: Central Bank of Iran

WTO: World Trade Organisation

DCF: Discounted cash flow

NPV-CTO: NPV-Cumulative Total Ore

List of abbreviations for lithological units, hydrothermal alterations, ore minerals and ore-type zonation in the Kahang deposit

Lithology			Alteration		
	ALL	ALLUVIUM		ARG	ARGILLIC
	ANS	ANDESITE		CAL	CALCITIZED
	ANS–D	ANDESITE–DIORITE		CHL	CHLORITIC
	CLS	CORE LOSS		NA	Not Available
	DAC	DACITE		PHY	PHYLLIC
	DIO	DIORITE		POT	POTASSIC
	GRD	GRANODIORITE		PRP	PROPYLITIC
	QAN	QUARTZ ANDESITE		QCS	QUARTZ–CHLORITE–SERICITE
	QAN–D	QUARTZ ANDESITE–DIORITE		SER	SERICITIC
	QDI	QUARTZ DIORITE		SLC	SILCIFIC (SILICIC)
	TUF	TUFF			
Zonation			Mineralization	CCA	CHRYSOCOLLA
				CHA	CHALCOCITE
				COV	COVELLITE
	HYP	HYPOGENE		CPR	CUPRITE
	LEA	LEACHED		CPY	CHALCOPYRITE
	OXI	OXIDISED		FEX	IRON OXIDE
	SUP	SUPERGENE		LIM	LIMONITE
				MAL	MALACHITE
				MDL	MOLYBDENITE
				NTS	NEOTOCITE
				PYY	PYRITE
				TRT	TENORITE

Glossary of Notations

F: F-distribution or continuous probability distribution

S_1 and S_2: Variances for pair of samples

n_1 and n_2: Number of observations

α: Probability value

H_0: Null hypothesis

H_1: Alternative hypothesis

σ_1 and σ_2: Variances of populations

n: Degrees of freedom

$\bar{d}$: Mean difference of the pair samples in terms of their grades

S_d: Differences of standard deviation

SE: Standard error of the mean difference

$\bar{n}$: Number of paired samples

T: T-test statistic

e: Error analysis

Xi and Yi: Measured values for duplicated samples

U: Interpolated value

x: An interpolated unknown point

x_i: An interpolating known point

D: A given distance

N: Total number of known points used in interpolation

P: Positive real number called the power parameter

$\gamma(h)$: Theoretical variogram

h: Lag separate distance

χ_q: Partition function

ε: 2D or 3D blocks dimensions

μ: A parameter in investigation

q: value of ε at any given moment

A: Area

ρ: Concentration, density, RQD, PV values

υ: Threshold

$a1$ and $a2$: Characteristic exponents

A_h and A_v: Areas horizontal (Plans) and vertical (cross sections) directions

$A_h(\rho \leq \upsilon)$, $A_h(\rho \geq \upsilon)$, $A_v(\rho \leq \upsilon)$ and $A_v(\rho \geq \upsilon)$: Areas with concentration values smaller and values greater than the contour value ρ

h and v: Horizontal and vertical section

$f(\alpha)$: Continuous function

$\tau(q)$: Auxiliary function

$\acute{a} = \acute{a}_{Max}$ or $\acute{a} = \acute{a}_{Min}$: Fixed values

$V(\varepsilon)$: Containing volume

C: constant value

$V(\rho)$: Occupied volume

$V(\rho \leq \upsilon)$ and $V(\rho \geq \upsilon)$: Occupied volume with values that is smaller or greater than contour value ρ

D: Fractal dimension

J_v: Volumetric Discontinuity Count for RQD

I_1: Income of Cu per each voxel

I_2: Income of Cu and Mo per each voxel

MC: Mining cost for a voxel

MR: Mining recovery

PC_1: Processing cost for Cu

PC_2: Processing cost for Mo

P_{Cu}: Metal commodity price for Cu

P_{Mo}: Metal commodity price for Mo

PR: Fraction recovery

D: Voxel density

V: Voxel volume

MCPU: Mining cost per volume unit

PCPU: Processing cost per tonnage unit

G_1: Cu concentration values

G_2: Mo concentration values

$V(\rho_{PV} \leq v)$ and $V(\rho_{PV} \geq v)$: Volumes (*V*) with PV values that are smaller and greater than PV threshold values

ρ_{PV}: PV values

$CTO(\rho_{NPV} \leq v)$ and $CTO(\rho_{NPV} \geq v)$: Cumulative total ore with NPV values that are smaller and greater values than NPV threshold values

ρ_{NPV}: NPV values

CHAPTER ONE. Introduction

1.1 Problem Description

Mineral excavation by open pit mining methods requires huge investment which will inevitably rise over the life of a mine due to increases in the amount of cumulative waste materials and mining costs (e.g., See Appendix. H for cumulative data; Caccetta and Giannini, 1988; Hustrulid and Kuchta, 2006; Akbari et al., 2008; Elkington and Durham 2011). Before starting the mining operation, it is necessary to design the final shape and size of the pit in order to determine the minable reserve and amount of waste to be removed. Following this, an optimised block model should be produced showing ore grades, density and Rock Quality Designation (RQD). RQD is the method perhaps most commonly used for characterising the degree of jointing in drill cores and can be considered as an expression of intact core lengths greater than a threshold value of 0.1 m along any bore hole. An increase in the number of joints in a rock mass causes a decrease in RQD (Bieniawski, 1984) and Net Present Value (NPV), the latter which is defined as the sum of all cash flows discounted to a specific time in an investor's minimum rate of return, or discount rate. NPV is a measure of value created by investing in a project (a mining project in this scenario) and not investing capital in any other project at the minimum rate of return. NPV higher than zero is acceptable however; an NPV equal to zero is a breakeven. The cumulative NPV indicates the value of one additional year of cash flow and its impact on the overall project NPV (Stermole and Stermole, 2012). Calculation of the final pit limit, which this study aims to optimise, is a function of numerous variables, especially NPV, and may be re-evaluated many times over the mine life (Lerch and Grossmann, 1965; Dowd and Onur, 1992; Akaike and Dagdelen, 1999; Hustrulid and Kuchta, 2006).

Separation of different populations based on ore grades and consequently the ID of mineralised zones in geological modelling for excavation of minable ores, specifically identifying 'barren' host rock from the main ore body, is one of the fundamental issues within a mining operation. Conventional methods for characterising mineral assemblages (e.g. X-ray Diffraction (XRD), Electron Probe Micro Analyser (EPMA), Scanning Electron Microscopy (SEM) and Portable Infrared Mineral Analyser (PIMA)) have been used since the 1960s to delineate mineralised zones however these do not have enough detailed information based on ore grades particularly in the porphyry deposits due to variation of ore grade distribution within block models (Schwartz, 1947; Lowell and Guilbert, 1970; Cox and Singer, 1986; Sillitoe, 1997; Beane, 1982; Berger et al., 2008).

Fractal geometry has a distinctive power to distinguish natural populations (zones) within orebodies. The research within this thesis utilises the Concentration-Volume (C-V) fractal model developed by Afzal et al. (2011) to delineate mineralised zones in terms of grades to obtain an optimised orebody model. Data from rock mass characterisation is then input into newly developed Density-Volume and RQD-Volume fractal models to determine an ultimate pit limit for a maximum NPV.

The importance of zone separation in porphyry ore deposits is as follows:

1. The key property of porphyry ore deposits is their low ore grades and high tonnage. However, the importance of this issue should be attributed to this fact that the different mineralised zones (leached, oxidised, supergene and hypogene) of those deposits are to

be distinguished carefully in order to demonstrate a comprehensive mine design and planning (Sim et al., 1999; Cheng and Agterberg, 2009; Sadeghi et al., 2012). For example, supergene enrichment zones are generally accepted to be the primary target when mining porphyry deposits (Hartley and Rice, 2005; Berger et al., 2008; Asadi et al., 2015). They are enriched in ore elements especially copper. The supergene enrichment zone consequently has high values in terms of money pay-back due to high grades. It is also usually located near surface which can reduce the costs of mining (Alpers and Brimhall, 1989; Sillitoe, 2005). In addition, the concentrator capacity is usually determined during the pre-feasibility study so it is necessary that the various zones with corresponding different grades and tonnage be identified to regulate the concentrator (Hustrulid and Kuchta, 2006). Detailed theoretical and experimental investigations of porphyry ore deposits have provided us with a good knowledge of how they were formed. It is now relatively easy to establish natural geochemical variability in terms of ore grades. However, geoscientists are now able to decipher the reasons for extreme variability in element concentrations using mathematical-oriented practices such as fractal modelling. This type of approach would continue to enhance the potential to identify relations between ore grade and their spatial distribution within a deposit (Monecke et al., 2005; Davies and Mundalamo, 2010; Spalla et al., 2010; Sadeghi et al., 2012).

2. The hypogene zone, which often comprises the bulk of a porphyry Cu deposit, is generally located below the supergene enrichment zone and contains lower grades with high tonnages of ore. Therefore, the location of this zone must be accurately determined

because huge amount of feed input to the processing plant is generally from this zone (Atapour and Aftabi, 2007).

3. The oxidised zone, which overlies the enriched supergene blanket, contains generally low but variable levels of Cu. By the end of the 20th century, this zone was generally treated as waste but after developing leaching and bioleaching methodologies, Cu has been exploited from this zone (e.g., copper (I) oxide or cuprous oxide for example cuprite (Cu_2O), copper (II) oxide or cupric oxide for instance tenorite (CuO), copper carbonates such as azurite and malachite, copper sulphate mineral such as chalcanthite, copper silicates for example chrysocolla and dioptase). Therefore, determination of the boundaries for this zone is fundamentally important so as to specify the distinct section exposed to leaching.

4. The discrimination of 'barren' host rock from the orebody and delineation of the zone's boundaries play a significant role in determining an optimised block model to be examined for final pit limit and correspondingly pit optimisation. Unfortunately, in most cases the 'barren' host rock is mistakenly identified as ore and consequently the size of the reserve is exaggerated (Agterberg et al., 1993; Panahi et al., 2004; Zuo et al., 2012; Zuo and Wang, 2015). This results in egregious errors during production planning. On the other hand if 'barren' rocks and ore are not properly delineated, some parts of the ore deposit may be lost. As a result, an exact determination of the boundary and the locations of the zones is necessary for the long-term planning of Cu mines and consequently should not be subject to major changes during mining. For example, if basic requirements are not

met, the formerly selected input feed grade (considering plant initial ore grade) to the processing plant will be lowered significantly which will reduce production. This is typically the case in the large copper mines of Chile and the USA (Carrasco et al., 2004; Parhizkar et al., 2011 and 2012).

The use of geological data including structure, lithology and mineralogy, main ore types and associated secondary elements, geophysical and geochemical anomalies as well as morphology of the ore deposit is considered to be the most important method for separating the various mineralised zones in descriptive models which were proposed and developed by Cox and Singer (1986). These models have major disadvantages as follows:

1. Geological core-logging is subjective rather than quantitative. In the event that both thin and polished sections of all cores are prepared to improve the accuracy, this process is both costly and time-consuming.

2. The grade of the ore element (particularly Cu) is not observed (visual assessment) with these methods while the variation of the grades in each zone is an obvious and salient feature which has to be always measured in a laboratory. Fractal modelling has proved their superiority to the classical statistical and conventional geological methods as follows:

- ➢ In classical statistics, for the purpose of determining the boundaries in mineralised zones, frequency distribution of a related ore element in an intended area must

adhere to a normal distribution. In addition, separation of different populations based on mean and standard deviation should be carried out with normalised data. This requirement is not always met in data. In addition, local neighbourhood statistics can provide less statistical information which is less biased than that of global statistics, such as mean and SD, because geochemical data generally satisfy non-normal distributions and contain outliers. However, there is no need to normalise data when the distribution of elemental concentrations is determined through fractal modelling (Agterberg et al., 1993; Cheng et al., 1994; Agterberg et al., 1996; Sim et al., 1999; Zhang et al., 2007).

➢ Traditional methods consider only the frequency distribution of the elemental concentration and ignore its spatial variability. Specifically, the information about the spatial correlation is not always available. Moreover, statistical methods e.g., by histogram analysis or Q–Q plots assume normality or log-normality and do not respect the shape, extent and magnitude of a studied area (Armstrong and Boufassa, 1988; Clark, 1999; Reimann and Filzmoser, 2000; Limpert et al., 2001). A power law relationship between quality parameters (e.g., ore element) and their occupied spatial positions (e.g., volume, area and perimeter) are illustrated in the fractal/multifractal modelling to solve the problematic issues mentioned above (Rafiee and Vinches, 2008; Sadeghi et al., 2015).

➢ Those values which are not within the range (outliers) must be identified and eliminated accordingly; otherwise they lead to the intended study having unreal

results. All data are contributed to fractal/multifractal modelling which is help for better separation of different mineralised zones (Xiao et al., 2014; Zuo, 2014).

Given the problems as mentioned above, using a series of newly established methods based on mathematical analyses seems to be inevitable. By using these methods, one is able to delineate the various mineralised zones in terms of grade and therefore the accuracy of one's pit limit optimisation. As a result, a C-V fractal modelling technique is proposed as a better method in order to identify geochemical zones, rock mass characteristics and economical populations in the Kahang Cu-Mo Porphyry deposit. The deposit is identified as an important Cu-Mo and deposit located approximately 73 km NE of Isfahan in Central Iran. It contains more than 100 million tonnes of sulphide ore with an average grade of 0.5 wt.% Cu and 90 ppm Mo. This deposit occurred within the Cenozoic Urumieh–Dokhtar magmatic belt, one of the subdivisions of the Zagros Orogenic Belt. This belt extends for some 2,000 km from NW to SE Iran. Many of the Iranian large porphyry Cu deposit such as Sarcheshmeh, Sungun and Meiduk are situated within this belt. Geological, geophysical, geochemical, alteration patterns as well as drilling data show that there could be a large Cu porphyry deposit at Kahang.

1.2   Objectives of the Research

The most important issue of this PhD thesis is to attempt to develop an innovative method to separate oxidised, supergene-enriched and hypogene zones from 'barren' host rock in a Cu-Mo porphyry deposit on the basis of fractal geometry using geochemical data. As a

result, an approach called C-V fractal modelling has been developed to determine proxies from grades, densities, RQDs and Present Values (PVs) within a deposit for pit limits. The general objectives of this study are as follows:

- ➢ To create a 3D geological model for lithology, alteration, zonation and mineralisation
- ➢ Generate a grade block model via the C-V model
- ➢ Rock mass characterisation using fractal/multifractal modelling
- ➢ Determine economic principals
- ➢ Calculate final pit limit for the Kahang deposit
- ➢ Create an economic block model from Present Value-Volume (PV-V) fractal modelling
- ➢ Calculate pushbacks resulting from the PV-V fractal model

1.3 Application of Fractal/Multifractal Modelling with Reliance on Geochemical Population

Euclidian geometry identifies geometrical shapes with an integer dimension say 1D, 2D, 3D, etc. However, there are many other shapes amongst spatial objects, whose dimensions cannot be mathematically described by integers but by real numbers or fractions (Bölviken et al., 1992; Agterberg et al., 1996; Aghanabati, 2004; Ali et al., 2007). These spatial objects are called fractals. In an abstract form, fractals describe complexity in data distribution by their fractal dimensions. A wide range of complex structures/features and geological phenomena of interest to geologists and geochemists have been quantitatively recognised using fractal/multifractal modelling over the past

several decades, mainly how to identify geochemical populations and quantify the spatial distribution of geochemical data. Various geochemical processes can be described based on differences in fractal dimensions obtained from analysis of relevant geochemical data. Recognition of geochemical populations is a crucial aspect for applied geochemists to effectively detect geochemical populations from background (Darnley et al., 1995; Plant et al., 2001; Lima et al., 2003, 2005 and 2008; Albanese et al., 2007).

Ore elements, especially trace elements, do not follow a normal or lognormal distribution. However, they follow a positively skewed distribution toward high values (Ahrens, 1954 and 1957; Krige, 1966; Turcotte, 1986; Reimann and Filzmoser, 2000; Agterberg, 2007; Carranza, 2009). Recent investigations of geochemical features have shown that self-similarity or self-affinity are significant properties of geochemical data (Bölviken et al., 1992; Cheng et al., 1994; Zuo et al., 2009a and b; Afzal et al., 2011; Zuo and Wang, 2015). The most effective way to distinguish geochemical anomalies from the background is to suggest a comprehensive technique which can be mathematically interpreted. The typical and most widely used method for detection of geochemical anomalies is the setting of threshold values which include upper and lower limits of background variations (Hawkes and Webb, 1962; Cheng et al., 1994; Xu and Cheng, 2001; Li et al., 2003; Lima et al., 2003; Afzal et al., 2010, 2011and 2012; Agterberg, 2012; Zuo et al., 2015). However, conventional geological methods, exploratory data analysis and multivariate statistics are based on the frequency distribution of geochemical values and neglect spatial variation (Tukey, 1977; Behrens, 1997; Yousefi et al., 2012 and 2014). In addition, exploration geochemical data are typically spatially dependent and therefore a couple of

frequency–space-based methods such as the inverse distance weighted (IDW) and different kriging methods have been used (Lam, 1983; Zimmerman et al., 1999). Although these methods consider the spatial distribution of elemental concentrations, they do not consider that spatial variability is rugged and singular rather than smooth and differentiable. The main attraction of fractal/multifractal theory is its capability to quantify irregular and complex phenomena or processes that exhibit similarity over a wide range of scales; this is regarded as self-similarity (Mandelbrot, 1983; Zuo and Wang, 2015).

Fractal theory, which was developed by Mandelbrot (1983), has been widely applied in the geosciences sector since the 1980s and up to the present (e.g., Turcotte, 1986; Agterberg et al., 1993; Cheng et al., 1994; Sim et al., 1999; Goncalves et al., 2001; Shen and Zhao, 2002; Ali et al., 2007; Yasrebi et al., 2013a). Methods of fractal analysis also serve to illustrate relationships between geological, geochemical and mineralogical data and spatial information derived from analysis of mineral deposit occurrence data (Carranza, 2008; Carranza et al., 2009; Goncalves et al., 2001). A good understanding of geological and geochemical controls on mineralisation is essential in the recognition and classification of geochemical populations based on methods of fractal analysis which indicate relations between ore grade and their spatial distribution within a block model (Cheng, 1999; Sim et al., 1999; Li et al., 2003; Carranza and Sadeghi, 2010). Fractals are characterised by a scaling law that relates two variables: the scale factor and the physical properties of the object being measured. This scaling relationship is described by a power law function, which in turn describes the inherent physical attributes of the object being analysed (Takayasu, 1990; Lauwerier, 1991; Ortega et al., 2006). The

exponent of the power law function refers to the fractal dimension. Fractal dimensions in geological and geochemical processes correspond to variations in physical attributes such as rock type, nature of the hydrothermal fluids and alteration, structural features and dominant mineralogy, and so on (Sim et al., 1999; Cheng, 2007; Cheng and Agterberg, 2009; Afzal et al., 2013a and 2014; Yasrebi et al., 2013a, b and 2014). Therefore, fractal dimensions of variations in geochemical data can provide useful information and applicable criteria to recognise and classify mineralised and 'barren' zones within a study area. Various log–log plots in fractal methods are considered to be useful tools in separating geological populations. Classification of geochemical data within threshold values can be recognised and determined to indicate breakpoints within these plots. These geochemical threshold values recognised via fractal analysis are usually correlated with geological field information. Multifractal theory is used as a theoretical framework to explain the power–law relationship between areas enclosing concentrations below a given value and the actual concentrations themselves (Halsey et al., 1986; Evertz and Mandelbrot, 1992).

The fractal method has several limitations and accuracy issues, especially when the boundary effects on irregular geometrical data sets are involved (Agterberg et al., 1996; Goncalves, 2001). The Concentration-Area (C-A) method (Evertz and Mandelbrot, 1992; Cheng et al., 1994), which is the basis of the C-V fractal model, seems to be equally applicable in all cases, which is probably rooted in the fact that geochemical distributions mostly satisfy the properties of a multifractal function. There is some evidence that geochemical distributions are fractal in nature and behaviour, at least

empirically according to Bölviken et al. (1992). Some approaches seem to support the idea that geochemical data distributions are multifractal, although this point is far from proven (Cheng and Agterberg, 1996; Turcotte, 1997; Goncalves, 2001; Afzal et al., 2010, 2013a and b). This idea may help in the development and validation of a method for elemental geochemical distribution analysis.

1.3.1 Introduction to Common Fractal Models

Cheng et al. (1994) proposed the Concentration-Area (C-A) fractal model, which is used frequently for modelling geochemical anomalies and discriminating geochemical anomalies from background, relates the element concentration to the area enclosed by concentration contours by a power law relation (Carranza, 2009; Zuo et al., 2012). He applied the C–A fractal model to lithogeochemical data of the Mitchell-Sulphurets precious metal district, British Columbia and found that various fractal patterns exist inside and outside the potassic, sulfidic, and silicic alteration zones. The Spectrum-Area fractal model (S–A), which was proposed by Cheng et al. (1999), is a version of the C–A (Concentration–Area) model which separates overlapping populations using more than one cut-off value. Li et al. (2003) introduced the Concentration–Distance (C–D) fractal model for discriminating geochemical anomalies from background. These models have been widely used to identify anomalies as well as for determining the geochemical baseline in environmental studies (e.g., Cheng et al., 1994; Cheng and Agterberg, 1996; Cheng, 1999; Gonçalves et al., 2001; Xu and Cheng, 2001; Li et al., 2003; Panahi et al., 2004; Cheng, 2007; Albanese et al., 2007; Afzal et al., 2010; Wang et al., 2013; Asadi et al., 2014 Luz et al., 2014; Sun et al., 2014). Cheng (2012) suggested a Density–Area

Power-Law model to systematically confirm that singularity analysis is effective for the identification of weak geochemical anomalies. Furthermore, Wang et al. (2012) investigated the fractal relationship between orebody tonnage and thickness by tonnage–thickness model and metal tonnage–grade thickness model for better understanding orebody spatial distribution (Zuo and Wang, 2015).

1.4   Methodology

The determination of a final pit limit in the Kahang Cu-Mo porphyry deposit is the major aim of this research. To achieve this, subsurface data obtained by boreholes is entered into the RockWorks^{TM} software enabling one to generate a 3D geological model based on lithology, alteration, mineralisation and zonation. Geostatistical studies were then conducted in order to build the Cu and Mo block models based on the dataset with utilisation of SGeMS software. The next step was to test different approaches, namely Concentration-Volume (C-V), Density-Volume (D-V), RQD-Volume (RQD-V) and Present Value-Volume (PV-V) fractal models, to delineate various populations in terms of Cu and Mo values, densities, RQDs and valuable voxels respectively. Consequently, data for the main ore body of the Kahang, including ore grade, density, tonnage and rock type (ore and waste), was used to generate a prototype for the determination of internal pit shells, extraction sequences (Nested pits) and ultimate pit limit, which is a collection of optimised pits. All pits were calculated on the basis of the Lerch & Grossman algorithm (Hustrulid and Kuchta, 2006). Indeed, constructing optimised nested pits is considered an 'art' applied by design engineers to specify the ultimate optimised pit as well as to determine the extraction sequence of the blocks, with respect to the obtained thresholds via fractal

modelling log-log plots. The result of this study will be a reserve estimation and the modification of existing mineralised zones with respect to the different ore grades within the deposit. Finally, NPV Scheduler was employed in order to establish the final pit limit in terms of the maximum NPV and associated ''Nested pits'' to produce an optimised pit limit.

1.4.1 Introduction to NPV Scheduler

Since the 1960s, computerised open pit optimisation methods have been used and most major mining companies employ some form of these methods in the design of their open pit operations. These computerised optimisations can also be utilised to aid in the transition from open pit to underground mining methods. Examples of widely used systems include the NPV Scheduler. The primary focus of these software systems is to determine an optimum size and shape of open pits to enable the generation of production schedules. This software encompasses a number of processes which utilise computerised grade block models and generate detailed economic analysis of different open pit mines (See chapter 5 of this thesis and Appendices F and H). This analysis, which includes discounted cash flows, also demonstrates productive information to assist in the mine planning and scheduling of open pits (NPV – Scheduler, 2001).

1.4.2 Introduction to Lerch and Grossmann Algorithm with Reliance on Resource Modelling

In the late 1960s, researchers were only focused on the determination of the ultimate pit limit (Zhao and Kim, 1992; Shishvan and Sattarvand 2015). The Lerch and Grossmann algorithm, which is based on three-dimensional graph theory, is the most commonly used

optimisation algorithm which takes into account the influence of a grade block model, operating costs, product prices, slope geometry, etc (Lerch and Grossmann, 1965; Dimitrakopoulos et al., 2007). It is also used in mining optimization software as the industry standard, for example in NPV Scheduler and Gemcom's Whittle software (Whittle 1998a, b and 1999), to find the optimal pit and pushbacks. The algorithm uses different revenue factors to generate a value-based mining sequence strategy to design pit shells (Dincer 2001; Bastante et al., 2008; Grenon and Hadjigeorgiou, 2010; Shishvan and Sattarvand 2015). Early pit shells are constructed using high-grade blocks and a low stripping ratio. The results also consider practical considerations such as haul road access, cut-off grades and processing, etc. To maximise the use of block modelling functions and optimise the pit design process, block modelling and slope stability analysis have to be fully integrated. This is a logical extension to assign mines rock types and grades to every block .This process will be further optimised by defining every block location especially those blocks with high value of NPV (e.g., the use of fractal geometry in this thesis: See chapter 6). The algorithm works as follows:

First, a directed graph (Bondy and Murty, 1976) is produced with the nodes of the orebody, the blocks in the orebody model. These connected blocks have certain restrictions, for example precedence and slope limitations. The method produces a tree regarding Lerch & Grossman algorithm as a set of combined voxels with a dummy node and strong and weak arcs between the nodes (Fig. 1. 1). When the restrictions are satisfied, the pit has the maximum closure graph at a scaled capacity (Lerch and Grossman, 1965; Zhao and Kim 1992; Seymour, 1995; Hustrulid and Kuchta 2006;

Meagher et al., 2010). In step one, the blocks/nodes are connected to the dummy node, X0, with arcs from X0. Step two indicates the initial normalised tree, the positive strong (PS) arcs are plus arcs supporting blocks with NPVs higher than zero (strong vertices) and positive weak (PW) arcs indicates blocks with NPVs less than zero (weak vertices) which have negative significance in calculation of the total open pit mining project NPV. Step three indicates merging vertices X4 and X6; the arc between X0 and X6 will be removed out. Minus weak (MW) denotes a minus arc supporting a strong arc. Step four illustrates the tree when all the weak vertices above X6 are merged. Step five shows the final graph closure with the strong vertices associated to the dummy node. In total, The Lerch and Grossmann algorithm is based on two theorems (Caccetta and Giannini, 1986):

1. The maximum closure of a normalised tree is the set of that tree's strong vertices.

2. A normalised tree can be found such that the set of strong vertices in this tree constitutes a closure of the graph so the set of strong vertices is the maximum closure of the graph with the highest NPV.
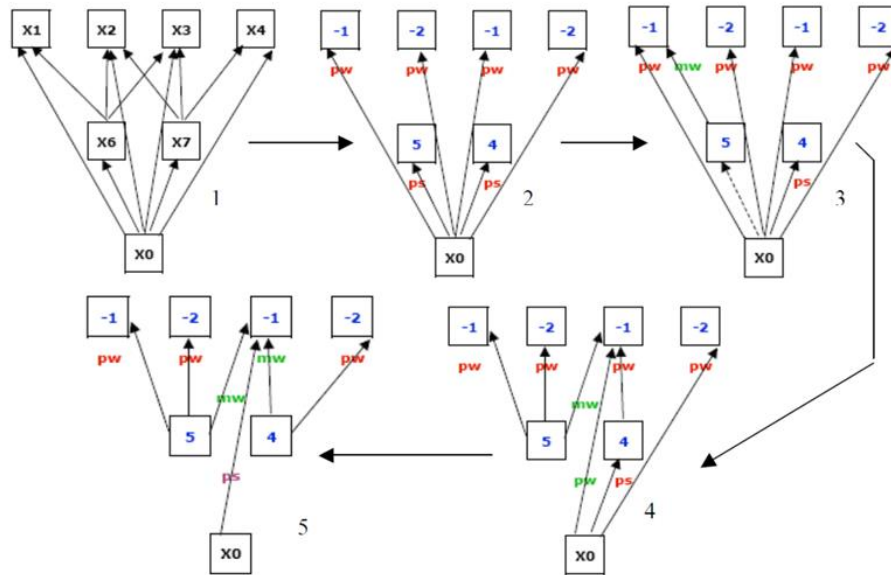
Fig. 1. 1. An example of the graph closure in the Lerch and Grossman algorithm

(Meagher et al., 2010)

The optimised pit generated by the Lerch and Grossmann algorithm always has a crest within a studied block model so no produced pit will break through the side of the model. Consequently, if the region or model area is too small, an underestimated optimised pit will be resulted (Kim, 1978; Frangois-Bongarcon and Guidal, 1982; Koenigsber, 1982; Seymour, 1995; Hochbaum and Chen, 2000; Bernabe, 2001; Ramazan, 2007). On the other hand, if the block model is too large and the optimisation software (NPV Scheduler used in this thesis) cannot fit into RAM, so the optimisation software will work slowly. To offset this, engineers wish to bulk the block model voxels together as depicted in Fig. 1. 2.
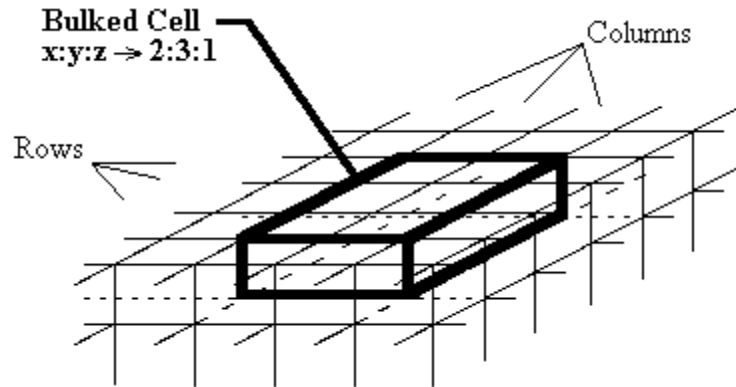
Fig. 1. 2. Bulking the block model voxels together (Mart and Markey, 2013)

1.4.2.1 Introduction to Other Methods for Mine Planning

A 3D program called GEOVIA Whittle™, introduced by Whittle (1985), was a computer-based implementation of the Lerch and Grossmann method which used a block model, whose blocks have economic values representing the net cash flow that result from mining the block in isolation (Whittle, 1988, 1989 and1999). However, the resulting optimal pit did not use discounted cash flows.

The Floating Cone method, which is the simplest and fastest technique to determine optimum ultimate pit limits to which variable slope angle can be easily applied, repeatedly searches for and checks the total value of block groups forming inverted cones. Total cones are identified for mining if their total value was positive. This procedure is iterated until no more positive cones are recognised. However, this method cannot guarantee the final pit is optimum. Other block groups (as mentioned above) also implemented a two-and-a-half dimensional Lerch and Grossmann algorithm (Dimitrakopoulos et al., 2002; Osanloo et al., 2008a; Asad and Dimitrakopoulos, 2013).

The 4D (and subsequently Four-X) programs also use the same Lerch and Grossmann technique to generate a set of nested optimal pits. Each pit that is optimal is used to guide different mining schedules. Financial analysis of these programs which consider discounted cash flows allows selection and sensitivity analysis of the best pit (Dowd, 1994; NPV – Scheduler, 2001; Osanloo et al., 2008a; Askari-Nasab et al., 2011).

1.5 Specific Economic and Political Context of Mining in Iran

The mining sector is key to sustainable development in many countries such as Iran (Sameni Keivani and Khalili Sourkouhi, 2014). The following text describes Iranian government policy, programs and aims with regard to the mining sector (revealed by Mr.Nematzadeh, the minister of Industries, Mines and Commerce of Iran, at the Iran Parliament, 2015).

"Governmental and private mining sectors in Iran are one of the largest and most effective sectors of the country's economy and own a vast diversity and complexity compared with other sectors, providing considerable and noteworthy effect on the economy improvement of Iran. Mining and in one single word mineral productions, is the motive engine of the country's economy which has a crucial role in the economic growth, decrease of inflation, unemployment and improvement in competition and rivalry.

The general policy of the Iranian government is to set up an economic development to move towards a position in which it will be able to have a noteworthy position in the world economy based on mining industries to generate national wealth.

Iran by owning 57 billion tonnes of mineral ores (proved and probable), with 69 different ore minerals, ranks first in the Middle East and is on a par with the top 10 mineral producers globally. From among 7036 licensed mines, 5060 mines with reserves amounting for 40 billion tonnes are active and in recent years, around 341 million tonnes of minerals valued at 3.7 billion US dollars (with an average of each tonne equal to 21.4 dollars) have been extracted and nearly 3 billion US dollars of these have been exported. Only two percent of the total mines of the country belongs to the governmental sector, including 25% of total extracted minerals in the country, which is over 35% of minerals production in terms of economic value. General aims of the Iranian government regarding mines and mining industries development are as follows:

1- Increase competition within the country's mining sectors.

2- Increase the value added share of mineral products within the country.

3- Increase the country's minerals exports.

4- Increase the amount of mineral products with high technology/value added and consequential exports.

5- Increase the role of the private sector mining activities.

6- Promotion of environmental standards towards access to universal sustainable development goals.

7- Effort towards joining the World Trade Organisation and utilisation of the capacities thereof.

The Iranian Government's quantitative goals regarding mining development are:

1-   Reach an annual average growth of value added of 12 percent.

2-   Export high quality mineral products up to 30 percent of the total country's export by the end of tenure of the presidency of Dr. Rohani.

3-   Industrial and mineral exports portion compared to total world industrial exports at the closure of presidency of Dr. Rohani to be up to 3 percent.

4-   The ratio of industrial and mineral exports to industrial and mineral imports at the end of presidency of Dr. Rohani to be equal to 100 percent.

5-   Absorption of direct foreign investment for the country's mining projects (annual average of 8 billion dollars).

The Iranian Government policies regarding mining development are:

1-   Review of strategic documents covering development of industry, mining and trade.

2-   Upgrading the potential of small and medium mineral industries towards expansion of their products as exports.

3-   To facilitate absorption and development of foreign investment.

4-   Protection of private mining sectors for renovation and amelioration.

5-   To help promote competitiveness.

6-   To develop industrial and mining facilities and help restart ceased or inactive mines.

7-   To help develop an optimal consumption management of energy in the mining sector.

8-   Efficient support for research and development in the mining sector.

Here it is worth mentioning that the data sources to conduct this PhD research were provided by the Kahang deposit owner (Appendix. A), the National Iranian Copper Industries Co (NICICO) which has numerous responsibilities including extraction and utilisation of copper mines, production of copper concentrates and manufacturing copper products such as cathodes, slabs, billets and 8 mm wire rods.

1.6   Organisation of the Thesis

Chapter one gives the background to, and the problem statement for the research undertaken on the importance of delineation of mineralised zones in a Cu-Mo deposit. The aims and objectives of the research are presented along with a brief description of the methodology to achieve the outlined objectives.

Chapter two deals with the geology and associated mineralisation in the Kahang deposit providing 3D models of lithology, alteration, zonation and mineralisation.

Chapter three introduces the C-V fractal model. Additionally, a correlation between results achieved from the C-V fractal model and those from geological models is used to optimise the delineation of mineralised zones. A logratio matrix has been employed to validate the C-V fractal model for the Cu and Mo main mineralised zones.

Chapter four proposes the D–V and RQD-V fractal models to delineate rock characteristics including density and RQD within the Kahang porphyry deposit. A correlation of results from the D–V fractal and lithology models was carried out to illustrate that the main lithological unit is associated with high values of density and also has a strong correlation with high values of RQD. The log-ratio matrix was employed to validate the D–V fractal model for density with the main rock type of the deposit. The results reveal that there is a multifractal pattern of rock characteristics with respect to RQD for the Kahang deposit.

Chapter five discusses the determination of an ultimate pit limit using the results achieved from the proposed fractal models in the former chapters. Following this, the NPV Scheduler was employed in order to establish the final pit limit in terms of the maximum NPV and associated mining sequences. Finally, a comparative case study was also conducted by ignoring three isolated boreholes located in the NW part of the deposit.

Chapter six introduces a fractal model to achieve a best mining scenario and strategy for an earlier pay-back. In addition, a new method is proposed to identify an optimal extraction sequences (OES).

Chapter seven summarises the main conclusions drawn from the entire research project. The knowledge gained from each specific investigation is summarised along with the contributions to knowledge. The chapter concludes with the author's recommendations for future work on the topic.

CHAPTER TWO. Geology and Associated Mineralisation

2.1 Regional Geology

The Kahang Cu Porphyry deposit is located approximately 73 km from Isfahan, in Central Iran. This deposit is situated in the central part of the Cenozoic Urumieh-Dokhtar magmatic belt, which extends for 2000 km and is 150 km wide, from NW to SE Iran (Fig. 2. 1; Alavi, 1994; Aghanabati, 2004; Alavi, 2004). This magmatic belt has been interpreted as a subduction related Andean-type magmatic arc that has been active since the late Jurassic within the collisional Alpine–Himalayan orogenic belt, reflecting subduction and collision of the Afro-Arabian plate with Eurasia (Schroder, 1944; Dewey et al. 1973; Dargahi et al., 2010). The rock units of this belt are composed of voluminous tholeiitic, calc-alkaline, and K-rich alkaline intrusive and extrusive rocks, with associated pyroclastic and volcanoclastic successions, formed along the active margin of the Iranian plate (Berberian and King, 1981; Berberian et al., 1982). The belt hosts the largest of the Iranian porphyry deposits, including Sarcheshmeh, Sungun, Meiduk, Dali, and Darehzar (Shahabpour, 1994; Atapour and Aftabi, 2007; Boomeri et al., 2009).

The closure of the Neotethyan ocean and prevailing collisional tectonics during Tertiary times built a highly fertile metallogenic environment with massive porphyry copper deposits/prospects in the Urumieh–Dokhtar magmatic belt clustering in narrow arc segments, typically a few tens of kilometres wide (e.g., Agard et al., 2005; McInnes et al., 2005; Shafiei et al., 2009; Dargahi et al., 2010; Richards et al., 2012; Asadi et al., 2014). Cenozoic tectono-magmatic activity and porphyry Cu-Mo mineralisation along the Urumieh-Dokhtar magmatic belt are attributed to three time-windows: (1) Eocene–Oligocene (Ahmadian et al., 2009); (2) mid-late Oligocene (Kirkham and Dunne, 2000;

McInnes et al., 2005); and (3) mid-late Miocene (McInnes et al., 2005; Razique et al., 2007; Richards et al., 2012). The Urumieh–Dokhtar belt occurred during the Cenozoic magmatism which started in late Cretaceous-Paleocene, peaked in Eocene and extended into the Miocene and Quaternary. The magmatism was accompanied by the formation of a wide range of ore deposits, consisting of epithermal ore deposits, skarn-type ores, porphyry-type Cu-Mo-Au deposits and a variety of industrial minerals (Mirnejad et al., 2010).

Most Iranian Cu porphyry deposits have been explored in the SE part of Iran especially in Kerman province (e.g., Sarcheshmeh and Meiduk mines) and the NW part of Iran in Azerbaijan province (e.g., Sungun deposit) since the 1970s. The central part of the Urumieh-Dokhtar belt has recently received attentions for their porphyry-style ores. Few porphyry Cu deposits are present in the central part of Urumieh–Dokhtar belt, typical examples being Aliabad, Darehzereshk, Dali and Kahang (Zarasvandi et al., 2005; Ayati et al., 2008).

2.2   Geology of the Kahang Deposit

The Kahang Cu-Mo porphyry deposit was initially discovered in 2003 from remote sensing (Landsat TM) and geophysical studies and then from drilling (Tabatabaei and Asadi Haroni, 2006; Afzal et al. 2012). Subsequently, stream sediment sampling, alteration mapping and lithogeochemical exploration were undertaken as well as geophysical exploration using induced polarization (IP) and resistivity (RS) which showed the existence of a Cu-Mo prospect with Cu and Mo average grade of 0.1 wt.% and 33 ppm, respectively (Afzal et al., 2010). This led into further subsurface exploration to find out if

there would be a deposit in this area. On the basis of alteration assemblages, the Kahang prospect was divided into three divisions namely; Eastern, Central and Western Kahang (Fig. 2. 4a). Within these, 48 boreholes were drilled in the Eastern Kahang with total depth of about 22,000 m. There is a Cu resource greater than 100 Mt of sulphide ore with a Cu mean value equal to 0.23 wt.% if the Cu threshold is 0.1 wt.% (See Chapter 3, Fig. 3. 18) so the Kahang is not a prospect, and can appear to be promising.

The Kahang deposit lies within Eocene volcanic–pyroclastic rocks, which have been intruded by Oligo-Miocene porphyritic granitoid rocks, quartz monzonites, monzodiorite-monzogranites and diorites (e.g., Alavi, 1994; Tabatabaei and Asadi Haroni, 2006: Fig. 2. 1a and b). The Eocene rock units consist of andesite, trachyte, trachy-andesite, silicic breccias and tuffs. The main geological structure in the area is a NW–SE and NE–SW trending fault system. The extrusive rocks, including tuffs, breccias and lavas, are dacitic to andesitic in composition. Magmatic events in the Kahang area have been interpreted as followings (Afzal et al., 2010):

1. Explosive eruptions of pyroclastics such as tuffs and tuff breccias.

2. Flows of andesitic to dacitic lavas with porphyritic textures. It is probable that eruptions of pyroclastic rocks and lavas were repeated periodically.

3. Emplacement of sub-volcanics and intrusive rocks with dacitic, andesitic, monzonitic and dioritic compositions.
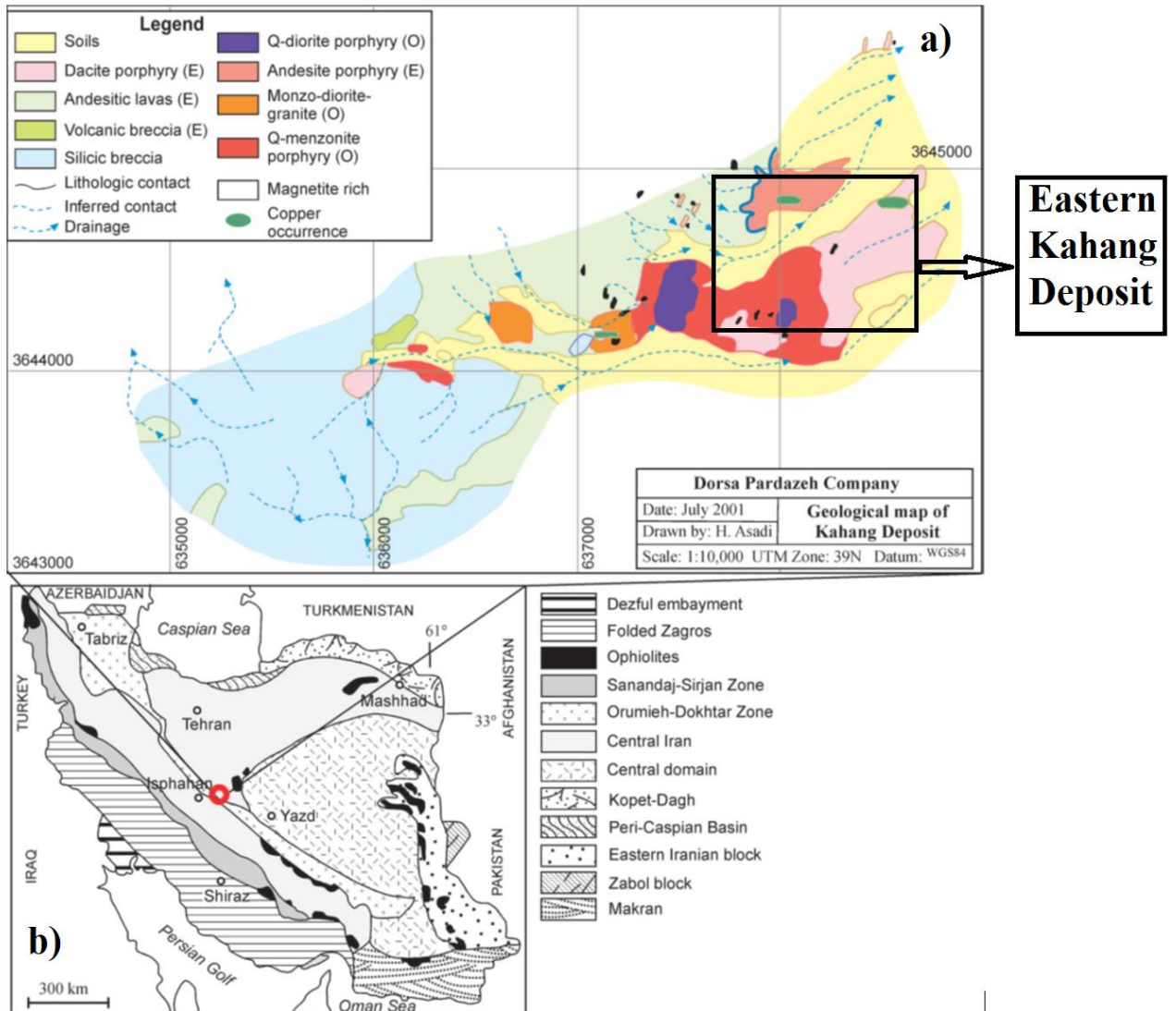
Fig. 2. 1. a) Geological map of the Kahang study area, scale: 1: 10,000 (Alavi, 1994; Tabatabaei and Asadi Haroni, 2006), and b) structural map of Iran, showing the Urumieh-Dokhtar volcanic belt (Alavi, 1994)

2.2.1 Mineralisation Characteristics of the Kahang Deposit

The Kahang deposit is a Cu-Mo porphyry deposit. Mineralisation is mainly hosted within Eocene sub-volcanic rocks, especially porphyritic quartz diorites, monzodiorite-monzogranite and dacitic rocks (Tabatabaei and Asadi Haroni, 2006; Afzal et al, 2011,

2012 and 2013b: Fig. 2. 2). Ore minerals are dominated by chalcopyrite, pyrite, bornite and lesser amounts of chalcocite, covellite, malachite, molybdenite and Fe ores (i.e., hematite, magnetite, goethite and jarosite: Fig. 2. 3c).

Fig. 2. 2. Eocene sub-volcanic rocks in the Kahang deposit (View towards SE)
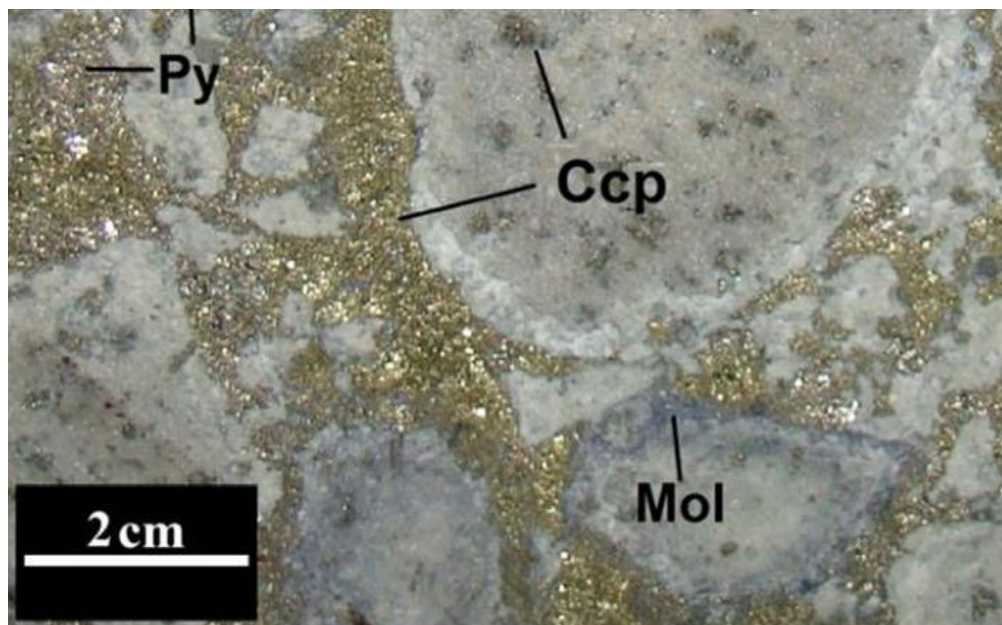
(a)
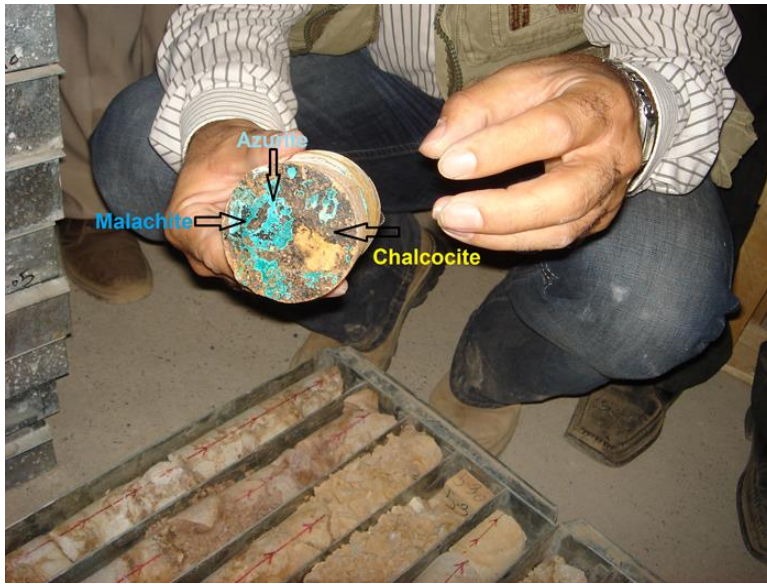
(b)

(c)
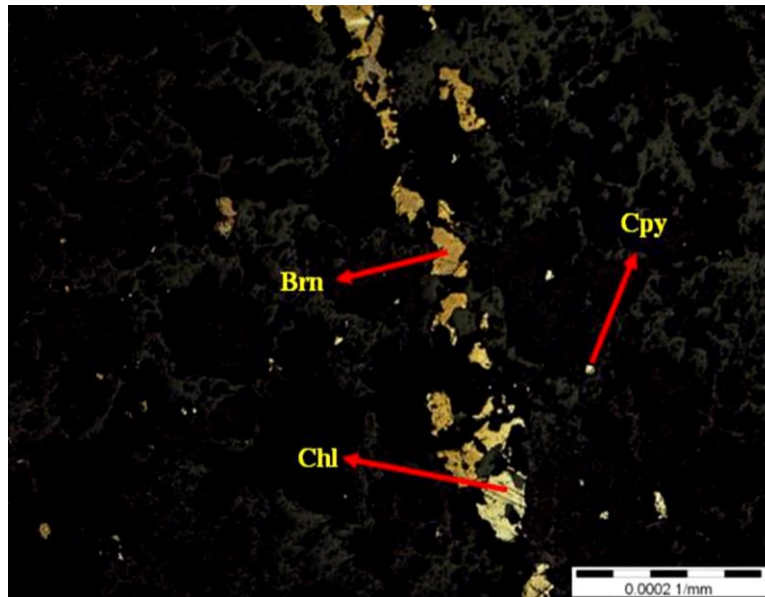
(d)

Fig. 2. 3. a) Pyrite (Py), chalcopyrite (Ccp) and molybdenite (Mol), b) Copper secondary sulphides and carbonate minerals from the oxidised zone (Azadi et al., 2014), c) Fe-oxides, and d) reflected light photomicrograph showing bornite (Brn), chalcocite (Chl) and chalcopyrite (Cpy) in the Kahang porphyry deposit

Based on vein morphology, mineral paragenesis and cross-cutting relationships, seven groups of veins and veinlets were distinguished in the Kahang deposit (Afzal et al., 2010 and 2012; Azadi et al., 2014) namely; (1) Early biotite veinlets followed by (2) magnetite-chlorite ± quartz ± sericite veins, (3) quartz-magnetite ± chlorite ± chalcopyrite ± pyrite veins, (4) quartz-molybdenite ± chalcopyrite ± pyrite veins, (5) pinkish anhydrite-chalcopyrite ± pyrite ± white anhydrite ± gypsum veins, (6) quartz-sericite-pyrite ± chalcopyrite ± chlorite veins, (7) tourmaline ± quartz ± chalcopyrite ± pyrite veins and (8) late poly-mineral calcite-sphalerite ± galena ± pyrite ± chalcopyrite veins (Afshooni et al., 2010, 2011 and 2013; Azadi et al., 2014). The main mineralisation at the Kahang deposit is Cu-Mo porphyry that occurs within intrusive bodies and their surrounding sub-volcanic

rocks. The ore minerals, consisting of chalcopyrite, pyrite, malachite, magnetite, limonite, jarosite, goethite, bornite, sphalerite, galena, digenite, covellite, hematite, chalcocite and molybdenite are distributed in leached, oxidised, supergene and hypogene zones (e.g., Berberian and King, 1981; Alavi, 1994; Ayati et al., 2008; Afshooni et al., 2010, 2011 and 2013; Asadi et al., 2015), as depicted in Fig. 2. 4. Gold occurs as fine inclusions within pyrite and chalcopyrite and as native gold (electrum) within grey quartz veins in hypogene zone (Fig. 2. 4L). Drilling data shows that a large-scale Cu–Mo mineralisation also occurs in the hypogene zone. Pyrite in the hypogene zones generally occurs as aggregates, composed of optically homogeneous euhedral to subhedral crystals, ranging in size from 20 μm to 5 mm which occurs in two generations: early pyrite (Py I) that is small rounded blebs (~20–50 μm) included in chalcopyrite crystals (Fig. 2. 4a) and late pyrite (Py II) distributed widely and formed later than chalcopyrite (Fig. 2. 4b). Chalcopyrite is the most common sulphide mineral in the Kahang deposit, and appears as small rounded blebs (50 μm–1 mm) as depicted in Fig. 2. 4b. Cu values increase within chalcopyrite especially in the deeper parts of the deposit (See Chapter 3, Fig. 3. 27e).
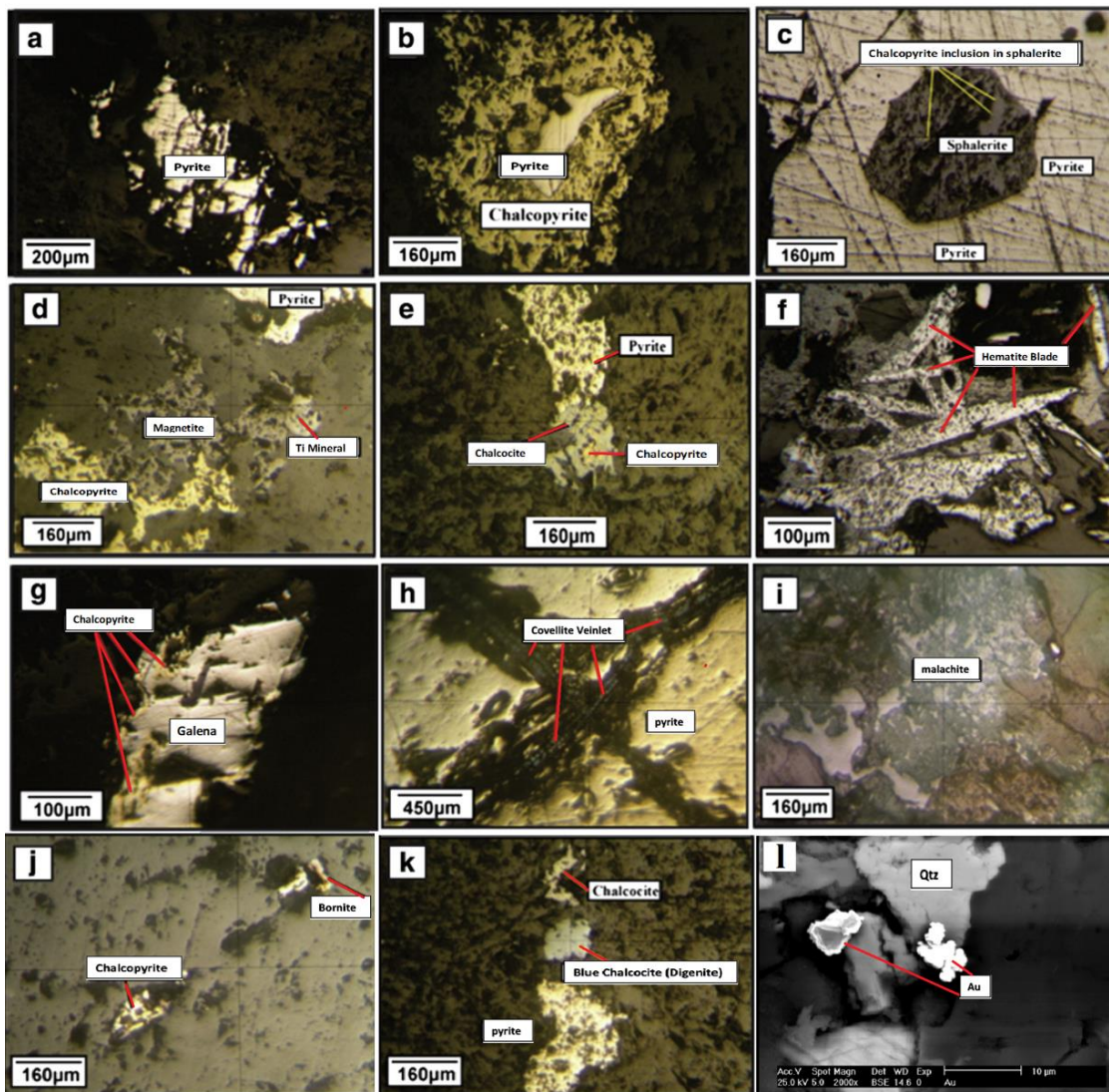
Fig. 2. 4. Photomicrographs of ore minerals in the Kahang deposit (Afshooni et al., 2013): a) type II pyrite (Py II) associated with chalcopyrite, b) replacement of pyrite by magnetite in type I pyrite (Py I), c) subhedral sphalerite, containing chalcopyrite inclusions enclosed by pyrite, d) magnetite grains associated with Ti-mineral, pyrite and chalcopyrite, e) ex-solution between chalcocite and chalcopyrite, f) hematite blades, g) galena grains associated with chalcopyrite, h) covellite occurs as fracture-filling in pyrite, i) malachite occurs as fracture-filling in micro-diorites, j) bornite together with chalcopyrite, k) chalcocite, digenite and pyrite occur as veins, l) Backscattered electron Image showing native gold (electrum) grains within late stage grey quartz

2.2.2   *Hydrothermal Alteration*

Hydrothermal alteration in the Kahang deposit (Western, Central and Eastern parts) is pervasive, occurring in an area greater than 10 km^2. Detailed alteration mapping shows four major types of hydrothermal alteration: potassic, phyllic, argillic and propylitic (Figs. 2. 5a) based on detailed studies of the mineralogy and petrography of drill cores and surface samples (Harati et al., 2013). As a result, hydrothermal alteration zones in the Kahang deposit can be divided into four types (Afshooni et al., 2013; Azadi et al., 2014): 1) Early potassic alteration (K metasomatism) which occurs within and proximal to mineralised veins and intrusions that contain Cu-Mo mineralisation, 2) Medial quartz-sericite-pyrite (phyllic) alteration that partially overprints the early potassic alteration zone and contains mineralised veins, 3) Argillic alteration in the outer and peripheral parts of the altered and mineralised zone that overprints the previous alteration zones, 4) Peripheral propylitic alteration of mainly sub-volcanic rocks, distal to the zone containing mineralised veins and breccias. Cu-Mo-Fe sulphides are spatially and temporally associated with the potassic and phyllic assemblages which include chalcopyrite, molybdenite and pyrite (Afshooni et al., 2010, 2011 and 2013; Harati et al., 2013). The alteration zones in this deposit follow the conceptual model of the alteration zones which was proposed by Lowell and Gilbert (1970: Fig. 2. 5b).
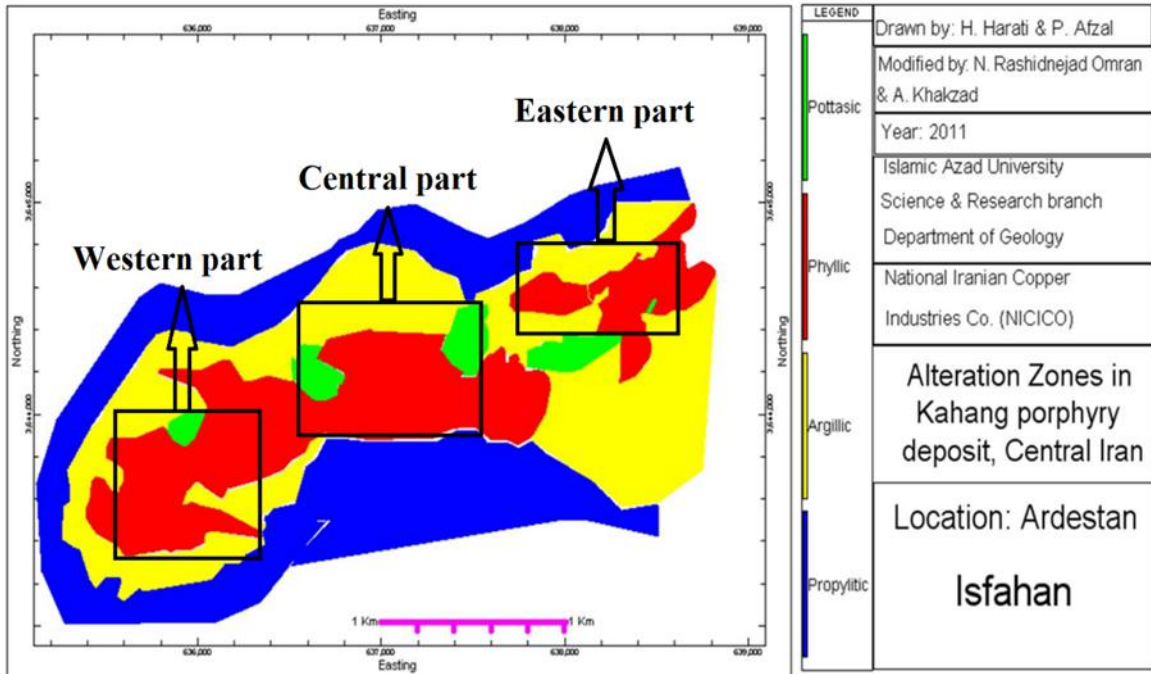
(a)
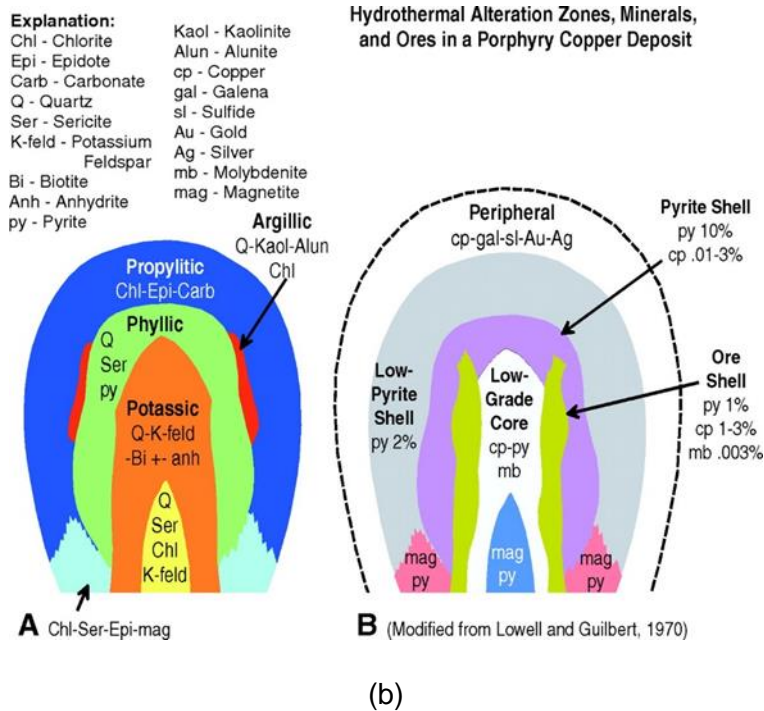
(b)

Fig. 2. 5. a) Alteration map of the Kahang deposit (Western, Central and Eastern parts; Harati et al., 2013) and b) Conceptual model of Lowell and Gilbert (1970)

The potassic alteration zone is located in the central part of the deposit with neo-formed biotite and KF veinlets (Fig. 2. 6a). This alteration and associated hypogene mineralisation mainly occurred within the deepest and central parts of the zone containing mineralised veins and breccias, within quartz diorite and quartz monzonite (Harati et al., 2013; Azadi et al., 2014). The common mineral assemblage within the potassic zone contains secondary biotite (S-Bt: Fig. 2. 6b), K-feldspar (Kf), quartz, sericite, pyrite, chalcopyrite, bornite, magnetite and lesser amounts of anhydrite, chlorite, zircon, rutile and hematite. Potassic alteration in this area is characterised by K-feldspar and irregularly shaped crystals of Mg-rich biotite (secondary biotite) within volcano-plutonic rocks (VPR). Petrographic observations and microprobe analyses point to the presence of two compositionally distinguishable types of biotite within this alteration zone: 1) primary biotite, which is Fe-enriched, brown in colour, and generally euhedral and 2) hydrothermal biotite (Fig. 2. 6c), which is mainly pale-brown to greenish-brown in colour and very ragged (Shahabpour, 1982). The hydrothermal biotite occurs interstitial to feldspar and quartz and locally replaces amphibole and primary biotite phenocrysts (Khayrollahi, 2003). Replacement biotite was formed commonly by the alteration of amphiboles (Fig. 2. 6d).
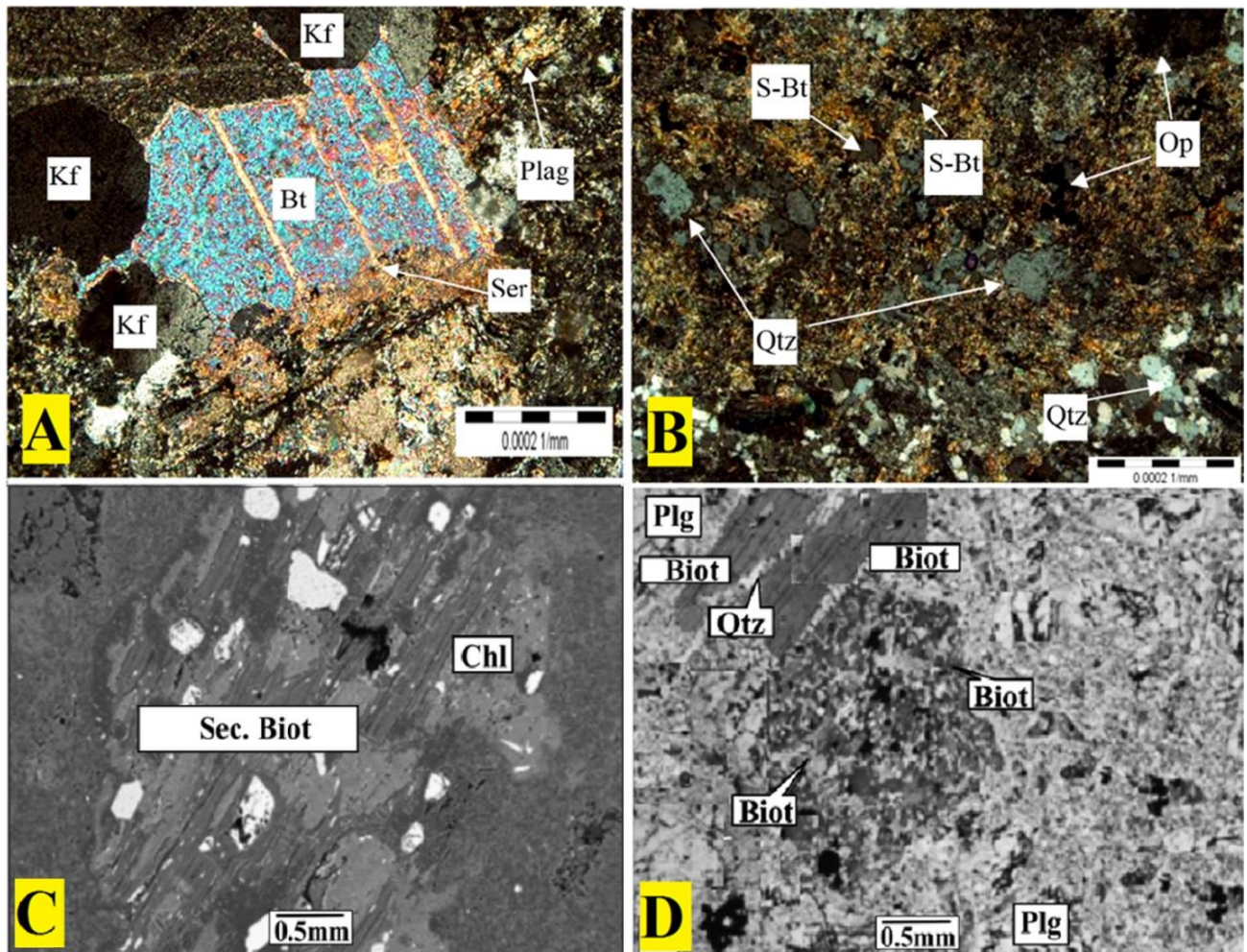
Fig. 2. 6. Photomicrographs of the potassic alteration zone of the Kahang deposit: a) neo-formed biotite (Bt) and KF veinlets, b) secondary biotite (S-Bt) and quartz (Qtz), c) secondary biotite–chlorite assemblage after igneous amphibole associated with the potassic alteration (Afshooni et al., 2013), and d) fine-grained biotite as pseudomorphs of amphibole phenocryst, and coarse-grained biotite cut by a quartz veinlet (Afshooni et al., 2013)

The phyllic alteration zone, developed in the eastern part of the deposit, contains high amounts of quartz, sericite and albite within an argillic matrix. The phyllic alteration is within acidic to intermediate sub-volcanic domes (Harati et al., 2013; Asadi et al., 2014). The pervasive feldspar-destructive phyllic alteration is characterised by sericite, quartz, pyrite, as main minerals and chlorite as an accessory phase. High abundances of quartz in this zone are present within several generations of quartz stockwork veins, veinlets and disseminations. Sericite also occurs as very fine grained to fine grained yellowish grains within groundmass, veins and veinlets (Fig. 2. 7a). Chalcopyrite, zircon, rutile and some clay minerals may be present. In sericitized rocks, K-feldspar is usually transformed into sericite or fine-grained muscovite (Fig. 2. 7b) while biotite and amphibole are converted to chlorite (Fig. 2. 7c). Phyllic alteration grades gradually into argillic alteration as indicated by increasing amounts of clay minerals. Mineralogical changes of typical phyllic alteration occur in granite–granodiorite in the study area.
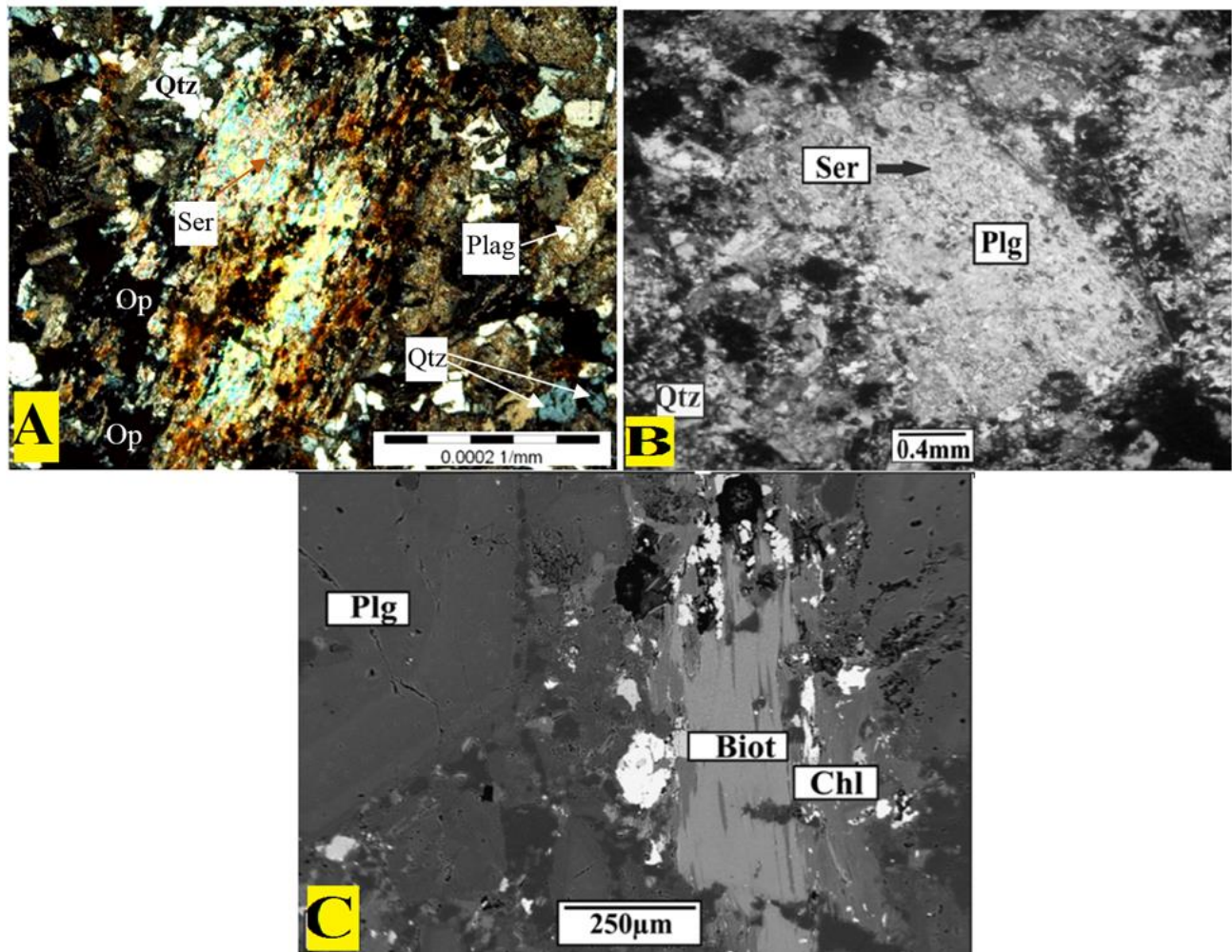
Fig. 2. 7. Photomicrographs of phyllic alteration zone in the Kahang porphyry deposit: a) presence of sericite (Ser) and quartz (Qtz), b) plagioclase (Plg) phenocrysts are pervasively replaced by sericite and surrounded by quartz grains in the phyllic alteration zone (Afshooni et al., 2013), and c) biotite (Biot) altered to chlorite (Chl) in the phyllic alteration zone (Afshooni et al., 2013)

The argillic alteration zone contains intermediate to high levels of alunite (especially in the western and central parts of the deposit) indicative of silicified epithermal alteration within the uppermost part of the deposit, predominantly in sub-volcanic rocks and porphyry and dacite–rhyodacite stocks. This alteration zone is associated with the formation of the clay minerals by extreme base leaching of alumino-silicate minerals (Fig. 2. 8a and b). This zone is represented by kaolinite, illite, and montmorillonite that replaced plagioclase and mafic minerals in andesites and tuffs. Clay occurs as fine grained white to brown coloured patches with increasing amounts of iron oxides within surface outcrops and the outer parts of altered rocks. Jarosite is the second major alteration mineral in this zone. In some places jarosite occupies a huge vol.% ($\geq$ 50%) of the rock probably indicating that it has undergone advanced argillic alteration (e.g., Azadi et al. 2014; Fig. 2. 8c).
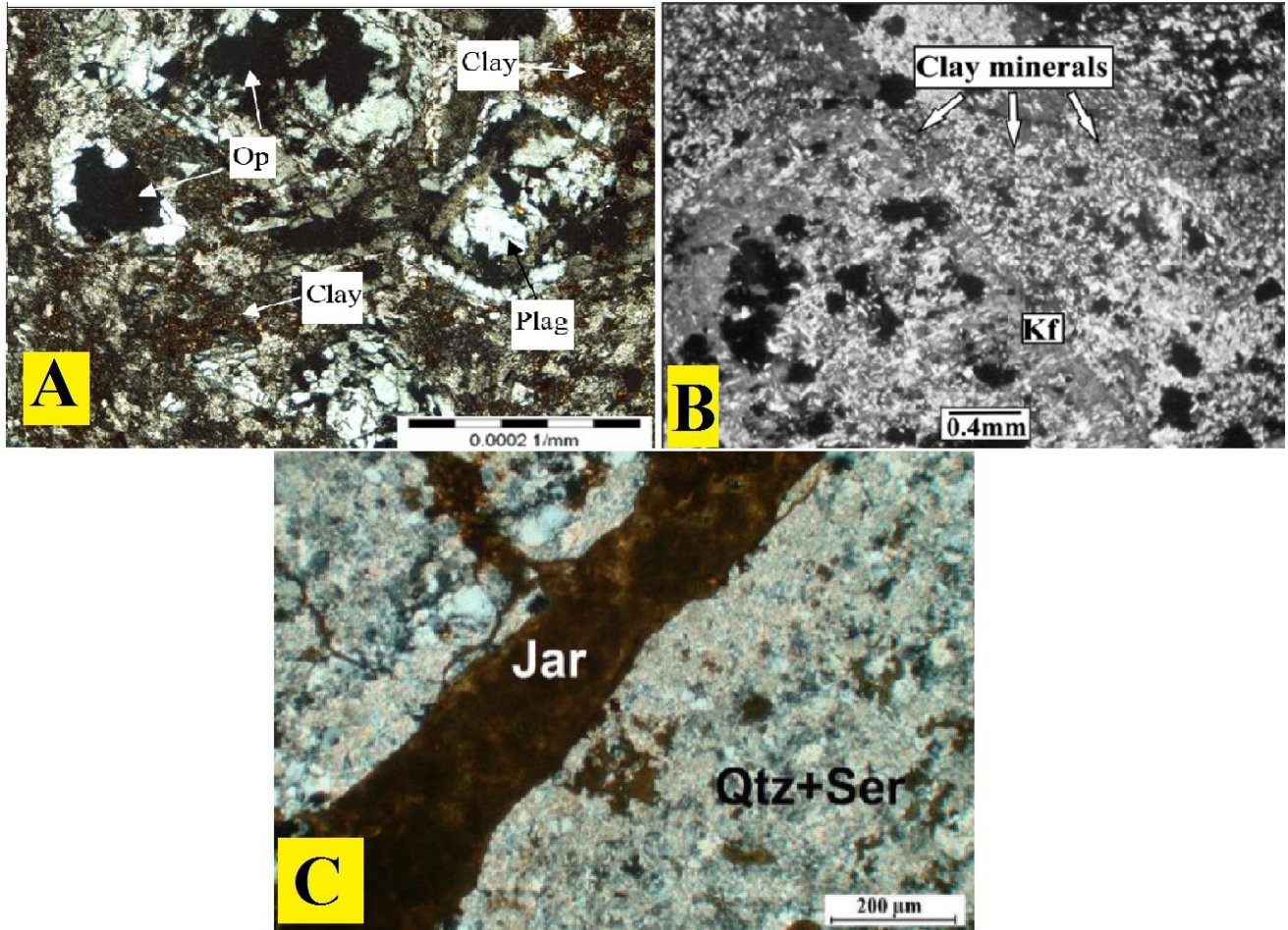
Fig. 2. 8. Photomicrographs of argillic alteration zone in the Kahang porphyry deposit: a) argillic alteration with clay minerals, altered plagioclase (Plag) and opaque minerals (Op), b) K-feldspar (Kf) phenocrysts partially replaced by clay minerals (fine grey material) in argillic alteration zone (Afshooni et al., 2013), and c) Advanced argillic alteration containing jarosite (Jar) overprinted on quartz-sericite (phyllic) alteration (Azadi et al. 2014)

The propylitic alteration zone marks the outer limit of the hydrothermal system and is dominated by chlorite, epidote and albite (Fig. 2. 9). This alteration zone is more developed in margins and upper parts of the deposit. The propylitic alteration is characterized by chlorite, epidote, albite, calcite, sericite, quartz, and clay mineral assemblages that are locally replaced by biotite, plagioclase, hornblende and groundmass.
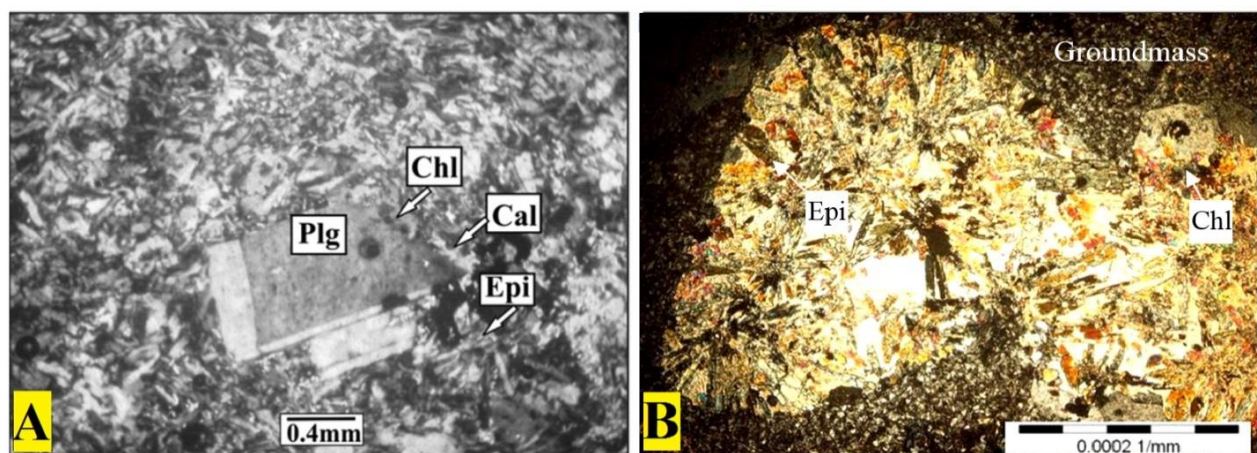
Fig. 2. 9. Photomicrographs of propylitic alteration zone in the Kahang porphyry deposit: a) plagioclase phenocrysts replaced by an aggregate of chlorite (Chl), epidote (Epi) and calcite (Cal) in the propylitic alteration zone (Afshooni et al., 2013), and b) propylitic alteration with pervasive epidote and chlorite

2.3   Dataset Particulars

From the outset, the 3D geological models for the Kahang deposit were created using RockWorks™ v. 15 software with data from 48 boreholes. The data, manipulated in an Excel database, included lithology, alteration type, and ore grades, were modelled using the "Lithoblending" algorithm of the mentioned software. This subsurface data included collar coordinates of drill cores, azimuth and dip (orientation), lithology, alteration, mineralogy and zonation. The project dimensions were 600×660×780 m in the x, y and z

orientations and each voxel had a dimension of 4 m × 4 m × 10 m, respectively. Topographical features of the deposit as well as other related data mentioned above were formed into a 3D geological model (Fig. 2. 10).
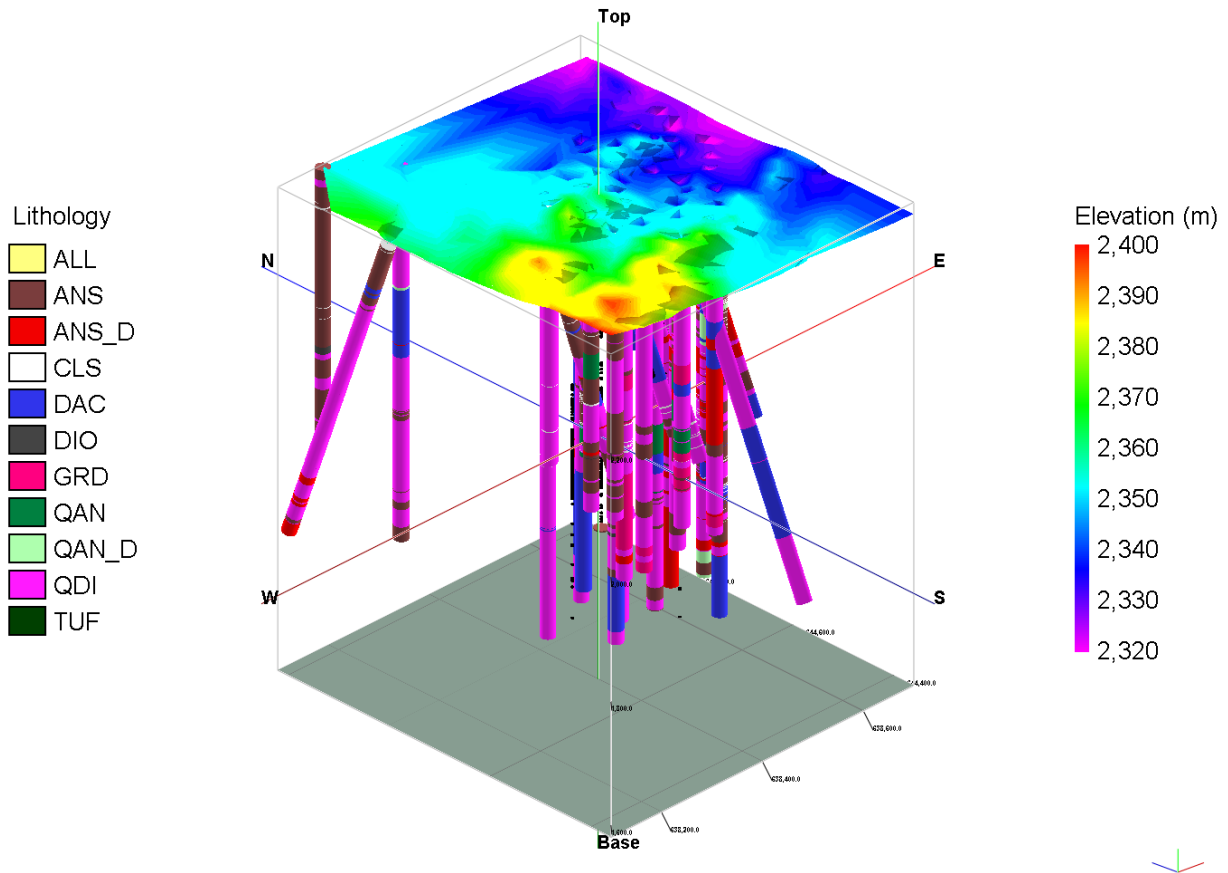
Fig. 2. 10. The locations of drill cores with lithological units within the Kahang deposit and its 3D surface topography

2.4 Assay Quality Assurance and Quality Control

Sampling is the fundamental part in a geochemical investigation for different stages of mineral exploration and environmental purposes. The optimum sampling strategy, to meet the company's objectives, should be based on geochemical methods followed by the field observations, variety of sampling, sample preparation and analytical approaches.

The estimate of reproducibility (precision) allows us to quantify variation of sampling and laboratory analysis which is an integral part of the geochemical data interpretation. As a result, any mistake in sampling and sample preparation may influence the results of the survey (Thompson and Howarth, 1976; Fletcher, 1981; Demetriades, 2014).

From 48 drill holes in the Kahang deposit, 7146 lithogeochemical samples have been collected at 2 m intervals. These samples were analysed using ICP-MS for 48 elements by ALS Chemex (ALS Canada Ltd) and Zarazma Mineral Studies Company certified by Geostats Pty Ltd (Australia: Appendix. A). Detection limits for Cu and Mo are 0.2 ppm and 0.05 ppm, respectively. Moreover, 399 (Appendix. B) randomised samples for Cu determination were selected and analysed for quality assurance and quality control purposes, assessed using Thompson-Howarth error analysis (Thompson and Howarth, 1976 and 1978). The following procedure is suggested for estimation of precision from a minimum of 50 pairs of duplicate samples (Thompson and Howarth, 1976):

(1) From the duplicate analyses, obtain a list of the means and absolute difference.

(2) Arrange a list (in Excel software) in increasing order of concentration means.

(3) From the first 11 results obtain the mean concentration and absolute difference of the two results (controlling samples) from that group (each group contains 11 duplicated/reanalysed samples).

(4) Repeat step 3 for each successive group of 11 results, ignoring any remainder less than 11.

(5) The mean of each replicate pair is plotted against the absolute difference between the two analyses.

The highest value up the % scale on the right axis gives the precision. A precision around 5% is normal. If the precision is around 1%, the Y axis has not been properly calculated with respect to the procedure mentioned above. The precision greater than 5% may have cause for concern and reconsideration. However, the precision for Cu is around 2% in the Kahang deposit with respect to 399 duplicated sample for Cu (Fig.2. 11; Appendix. B).
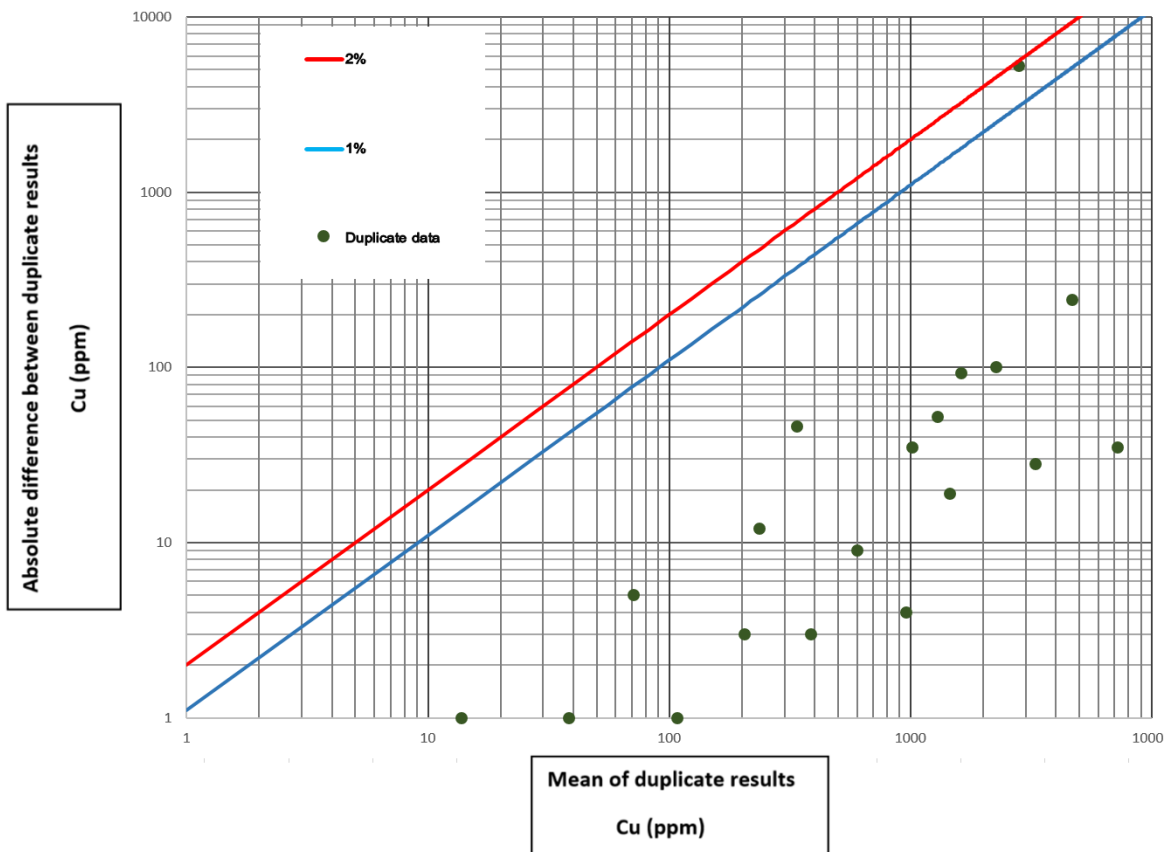
Fig. 2. 11. Estimation of precision of the Cu analyses using diagram of Thompson and Howarth (1978). The mean of the replicate pairs is plotted along the X-axis, the absolute difference of the two results along the Y-axis

2.4.1 Comparison of Geochemical Data Variances via F-Distribution

F-distribution test is used to identify variances equality of duplicated samples (e.g., geochemical data), which was introduce by the famous statistician, Sir Ronald Fisher (1890–1962). This is the theoretical distribution of values which are expected by randomly sampling from a normal population and calculating, for all possible pairs of sample variances, the ratios as follow (Deutsch and Journel, 1998; Davis, 2002; Emery, 2012):

$$F = \frac{S_1^2}{S_2^2} \qquad S_1 \geq S_2$$

<div align="right">Equation 2-1</div>

Where F, S_1 and S_2 represent F-distribution or continuous probability distribution and variances for pair of samples (S_1 = 0.222 and S_2 = 0.219). The variances of double samples vary if the number of observations used in their calculation is small. Therefore, the shape of the F-Distribution is expected to change with changes in terms of samples amounts.

The F-Distribution has two degrees of freedom equal to n_1-1 and n_2-1 in which n_1 and n_2 represent the number of observations equal to 398. Fisher showed that significance level, 1-α (α: probability value) is calculated in the cases of one-tailed and two-tailed distributions depending on the defining alternative hypothesis. The hypotheses are as follows (Fisher and Tippett, 1928; Emery, 2012):

$$\text{Null hypothesis: } H_0 : \sigma_1^2 = \sigma_2^2$$

<div align="right">Equation 2-2</div>

$$\text{Alternative hypothesis: } H_1 : \sigma_1^2 \neq \sigma_2^2$$

<div align="right">Equation 2-3</div>

Where σ_1 and σ_2 denote variances of populations. Based on the F-test, $F_{(398,398)} \approx$ 1.015 which is less than 1.2175 (obtained from Appendix. C) With respect to the confidence level of 97.5% ($\alpha = 0.025$). As a result, the Null hypothesis is acceptable representing that two variances obtained from the paired samples are almost equal to each other.

2.4.2 Comparison of Geochemical Data Means via Paired T-Test

A paired T-test is utilised to compare between means of two populations. The paired sample T-tests typically include a sample of matched pairs of similar units (e.g., Cu wt.% in this scenario), or one group of units that has been tested twice (e.g., Davis, 2002; Emery, 2012; see Appendix. B).

The correct rejection of the null hypothesis (no difference between mean values) can become much more likely. Because half of the sample now depends on the other half, the paired version of Student's T-test has only "n/2–1" degrees of freedom (n is the total number of observations). Pairs are individual test units and the sample has to be doubled to achieve the same number of degrees of freedom.

To achieve the null hypothesis which the true mean difference is zero, the procedure is as follows:

Calculate the difference between the two observations on each pair as follow:

$$d_i = y_i - x_i$$

2. Calculate the mean difference of the pair samples in terms of their grades ($\bar{d}$). The grades means for the paired samples are 0.194% and 0.196% so $\bar{d}$ is 0.002%.

3. Calculate the differences of standard deviation ($S_d = Sd_1^2 - Sd_2^2$) for the pair of samples. To do this, the standard deviation of each sample (sd_1 and sd_2) was calculated and they are equal to 0.468 and 0.472, respectively. Subsequently, standard error of the mean difference was calculated (Equation 2. 5) which is 0.47.

$$SE(\bar{d}) = \frac{S_d}{\sqrt{\bar{n}}}$$

Where $\bar{n}$ is equal to 2 because there is a pair of samples.

4. Calculate the T-test statistic under the null hypothesis, this statistic follows a T-distribution with n − 1 degrees of freedom.

$$T = \frac{\bar{d}}{\mathrm{SE}(\bar{d})\sqrt{\frac{2}{\bar{n}}}}$$

Equation 2-6

Where $\bar{n}$ is the number of paired samples which is 399 (See Appendix. B).

5. Use table of the T-distribution (Appendix. D) to compare value for T to the T_{n-1} distribution. This will give a T critical (p-value), defined as the smallest level of significance at which the null hypothesis would be rejected for a specific test, for the paired T-test (Davis, 2002). The calculated T from paired samples is -0.06 according to the Equation 2. 6 and the T critical for "two-tailed test" resulted from Appendix. D with respect to confidence level (probability value for α = 0.025) of 97.5% is equal to ∓ 1.9629 which indicates that the Null hypothesis is again acceptable. Therefore, the mean values of the paired samples are equal.

Consequently, results derived from T- and Fisher tests show that there is no significant differences between results obtained via raw and controlling samples giving an analytical accuracy in this deposit.

2.5   3D Geological Modelling of the Deposit

2.5.1   Lithological Model

Major rock types in the eastern part of the deposit are sub-volcanic units such as andesite, andesite–diorite, dacite, diorite, granodiorite, quartz andesite, quartz andesite–diorite,

porphyric quartz diorite and tuff (See list of abbreviations). Dacitic rocks host ores in the SE part of the study area.

The most heavily mineralised rocks are composed of porphyritic quartz diorite (Fig. 2. 12), accompanied by granodiorite and dacitic rocks. The quartz-diorites are porphyritic containing phenocrysts of plagioclase, biotite and rounded quartz.

The 3D lithological models in Figs. 2. 12a; 2. 13a; 2. 14a and c were generated using the "Lithoblending" algorithm of RockWorks™ v. 15 software using data from 48 boreholes. RockWorks^{TM} uses a specific lithology modelling algorithm to do this extrapolation. As a result, "lithoblending" is a solid modelling method that is utilised for generating geological solid models (lithology, alteration, mineralisation and zonation) by the RockWorks^{TM} software which assigns the solid model by looking outward horizontally and vertically from each borehole. The "lithoblending" first assigns the voxels immediately surrounding each borehole according to the closest geological units (e.g., lithology). Then, it moves out by a voxel to other neighbouring voxels located in one lithological unit or mineralised zone and this action will continue in this manner until the program encounters a voxel that is already assigned (Sweetkind and Drake, 2007; RockWorks^{TM} 15, 2010; Amit et al., 2014; Eslamian, 2014). Following this, the RockWorks™ v. 15 software looks at the observed lithology intervals (2 m samples' interval in the Kahang deposit), which are viewed in logs and log sections already, and extrapolate the lithology throughout the project, outward from the boreholes. This modelling process basically fills in the blanks between the logs.

The Borehole Manager Fence tools of RockWorks™ are available within the geological model (e.g., lithology) which is utilised to display one or more vertical slices from the inside of a lithological solid model. Subsequently, a lithological fence diagram was built up using RockWorks™ software based on the constructed lithological model (Fig. 2. 12b). This fence diagram contains two sections, showing NW-SE and SW-NE trends, which contain high volume of PQD within the deposit. Furthermore, the andesitic rocks are marginal in this area (Fig. 2. 12b).
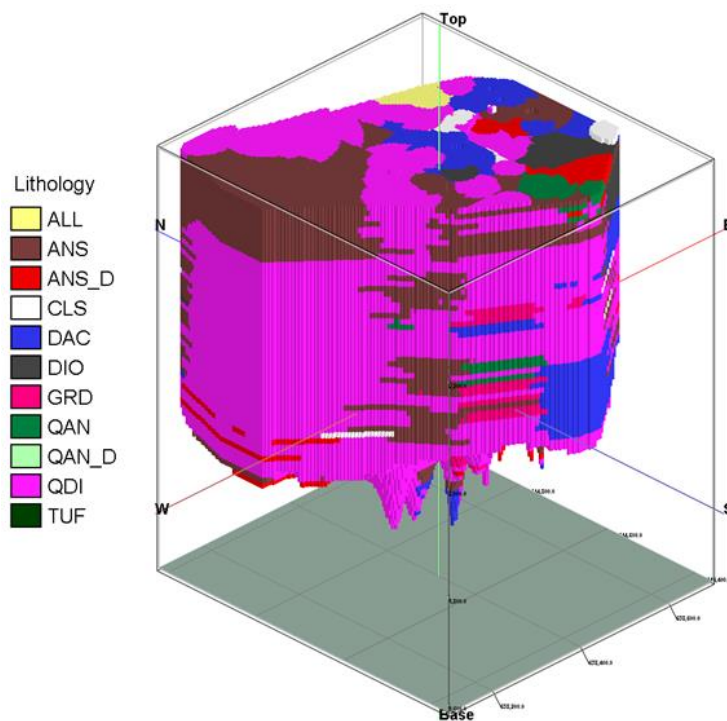
(a)
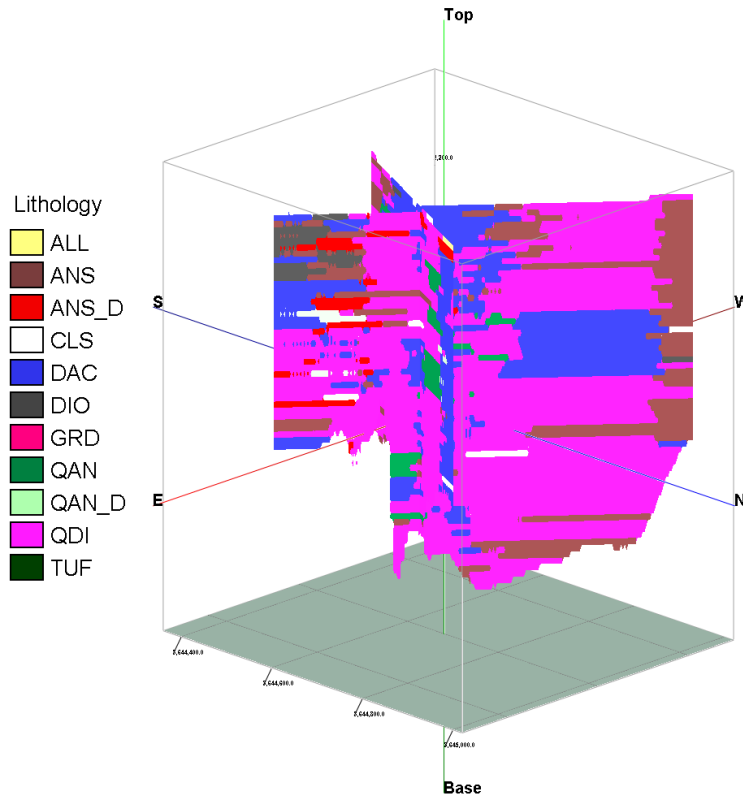
(b)

Fig. 2. 12. a) 3D lithology model of the Kahang eastern part (Yasrebi et al., 2012), and b) lithological fence diagram (See abbreviation list for more details)

2.5.2   3D Alteration Model

Phyllic is the most spatially extensive alteration style in the eastern part of the Kahang deposit, as illustrated in Fig. 2. 13. Potassic alteration is situated at depth and it is deeper towards the eastern part of the deposit, although it does exist near surface in the western part. Argillic and propylitic alterations are low in terms of their volume and occur near surface as illustrated in Fig. 2. 13a. In addition, quartz-sericite and sericite alteration zones are scattered throughout the deposit.

An alteration fence diagram was created based on alteration model, as shown in Fig. 2. 13b. The fence diagram includes two NW-SE and SW-NE sections which reveal that

phyllic alteration is within the uppermost part of the deposit. Potassic alteration is limited and scattered throughout the deposit at depth. Moreover, argillic alteration is dominant along the SE margin of the area.
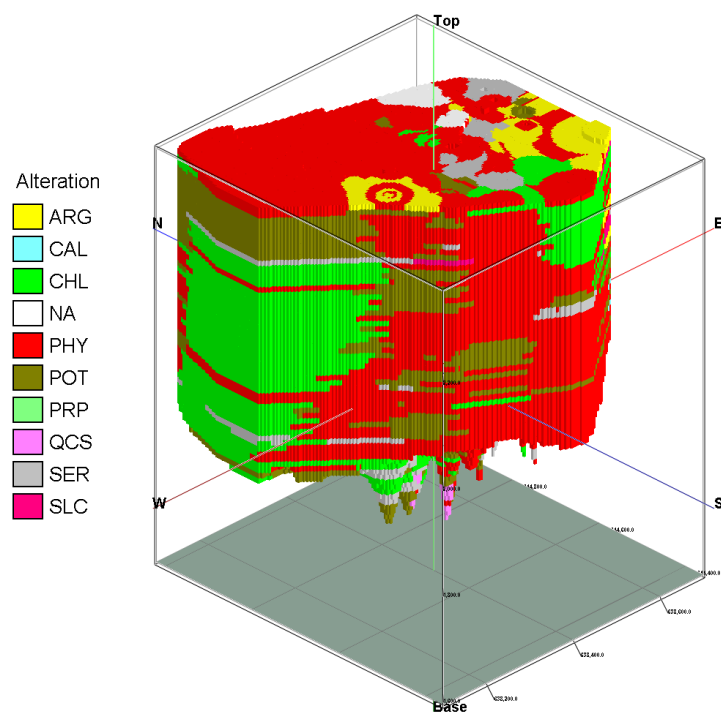
(a)
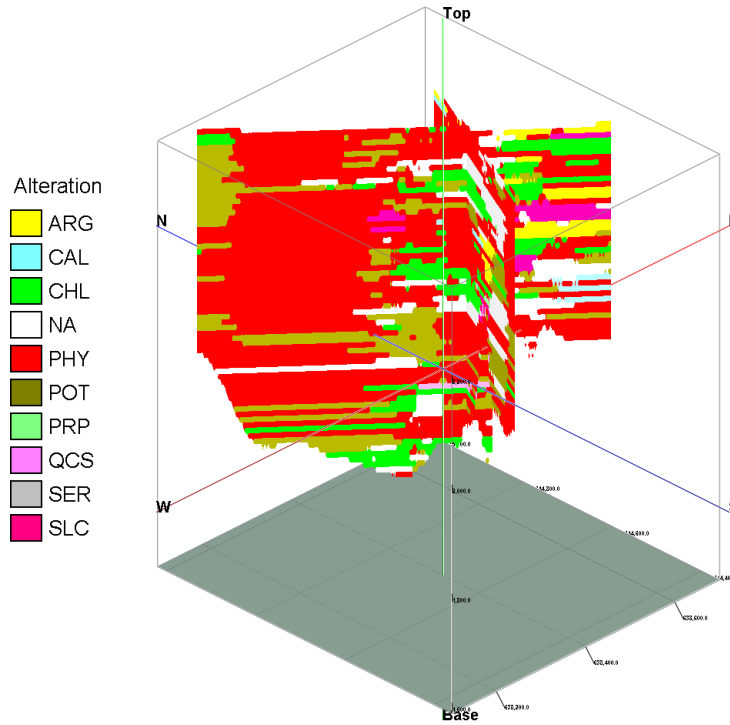
(b)

Fig. 2. 13. a) Alteration model of the Kahang eastern part (Yasrebi et al., 2012), and b) alteration fence diagram (See abbreviation list for more details)

2.5.3 Ore-type Zonation Model

The main criteria for determining of mineralised zones is their index ore minerals. Index ores consist of chalcopyrite and pyrite for hypogene, chalcocite, bornite and covellite for supergene enrichment and malachite, azurite, tenorite and cuprite for oxidation zone (Robb, 2005; Berger et al., 2008; Mihalasky et al., 2013). Studies of the pattern of zonation in the eastern part of the Kahang deposit show that the most significant mineralisation (in terms of ore zone size) is hypogene containing a high percentage of chalcopyrite accompanied by pyrite. This can be easily seen in the 3D models in Fig. 2. 14c and d. Molybdenite is present as vein and veinlet mineralisation with pyrite and chalcopyrite in the hypogene zone (Fig. 2. 14f). The fence diagrams for mineralisation and zonation

models show the existence of high amounts of chalcopyrite and pyrite within the hypogene zone (Figs. 14b and d).
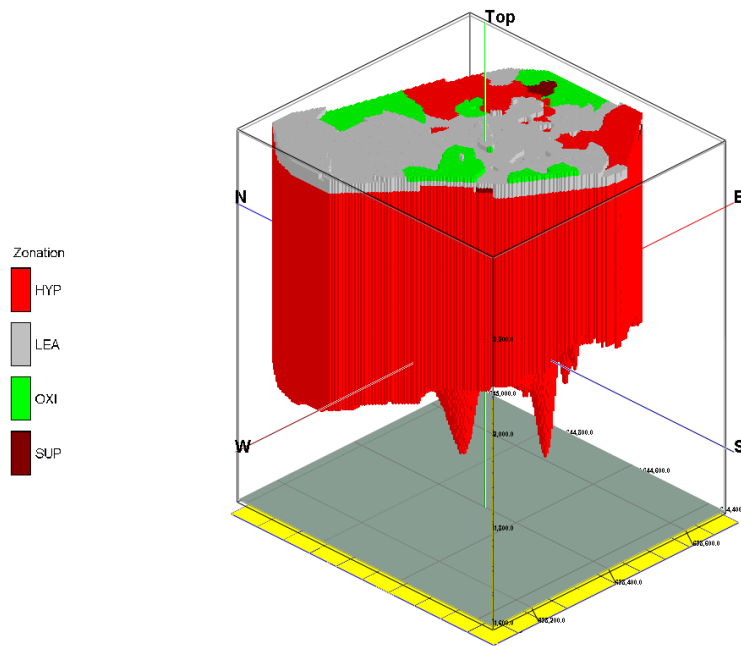
(a)
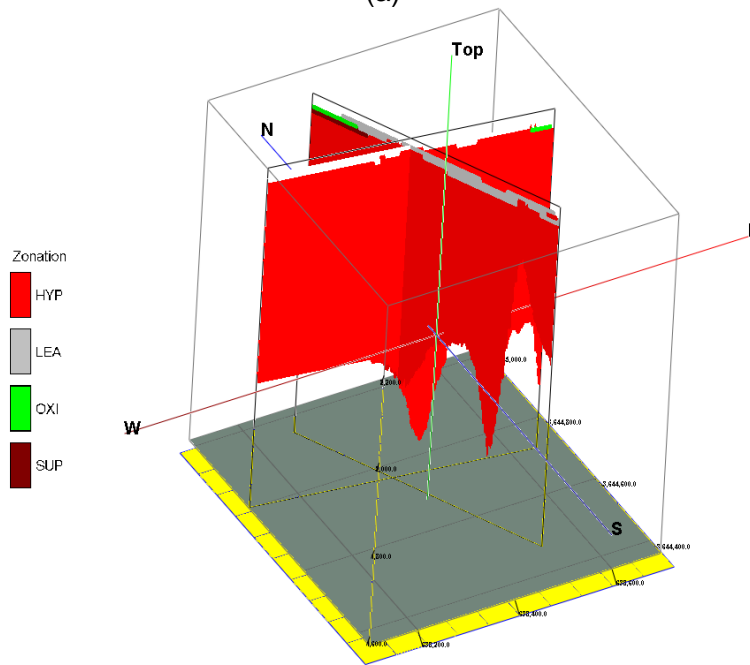
(b)
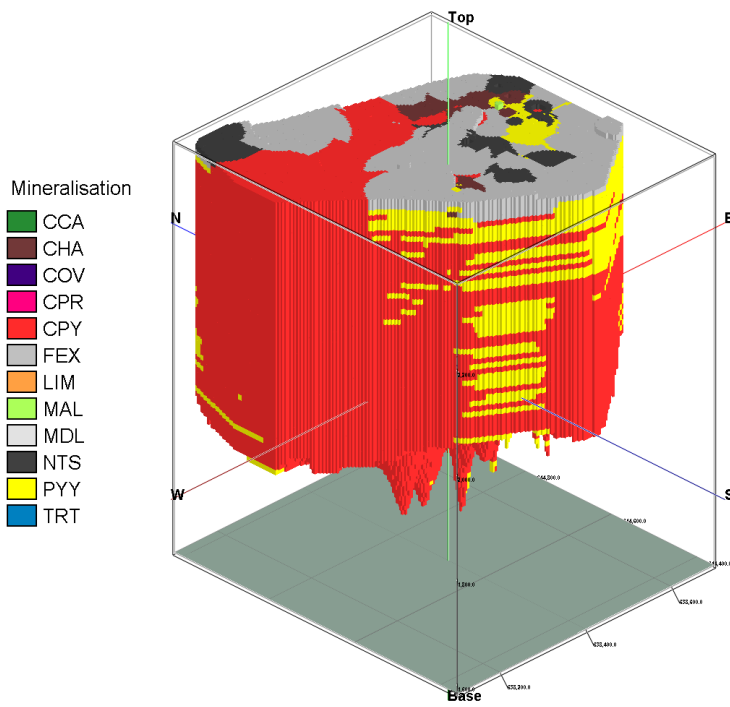
(c)
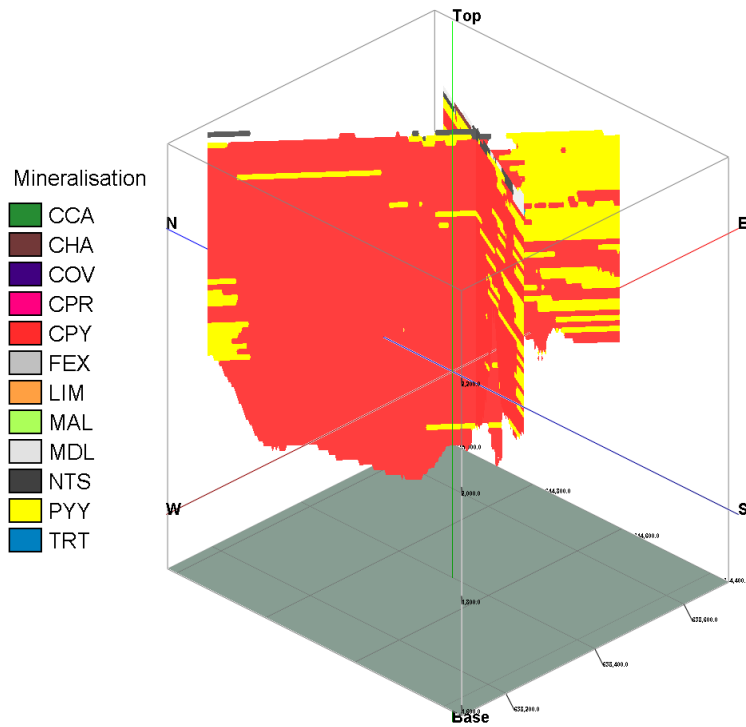
(d)
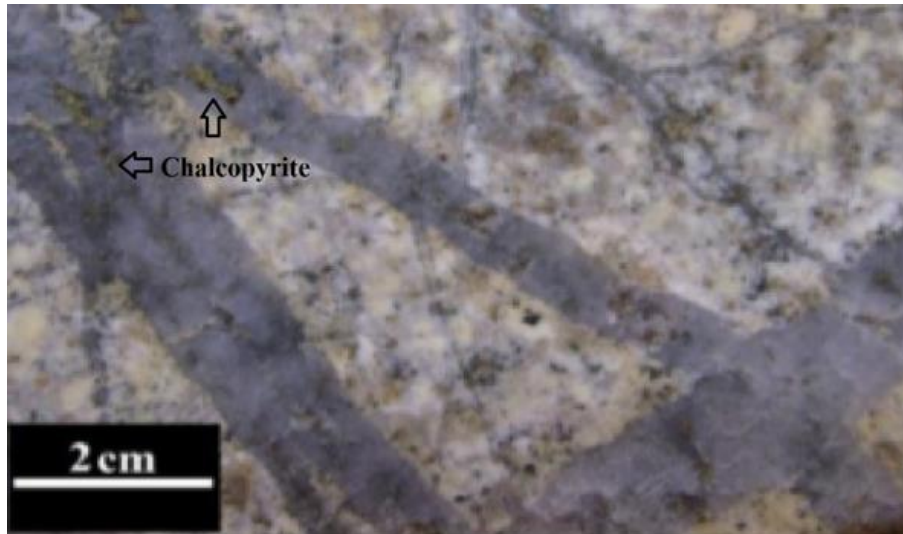
(e)
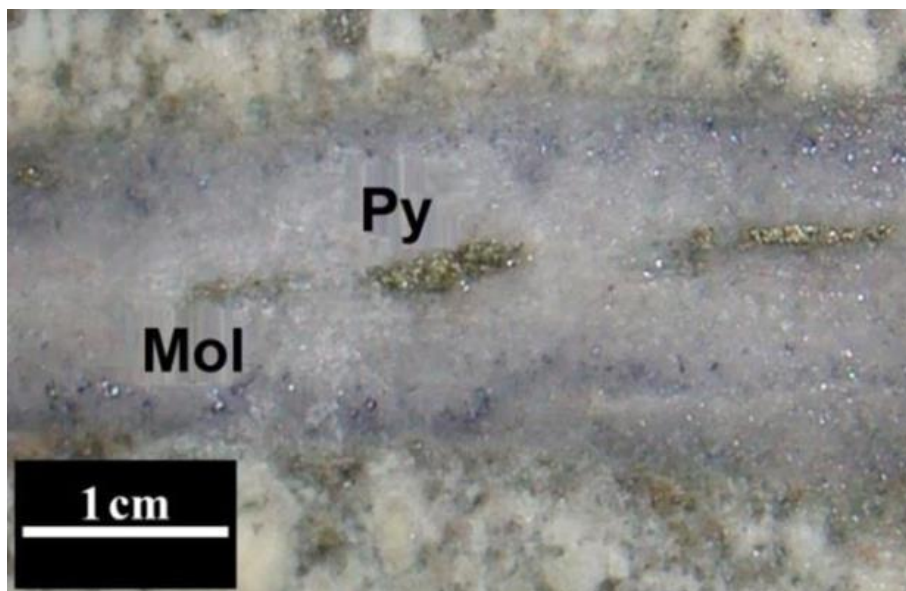
(f)

Fig. 2. 14. a) 3D ore-type zonation model, b) fence diagram of ore-type zonation model, c) 3D dominant ore minerals, d); fence diagram of dominant ore minerals, e) chalcopyrite in stockwork copper mineralisation from hypogene zone, and f) pyrite (Py) and molybdenite (Mol) mineralisation in hypogene zone (See abbreviation list for more details)

CHAPTER THREE. Concentration-Volume (C-V) Fractal Modelling for Separation of Mineralised Zones

3.1 Introduction

Identification of supergene enrichment, hypogene, oxidized, leached zones from 'barren' host rocks (weakly mineralised zones) is one of the major purposes of ore deposit modelling (Cheng et al., 1994; Li et al., 2003; Gałuszka, 2007; Makkonen et al., 2008; Zeng et al., 2009; Afzal et al., 2012). Conventional geological methods for zone recognition in porphyry deposits are generally based on mineralogical, petrographical and alteration criteria (Schwartz, 1947; Beane, 1982; Sillitoe, 1997; Berger et al., 2008). A conceptual model for lateral and vertical variations in alteration style was initially suggested by Lowell (1968) and later by Lowell and Guilbert (1970), based on deposits in the North American Cordillera Orogenic Belt. These models have been further developed by Cox and Singer (1986) and Melfos et al. (2002). In addition, fluid inclusion (e.g., Roedder, 1971; Nash, 1976; Ulrich et al., 2001; Asghari and Hezarkhani, 2008) and S isotope studies (Wilson et al., 2007) have been utilised for determination of different zones within porphyry Cu deposits. The mentioned models above do not consider the distribution of elemental concentrations within ore deposits and do not rely on resource modelling (See chapter 1, sections 1.1 and 1.3 for more information). It is a fact that ore grades vary with changes in geological properties such as mineralogy and alteration zones in porphyry Cu deposits (Zarasvandi et al., 2005; Berger et al., 2008; Pirajno, 2009; Mihalasky et al., 2013; Xiao et al., 2014). Different geological clarifications would be presented for defining boundaries of different zones in porphyry Cu deposits which may also lead to different results if the ore element grade distribution is not taken into consideration (Afzal et al., 2013c; Wang et al., 2013; Soltani et al., 2014; Sun and Liu, 2014; Yang et al., 2015).

3.2   Geometry of Natural Processes

The famous Greek mathematician Pythagoras of Samos, around 2500 years ago, suggested that natural processes and behaviours are in accordance with mathematical principles (Zhmud, 1989; Neimark, 2003; Hejazi, 2005; Neto, 2006; Rainer and Ruff, 2013). This hypothesis was not accepted by most scientists until the twentieth century. Nowadays, models and theories based on mathematics are widely used by geoscientists to better interpret natural processes.

Lobachevsky and Bolyai (around 1830) established non-Euclidian geometry in the 19th century which showed that nature is not just in compliance with Euclidian geometry. Benoît Mandelbrot and Gaston Julia (1959) invented a new geometry called "Fractal". However, in the 1960s, Mandelbrot started writing about self-similarity in papers such as "How Long the Coast of Britain Is". Mandelbrot reached the point where measuring of any length with a large scale (e.g., continental and regional) is more time consuming when measured by a small scale (e.g., local scale mapping). However, how long this measurement takes is relevant to the various feature changes of the coastline which does not follow the regular dimensions. On the other hand, fractals are not limited to Euclidian geometric patterns, but can also describe processes such as structure and texture of minerals and rocks in thin/polished sections (Mandelbrot, 1983; Das and Edgar, 2005; Afzal et al., 2013c). In addition, this theory presented a geometry in which the features do not follow up dimensions with integer numbers and are not discrete, but they meet decimal, irregular and continuous numbers. The general agreement is that theoretical fractals are infinitely self-similar, iterated and detailed mathematical features containing

fractal dimensions, of which many examples have been formulated and examined precisely (Mandelbrot, 1983; Falconer, 1991; Falconer and Hu 2001). The self-similarity of a feature is its shape on a much smaller scale, as depicted in Fig. 3. 1. Fractal patterns with different degrees of self-similarity have been rendered or studied in images, sounds and structures in nature (Turcotte, 1986; Cheng et al., 1994; Cheng, 1999; Zuo et al., 2009a; Deng et al., 2010; Wang et al., 2010a and b; Afzal et al., 2011and 2014; Yasrebi et al., 2013a, b and 2014).
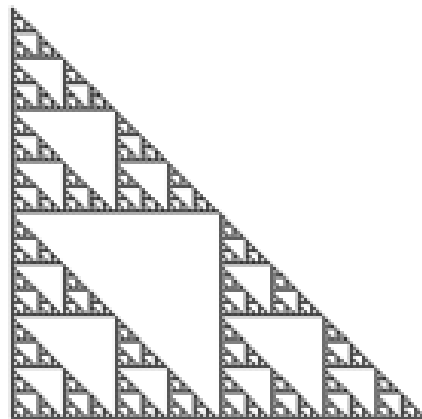
Fig. 3. 1. Self-similarity in a triangle

The word "fractal" was coined by Mandelbrot (1976) from the Latin word "fractus" or "fractum", meaning broken, which he has applied to objects that were too irregular to be defined by ordinary Euclidean geometry (Davis, 2002). Mandelbrot (1983) wrote a famous book entitled "Fractal Geometry of Nature" and introduced "fractal" as a new branch of non-Euclidian geometry.

The fractal geometry of each shape and its complications are shown in the form of real numbers, as in Euclidean geometry concepts of measured angle, length, area and volume. There are fractal dimensions which are not integers and can be real and decimal such as 1.4, 2.3 and 3.5 (Fig. 3. 2).
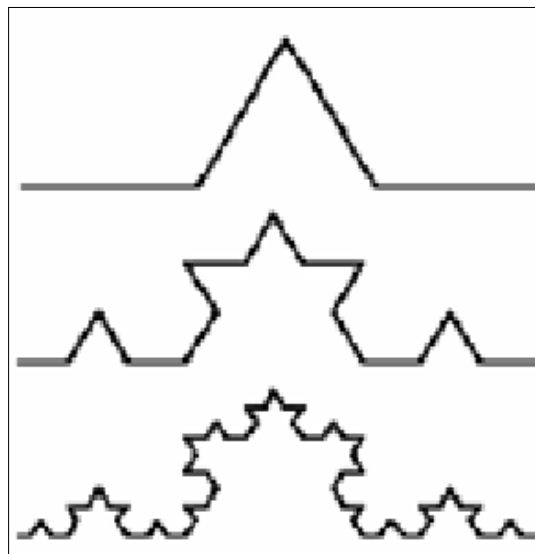
Fig. 3. 2. Changes in dimensions of a fractal shape of Koch Curve (Zhu et al., 2003)

Many studies have indicated that hydrothermal ore deposits such as porphyry Cu, orogenic gold and epithermal polymetallic deposits present non-Euclidean variations in ore element values in rocks, alterations and related surface materials such as water, soils, stream sediments, humus and vegetation (Cheng, 2007; Cheng and Agterberg, 2009; Afzal et al., 2011 and 2013a, c; Heidari et al., 2013; Yasrebi et al., 2013a; Soltani et al., 2014). As a result, variation of fractal dimensions in geochemical data can furnish complementary information and applicable criteria to delineate mineralised and 'barren' zones from host rocks within a studied area. Different log–log plots in fractal/multifractal models are proper tools for separation of geological populations based on geochemical

88

data since threshold values (breakpoints) can be determined in those log-log plots (Cheng et al., 1994; Agterberg et al., 1996). These geochemical threshold values are identified via fractal analysis which is usually correlated using geological field observations (e.g., mineralisation, alteration, lithological units and ore seams). In other words, fractal analysis is able to indicate differences within mineralisation, alteration, lithology and zonation of ore deposits especially in hydrothermal occurrences such as porphyry Cu deposits (Goncalves et al., 2001; Cheng, 2007; Carranza, 2008; Carranza et al., 2009; Cheng and Agterberg, 2009; Afzal et al., 2011 and 2012). However, proper knowledge of the geological and geochemical aspects of a deposit is important in order to identify characteristics of geochemical populations on the basis of fractal analysis (Cheng, 1999; Sim et al., 1999; Li et al., 2003; Carranza, 2009; Carranza and Sadeghi, 2010).

The aim of this chapter is to use a Concentration-Volume (C-V) fractal model to delineate Cu and Mo mineralised zones in the Kahang porphyry deposit of Central Iran in order to generate an optimised block model for determination of an ultimate pit limit and a best mining strategy. Moreover, to correlate and validate the results, the outcomes of the fractal models will be compared with geological models using a logratio matrix proposed by Carranza (2011).

3.3   Statistical Characteristics

In the studied deposit, 7146 core samples were collected from 48 boreholes at 2 m intervals, and analysed by inductively coupled plasma mass spectrometry (ICP-MS) for Cu and Mo (See section 2.3 and Appendix. A). The Cu and Mo distribution functions are

not normal, with Cu and Mo averages of 0.166 wt.% and 28 ppm, respectively (Fig. 3. 3). The elemental distributions show an L shape with most of the volume of the deposit containing low grades for Cu and Mo. Most values of Cu and Mo are lower than 1 wt.% and 200 ppm, respectively. Variation between maximum and minimum of these data shows a wide range among elemental concentrations (Table. 3. 1). Based on the abnormal elemental distributions, Cu and Mo medians are assumed to be equal to threshold values for separation of 'barren' host rocks and mineralisation which are 0.08 wt.% for Cu and 9.9 ppm for Mo (Davis, 2002). In this deposit, 33 and 14979 samples were determined from 11 and 42 boreholes respectively out of a total of 48 boreholes carried out in the deposit for density and RQD analysis, respectively (Tables. 3. 2 and 3. 3). Figures for the original data sets used: Cu and Mo grades, RQD and density values have been generated using MATLAB software, as depicted in Fig. 3. 4. Since the Kahang deposit is at a pre-feasibility stage, and the main target is Cu, only 399 randomised samples for Cu (section 2.4 and Appendix. B) were analysed. The error for Cu is 4.04%, calculated from the following equation (Govett, 1983):

$$e = \frac{2}{n} \sum_{i=1}^{n} \frac{|Xi - Yi|}{Xi + Yi}$$

Equation 3-1

Where e and n are error value, amount of re-analysed samples (399 duplicated sample for Cu). X_i and Y_i denote measured values for duplicated samples (See Appendix. B, second and fourth column for Cu wt.% in Table. B. 1 for X_i and Y_i).
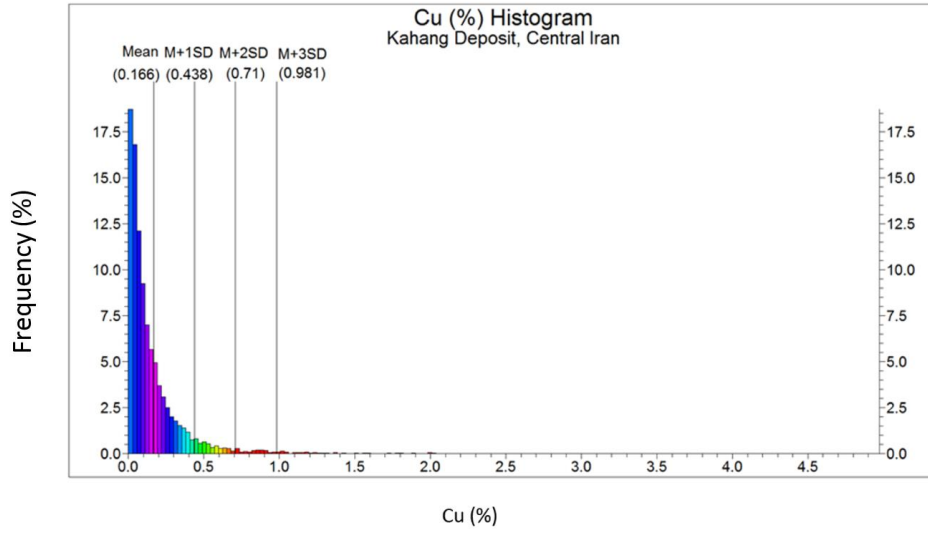
(a)
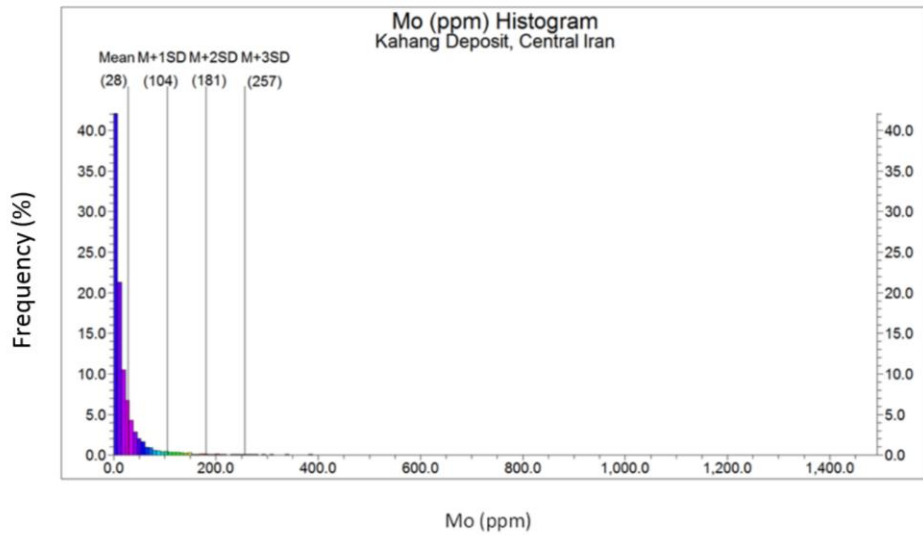
(b)

Fig. 3. 3. Histograms for data from the Kahang deposit: a) Cu wt.%, and b) Mo ppm

Table. 3. 1. Statistical characteristics for Cu and Mo

Elements Grades	Minimum Value	Maximum Value	Range	Mean	Standard Deviation	Median	Variance	Skewness	Kurtosis
Cu (wt.%)	0.0003	4.92	4.91	0.16	0.271	0.087	0.073	6.6	74.5
Mo (ppm)	0.5	1,479	1,478.5	28.27	76.178	9.9	5,803.132	8.4	96.1

Table. 3. 2. Density analysis from 11 boreholes in the Kahang deposit (See abbreviation list for rock type)

BHID	Depth (m)	Rock Type	Density (t/m³)	BHID	Depth (m)	Rock Type	Density (t/m³)
KAG_27	151.7	PQD	2.67	KAG_50	148.6	PQD	2.68
KAG_27	459.55	PQD	2.8	KAG_50	266.1	QAN-D	2.67
KAG_27	580.3	ANS	2.7	KAG_50	332.95	DAC	2.74
KAG_28	65.7	PQD	2.67	KAG_51	78.6	DAC	2.63
KAG_28	232.1	PQD	2.66	KAG_51	174.2	ANS-D	2.59
KAG_30	141.5	PQD	2.7	KAG_51	547.3	PQD	2.81
KAG_30	240.7	PQD	2.72	KAG_52	235.85	PQD	2.72
KAG_33	51.2	DAC	2.7	KAG_52	376.45	PQD	2.69
KAG_33	128.15	DAC	2.63	KAG_52	462.55	PQD	2.69
KAG_33	223.6	DAC	2.71	KAG_52	530	PQD	2.73
KAG_33	348.8	DAC	2.64	KAG_54	644.5	DAC	2.7
KAG_36	72.9	PQD	2.34	KAG_55	73.15	QAN	2.62
KAG_36	327.9	DAC	2.69	KAG_55	108.4	QAN	2.69
KAG_36	421.15	ANS	2.68	KAG_55	267.55	QAN	2.77
KAG_49	359.75	ANS	2.71	KAG_55	470.85	PQD	2.62
KAG_49	545.25	PQD	2.76	KAG_55	361.75	ANS	2.71
				KAG-55	634.55	PQD	2.7

Table. 3. 3. Distribution number of RQD samples among drill cores in the Kahang deposit

Drillcore	Kag_03	Kag_04	Kag_05	Kag_06	Kag_07	Kag_08	Kag_09	Kag_10	Kag_11	Kag_12	Kag_13	Kag_14	Kag_15	Kag_17	Kag_18	Kag_19
Samples	547	406	265	382	440	438	401	351	428	504	372	267	239	291	265	395
Drillcore	Kag_20	Kag_27	Kag_28	Kag_30	Kag_33	Kag_36	Kag_38	Kag_41	Kag_42	Kag_43	Kag_46	Kag_47	Kag_48	Kag_49	Kag_50	Kag_51
Samples	329	330	437	377	131	435	301	458	328	254	437	310	434	541	331	341
Drillcore	Kag_52	Kag_54	Kag_55	Kag_57	Kag_59	KH-DDH02		KH-DDH09		KH-DDH10		KH-DDH11		KH-DDH12		
Samples	434	444	365	415	353	128		210		274		279		309		
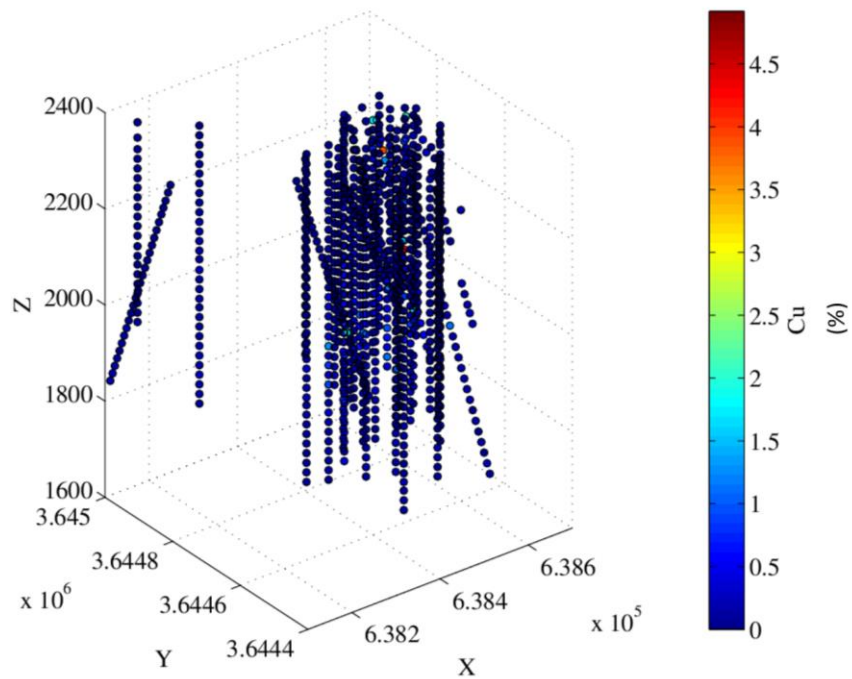
(a)
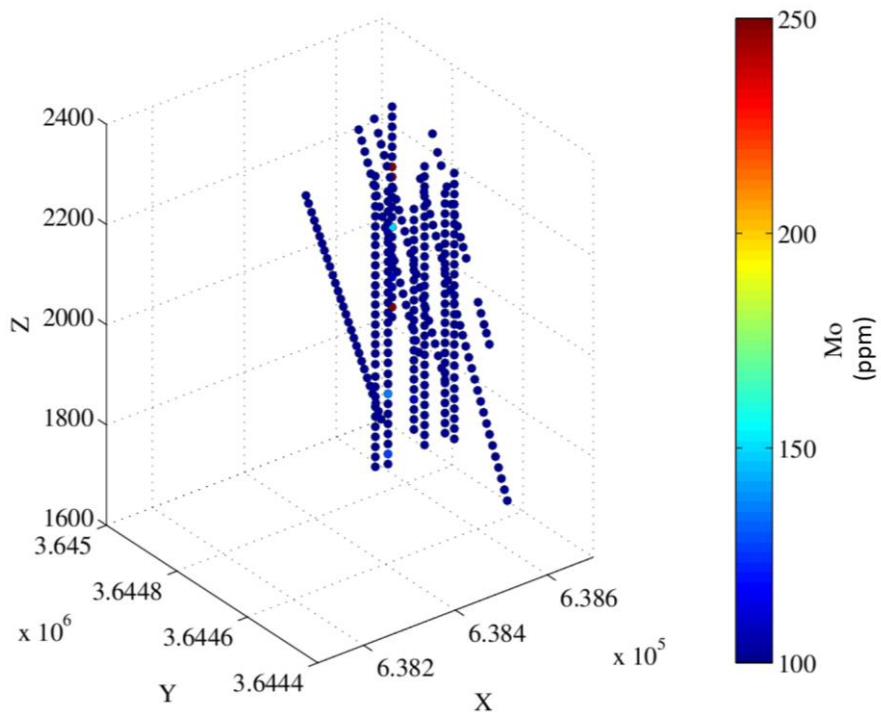
(b)
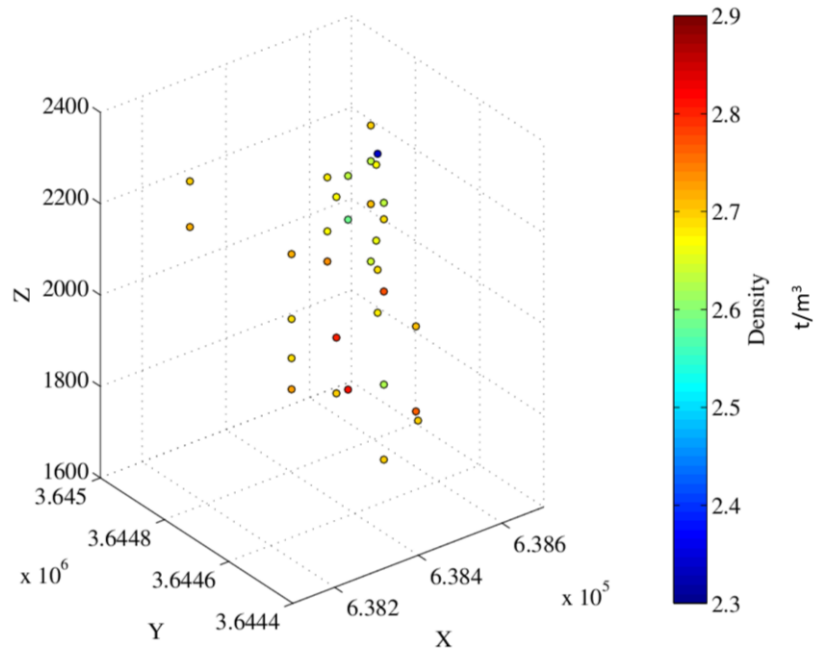
(c)
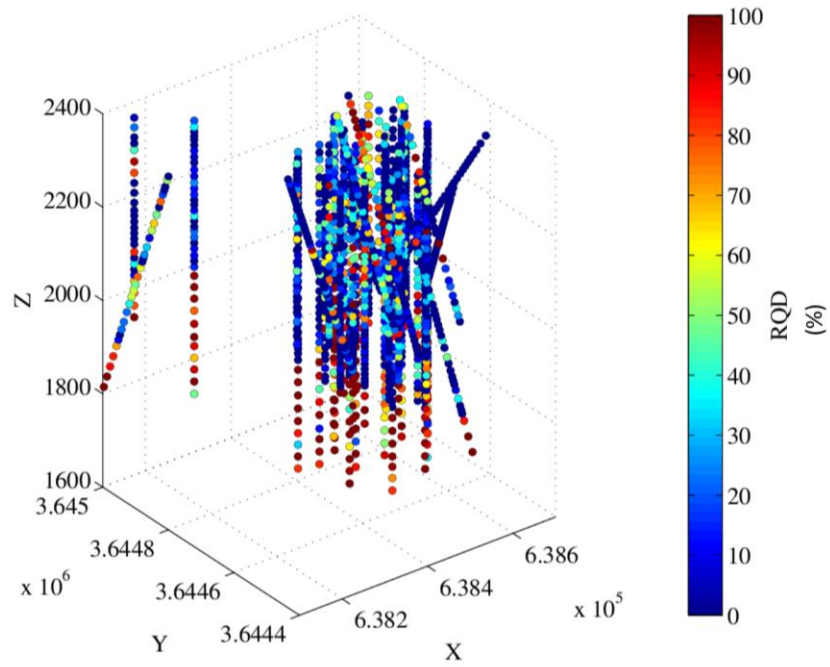
(d)

Fig. 3. 4. 3D maps for original datasets: a) Cu wt.%, b) Mo ppm, c) density t/m^3, and d) RQD %

3.4   Block Modelling

Choosing a suitable voxel size for evaluation of a reserve/resource is crucial for minimising errors (Asghari and Madani Esfahani, 2013; Shahbeik et al., 2014). This problem has been assessed for estimated block models using different geostatistical methods such as ordinary kriging (OK) and inverse distance weighted (IDW). Results obtained by the estimation methods relate to the determination of voxel size in block modelling (David, 1970; Cressie, 1993; Soltani Mohammadi et al., 2012).

Utilising a larger voxel size will increase the averaging effect in the estimated block model in terms of concentrations, geophysical data, rock mechanical data and other attributes. Additionally, a smaller voxel size will show more details, but potentially more error in an anisotropic environment (Journel and Huijbregts, 1978). On the other hand, reducing the voxel size results in an increase in estimated errors (variance and standard deviation) for the final block model. Moreover, increasing the voxel size in the block model changes the higher or lower grades of mineralised zones by smoothing of these points with high or low values within a large voxel.

Identification of an optimised voxel size is one of the most important aspects of building an estimated 3D block model. Therefore, it is necessary to select an optimal voxel size with respect to the deposit geometry and drilling pattern because most of the geostatistical software, e.g. RockWorks^{TM} which was employed in this study, estimates an ultimate block model based on the closest points considering particular parameters such as ore element concentrations (Verly, 1984; Journel, 1993).

Statistical parameters such as mean and median can be used for recognition of optimum voxel dimensions in various types of ore deposits (David, 1970; Journel and Huijbregts, 1978).

David (1970) proposed an applicable method for an operation based on geometrical particulars of the different types of ore deposits and grid drilling. Based on the method, voxel dimensions are calculated as follows:

a)   Length and width of each voxel is equal to between half and quarter of the distance between the drill cores according to along the least variability deposit.

b)   Height of each voxel is delineated due to the type of the deposit. In 'massive' deposits such as magmatic deposits (e.g., porphyry deposits), the parameter is equal to the height of excavating benches in the open pit mines (Hustrulid and Kuchta, 2006).

For recognition of the optimum voxel dimensions in the Kahang Cu porphyry deposit, statistical characteristics consisting of mean, median and median absolute deviation (MAD) were utilised. In addition, standard deviation (SD) was used for further comparison and validation through the obtained results in the different scenarios of voxel size. If SDs include very low changes then voxel size selection is carried out based on the Cu estimated mean. The voxel sizes with the lowest value of Cu mean should be selected because this is a worse scenario for mine planning and exploitation due to conservative

mine strategy and risk analysis. Moreover, the median and MAD are used for determination of voxel sizes and development of conventional method, as proposed by David (1970).

The 2D map which indicated the location of 48 boreholes drilled in the Kahang deposit was constructed by RockWorks™ v. 15 software (Fig. 3. 5a). From this, a grid model of the boreholes on the surface was created to illustrate drill core locations including the location information, symbol style and borehole names for the studied area. Since the grid drilling pattern within this deposit is not homogeneous and systematic, 14 pairs of closest boreholes were selected for an optimum voxel size investigation because this action can improve the interpolation of voxel values (Cu grades in this scenario) that lie between data point clusters (Fig. 3. 6). The particulars of these pairs are revealed in the Table. 3. 4. The distance range of the selected boreholes varies between 5 to 27 m. For identification of an optimum voxel size in the directions of X and Y, the vector analysis was employed. The ranges of distances in the X and Y directions are 0.38-18.97 m and 3.47-25.97 m, respectively (Table. 3. 4). Based on the David (1970) method (as described in the last page), the voxel size in the Z direction was determined as 10 m on the basis of the ore deposit geometry and particularly height of the working bench.
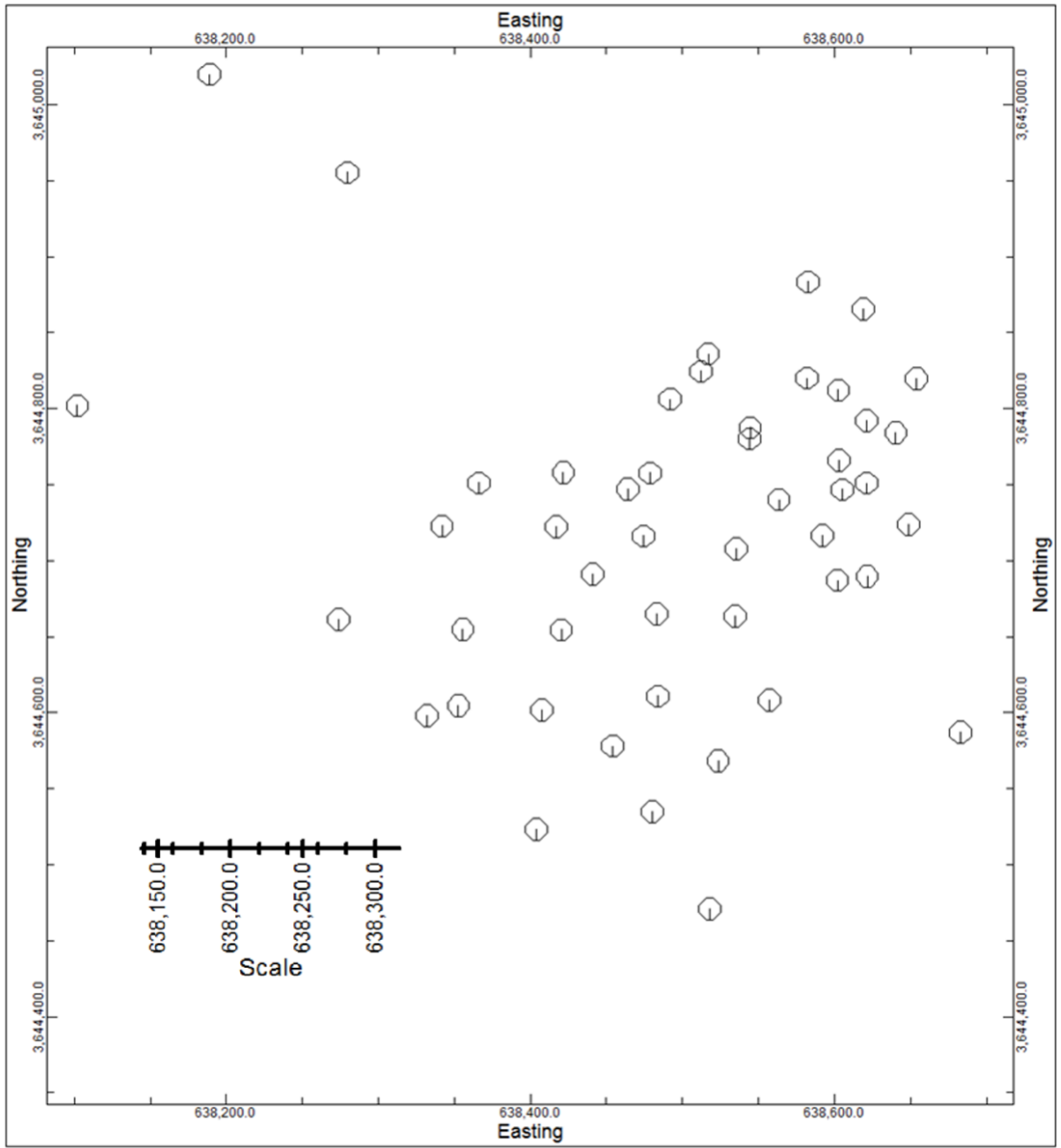
(a)
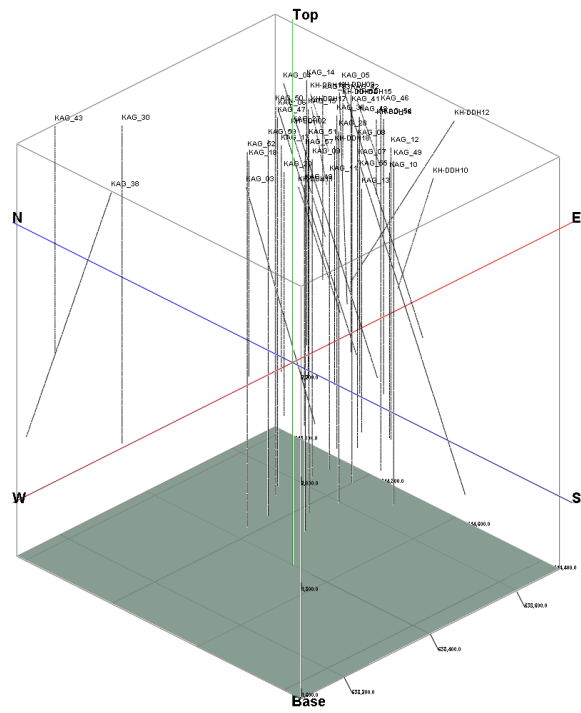
(b)

(c)

Fig. 3. 5. a) 2D, b) 3D, and c) Google Earth maps of the grid drilling in the Kahang deposit

In the first step, the mean of distances between selected borehole pairs were calculated, as depicted in Table. 3. 5. In the simple method, the range of voxel sizes in the X and Y directions was considered between half and quarter of the mean value which is equal to 4.67-9.34 m. Moreover, the ranges of the voxel size according to median and MAD values are 5-10 m and 2.5-5 m, respectively.
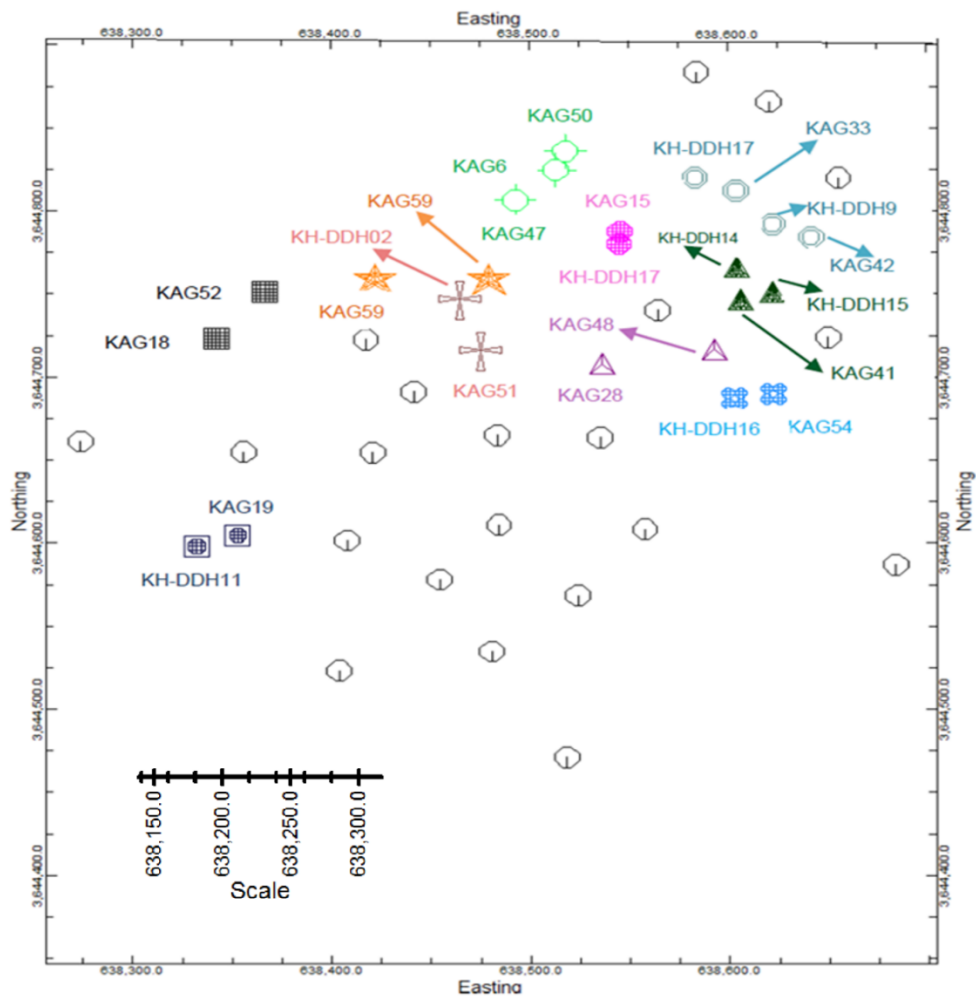
Fig. 3. 6. Boreholes location (ignoring the three isolated boreholes in the NW) map in the Kahang deposit with selected closest borehole pairs

In the second step, the voxel size was investigated via vector analysis between boreholes based on the closest surface location on the 2D map. The mean values in the directions of X and Y are 12.91 m and 11.76 m, respectively, meaning that the voxel size varies between 3.23 m and 6.46 m in X and between 2.94 m and 5.88 m in Y. Based on the median values, the voxel size value ranges are 3.8-7.6 m and 2.32-4.65 m in terms of X and Y. The MAD values for X and Y are less than 3 m indicating that the voxel size is less than 1 m, resulting in an increase in the error for the construction of a final block model (Goovaerts, 1997). For a massive ore body, and homogenous distribution of element concentrations in porphyry deposits, X and Y directions have equal values in terms of voxel size (Davis, 2002). As a result, five different voxel size scenarios of 5 m x 5 m x 5 m, 4 m ✕ 4 m ✕ 10 m, 5 m ✕ 5 m ✕ 10 m, 10 m x 10 m x 10 m and 15 m x 15 m x 15 m have been allocated to build the Kahang deposit pre-Cu block model. In order to find an accurate voxel size, declustering should be conducted previously because it is believed that the proper voxel size with respect to the different voxel alternatives is the one with the minimum standard deviation. In addition, Cu mean of a pre-Cu block model with an accurate voxels size should be close to Cu mean value obtained from the declustered data (e.g., Fig. 3. 7; Table. 3. 6; Deutsch and Journel, 1998; Richmond, 2002; Emery and Ortiz, 2005 and 2011; Olea, 2007; Sadeghi et al., 2015).

3.4.1 Cell Declustering

Data are often spatially clustered which makes it difficult to determine whether they are representative of the entire area of interest (Fig. 3. 7). To obtain a representative distribution, one approach is to assign declustering weights whereby values in cells with

more data receive less weight than those in sparsely sampled areas. The grid drilling in the area is non-uniform and the data need to be declustered. This operation was carried out using the Declus program which incorporates the GSLIB library (Deutsch and Journel, 1998). The Cu mean and standard deviation of the declustered data are 0.145 wt.% and 0.22077. Subsequently, the Cu block models were generated by IDW utilising RockWorks^{TM} software. For determination of optimum voxel dimensions based on the statistical parameters depicted in Table. 3. 5, standard deviation (SD) and an average Cu value have been calculated.
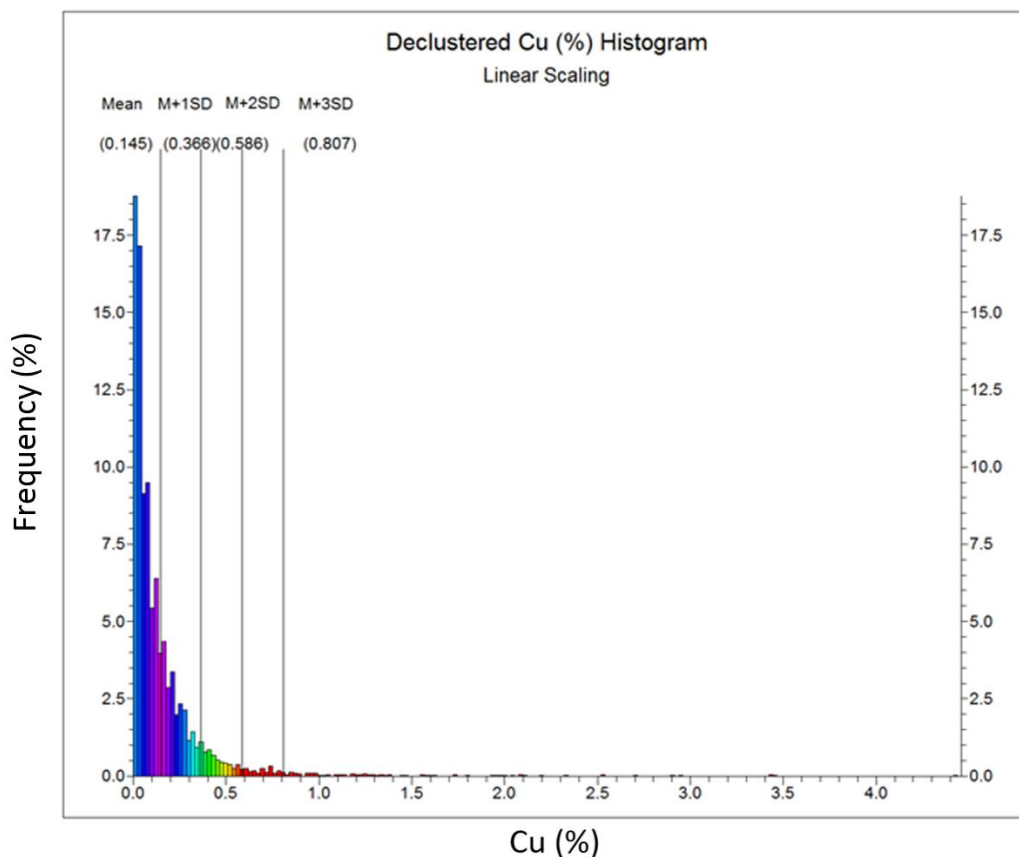
Fig. 3. 7. Cu histogram based on declustered data

Table. 3. 4. The particulars of the selected borehole pairs in the Kahang deposit

Borehole ID		Distance	Distance (m)	
From	To	(m)	X	Y
KAG50	KAG6	11	4.4	10
KAG6	KAG47	23	17.14	15.33
KAG15	KH-DDH17	5	0.38	4.98
KAG33	KH-DDH13	20	18.69	7.1
KAG42	KH-DDH9	14	12.88	5.47
KH-DDH14	KH-DDH15	21	16.32	13.21
KAG41	KH-DDH15	15	14.59	3.47
KAG59	KAG27	15	12.28	8.6
KAG54	KH-DDH16	16	15.58	3.59
KAG52	KAG18	28	17.77	21.63
KH-DDH11	KAG19	20	18.97	6.31
KAG51	KH-DDH02	22	7.41	20.71
KAG33	KH-DDH9	25	17.04	18.28
KAG48	KAG28	27	7.39	25.96

Table. 3. 5. Variation of voxel size based on mean, median and MAD

Statistical Parameters	Total Distances (m)	Distances in X (m)	Distances in Y (m)
Mean	4.67-9.34	3.23-6.46	2.94-5.88
Median	5-10	3.8-7.6	2.94-5.88
MAD	2.5-5	< 1	< 1

Topographical features of the deposit were formed into a block model. The block model for Cu was produced by applying an upper and lower filter using RockWorks™ software, based on the surface data (Fig. 3. 8) and borehole data collar heights, given by NICICO. Those voxels located above the upper and below the lower topographical surfaces and bed rock are considered as the waste voxels and are not included in the deposit block model as the voxels are of negative significance (Todorov et al., 2002; Popov et al., 2003; Hustrulid and Kochta, 2006; Yasrebi et al., 2011). The use of IDW to construct the block model was employed in this research. The amounts of voxels with positive values (Non-Zero) are shown in Table. 3. 6. The more Non-Zero voxels consequently correspond to the voxel dimension of 5 m × 5 m × 5 m. The standard deviation value for the voxel size of 4 m x 4 m x 10 m is lower than other voxel alternatives (Table. 3. 6). Moreover, the averages for estimated Cu values were compared and the lowest value occurs in the 4 m × 4 m × 10 m block model which is conservatively suited for identification of Net Present Value (NPV) and subsequently mine planning (Hustrulid and Kochta, 2006). The Cu mean for 4 m × 4 m × 10 m block model (0.15823 wt.%) is relatively close to the Cu average obtained from the declustered data (0.145 wt.%) in comparison with the other voxel scenarios. (Fig. 3. 7 and Table. 3. 6).

Table. 3. 6. Voxel numbers and Standard deviations and averages of Cu for different block models

Block Model Dimensions (m³)	Total Voxel No.	Non-Zero Voxel No.	Standard Deviation (%)	Cu Average (wt.%)
4 × 4 × 10	1,113,742	263,414	0.20134	0.15823
5 × 5 × 10	718,505	169,091	0.20136	0.15833
5 × 5 × 5	2,526,601	345,578	0.20352	0.15895
10 × 10 × 10	322,873	42,284	0.20138	0.15828
15 × 15 × 15	97,785	12,486	0.21641	0.16266
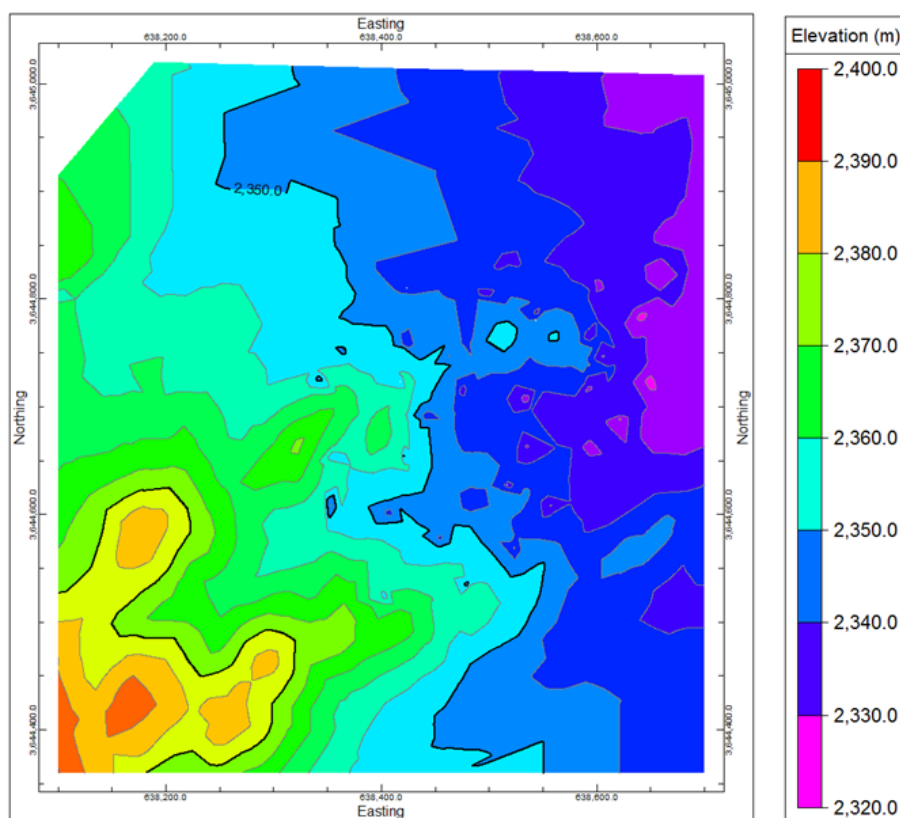
Fig. 3. 8. 2D topographical surface of the Kahang deposit

Borehole collar heights were compared with topographic surface heights to check that they are comparable, as depicted in Fig. 3. 9. The coordinates of collar boreholes correlate with used topographical points to provide a topographic surface for resource modelling and further optimisation studies. For the optimised pit scheduling software, a topography model is a three-dimensional surface model (See chapter 5, section 5.4) which is analogous to wireframe surfaces in most mining software systems (NPV – Scheduler, 2001).
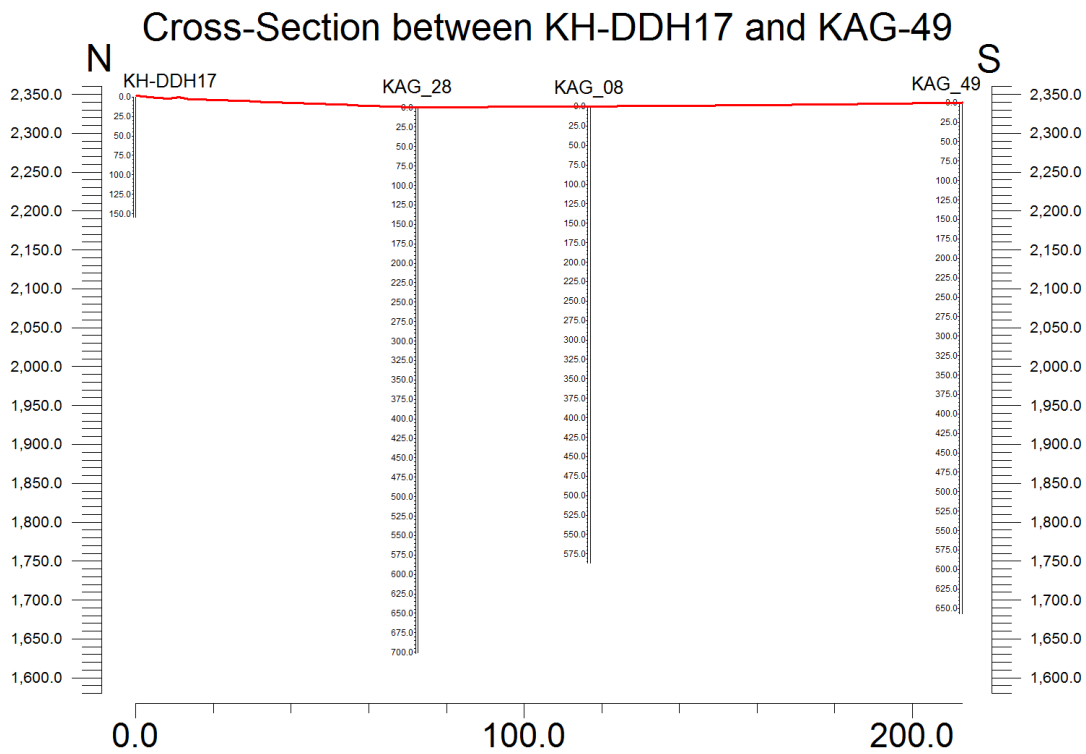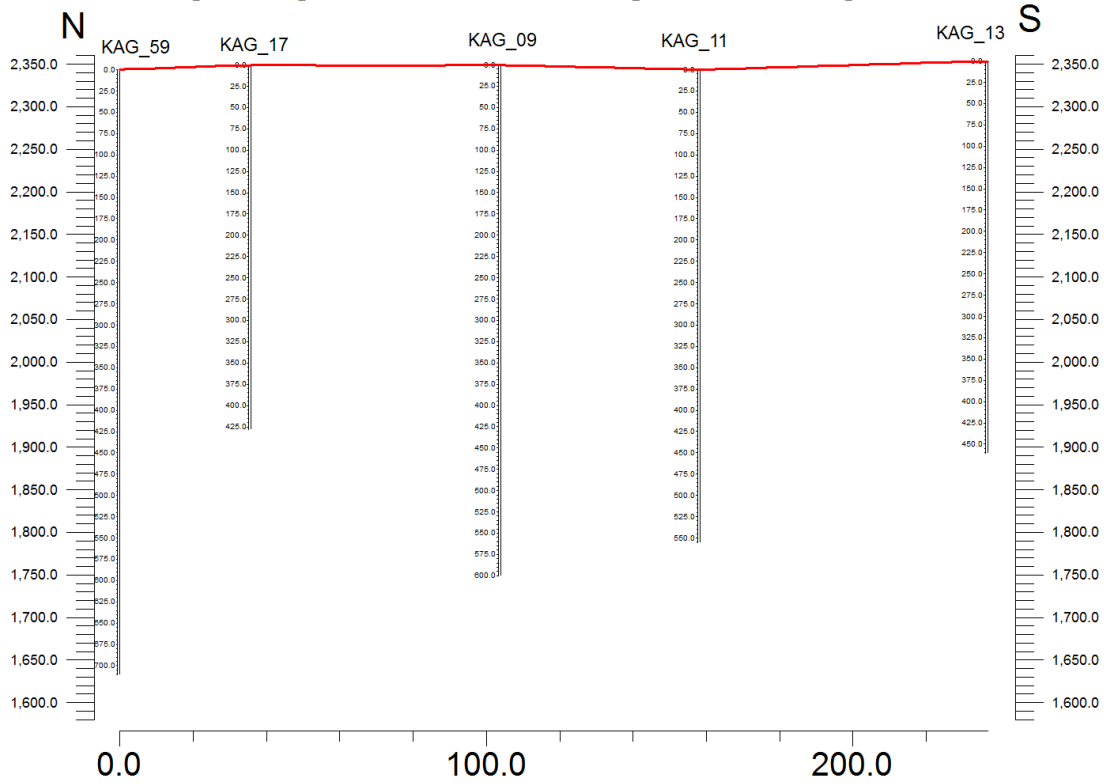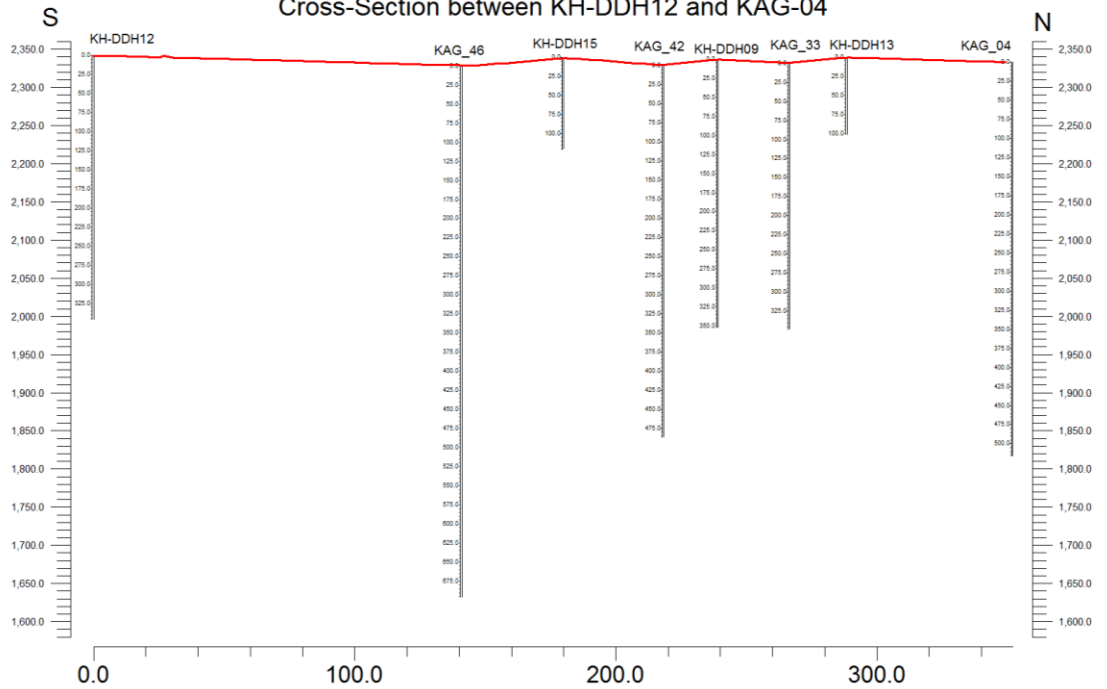
Fig. 3. 9. Correlation between borehole data collar heights and topographical surface

3.5 Geostatistical Modelling

Geostatistical estimation methods are used commonly for interpolation and estimation of different regional variables in 1D, 2D or 3D environments. Employment of an accurate estimation method with respect to geometry and geological properties of different ore deposits and also drilling patterns is a problematic issue in resource/reserve estimation (David, 1970; Yasrebi et al., 2009; Shahbeik et al., 2014). Determination of estimation methods is essential for decreasing the error estimation and increasing the accuracy of resource and reserve evaluation (Dimitrakopoulos et al., 2007; Parhizkar et al., 2011). Selection of an estimation method is essential for fractal/multifractal modelling, especially in the C-V model. On the other hand, accuracy of the estimation methods and their errors of interpolation affect the C-V fractal/multifractal modelling (Agterberg et al., 1993; Cheng and Agterberg, 1996; Lima et al., 2003; Agterberg, 2012; Afzal et al., 2013a; Heidari et al., 2013).

Linear and non-linear Kriging methods, Inverse Distance Weighted (IDW), have been used to interpolate polynomials and splines, to overcome the mentioned problem (Franke, 1982; Zimmerman et al., 1999; Juan et al., 2011). Among these methods, kriging and IDW are usually utilised in most cases in mineral exploration and mining engineering. Using real data rather than synthetic data has several advantages; for example, it precludes one method from having an unfair advantage merely because the data used for the comparison is generated under the same model on which the method is based. On the other hand, only with synthetic data can the effect of certain data characteristics on interpolation accuracy be systematically evaluated (Englund et al., 1992; Weber and

109

Englund, 1992 and 1994; Zimmerman et al., 1999). Evaluation of ore element distribution

is an important parameter for mine planning and design (Hustrulid and Kochta, 2006).

3.5.1 *Inverse Distance Weighted Anisotropic Method (IDWAM)*

Inverse Distance (ID) is one of the more common gridding and estimation methods. With

this method, the value assigned to a voxel is a weighted average of either all of the data

points or a number of directionally distributed neighbours. The value of each of the data

points is weighted according to the inverse of its distance from the voxel (Zimmerman et

al., 1999; Homayoon et al., 2010; Shahbeik et al., 2014).

Inverse Distance Weighted Anisotropic (IDWAM) is a method for interpolation of scattered

points that estimates voxel values (e.g., ore grade) by averaging the values of sample

data points in the neighbourhood of each processing voxel. IDWA has a crucial

assumption that the interpolating surface is mostly influenced by the nearby points and

less by the more distant points. The interpolating surface is a weighted average of the

scatter points and the weight assigned to each scatter point diminishes as the distance

from the interpolated point to the scattered point increases. The main advantage of the

IDW method is to produce a smooth and continuous grid and does not exaggerate

extrapolations beyond the given data points (Franke, 1982; Goovaerts, 1997).

Therefore, the IDWAM is recommended for geochemical mapping where the data

boundaries (geochemical populations) are critical for threshold-based target separation

(e.g., in C-V fractal models). The range of element concentrations will be smaller than the

raw data range meaning that highest grade values will be less than the maximum of raw

data, and the lowest grade values will be greater than the minimum data point (Tahmasebi and Hezarkhani, 2010). A general form of finding an interpolated value u at a given point x based on samples $u_i = u(x_i)$ for $i = 1, 2, ..., N$ using IDW is an interpolating function:

$$u(\mathbf{x}) = \begin{cases} \dfrac{\sum\limits_{i=1}^{N} w_i(\mathbf{x}) u_i}{\sum\limits_{i=1}^{N} w_i(\mathbf{x})}, & \text{if } d(\mathbf{x}, \mathbf{x}_i) \neq 0 \text{ for all } i \\ u_i, & \text{if } d(\mathbf{x}, \mathbf{x}_i) = 0 \text{ for some } i \end{cases}$$

Equation 3-2

where

$$w_i(\mathbf{x}) = \frac{1}{d(\mathbf{x}, \mathbf{x}_i)^p}$$

Equation 3-3

x denotes an interpolated (arbitrary) point, x_i is an interpolating (known) point, d is a given distance (metric operator) from the known point x_i to the unknown point x, N is the total number of known points used in interpolation and p is a positive real number, called the power parameter (e.g., an exponent of "2" = Inverse Distance Squared, "3" = Inverse Distance Cubed; Shepard, 1968). The greater the value of the exponent, the less influence distant control points will have on the assignment of the voxel value.

The disadvantages of conventional IDW methods are choice of weighting function which may introduce ambiguity; especially where a fixed search radius requires a neighbourhood distance and a minimum or maximum number of points.

In the IDWAM, all points will be used which increases error in the form of under and over estimation so the samples located in a supergene enrichment zone (in a porphyry deposit) can be influenced by the leached zone which correspondingly reduces the voxels grade values within ore minerals consisting of say chalcocite, covellite and bornite (Pirajno, 2009). To overcome this problematic issue, variography, in combination with IDWAM, is employed for better estimations.

Directional and non-directional searching in this method can improve the interpolation of voxel values that lie between data point clusters and be useful for modelling drill-hole based data in the stratiform and massive ore deposits (Zimmerman et al., 1999). In this thesis, a combination of IDWAM and variography has been used in order to generate a block model in terms of Cu and Mo values based on the following criteria:

1- The grid drilling pattern is irregular and non-systematic, with an especially high drilling density in the NE part of the deposit, and low density in the NW part (e.g., three isolated boreholes: Fig. 3. 5a, b and c). Moreover, the grid drilling pattern has an anisotropic geometrical shape.

2- There are too many scattered drill holes in the marginal parts of the deposit which leads to a lack of data.

3- Simple Kriging (SK), as a common estimation method, is based on a moving average of the variable of interest, appropriate for various dispersed forms of data e.g. sparse sampling points. As a result, this estimator requires adequate drill holes and data analysis which are not met in the Kahang deposit. However, in this thesis a combination of IDWAM and variography (horizontal and vertical) has been carried out for the development of IDW.

4- According to field observations, the mineralisation and alteration zones, particularly hypogene and phyllic, continue through to the marginal parts of the deposit (especially in the SE area with high Cu and Mo values) which were not covered by the 48 boreholes conducted in the studied area. The IDWAM is therefore appropriate due to the lack of subsurface information.

5- Trends of Cu values in X, Y and Z show that there is no association between ore grade and X-Y location or depth within the deposit (Fig. 3. 10), indicating again that "Universal Kriging" is not appropriate for this deposit.
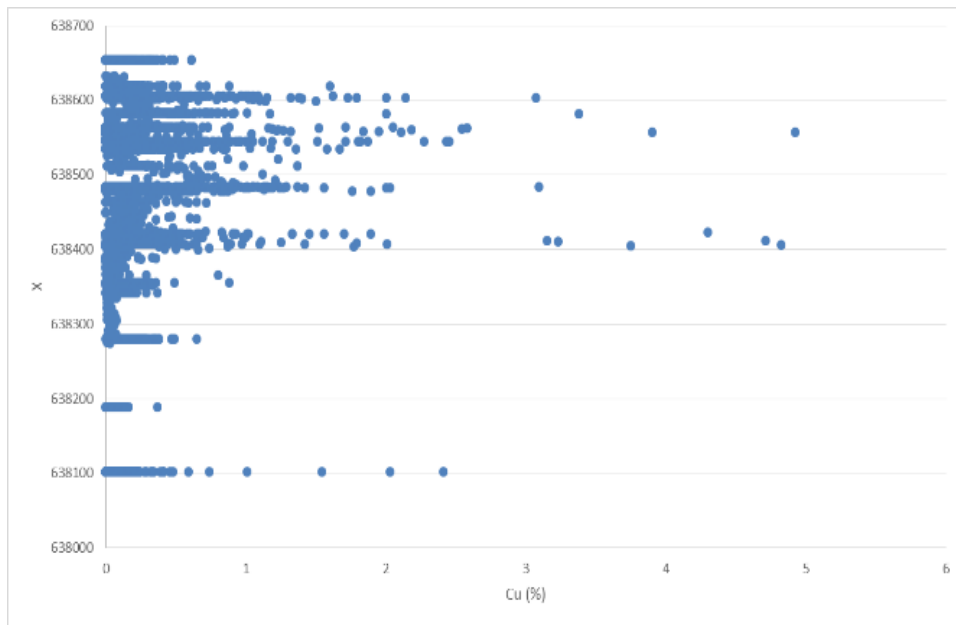
(a)
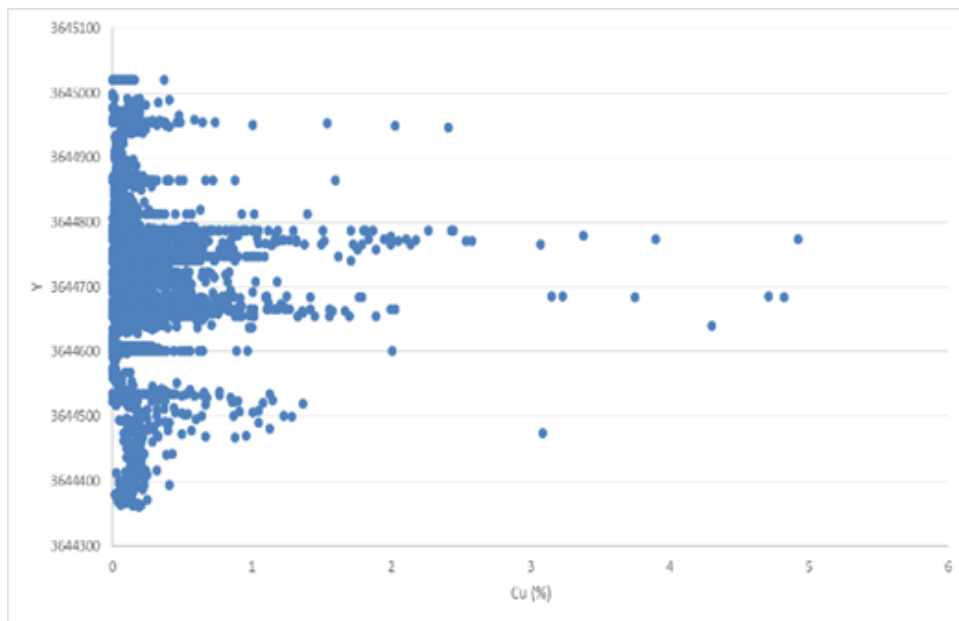
(b)
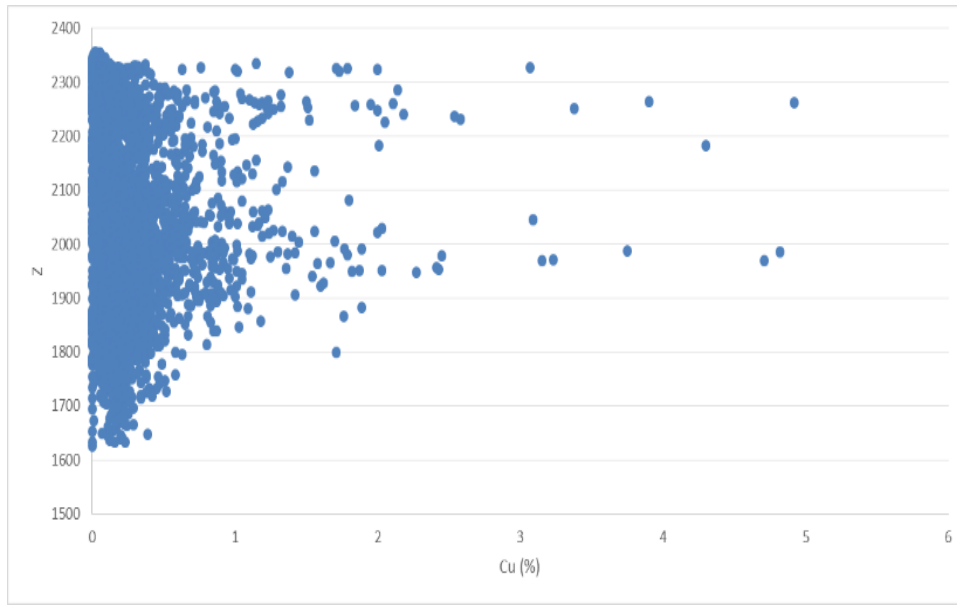
(c)

Fig. 3. 10. Scatterplots for correlation between Cu (wt.%) and coordinates: a) Cu values trend in X, b) Cu values trend in Y, and c) Cu values trend in Z

3.5.2 Application of IDWAM

The experimental variograms in Fig. 3. 11 in horizontal (Azimuth: 0 and Dip: 0) and vertical (Azimuth: 0 and Dip: -90) directions were generated using MATLAB software with respect to log transformations of Cu and Mo grades. The horizontal and vertical ranges for Cu are 56 m and 270 m, respectively. Moreover, the Mo horizontal and vertical ranges are equal to 40 m and 80 m, respectively. The spherical model was fitted to the experimental variograms. Accordingly, the theoretical variograms for Cu and Mo grade values are as:

$$\gamma_{Cu}(h) = 0.41 + 0.36 \, sph \, (10, 10, 25) + 0.85 \, sph \, (56, 56, 270)$$

$$\gamma_{Mo}(h) = 1.125 + 0.56 \, sph \, (10, 10, 10) + 0.36 \, sph \, (40, 40, 20) + 0.044 \, sph \, (\infty, \infty, 80)$$

Cu

(a)
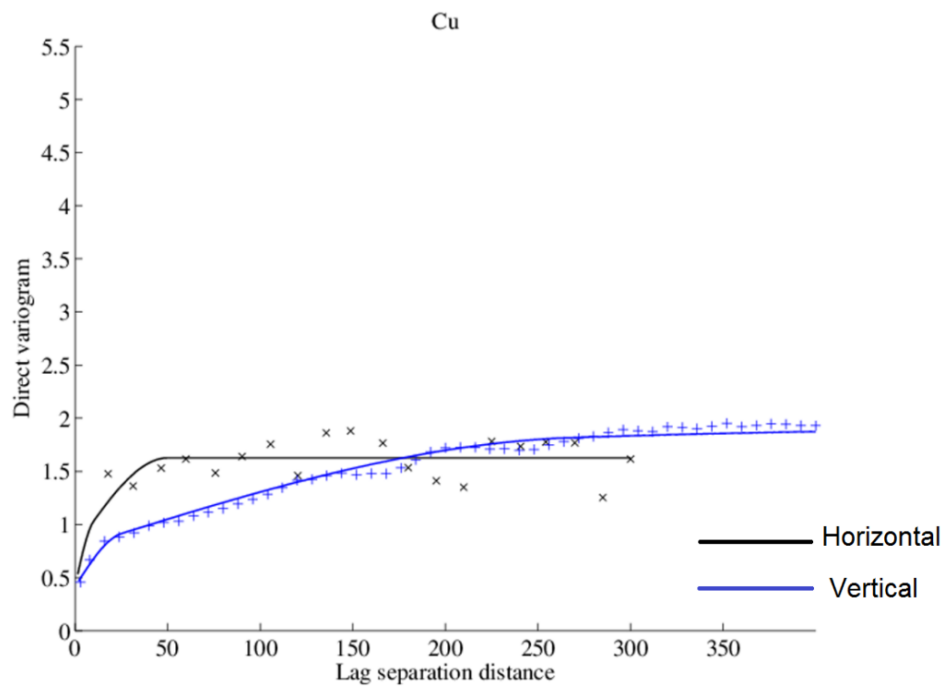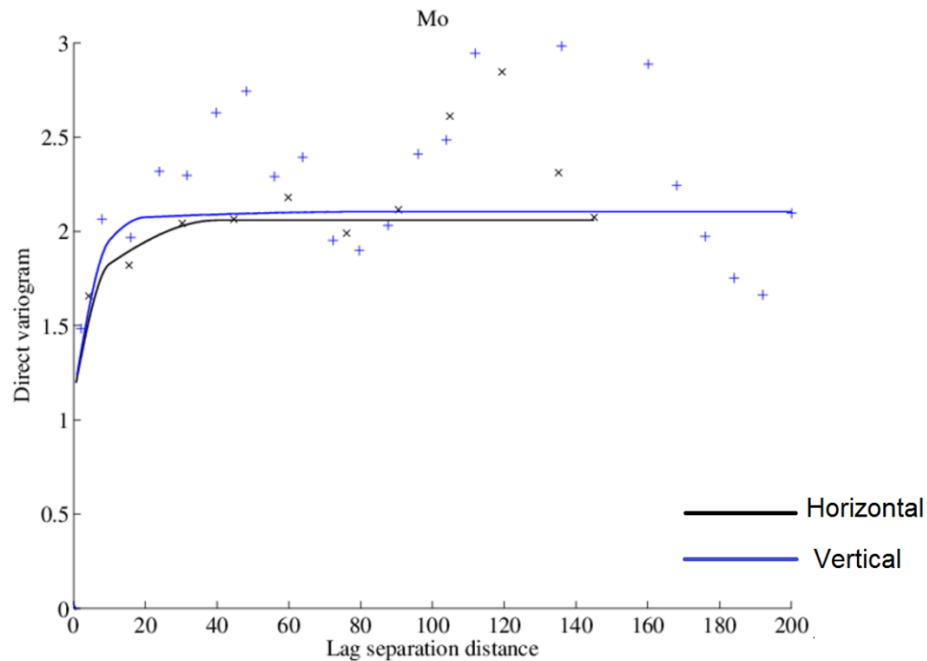
(b)

Fig 3. 11. Experimental and theoretical variograms: a) Cu, and b) Mo

In addition, 'Variogram Maps' have been created using Varmap software from the GSlib Library (Deutsch and Journel, 1998) in order to find out if there are any anisotropic characteristics within the deposit. Variograms are traditionally constructed as 1D curves: ɣ (h) as a function of the distance *h* along a particular direction. It is often useful to have a global view of the variogram values in all directions (X-Y, Y-Z and X-Z in this thesis). To do this, transformed Cu and Mo grades were calculated using a logarithmic function before variography was carried out in the cases of: one set for the X-Y orientation (with lag spacing of 15 m) to evaluate the range in plan view, and one set either X-Z and Y-Z with lag spacing of 8 m to evaluate the range in vertical sections. There is an isotropic behaviour in horizontal direction for Cu and Mo. Furthermore, there is a weakly

anisotropic behaviour in the studied area based on the X-Z and Y-Z (vertical) variogram maps, as shown in Fig 3. 12.

(a)

(b)

Variogram Map XZ

(c)
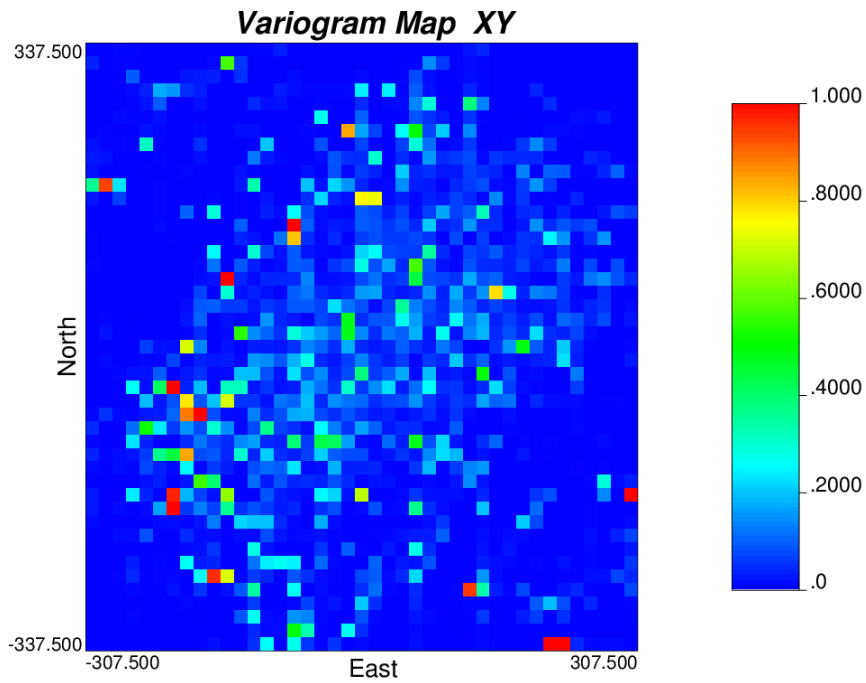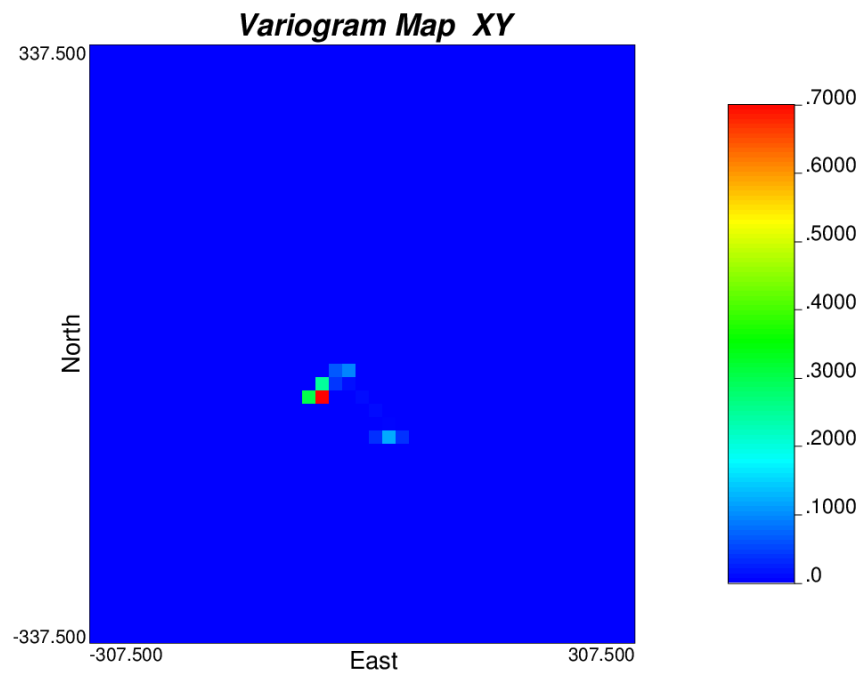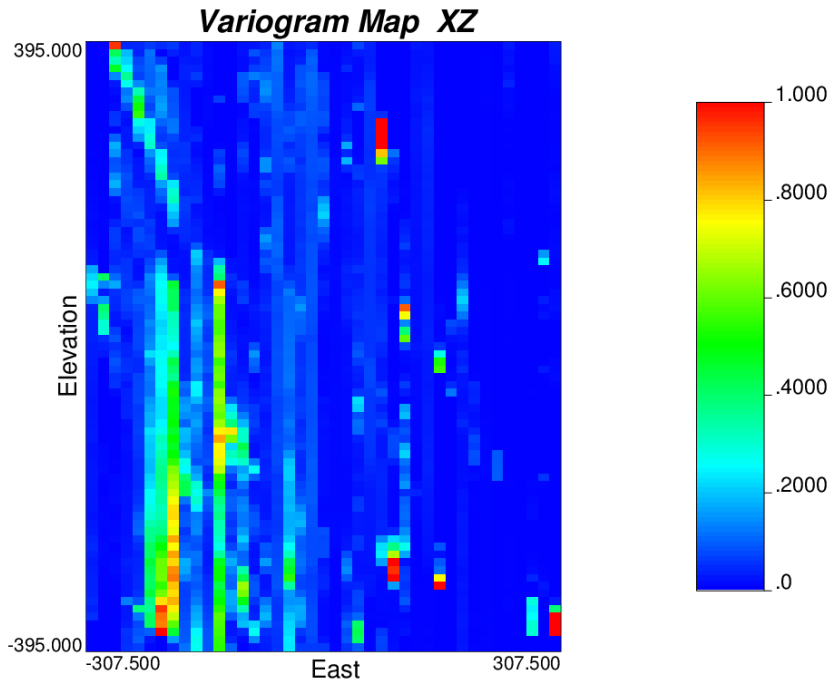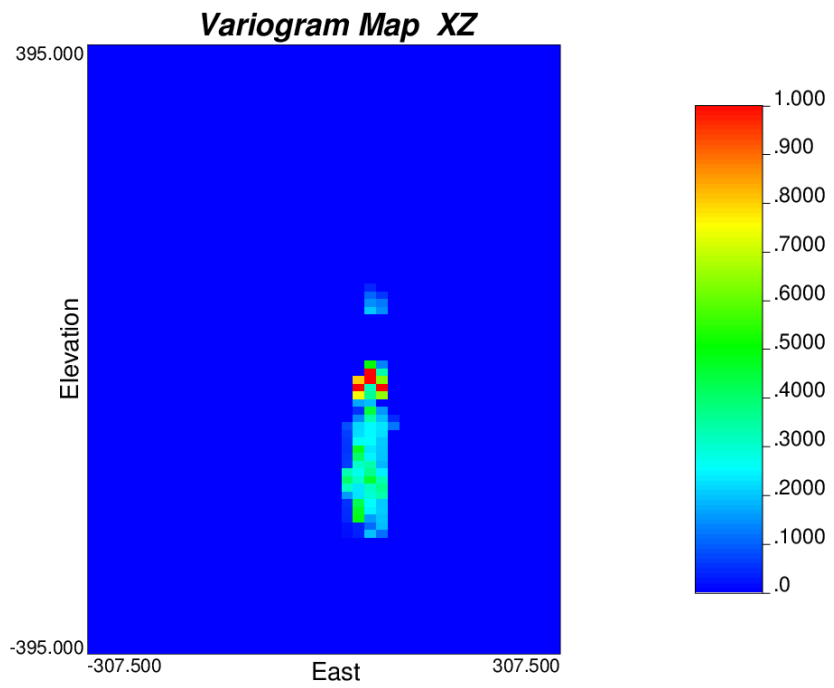
Variogram Map XZ

(d)
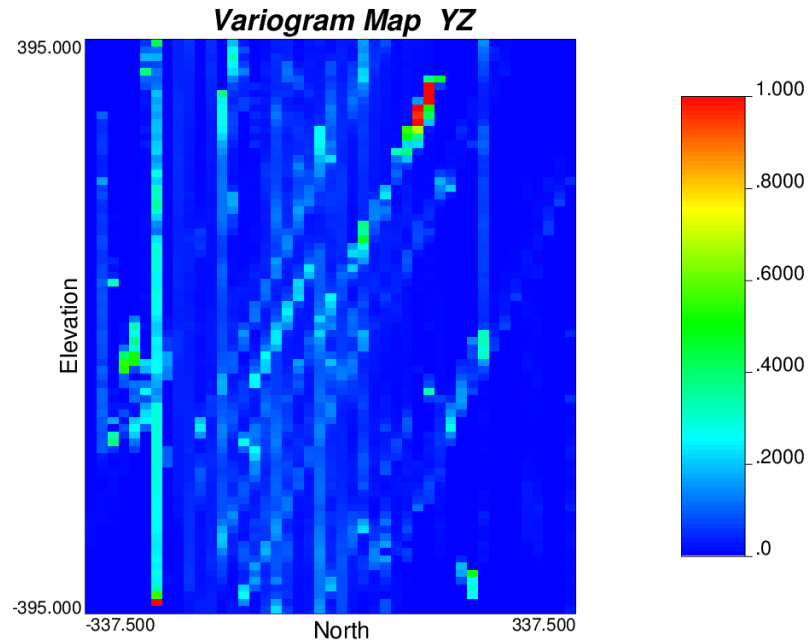
(e)
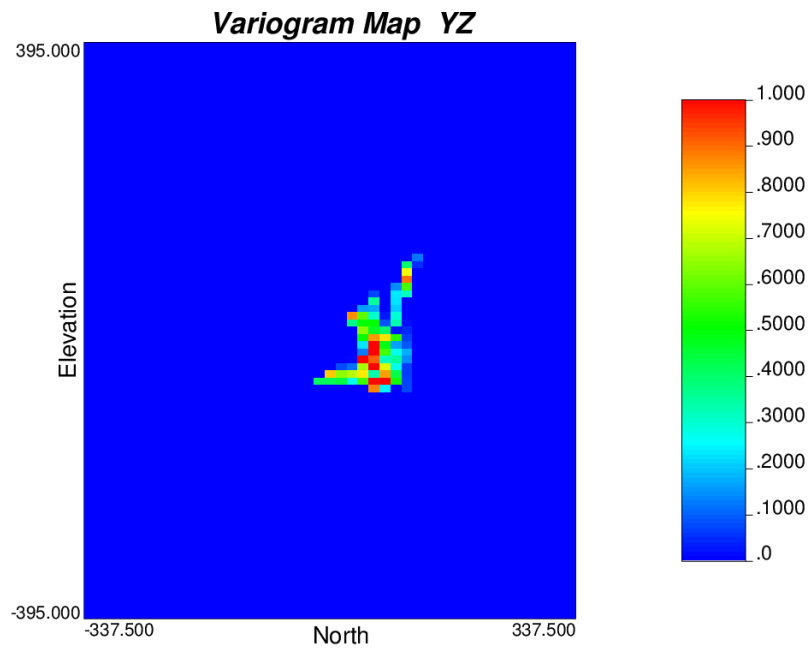
(f)

Fig. 3. 12. Variogram maps for a) Cu in plan 1730 m, b) Mo in plan 1730 m, c) Cu in E-W section with Northing = 3644585, d) Mo in E-W section with Northing = 3644585, e) Cu in N-S section with Easting = 638325, and f) Mo in N-S section with Easting = 638325

The Kahang deposit was modelled with 489,927 voxels with each voxel having a dimension of 4 m × 4 m × 10 m in the X, Y and Z directions. The project dimensions are 600, 660 and 780 m (Fig. 3. 13). 3D block models for Cu and Mo were evaluated by IDWAW using the RockWorks^{TM} software package, as depicted Fig. 3. 15. The ranges of Cu and Mo from the variograms in Fig. 3. 11 were imported into the vertical and horizontal distance cut-offs in the "Solid Modelling Options".

In order to achieve this using the RockWorks^{TM} software, the following tasks, in their relative order, were carried out (Fig. 3. 14):

The Weighting Exponent value was determined as being equal to 2 in order to prompt to enter a real number value for the Inverse-Distance exponent. Number of neighbouring points were defined between 3 and 15 data points that were to be used when computing the voxel value. The horizontal and vertical ranges (known as 'Cut-offs Distances' in the RockWorks^{TM} software) were recognised based on the combined variograms with lags' spacing of 15 m and 8 m for horizontal and vertical directions (Fig. 3. 11).
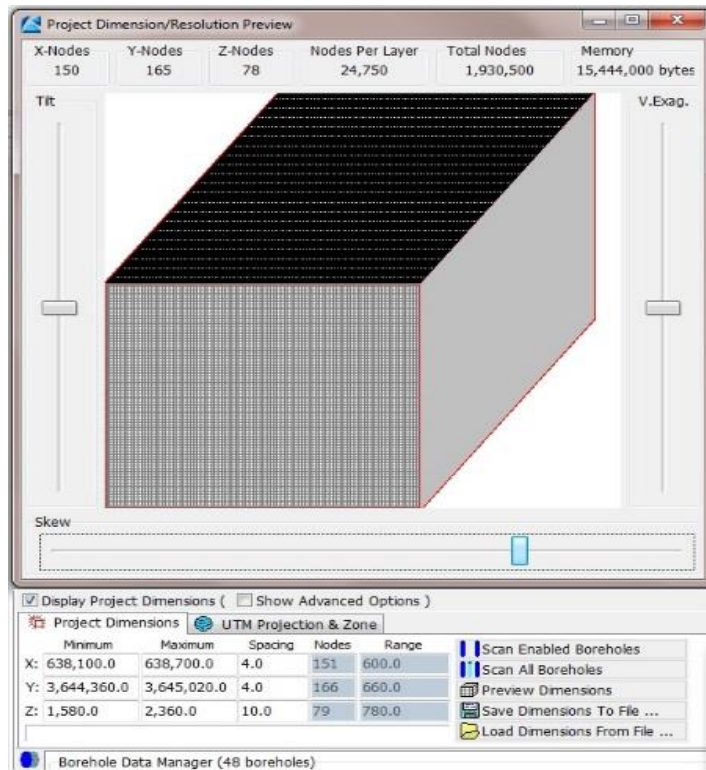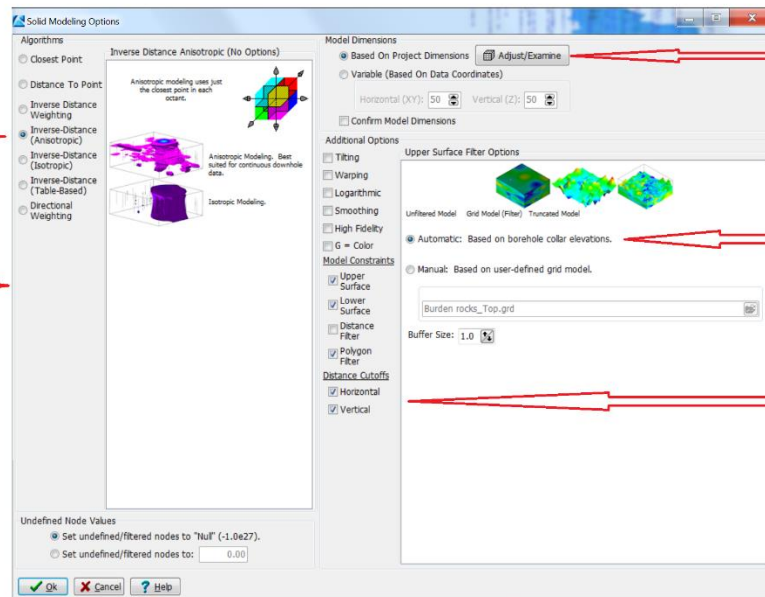
Fig. 3. 13. Project dimensions of the studied area

Fig. 3. 14. Steps of IDWAM run in RockWorks™ 15

The sections within 0.4 wt.% Cu and 200 ppm Mo were separated and showed that these parts were located in the central, NE and NW parts of the area (Fig. 3. 16). Additionally, Cu values higher than 0.4 wt.% exist in the SE part of the area and continue towards Kahang village.

Histogram and statistical characteristics of the Cu estimation indicate a standard deviation of 0.15 which is lower than the IDW (See Table. 3. 6), as shown in Fig. 3. 17 and Table. 3. 7. As a result, it shows that the variography decreases the values of error estimation in the IDW indicator. Histogram and statistical particulars of the Mo estimated model (Fig. 3. 17) illustrate a lower standard deviation in comparison with raw data which are 0.56 and 0.76 respectively. Moreover, the mean of the Cu and Mo in the estimated models are 0.14 wt.% and 27.49 ppm respectively (Table. 3. 7). If the Cu threshold is equal to 0.1 wt.% then the resource is greater than 100 Mt with a Cu mean value equal to 0.23 wt.%, as depicted in Grade-Tonnage (G-T) diagram (Fig. 3. 18). The G-T diagram shows that the deposit has a good potential as a porphyry type because the mean Cu in the different thresholds are comparable with other Iranian porphyry deposits such as Masjed Daghi, Darreh Zar and Sar Kuh with 340 Mt and 0.27 wt.% Cu, 475 Mt and 0.36 wt.% Cu and 110 Mt and 0.26 wt.% Cu, respectively (e.g., Shahabpour, 1994; Afzal et al., 2011; Aghazadeh et al., 2015). Several plans were generated for Cu and Mo, as depicted in Fig. 3. 19. The plans reveal that the main mineralisation occurs in the SE, NE and central parts of the deposit, especially in the NW section of the studied area (area around the three isolated boreholes: Fig. 3. 20). Cu values higher than 0.25 wt.% (Fig. 3. 20c) in the isolated bore holes (NW part) are more common at depth, and it may therefore be wise

to drill more bore holes in this area. Moreover, Cu samples with values higher than 0.15 wt.% are mostly accumulated in the central part of the deposit (Fig. 3. 20b). Cu values greater than 0.07 wt.% are scattered in majority parts of the deposit (Fig. 3. 20a).

Table. 3. 7. Statistical characteristics for Cu and Mo estimated models

Element	Minimum Value	Maximum Value	Range	Mean	Standard Deviation	Median	Variance	Skewness	Kurtosis
Cu (wt.%)	0.0003	4.00773	4	0.14	0.151	0.091	0.023	4.38	39.60
Mo (ppm)	0.65	790.82	784.75	27.49	56.44	12.56	3,185.515	6.82	59.91

(a)   (b)
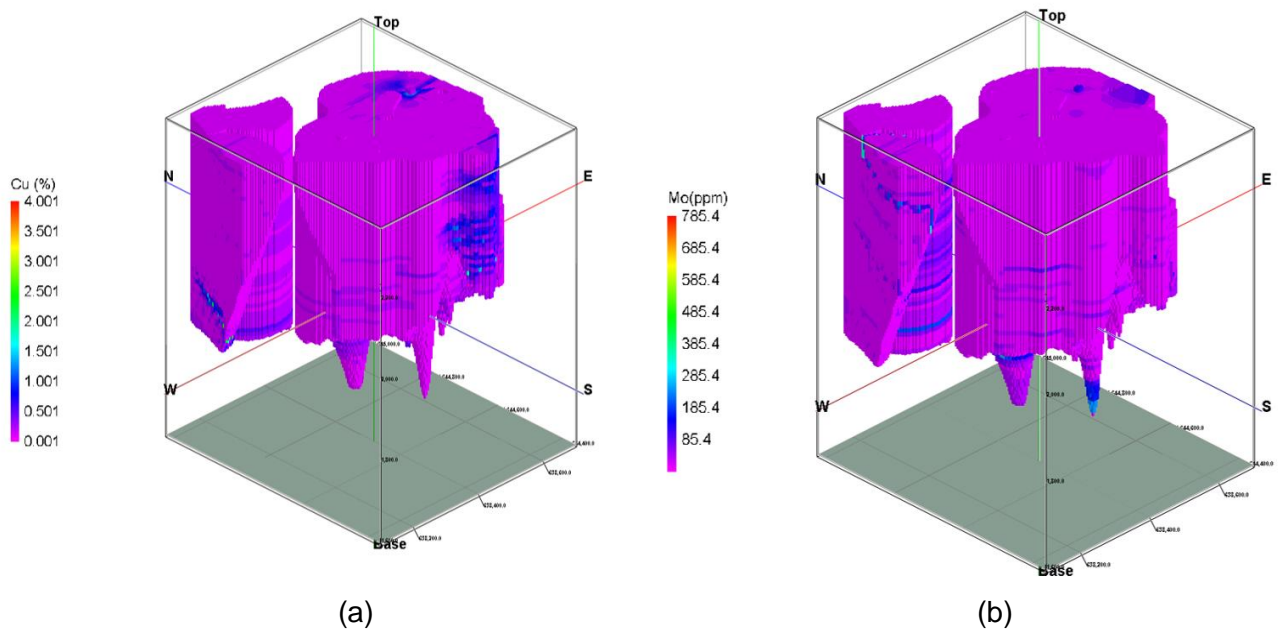
Fig. 3. 15. Block models in the Kahang deposit: a) Cu, and b) Mo

(a)   (b)
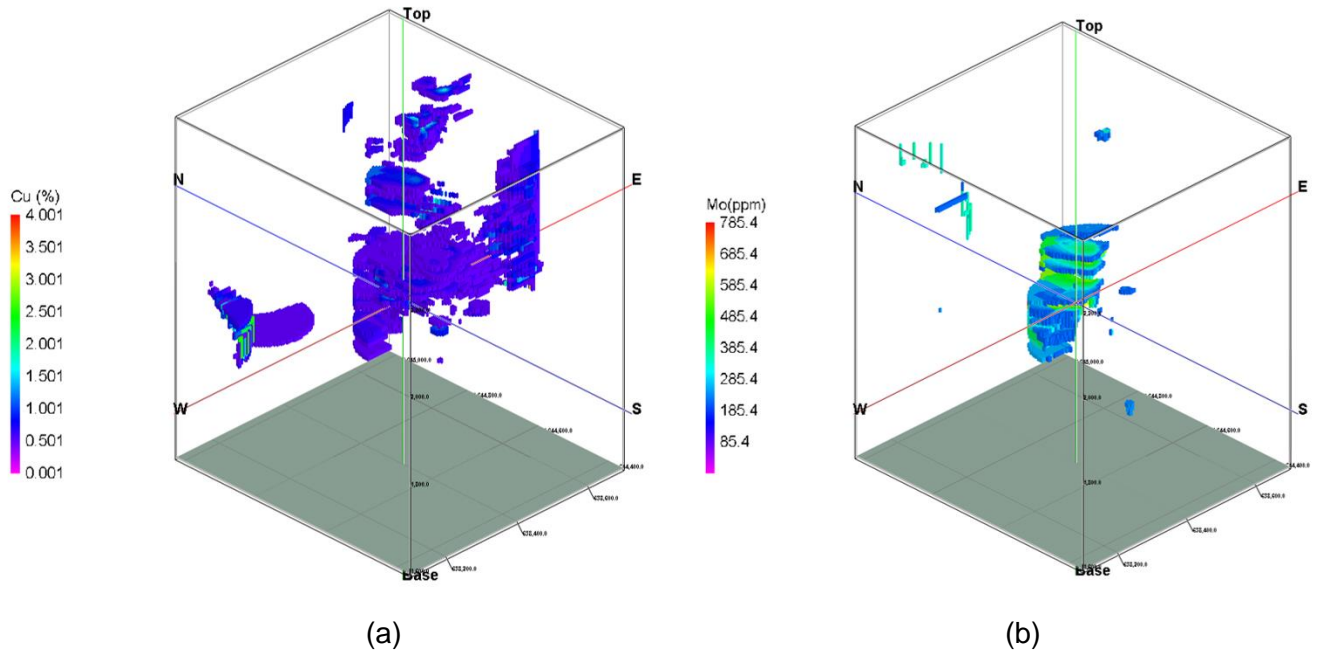
Fig. 3. 16. Distribution models in the Kahang deposit: a) Cu ≥ 0.4 wt.%, and b) Mo ≥ 200 ppm

(a)   (b)
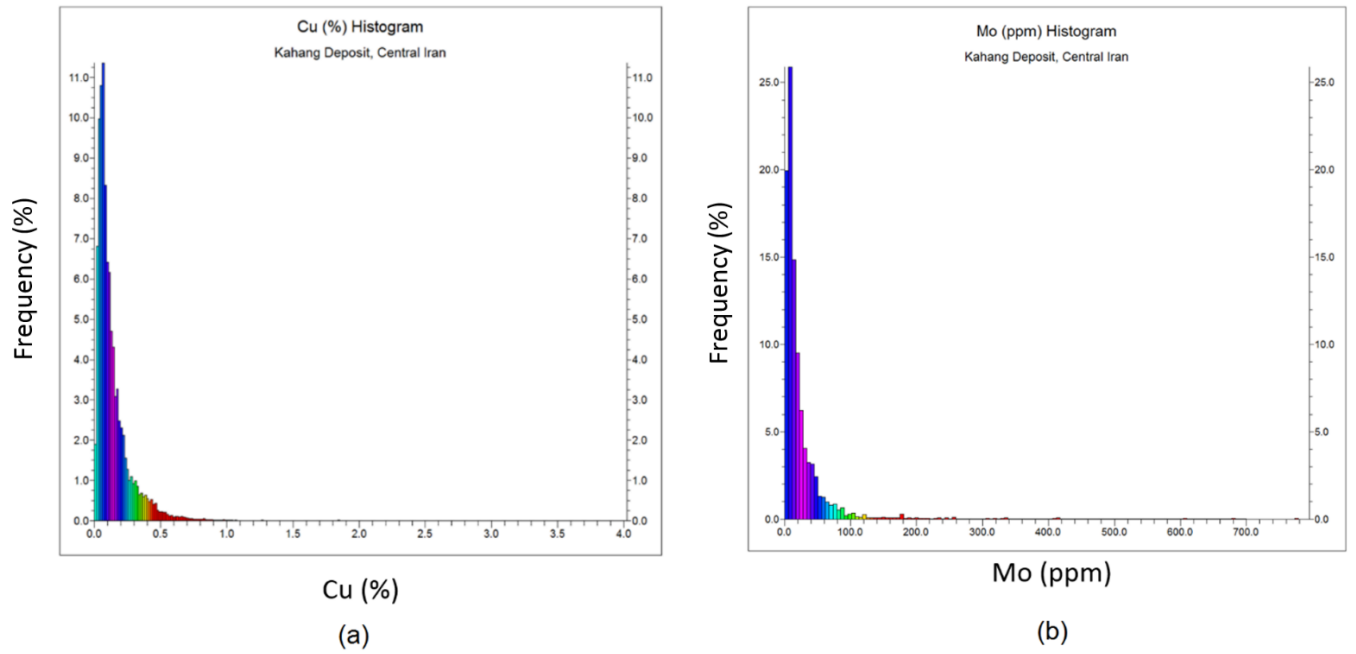
Fig. 3. 17. Histograms of estimated element concentrations: a) Cu, and b) Mo
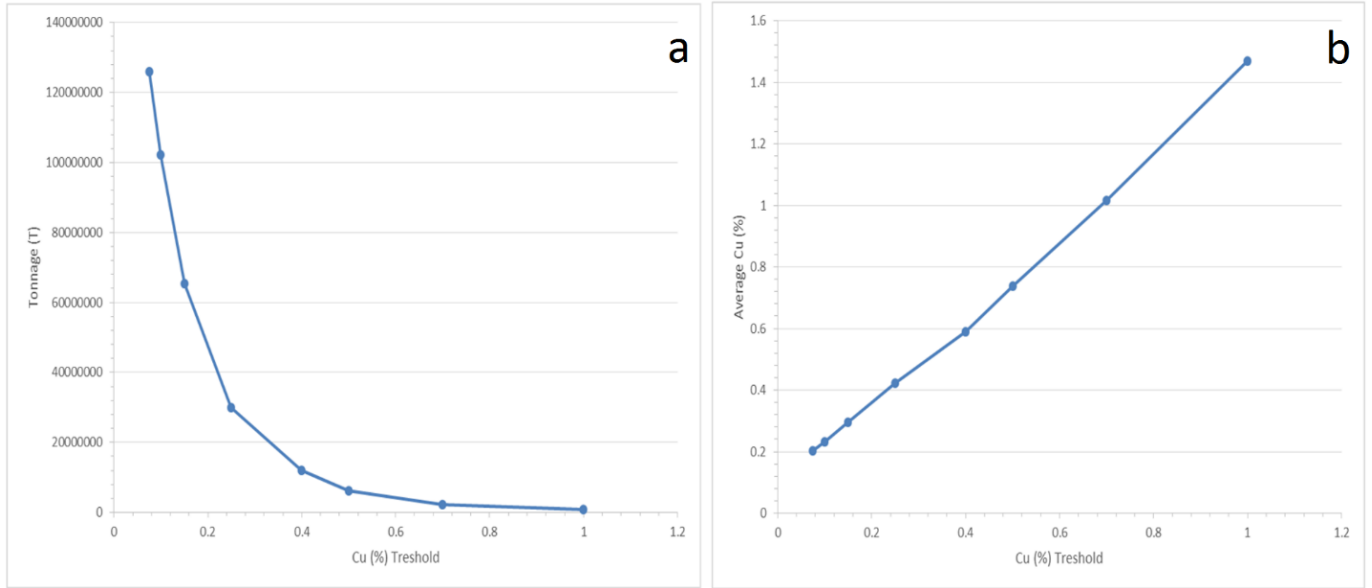
Fig. 3. 18. a) Cu (%) Grade-Tonnage, and b) Cu (%) average-cut-off diagrams for Kahang deposit

Z=2300 m

Z= 2250 m

Z= 1950 m

Z= 1900 m

Z= 1950 m

Z= 2200 m
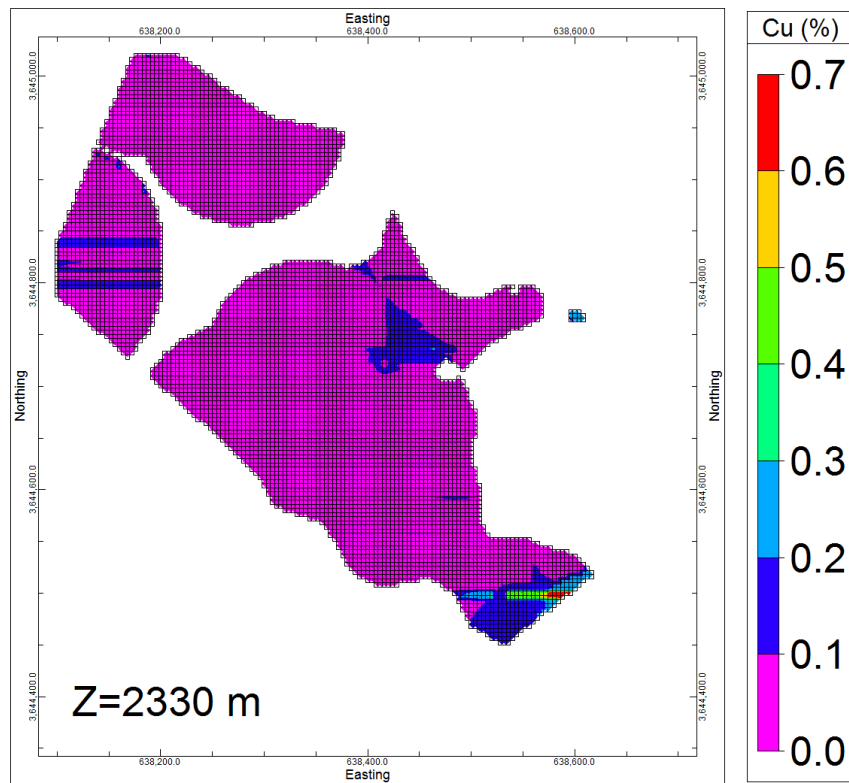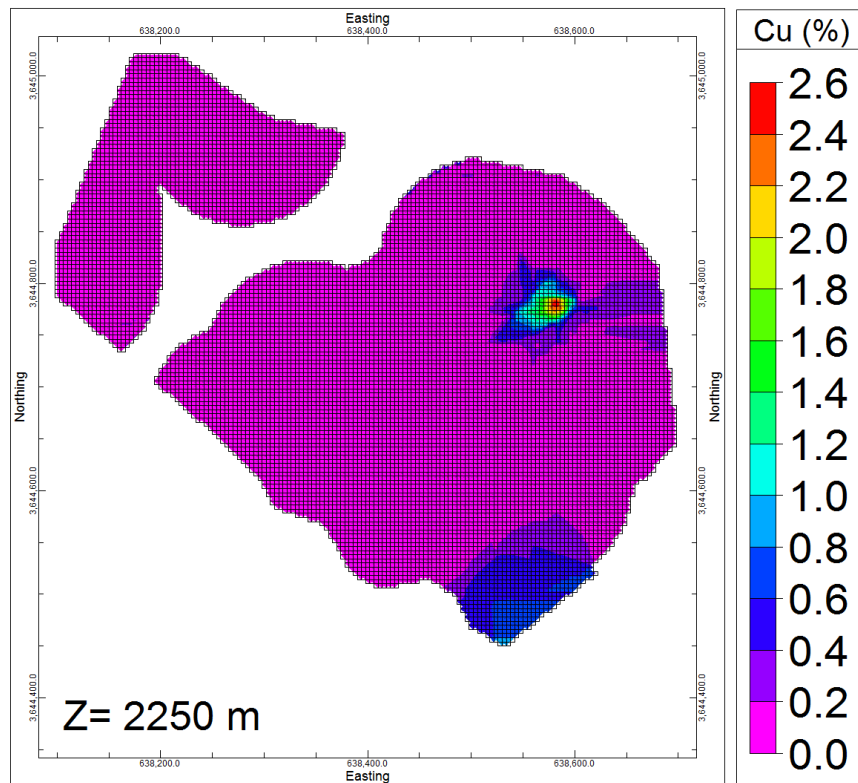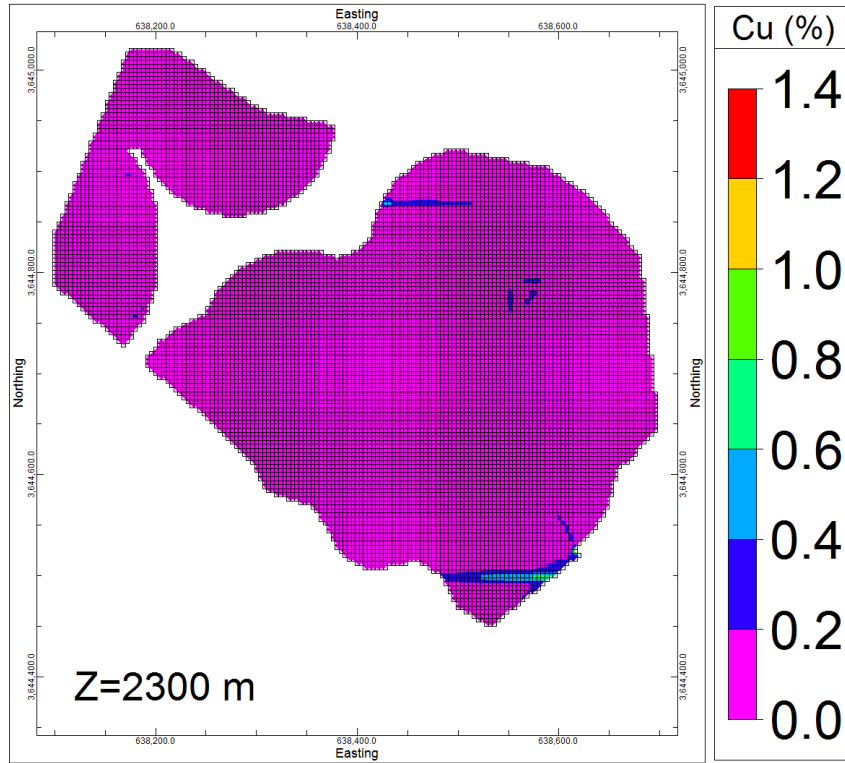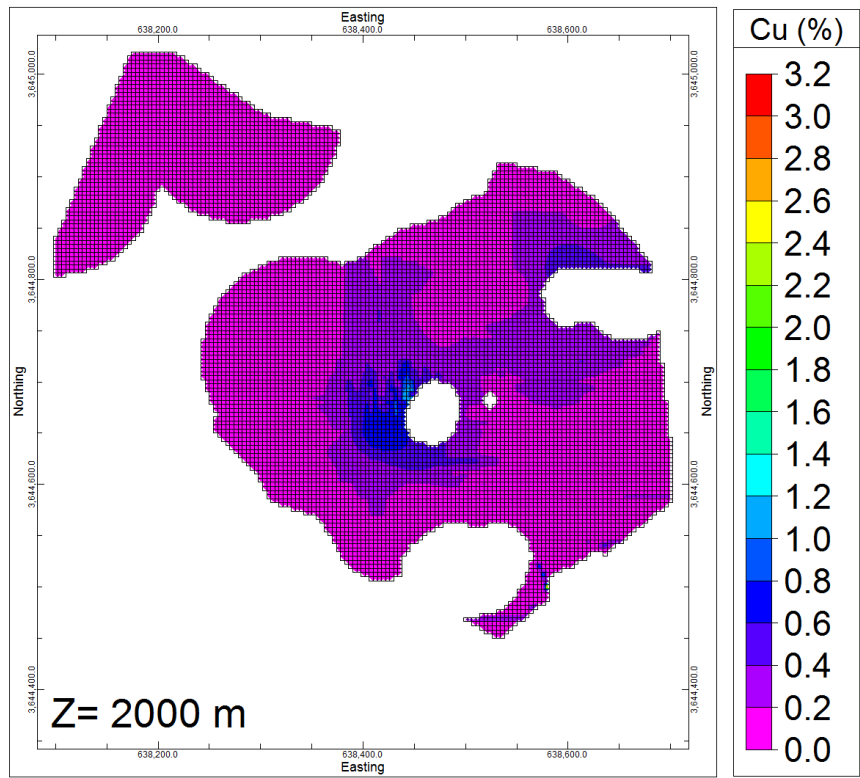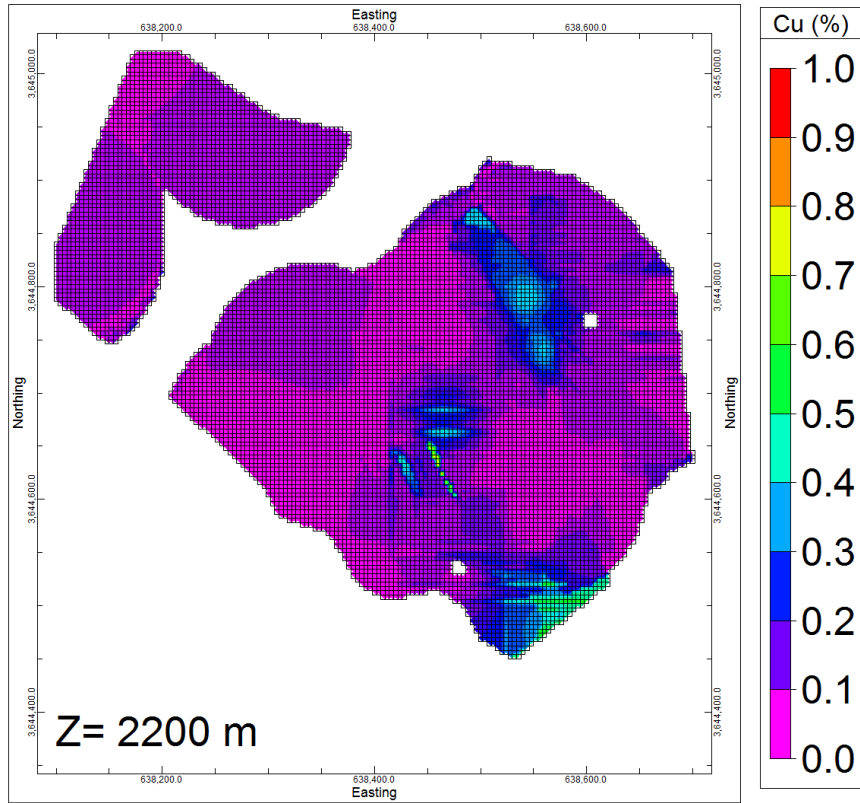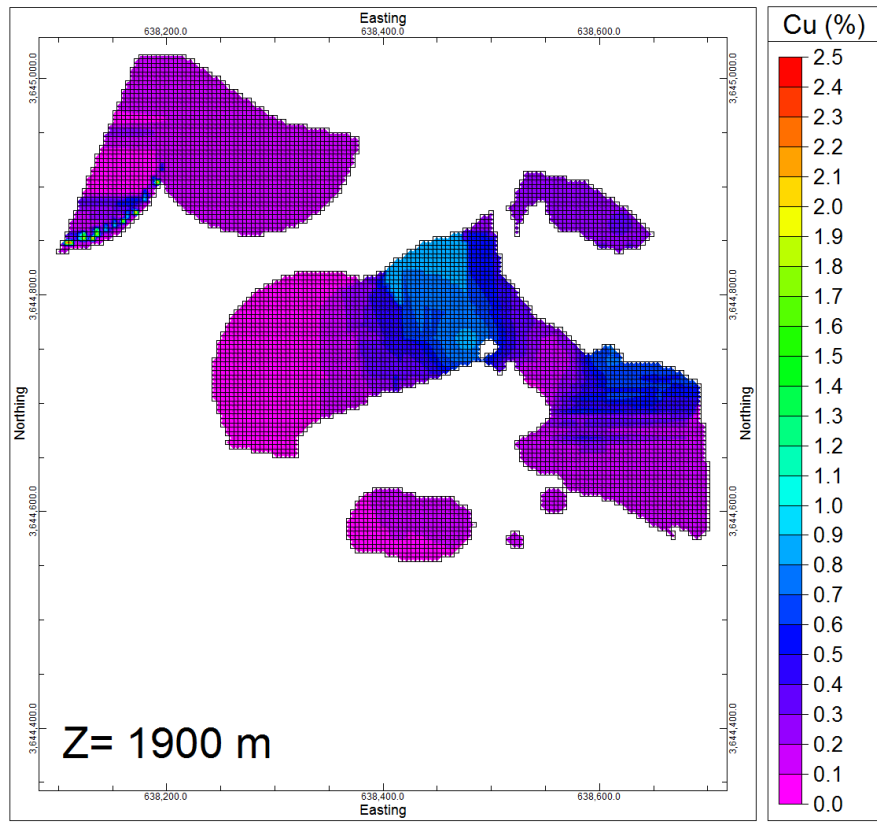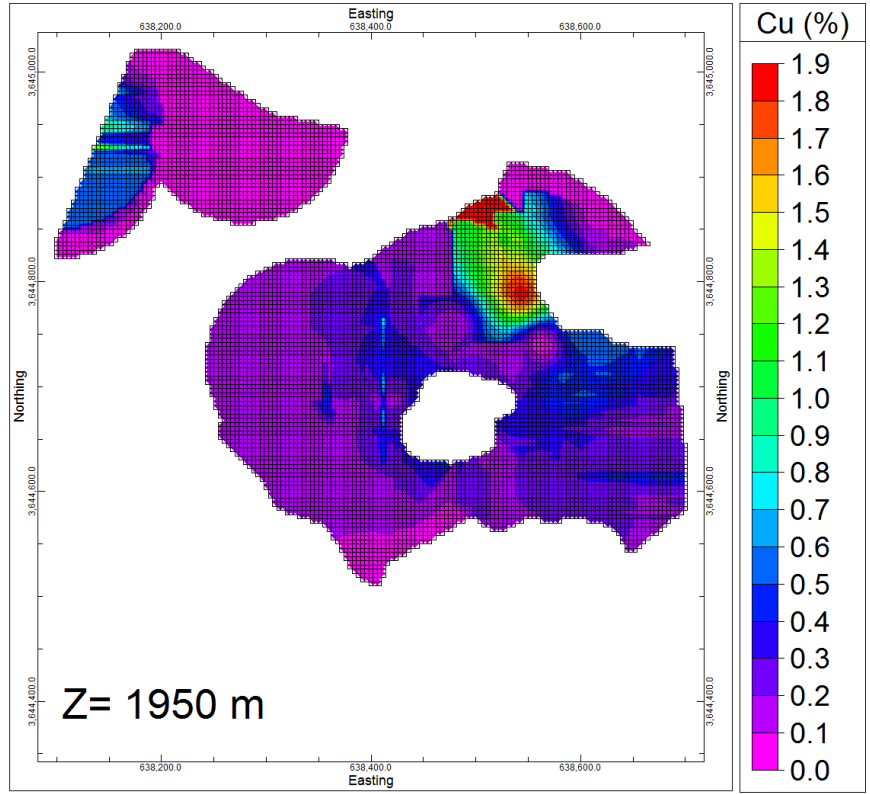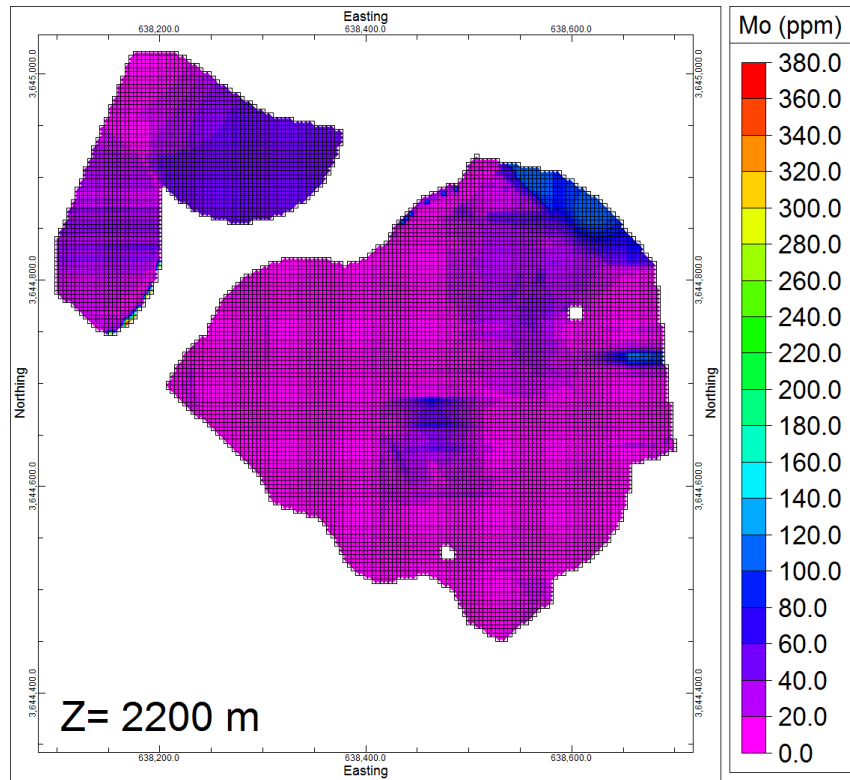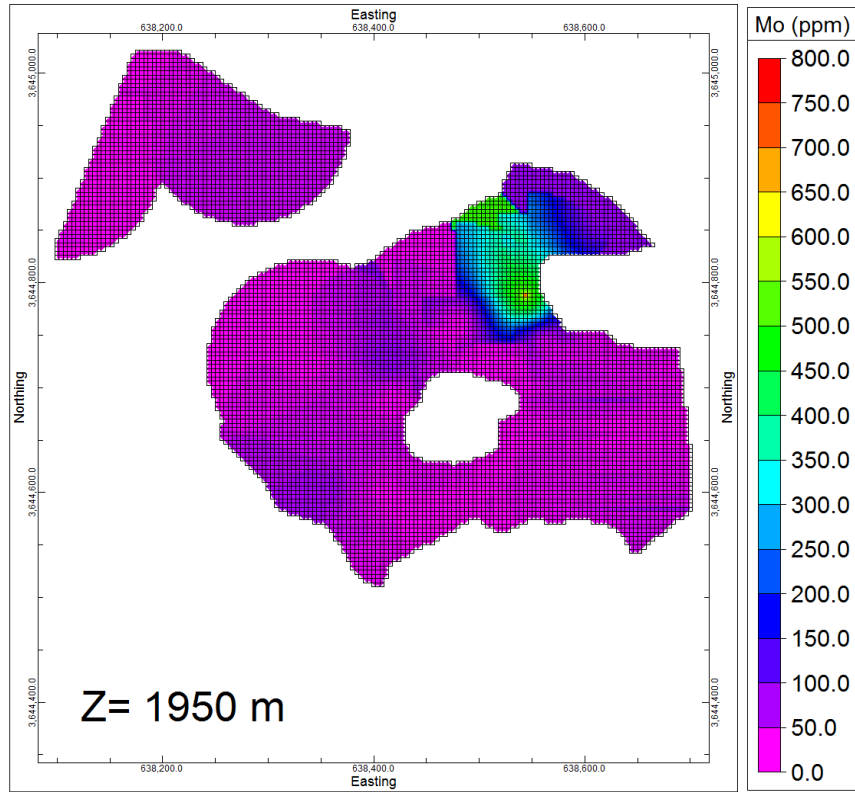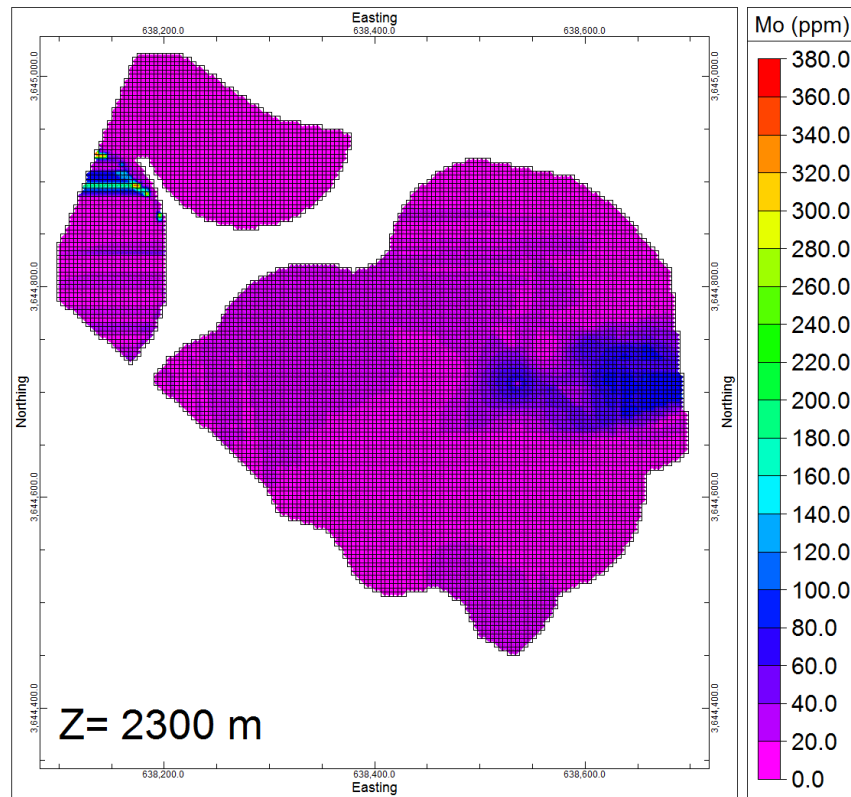
Fig. 3. 19. Cu and Mo plans in the Kahang deposit
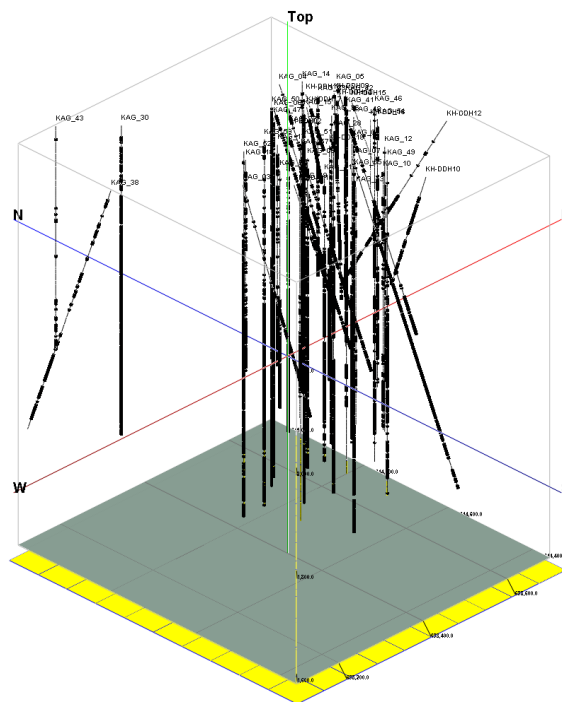
(a)
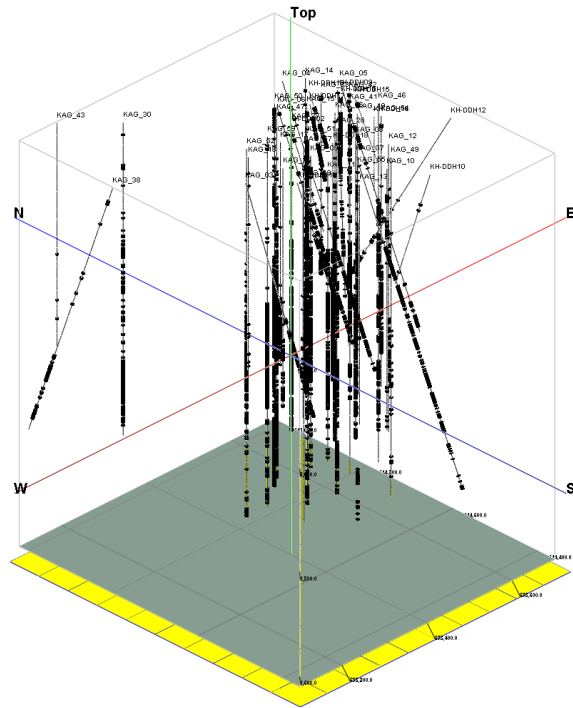
(b)
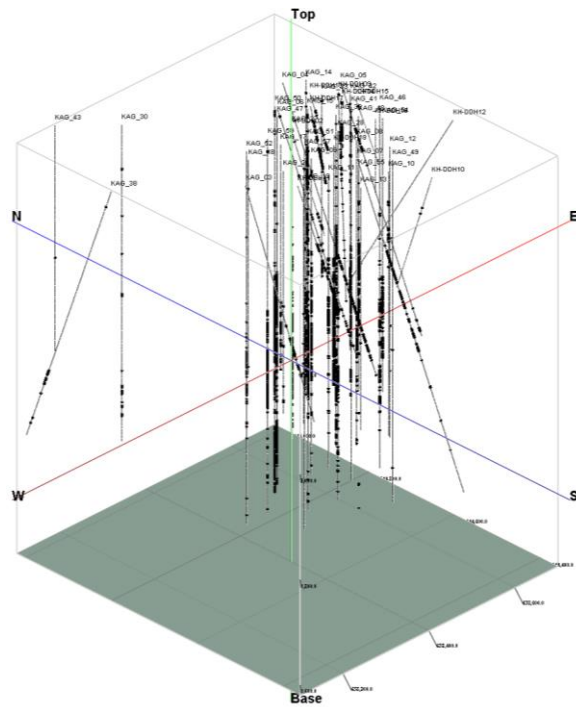
(c)

Fig. 3. 20. Samples (black discs) within Cu values higher than: a) 0.07 wt.%, b) 0.15 wt.% and c) 0.25 wt.% from boreholes carried out in the deposit

3.6   Validation Processes

For validation of the estimation, two methods were used: optical correlation and jackknife. Optical correlation is a visual verification which tries to visually show correlation coefficient between raw (original) and estimated data in cross-sections (Fig. 3. 21). It shows a positive relationship between Cu values from the boreholes (raw or original data) and the generated block model (estimated data) in the different cross-sections (Fig. 3. 21). For optical correlation, randomised groups of boreholes which are close to each other (e.g., Fig. 3. 21b: Kag_59, Kag_17, Kag_09 and Kag_11) were selected and, for each individual borehole, a histogram of original data was constructed. The areas between selected boreholes in the cross-sections indicate estimated Cu values. There is a general belief that when the Cu values of the original data which are shown in the form of histogram for each borehole (Fig. 3. 21) are high, the estimated Cu values within those two boreholes should be high (RockWorks^{TM} 15, 2010; Emery, 2012). For example, the Cu values of the original data from deeper parts of boreholes Kag_17 and Kag_09 reveal high values of element concentration therefor, the estimated Cu values between those original data should consider high value of the element concentrations, as depicted in Fig. 3. 21b. However, this method is not that sufficient because most of the boreholes were obliquely drilled.

There are so many interdependent subjective decisions in a geostatistical study that it is good practice to validate the results obtained by the estimation method (IDWAM in this thesis) prior to any production run. The generated block model is validated by re-estimating known values under implementation conditions, including the variogram

model, estimation method and search strategy, as close as possible to those of the forthcoming production run (Deutsch and Journel, 1998). These re-estimation techniques are discussed in most practical statistics and geostatistics books (Tukey, 1977; Efron, 1982; Davis, 1987; Isaaks and Srivastava, 1989; Goovaerts, 1997). The term jackknife applies to resampling without replacement, i.e., when alternative sets of data values are re-estimated from other non-overlapping data sets (Efron, 1982). The jackknife analysis in the Kahang deposit indicates that the correlation between original data and Cu estimated is 70%, as depicted in Fig. 3. 22. In this figure, the diagonal of the square plot (black line) and the linear regression (red line) was derived and calculated using MATLAB program.
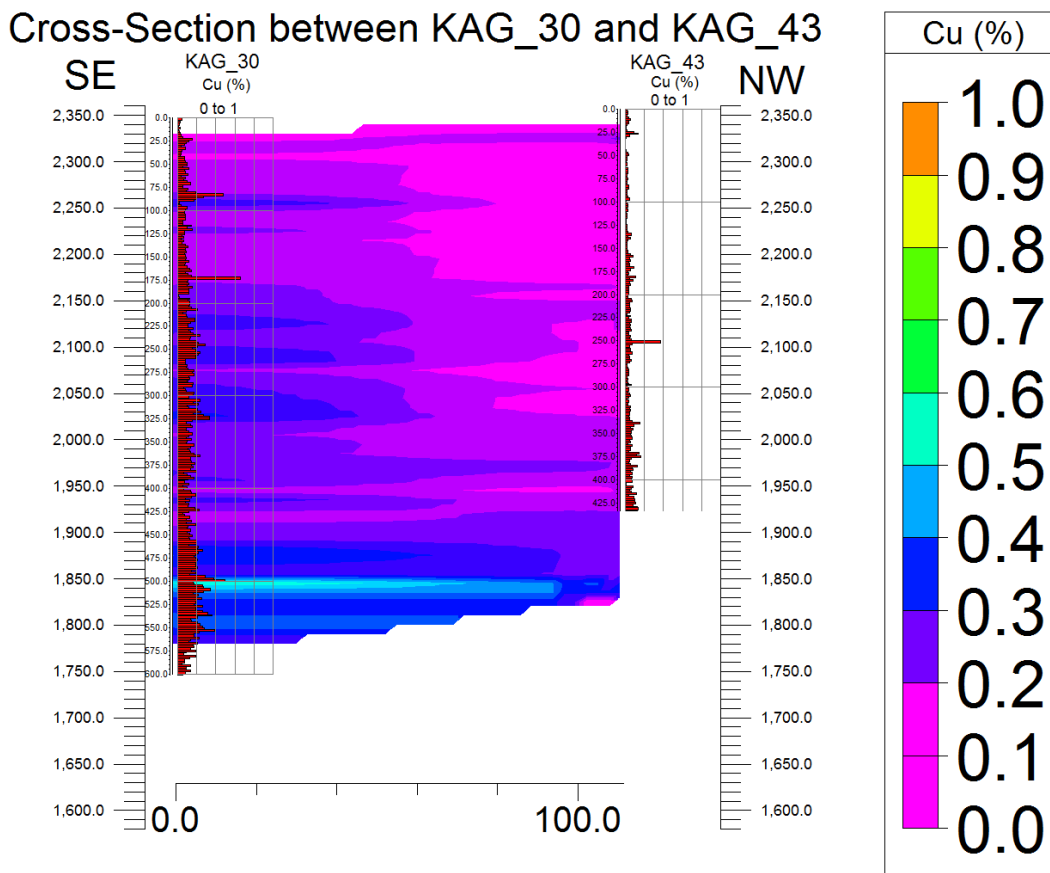
(a)
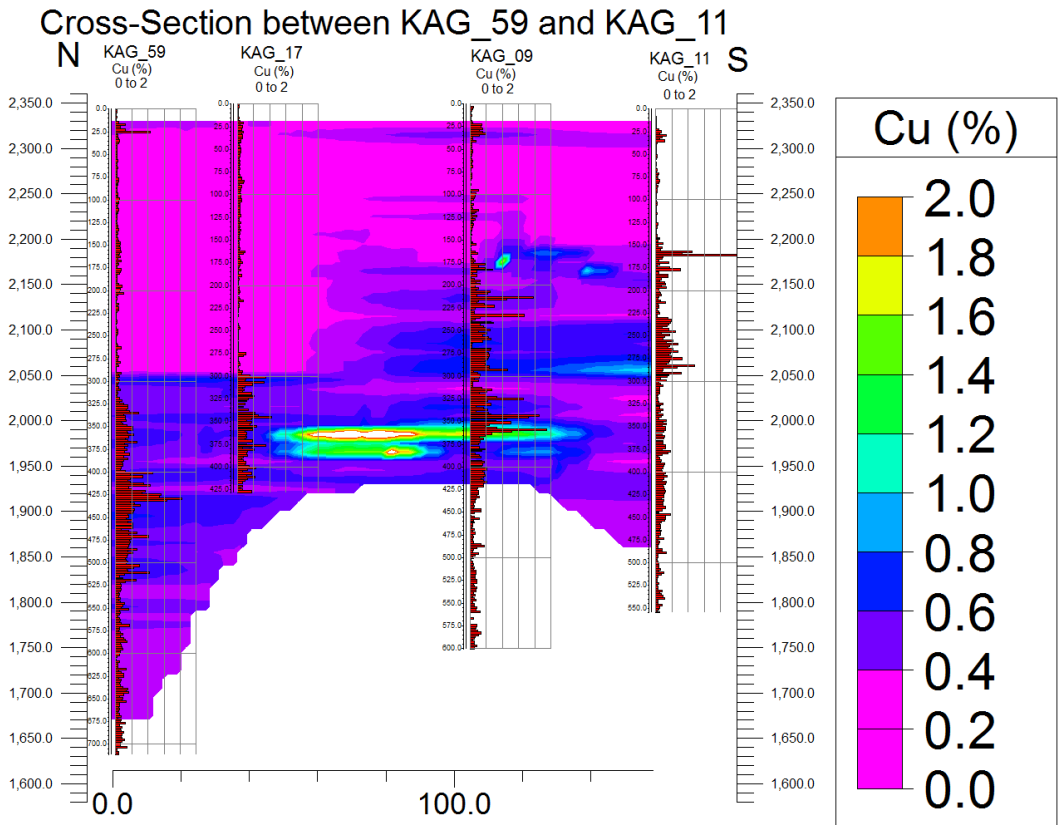
Fig. 3. 21. Optical correlation (visual verification) between Cu values of borehole and block model
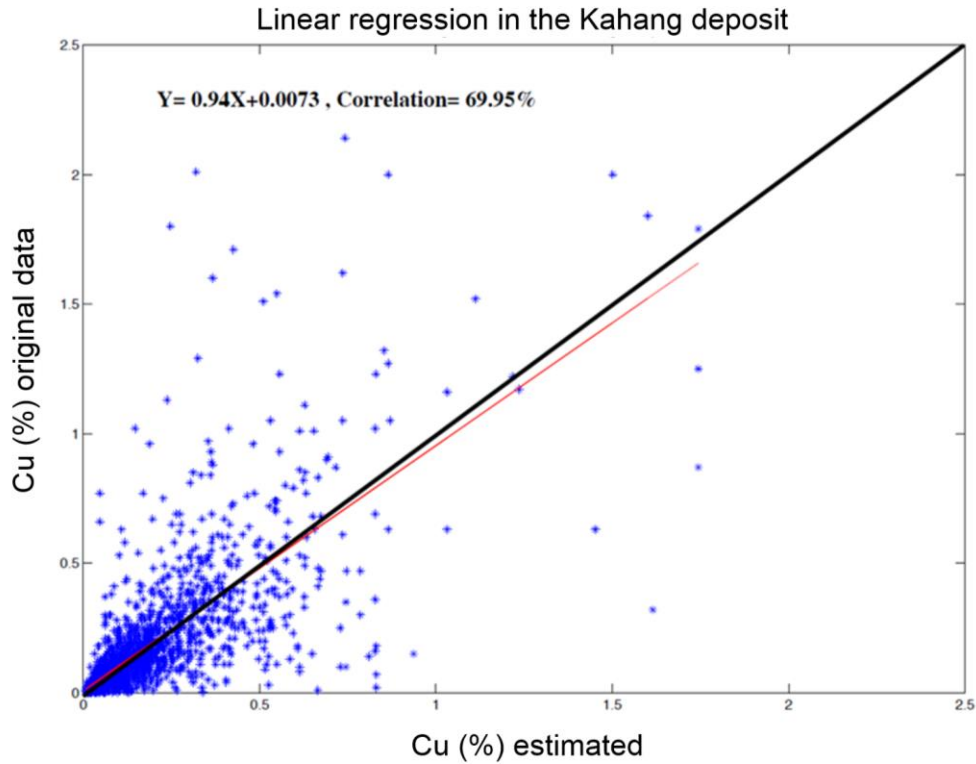
Fig. 3. 22. Correlation chart between original and estimated data using jackknife resampling

3.7 Delineation of Mineralised Zones Using C-V Modelling

3.7.1 C-V Fractal Model

According to a study by Everets and Mandelbrot (1992), the relationship between the measured parameters (e.g., ore grade, density and RQD) and numbers of 2D or 3D dimensional cells can be easily determined. Partition function is addressed as follows:

$$\chi_q(\varepsilon) = \sum_{i=1}^{N(\varepsilon)} \mu_i^q$$

Equation 3-6

Where χ_q, ε and μ are the partition function, 2D or 3D blocks dimensions and a parameter which is in investigation (e.g., ore concentration), respectively. If the investigated parameter has the multifractal nature/behaviour in itself, the following relationship is established:

$$\chi_q(\varepsilon) \approx \varepsilon^{\tau(q)}$$

In this case, the partition function is equal to the exponential relationship between the value of ε which is q at any given moment.

Cheng et al. (1994) proposed the fractal Concentration–Area (C–A) model for separating geochemical anomalies from background values in order to characterise the distribution of major, minor and trace element concentrations in relation to the Mitchell-Sulphurets porphyry system in British Columbia (Canada). This model has the general form:

$$A(\rho \leq v) \propto \rho^{-a1}; \ A(\rho \geq v) \propto \rho^{-a2}$$

where $A(\rho \leq v)$ and $A(\rho \geq v)$ denote areas (A) with concentration values ρ that are, respectively, smaller and greater than contour value ρ defining that areas v represents the threshold), which define those areas and $a1$ and $a2$ are characteristic exponents for both criteria. In log–log plots of concentration contours versus areas, certain

concentration contours representing breakpoints in the plots are considered threshold values separating geochemical populations in the data. Zou et al. (2009) applied the fractal C–A model to characterise the vertical distribution of element concentrations in the Qulong copper deposit, Tibet, western China. Fractal models have been used to identify the vertical distribution properties of Cu concentration values in mineralised and non-mineralised zones. Cheng (2007) described hydrothermal processes (for undiscovered mineral deposits in Gejiu, Yunnan Province, China) in the Earth crust associated with ore deposits, such as porphyry ore deposits, which are characterized by high metal concentrations having fractal or multifractal properties.

Cheng et al. (1994) and Zou et al. (2009) have suggested that the fractal C–A model is applicable in volume or can be extended to volumetric extensions because element distributions in horizontal or vertical directions are in accordance with fractal models. Concentration-Area is for recognition of anomalies clearly in the areas, namely a two-dimensional environment. As a result, the equations of C-A fractal model can be established in the forms of:

$$A_{h(\geq \rho)} \approx \rho^{-D}$$

Equation 3-9

$$A_{v(\geq \rho)} \approx \rho^{-D}$$

Equation 3-10

A_h and A_v indicate two areas containing grades within horizontal (Plans) and vertical (cross sections) directions, respectively. This reveals that the elemental distribution can also exist in 3D dimension. Different forms of the C–A model expressed in Equations 3-9 and 3-10 can be rewritten as:

$$A_h(\rho \leq v) \propto \rho^{-a1}; \; A_h(\rho \geq v) \propto \rho^{-a2}$$

Equation 3-11

$$A_v(\rho \leq v) \propto \rho^{-a1}; \; A_v(\rho \geq v) \propto \rho^{-a2}$$

Equation 3-12

where $A_h(\rho \leq v)$, $A_h(\rho \geq v)$, $A_v(\rho \leq v)$ and $A_v(\rho \geq v)$ denote two areas with concentration values smaller and values greater than the contour value ρ defining that area respectively for all variables are the same as those in Equation 3-6, but the subscripts h and v denote areas described in horizontal and vertical section directions, respectively.

In Equation 3-7, $\tau(q)$ is an auxiliary function. With respect to the Equation 3-7, the multifractal range of the ε and the power value of α (q) can be calculated using the following relationships:

$$\alpha(q) = \frac{\partial \tau}{\partial q}; f(\alpha) = \alpha(q) - \tau(q)$$

Equation 3-13

The multifractal range of $f(\alpha)$ is a continuous function between two values α_{Min} and α_{Max}. If $\tau(q)$ is a linear function with fixed values of $\acute{a} = \acute{a}_{Max}$ or $\acute{a} = \acute{a}_{Min}$, $f(\alpha)$ will be constant which means that multifractal property changes to mono-fractal. In both cases, the relationship between concentration and volume has to be discussed in various forms. In the format of mono-fractal in which $f(\alpha)$ and α are fixed, for better understanding of the relationship between concentration and its occupying volume (the volume containing specific grade) in the way that a database considering various grade is generated in accordance with a determined voxel size (ε), the following relationships are used where $V(\varepsilon)$ represents containing volume of $\rho(\varepsilon)$.

$$V(\varepsilon) \propto \varepsilon^{-f(\alpha)+2}$$

Equation 3-14

$$\rho(\varepsilon) \propto \varepsilon^{\alpha-2}$$

Equation 3-15

With the removal of ε from the two Equations 3-14 and 3-15, the relationship of concentration and volume in mono-fractal (bi-fractal) behaviour is defined as follows:

$$V(\rho) \propto \rho^{[2-f(\alpha)]/(\alpha-2)]}$$

Equation 3-16

In the above equation, values of $f(\alpha)$ and α vary between zero and two. If a multifractal model followed by a continuous range for $f(\alpha)$ values exist then, two scenarios will occur.

In the first case, the α value is allocated to $á_{\text{Min}}$ (lowest value) and in the second case α maximum value is equal to $á_{\text{Max}}$. As a result, to obtain the relationship between concentration and volume an integral equation is used as follows:

$$V(\alpha < \alpha^{+}_{min}) = V(\rho) = \int_{\alpha_{min}}^{\alpha_{min}} C\varepsilon^{-f(\alpha)+2} d\alpha$$

Where C, ρ and $V(\rho)$ denote constant value, ore grade and occupied volume. Finally, the relationship between concentration and volume in the multifractal mode can be addressed as:

$$V(\rho) \approx V(T) - C\varepsilon^{-f(\alpha)+2} d\alpha$$

In a 3D block model, the above equation can be expressed as:

$$V_{(\geq\rho)} \approx \rho^{-D}$$

Where $V(\rho)$ is a volume which contains ore grades equal and higher than ρ and D is a fractal dimension.

Consequently, the relationships defined in Equations 3-11 and 3-12 suggest that element distributions in a volume also follow a fractal model. The proposed fractal C–V model can be expressed, therefore, in the following general form:

$$V(\rho \leq v) \infty \ \rho^{-a1}; \ V(\rho \geq v) \ \infty \ \rho^{-a2}$$

<div align="right">Equation 3-20</div>

Where, $V(\rho \leq v)$ and $V(\rho \geq v)$ denote volumes (V) with concentration values (ρ) that are, respectively, smaller and values greater than contour values (v),which defines those volumes and $a1$ and $a2$ are characteristic exponents. Based on this kind of characterization, it is the assumed hypothesis that different zones in porphyry Cu deposits have fractal properties, which can be described by power–law relationships between ore element concentrations and volumetric extensions (Afzal et al., 2011 and 2012; Wang et al., 2013; Coghill et al., 2014; Sun and Liu, 2014; Awadelseid et al., 2015). In log–log plots of concentration contours versus volumes, certain concentration contours, representing breakpoints in the plots, are considered threshold values separating geochemical populations within the data. To calculate $V(\rho \leq v)$ and $V(\rho \geq v)$ enclosed by a concentration contour in a 3D model, in this study, the original borehole data of ore element concentrations were interpolated by using the geostatistical and inverse distance weighted (IDW) method. The interpolated 3D block model was used for the purpose of this study. Volumes $V(\rho \leq v)$ and $V(\rho \geq v)$ are equal to the unit volume of a voxel (or volume cell) multiplied by the number of voxels with concentration values (ρ) that are, respectively, smaller and greater than a certain concentration value (v). Log–log plots of

the concentration contours versus the corresponding volumes [$V(\rho \leq \upsilon)$ and $V(\rho \geq \upsilon)$] follow a power–law relationship.

Breaks between straight-line segments in those log–log plots represent threshold values separating populations of geochemical concentration values. In typical porphyry Cu deposits, which are mostly high tonnage – low grade, zones of high Cu concentrations comprise relatively few voxels in a 3D block model, whereas zones of low Cu concentrations comprise numerous voxels. Therefore threshold values in this are recognised by applying the proposed fractal C–V model that likely represents boundaries between different ore zones and 'barren' wall rocks.

3.7.2 Application of C-V Fractal Modelling

The C-V fractal model for Cu has been created according to the Cu 3D block model. Threshold values were identified from the log–log plot in Fig. 3. 23, which demonstrates a power–law relationship between Cu concentrations and volumes occupied. It reveals that there are five populations according to the log-log plot corresponding to 0.075 wt.%, 0.42 wt.%, 1.86 wt.% and 3.2 wt.% Cu in the deposit (Fig. 3. 23 and Table. 3. 8).

Depicted arrows in the log–log plot indicate threshold values (e.g., breakpoints: Fig. 3. 23). These separate various straight line segments in the log–log plots. There is a sudden change in the rate of decrease of the volume enclosed by high values of Cu. The first threshold of 0.075 wt.% represents the beginning of the Cu mineralisation in this scenario. As a result of this, the range of Cu concentrations less than 0.075 wt.% is deemed as

'barren' host rock including weakly mineralised zone within the deposit which may be assumed as waste from an exploitation point of view (e.g., propylitic alteration zone in Sungun porphyry copper deposit, NW Iran: Lowell and Guilbert 1970: Sim et al., 1999; Berger et al., 2008; Asghari et al., 2009; Wang et al. 2013; Soltani et al., 2014; Zuo and Wang, 2015). In addition, the first threshold value obtained by the C-V fractal modelling (Cu = 0.075 wt.%) can be defined as a Cut-off Grade (COG) of the deposit for the preliminary optimisation study but, the selection of an optimised COG is a dynamic process (See table 5. 3 of the chapter five for calculation of an economic COG), dependant on ore grade distribution, deposit geometrical shape and especially economical parameters (e.g., Krautkraemer, 1988; Ataei and Osanloo, 2003; Gu et al., 2010). However, what is classed as 'barren' today may be economic in the future particularly when there is an increase in the metal world commodity price (Caccetta and Giannini, 1988; Dagdelen and Mohammed, 1997; Cairns and Shinkuma, 2003; He et al., 2009). The second threshold value of Cu is 0.42 wt.% where the main Cu mineralisation starts. The range of Cu concentrations higher than 1.86 wt.% illustrates an enriched zone for Cu. For these Cu concentrations the slope of the straight line fit is near to 90°.

Based on the 3D model of Mo distribution, volumes corresponding to different Mo grades were used to generate a C-V fractal model. Threshold values of Mo were identified in the C-V log-log plot which revealed five geochemical populations and four threshold values equal to 13, 100, 316 and 645 ppm Mo in the deposit (Fig. 3. 23 and Table. 3. 8). Enriched mineralised zones are deemed to have higher than 645 ppm because with these Mo concentrations the slope of the straight line fit is close to 90°.

The main Mo mineralisation starts from the second threshold which is 100 ppm in this kind of scenario. It is important to bear in mind that the Mo concentrations which are greater than 13 ppm represent the start of Mo mineralisation. Cu and Mo log-log plots have a multifractal nature for the elemental mineralisation in the deposit.

Table. 3. 8. Cu and Mo thresholds defined by the C-V model in the Kahang deposit

Geochemical population	Cu (wt.%) threshold value	Mo (ppm) threshold value	Range Cu (wt.%)	Range Mo (ppm)
First (Barren host rock)	-	-	<0.075	<13
Second (Main mineralisation starting)	0.075	13	0.075-0.42	13-100
Third	0.42	100	0.42-1.86	100-316
Fourth	1.86 (Enriched zone for Cu)	316	1.86-3.24	316-645
Fifth	3.24	645(Enriched zone for Mo)	>3.24	>645

$$V(\geq \rho) = 10^{5.343}\rho^{-0.1896}$$

$$V(\geq \rho) = 10^{3.9066}\rho^{-1.5144}$$

$$V(\geq \rho) = 10^{3.2588}\rho^{-2.966}$$

$$V(\geq \rho) = 10^{3.9395}\rho^{-5.6969}$$

$$V(\geq \rho) = 10^{8.1318}\rho^{-13.417}$$

$$V(\geq \rho) = 10^{5.7691}\rho^{-0.2948}$$

$$V(\geq \rho) = 10^{6.792}\rho^{-1.3343}$$

$$V(\geq \rho) = 10^{6.6044}\rho^{-1.1583}$$

$$V(\geq \rho) = 10^{9.7578}\rho^{-2.4266}$$

$$V(\geq \rho) = 10^{45.621}\rho^{-15.194}$$
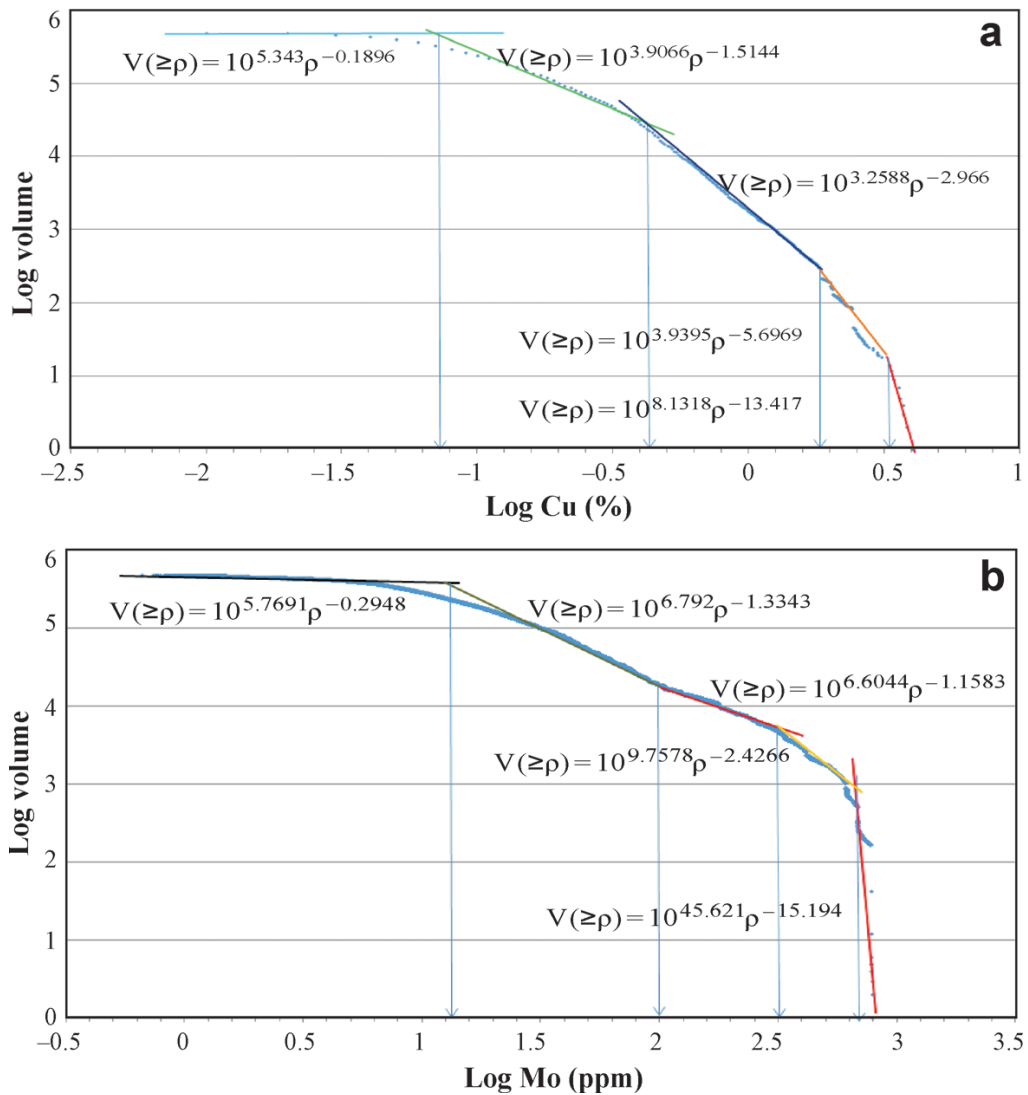
Fig. 3. 23. C-V log-log plots: a) Cu, and b) Mo

3.8 Comparison and Correlation between Results of C-V Fractal and Geological Modelling

To separate major mineralised zones including the supergene enrichment and hypogene zones, a correlation between the geological model (as mentioned in section 3.7.2) with Cu and Mo concentration distribution models has been constructed. In addition, results

from the C-V model were included in the combined model, where in consequence the supergene enrichment zone exists in small sections close to the surface and its Cu concentration value does not exceed that of 1.4 wt.% (Fig. 3. 24).
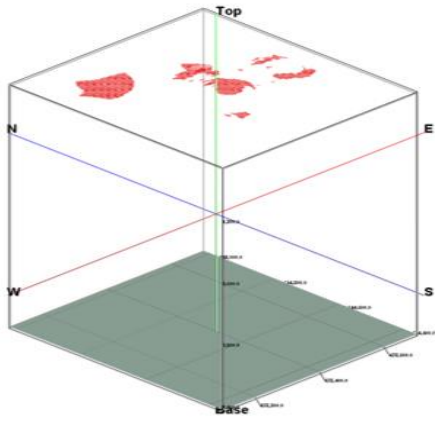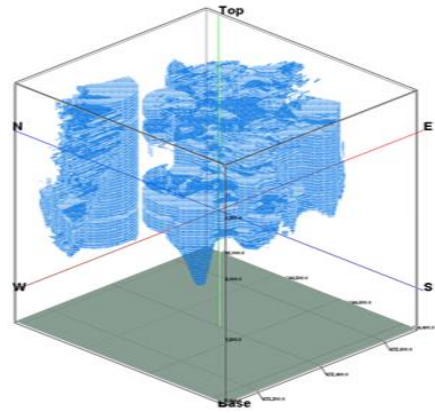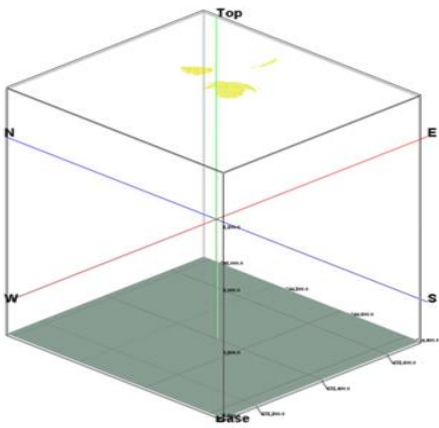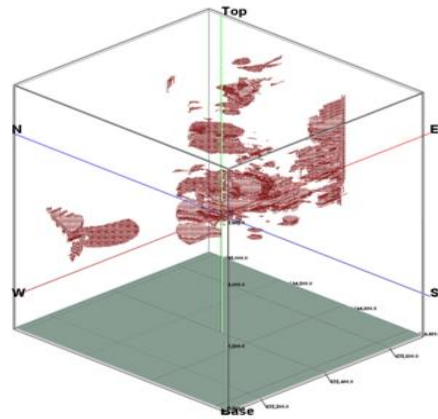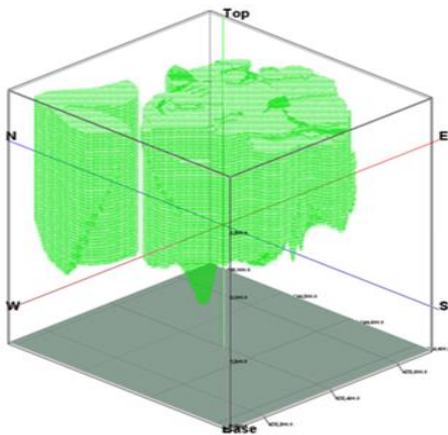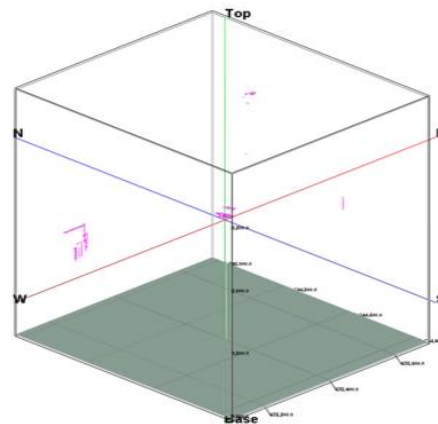
Fig. 3. 24. Geological zones (Cu distribution) including supergene enrichment (a) and hypogene (c) with modified zonation models via C-V showing regions of supergene enrichment (b), hypogene (d), main hypogene (e) and enriched hypogene (f)

Histograms of estimated Cu values for supergene enrichment and hypogene mineralised zones show that there are two populations within the supergene zone, one of which includes Cu values less than 0.2 wt.% and introduces weakly supergene mineralised zone (Sillito, 1997; Pirajno, 2009; Fig. 3. 25a). Moreover, most parts of the hypogene zone contain Cu values near to zero, as depicted in Fig. 3. 25b. It reveals that a correlation and validation between results obtained by geological and C-V fractal modelling is essential in order to achieve an accurate block model for a future optimisation study.

The supergene enrichment zone with Cu > 0.42 wt.% concentrations is located in a small area within both the central and the eastern surface parts of the deposit, as depicted in Fig. 3. 24. As can be seen, the supergene enrichment zone derived via the C-V model has a volume smaller than its geological equivalent model.

The correlation between the geological hypogene zone and the C-V model indicate that marginal parts of the geological model have Cu concentrations ≤ 0.075 wt.% and are consequently considered as weakly hypogene mineralised zone. However, the main hypogene zone with Cu ≥ 0.42 wt.% is located in the central, eastern and NW sections of the deposit especially at depth, but in the NE part of the deposit it is close to outcropping. The enriched hypogene zone with Cu ≥ 1.8 wt.% is situated in small sections of the central, NW, NE and SE parts of the deposit, as illustrated in Fig. 3. 24.

The Mo distribution model is correlated with the supergene enrichment and the hypogene zones, as shown in Fig. 3. 26. The maximum concentration of Mo in the supergene

enrichment zone is 104 ppm and high values of Mo are situated in the hypogene zone. The main Mo mineralisation with Mo ≥ 100 ppm in the hypogene zone correlates with the main hypogene zone (Cu ≥ 0.42 wt.%). The enriched Mo zone with Mo ≥ 645 ppm is located in the central part of the deposit and associated with the enriched hypogene zone (Cu ≥ 1.8 wt.%), as shown in Fig. 3. 26. These results indicate that the enriched mineralised zone is located within the hypogene zone especially in the central, NW and NE sections of the deposit.

In order to validate the results from the C-V model, a comparison between the mineralogical model (for chalcocite and chalcopyrite distributions: Fig. 3. 27a and b) and the main mineralised zones with Cu ≥ 0.42 wt.% (Table. 3. 8 and Fig. 3. 23a) was conducted. To do this, the chalcocite and chalcopyrite mineralogical units were distinguished using a mathematical filter facility within the RockWorks^{TM} software which is called "Boolean data type". As a result, the studied mineralogical units in the 3D model (See chapter 2, Fig. 2. 14c for the 3D dominant ore minerals) were allocated with binary codes (zero or one). Consequently, zones with the code number of zero are removed and the zones with the code number of one will remain in the 3D models (Fig. 3. 27a and b). Subsequently, another mathematical facility within the software called "Multiple of Model & Model" was used, which is a tool to manipulate the voxels in a solid model by the corresponding voxels in another equally-dimensioned solid model file between 3D mineralogical model and corresponding mineralised zones (e.g., RockWorks^{TM} 15, 2010; Fig. 3. 27c, d and e). After doing that, it has been shown that chalcocite is associated with the supergene enrichment zone (Fig. 3. 27a and c) and chalcopyrite is also located within

the main hypogene zone with Cu ≥ 0.42 wt.% (Fig. 3. 27b and d). In addition, the chalcopyrite from the mineralogical model containing Cu ≥ 0.42 wt.% has a proper correlation with the main hypogene zone, as depicted in Fig. 3. 27e.
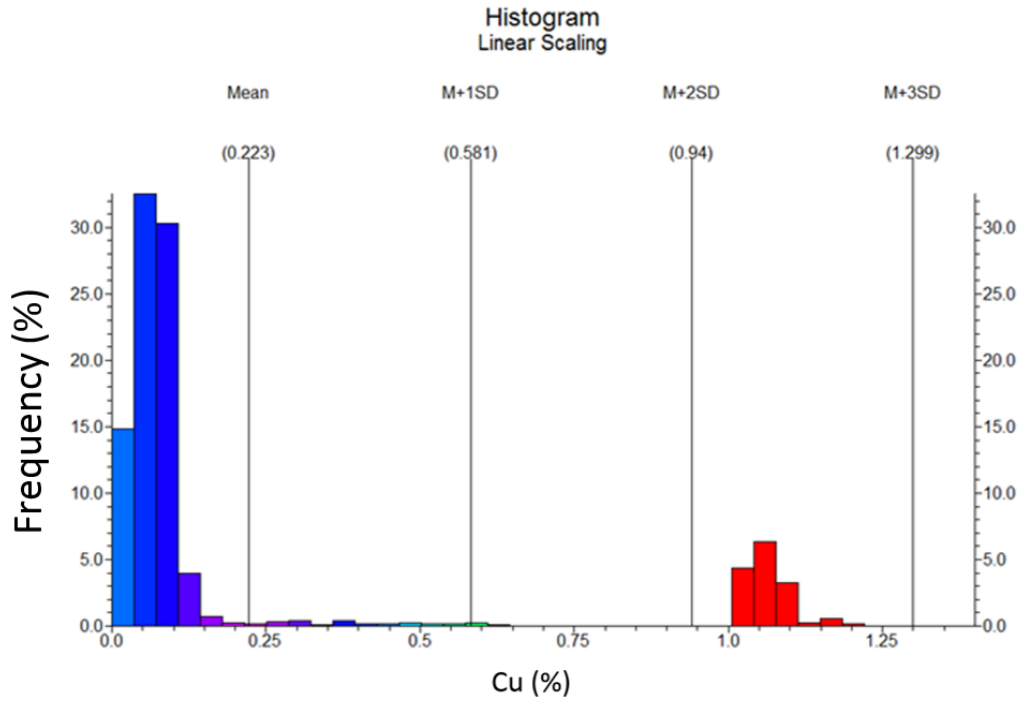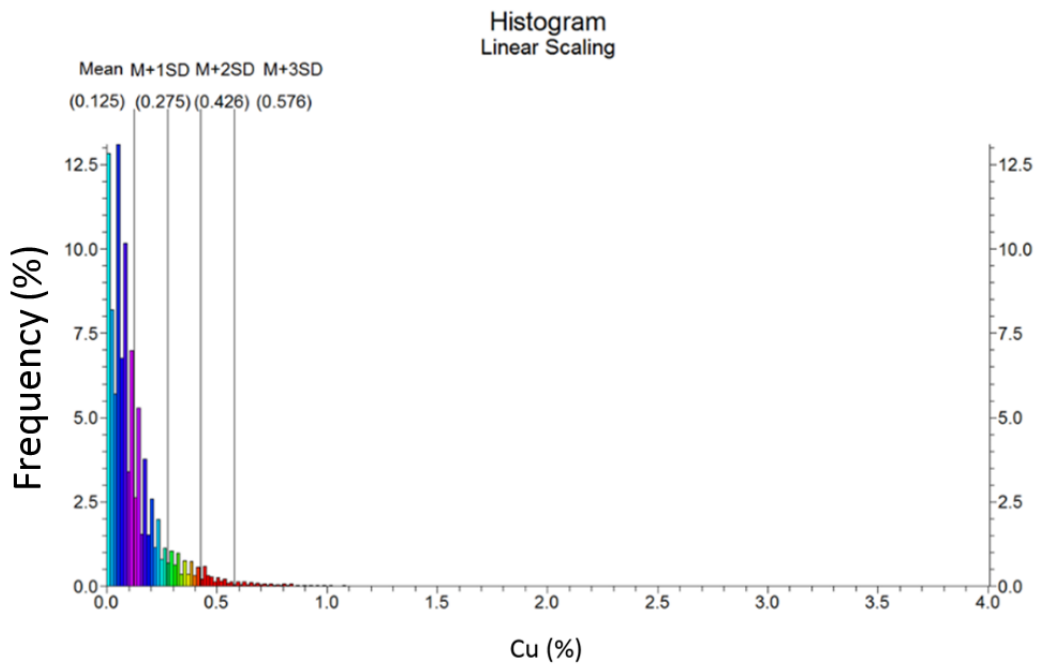
Fig. 3. 25. Histograms of estimated Cu values within the: a) supergene enrichment, and b)

hypogene zones
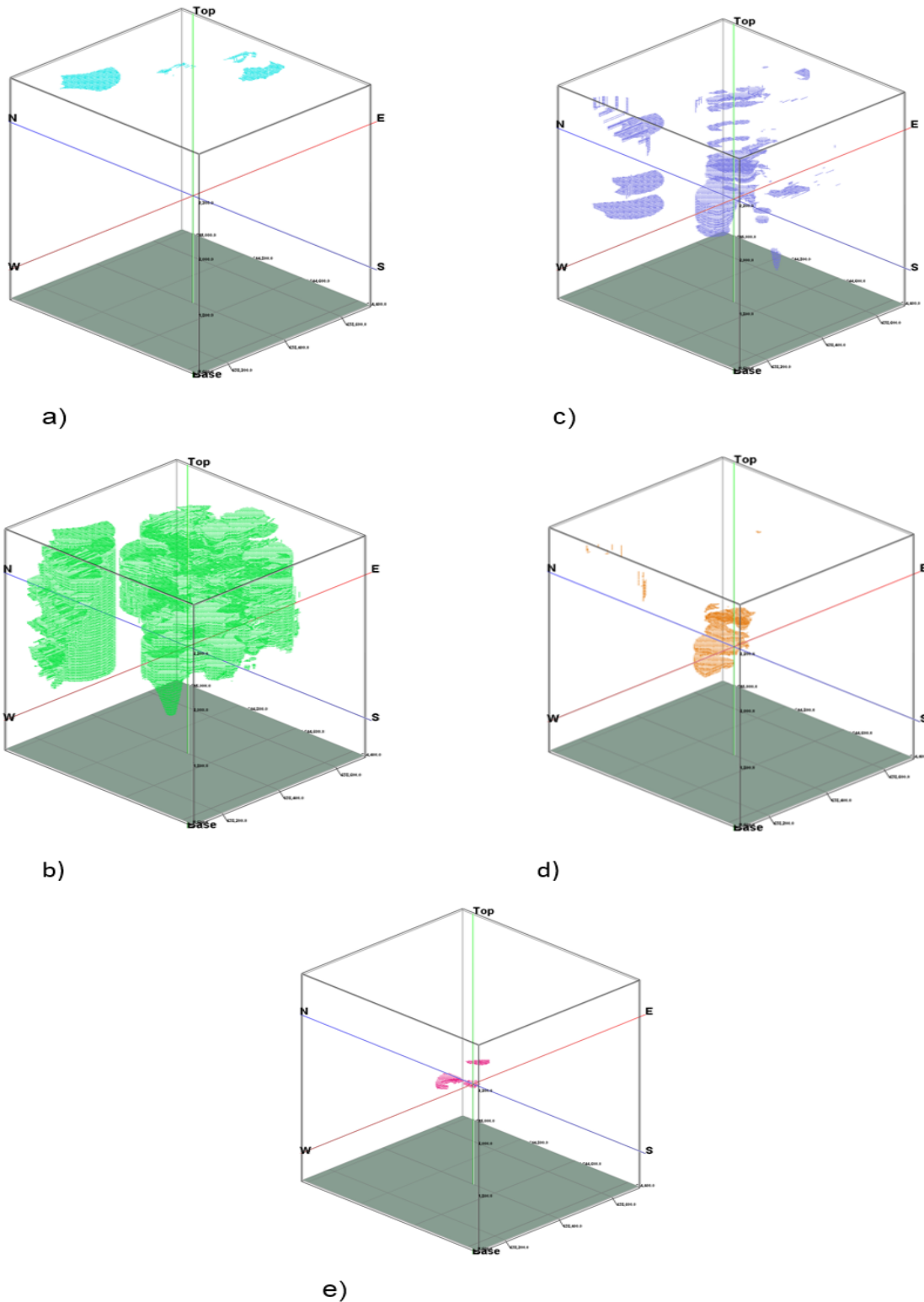
Fig. 3. 26. Mo distribution in supergene enrichment zone (a), hypogene zone based on Mo C-V model (b), hypogene with Mo > 100 ppm (c), hypogene with Mo > 316 ppm (d) and Mo enriched zone (e)
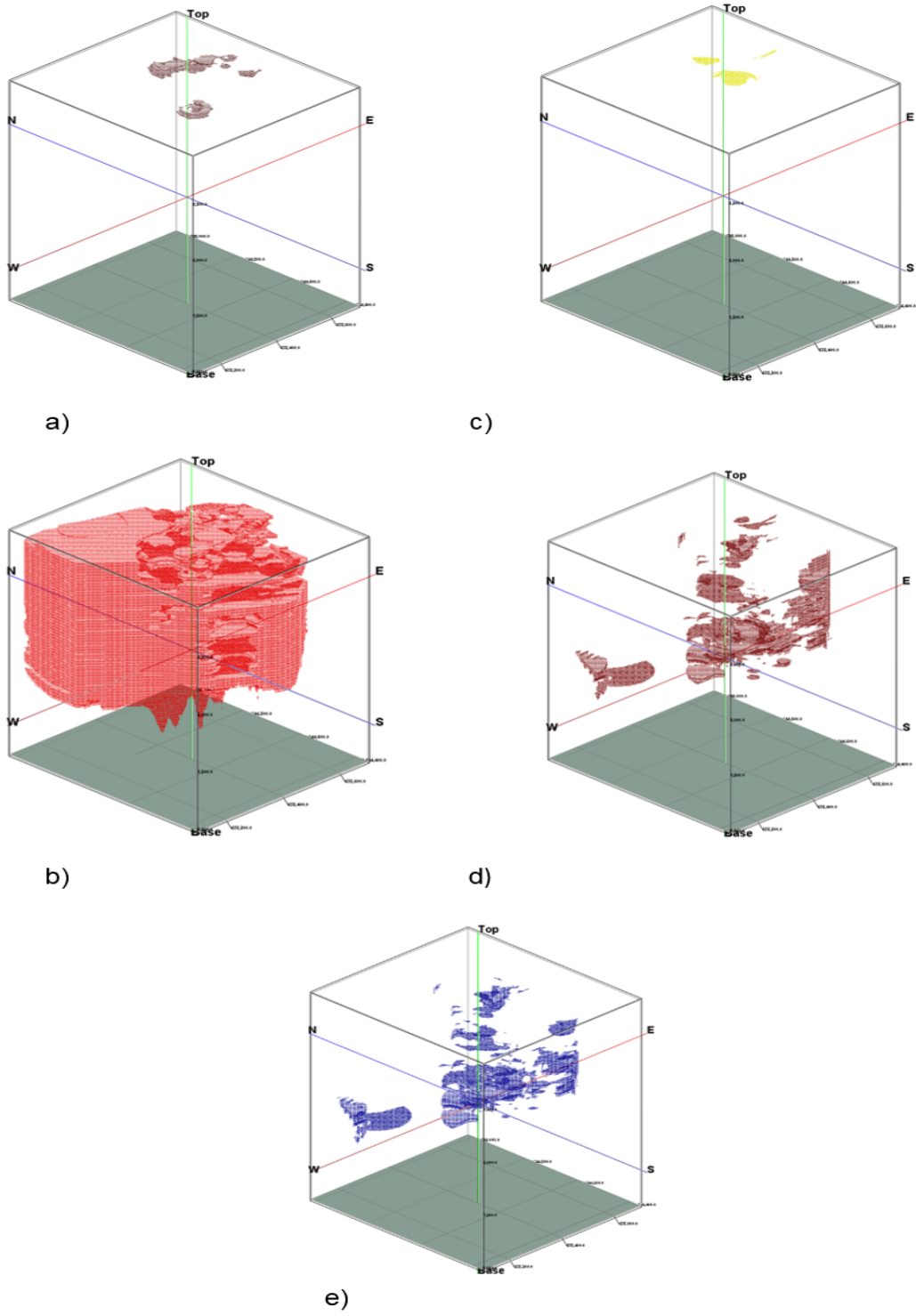
Fig. 3. 27. Correlation between chalcocite (a), chalcopyrite (b) and chalcopyrite ≥ 0.42 wt.% Cu (e) zones with supergene enrichment zone (c) and main hypogene zone (d) based on C-V model

3.8.1 *Application of Logratio Matrix*

Carranza (2011) has proposed a logratio matrix for further calculation of spatial correlations between two binary models. Using the mineralisation model, an intersection operation between a fractal mineralised zone model and different zones in the geological ore model was performed so as to obtain the numbers of voxels corresponding to each of the four classes of overlap zones as shown in Table. 3. 9 (the obtained values are the overlap number of voxels between two binary geological and fractal models). Using the obtained numbers of voxels, Type I error (T1E), Type II error (T2E), and overall accuracy (denoted as OA) relate to the ability of the analysis to define 'barren' host rocks (background) and mineralised zones delineated using the C-V fractal model with respect to the geological models. Type I error (denoted as T1E) relates to the ability of the analysis to define 'barren' host rocks whereas Type II error (denoted as T2E) relates to the ability of the analysis to define mineralised zones. The lower the error (i.e. the higher value for OA) the better the ability of the analysis to define 'barren' host rocks and mineralised zones. The values for OA of the C-V fractal and geological models (alteration and hypogene models) were compared with one another as follows:

Table. 3. 9. Matrix for comparing performance of fractal modelling results with geological model. A, B, C, and D represents the number of voxels overlapping between classes in the binary geological model and the binary results from fractal models (Carranza, 2011)

		Geological model	
		Inside zone	Outside zone
Fractal model	Inside zone	True positive (A)	False positive (B)
	Outside zone	False negative (C)	True negative (D)
		Type I error = C/(A+C)	Type II error = B/(B+D)
		Overall accuracy = (A+D)/(A+B+C+D)	

Comparison between the hypogene zone obtained from the geological model and the main Cu and Mo mineralised zones from the C-V fractal model demonstrates that the hypogene zone has a better correlation with the main Cu mineralised zone (Cu > 0.42 wt.%) because the number of overlapping voxels (A) in the main Cu mineralised zone obtained using the C-V model (20,839 voxels) is higher than in the main Mo mineralised zone (16,990 voxels), as depicted in Table. 3. 10. The overall accuracy of the main Cu and Mo mineralised zone derived via the C-V fractal model with respect to the hypogene zone of the geological model is equal to 0.154 and 0.146, respectively.

Alterations play a fundamental role in zone identification and also in presenting geological models, as described by Lowell & Guilbert (1970). Correlation (from OA results) between the main Cu mineralised zone obtained from C-V model and potassic alteration is higher than the phyllic alteration because the OA for potassic and phyllic alterations have been determined as 0.765 and 0.509 respectively (Table. 3. 11). As a result, the higher values

for overall accuracy in Tables 3. 10 and 3. 11 represent the higher overlap between geological zones with mineralised zones identified by the C-V fractal model.

Table. 3. 10. Overall accuracy (OA) with respect to hypogene zone as delineated in the geological model and Cu and Mo main mineralised zones obtained through C-V fractal model (Values are the number of voxels)

		Hypogene zone of Geological model			
		Inside zone		Outside zone	
C-V fractal model of Cu main mineralised zone	Inside zone	A	20839	B	3348
	Outside zone	C	411164	D	54576
		OA		0.154	
		Hypogene zone of Geological model			
		Inside zone		Outside zone	
C-V fractal model of Mo main mineralised zone	Inside zone	A	16990	B	1795
	Outside zone	C	414954	D	54674
		OA		0.146	

Table. 3. 11. Overall accuracy (OA) with respect to potassic and phyllic alteration zones and Cu main mineralised zones obtained through C-V fractal model (Values are the number of voxels)

		Potassic alteration zone of Geological model			
		Inside zone		Outside zone	
C-V fractal model of Cu main mineralised zone	Inside zone	A	2874	B	21313
	Outside zone	C	93484	D	372256
		OA		0.765	
		Phyllic alteration zone of Geological model			
		Inside zone		Outside zone	
C-V fractal model of Cu main mineralised zone	Inside zone	A	10345	B	13842
	Outside zone	C	226246	D	239494
		OA		0.509	

Validation between the main Mo mineralised zone (Mo > 100 ppm) based on the C-V fractal model and alteration zones from the geological model indicates that there is a difference between the two alteration zones. Overall accuracy for the potassic and phyllic zones has been determined as 0.770 and 0.524 respectively (Table. 3. 12). According to these results, the main elemental mineralised zones have better correlation with the potassic alteration zone.

Table. 3. 12. Overall accuracy (OA) with respect to potassic and phyllic alteration zones and Mo main mineralised zones obtained through C-V fractal model (Values are the number of voxels)

		Potassic alteration zone of Geological model			
		Inside zone		Outside zone	
C-V fractal model of Mo main mineralised zone	Inside zone	A	1699	B	17086
	Outside zone	C	95053	D	374575
		OA		0.770	
		Phyllic alteration zone of Geological model			
		Inside zone		Outside zone	
C-V fractal model of Mo main mineralised zone	Inside zone	A	11531	B	7254
	Outside zone	C	224919	D	244709
		OA		0.524	

3.9   Results

Results from this study show that the C–V fractal model can be used to recognise different mineralisation zones in porphyry Cu deposits. Different geochemical populations can be interpreted via the C–V fractal model. The C–V fractal model uses relationships between the ore element concentration and the enclosing volumes, for example the concentration of Cu associated with different zones, and satisfies power–law relationships. The proposed fractal model could be applied for delineating enrichment zones from the 'barren' host rock, or from the background value using the concentration values of the zones in combination with characteristic features of their geometrical shapes. The

159

proposed model is applicable to ore elements in the Cu and Mo porphyry deposits for which the spatial patterns of concentration values satisfy a multifractal model.

Results from this study reveal that the hypogene zone is a major mineralised zone within the Kahang Cu-Mo porphyry deposit. Based on the C-V fractal model, the threshold value of 0.075 wt.% Cu may be equal to the deposit COG however, further investigation in this regard has to be conducted considering economic aspects of the optimisation study (See chapter 5). The threshold values for the main Cu and Mo mineralisation are 0.42 wt.% and 100 ppm, respectively. Enriched Cu-Mo mineralised zones with Cu ≥ 1.8 wt.% and Mo ≥ 645 ppm are located in the central, NW and NE parts within the hypogene zone. The supergene enrichment zone exists in small parts within the deposit, especially in the central and eastern zones.

The supergene enrichment and hypogene zones delineated by the C–V model correlate well with the alterations and mineralogical data shown in the 3D models. The C–V log–log plots from the Kahang deposit show that there is a multifractal model for Cu and Mo. From a comparison of the C–V and geological models the supergene enrichment zone shows a spatial correlation with the chalcocite-rich zone within the Kahang deposit. The main hypogene zone of Cu ≥ 0.42 wt.% has an association with the chalcopyrite distribution model. According to the correlation between results driven by fractal modelling and geological models using the logratio matrix, the Cu and Mo main mineralised zones generated in the C-V fractal model have a strong correlation with the potassic alteration zone with respect to the OA.

CHAPTER FOUR. Rock Mass Characterisation Utilising Fractal Modelling based on Density and RQD Data

4.1 Introduction

Assessment of rock density and RQD are crucial aspects of mineral exploration, resource modelling and mine planning with huge cost implications for the design and the mining of each block (ore or waste tonnage). These are calculated using the dimension and density of each block. The results are assessed to identify a final pit slope angle and consequent pit stripping ratio (Lerch and Grossmann, 1965; Little, 2006; Grenon and Hadjigeorgiou, 2010). The tonnage of these blocks located in each extractive zone is determined on the basis of the density zones (e.g., ore and waste; Hamdi and Mouza, 2005; Hustrulid and Kuchta, 2006; Rafiee and Vinches, 2008; Yasrebi et al., 2011). Host rocks of porphyry deposits consist of sub-volcanic bodies such as porphyritic quartz diorite, granite, monzonite and quartz monzonite which are lithological units with high hardness (Hitzman et al., 1992; Laznicka, 2005). Parameters such as density, hardness, porosity and fracture frequency (number of fractures counted each meter) give additional indications of rock mass characteristics within porphyry deposits (Dershowitz and Einstein, 1988; Meyer and Einstein, 2002; Kalenchuk et al., 2006).

Numerical models in geosciences have been created and consequently utilised to better interpret the variability of geological parameters such as lithology, ore-type, alteration and mineralogy or for a better understanding of the different attributes such as density, rock mass characterisation and RQD (Jinga and Hudson, 2002; Rafiee and Vinches, 2008; Yasrebi et al., 2013b, 2014). However, the classical statistical methods for delineation of populations from a background level would be for example, a histogram analysis, box plot, summation of mean and standard deviation coefficients and median. These are not

considered overly accurate due to the fact that these statistical methods consider only the frequency distribution of information while not paying attention to the spatial variability (Boadu and Long, 1994; Ehlen, 2000). In other words, the classical statistical plots (i.e., histograms) are based on the data abundance distribution and cannot quantify the spatial positions of parameters such as RQD and density (Baecher et al., 1977; Rouleau and Gale, 1985; Villaescusa and Brown, 1990; Lu 1997; Rafiee and Vinches, 2008; Madani Esfahani and Asghari, 2013). As a result, numerical modelling of rock characteristics is a difficult task and requires 3D modelling for better interpretation of the problems found in a mining operation such as rock discontinuities, planar failure, circular failure, wedge failure and toppling failure (Zhang and Einstein, 2000; Lina and Kub, 2006; Yasrebi et al., 2013b, 2014).

The earliest model regarding the quantitative description of in-situ block size distribution (IBSD) was the Rock Quality Designation (RQD; See chapter 1, section 1.1 for the RQD definition), which was proposed by Deere (1964). Priest and Hudson (1976) applied the RQD method to scanline survey data with respect to an analytical relation between RQD and the discontinuity frequency resulted from a scanline survey. A borehole or a scanline are by their nature one dimensional. As a result, RQD values calculated using bore hole data or a scanline survey are influenced by the orientation in which the measurements are taken (horizontal or vertical) so the method does not consider calculation for the other direction (Lu, 1999; Carvalho et al., 2007; Slob, 2010). In order to overcome the dependence of RQD on orientation, Kazi and Sen (1985) proposed the use of the Volumetric Rock Quality Designation (V. RQD) which is a three-dimensional parameter.

This encloses the proportion of the volume of intact matrix rock blocks, equal to or higher than 0.001 m^3 in size, which can be associated with the average volume of a matrix block and the number of matrix blocks per m^3. To do this, the V.RQD is calculated by summation of the volumes of intact blocks divided by the total rock mass volume which is expressed as a percentage. However, the proposed model is limited to the estimation of the average block volume rather than the IBSD (Deere and Deere, 1989; Şen and Eissa, 1992; Lu, 1999). Palmstrom (1985) proposed different empirical equations to link Volumetric Discontinuity Count for RQD (known as J_v RQD) data and linear fracture frequency. He suggested that there is a correlation between the in-situ block size and J_v is represented in a figure incorporating various measurements of the block size or degree of jointing (e.g., density of joints, RQD, block volume and joint spacing). However, this model can only estimate a rough upper and lower range of block sizes and therefore has restricted practical applications (Şen and Eissa, 1991; Milne, 2007). Şen and Eissa (1992) derived values for J_v for RQD and block volumes of different shapes such as bars, plates and or prisms quantity. The proposed model provides a simple tool for rock engineers without the need for recourse to theoretical calculations. However, the block volume in this model is given in terms of average block size so it cannot describe the block size distribution (Lu, 1999; Palmstrom, 2005).

Techniques for selecting a theoretical function to describe rock mass characteristics based on RQD data are unsatisfactory, as mentioned above. As a result, an approach to introduce an analytical model to help achieve a proper fitted curve for interpreting the distributions of measured RQD combining with density data is needed (e.g., Tables. 4. 5

and 4. 6; Figs. 4. 8; 4. 10 to 4. 12). An accurate description of density and RQD distribution within a deposit plays a significant role in any optimisation study (See chapter 5, section 5.5 and 5.7). In recent years, models based on fractal geometry as a nonlinear mathematical method, proposed by Mandelbrot (1983), have been widely used in different branches of earth sciences since various geological processes and even mining-based issues like rock mass characterisation can be categorised by changes in fractal dimensions resulting from analysis of the relevant data and desirable attributes (density and RQD in this scenario). Therefore, fractal analysis has the abilities to identify the differences within ore deposits especially in hydrothermal occurrences such as porphyry Cu deposits (Agterberg et al., 1993; Cheng et al., 1994; Li et al., 2003; Cheng, Q., 2007; Harati et al., 2013). In other words, differences of fractal dimensions in density and RQD data can certify applicable criteria to identify rock mass characteristics.

Consequently, the aim of this chapter is to use the Density–Volume (D–V) and RQD-Volume (RQD-V) fractal models, which demonstrate that there is a power–law relationship between desirable attributes (e.g., density and RQD values within the deposit) and their cumulative volumes occupying spatial positions, to delineate density and RQD populations associated with the major rock types (e.g., porphyritic quartz diorite: PQD, andesite: ANS and dacite: DAC: Figs. 4. 8; 4. 11) which occupy 93% of whole deposit volume (Yasrebi et al., 2013b). The results derived via the RQD-V fractal model are validated using the Deere and Miller rock classification (1966; Table. 4. 1) to test whether the RQD-V fractal model defines the best result with respect to the volume of voxels (blocks) located within the mentioned lithological units in order to predict an

optimised experimental final pit slope. Moreover, for validation purposes and better understanding of rock characteristics in the studied deposit, the Log-ratio matrix proposed by Carranza (2011) has been employed.

Table. 4. 1. Classification of Rock Quality Designation, Deere and Miller rock classification (1966)

TERM	RQD
very poor	< 25
poor	25-50
fair	50-75
good	75-90
excellent	90-100

4.2   Statistical Characteristics

RQD and density histograms provide a means for quickly evaluating the range of density and RQD values for a selected data set (See chapter 3, section 3.3, figures for the original data sets used for RQD and density values) without creating a 3D solid model in order to illustrate the highest, lowest, sum, or average data values. These histograms are used to read a single column of data (RQD or density) from a data set to determine the frequency or percentage of the total number of measurements for that variable/attribute that falls within each user-defined grouping. Location of boreholes which have been analysed for density and RQD values is shown in Fig. 4. 1. In this deposit, 33 and 14979 density and RQD samples have been measured from 11 and 42 boreholes, respectively, out of a total of 48 boreholes carried out in the deposit (Fig. 4. 1; See chapter 3, Tables. 3. 2 and 3. 3; Fig. 3. 4c and d). The density and RQD distribution functions are shown in Fig. 4. 2 and

4. 3, and are not normally distributed, with averages of 2.68 t/m^3 and 48%, for density and

RQD, respectively.
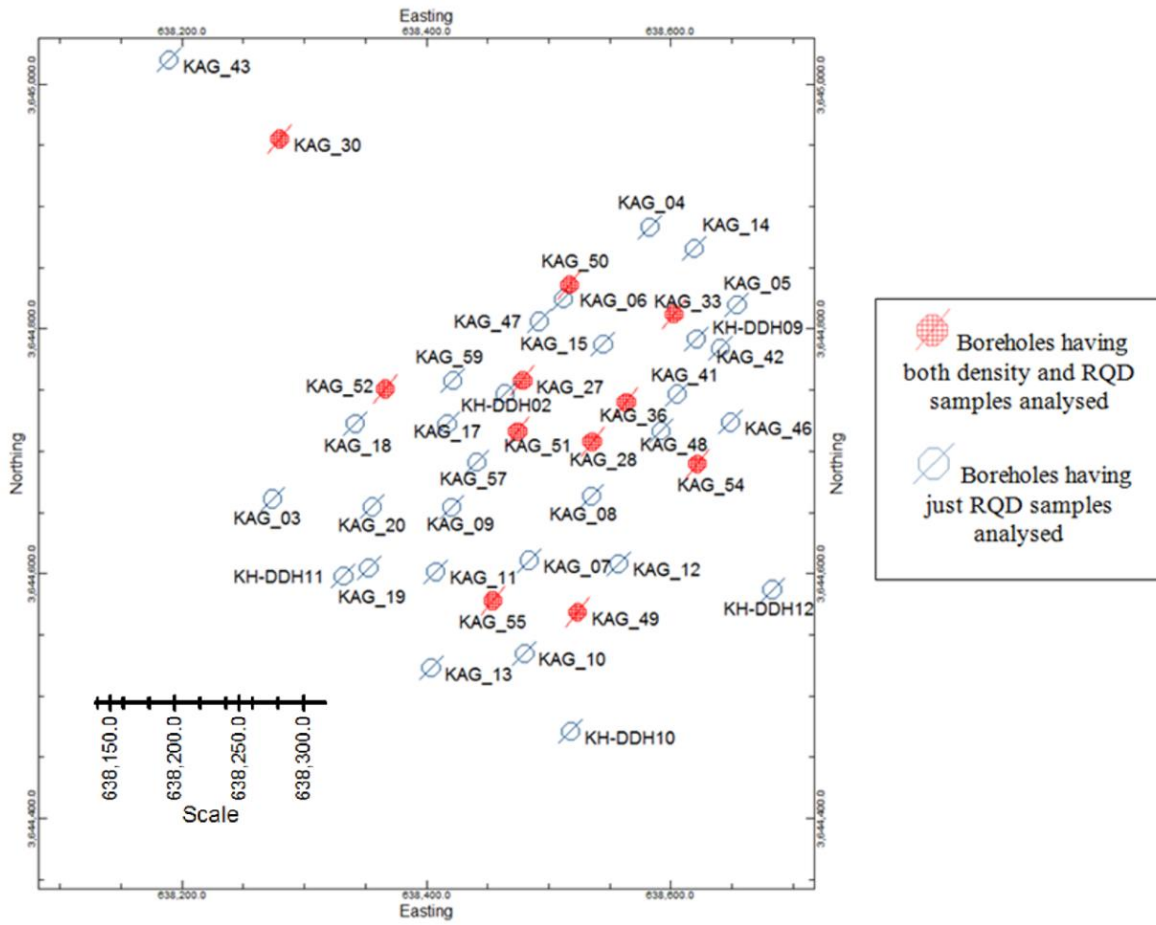
Fig. 4. 1. Location of boreholes sampled for density and RQD
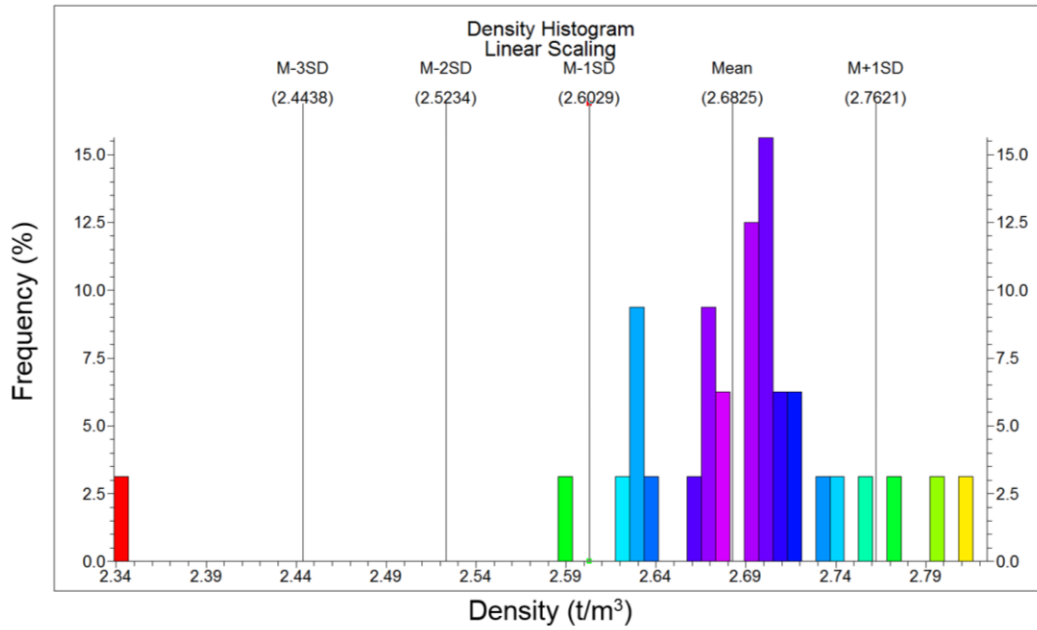
Fig. 4. 2. Density histogram based on raw data for the Kahang porphyry deposit
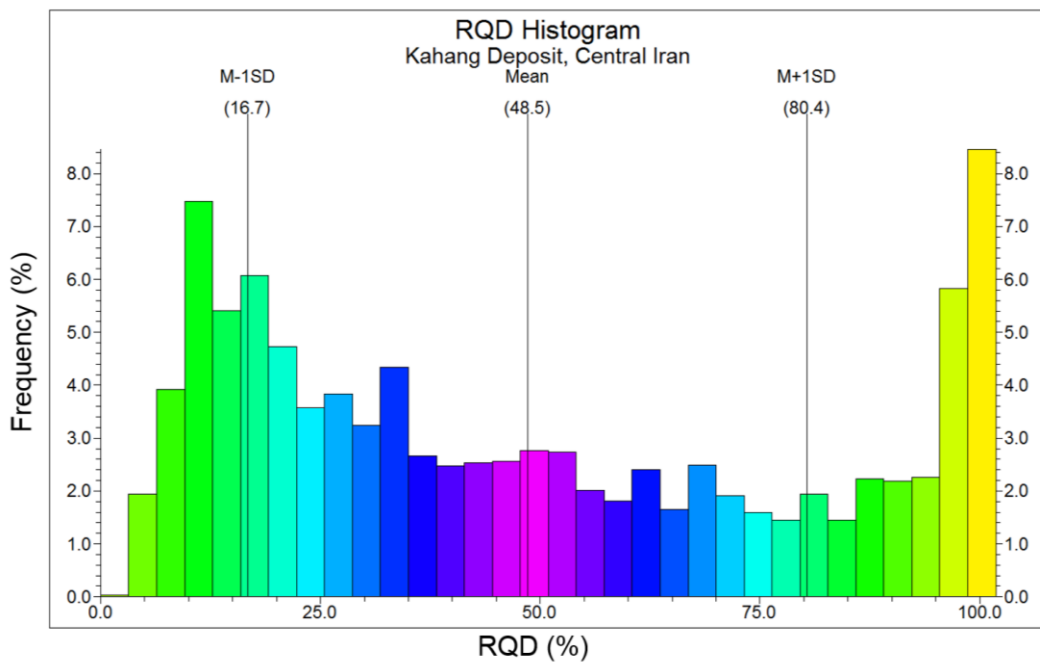
Fig. 4. 3. RQD histogram based on raw data for the Kahang porphyry deposit

The multi-modal distribution for density (Fig. 4. 2) indicates that the deposit has high values in terms of density especially in the major rock type of PQD occupying most parts of the deposit. As a result, most density values are higher than the mean point which increases the tonnage of each individual voxel and correspondingly produces a rise in the total rock tonnage. There is the bimodal distribution for RQD (Fig. 4. 3). As a result, there are two main populations with values of <25% and >90% for RQD which illustrates that there are two classifications of rock qualities (poor and excellent) with respect to the Deere and Miller RQD classification (1966). In addition, with respect to the RQD histogram, the greatest frequency of the RQD data corresponds to the excellent rocks within the deposit which will result in the highest stability of the final pit slope. The tonnage of extractive blocks in the deposit is calculated on the basis of rock density (ore and waste) which is used for pit optimisation study.

4.3   Methodology

Initially, a database was generated based on drill core data consisting of lithological units, density and RQD values. Secondly, the database was entered into the RockWorks™ 15 software package to build 3D density and RQD block models (Fig. 4. 5 and 4. 6) utilising IDWAM due to the lack of adequate density and RQD data and having a non-uniform drilling grid. For RQD, an experimental variogram in horizontal (with lag spacing of 15 m) and vertical (with lag spacing of 8 m) orientations was produced via MATLAB software with respect to log transformation of RQD values (raw data), as shown in Fig. 4. 4. From this, the horizontal (Azimuth: 0 and Dip: 0) and vertical (Azimuth: 0 and Dip: -90) ranges for RQD are 120 m and 270 m, respectively. However, no proper variogram can be fitted

for density because of so few data (just 33 samples: See chapter 3, Table. 3. 2 and Fig. 3. 4c). The next step was to propose the Density–Volume (D–V) and RQD-Volume fractal models to generate the separation of different populations in terms of density and RQD. Subsequently, a mathematical facility within software called "Multiple of Model & Model" was used to manipulate the voxels in a solid model using the corresponding voxels in another equal-dimension solid model. From this, a correlation between the density and RQD 3D block models interpreted via D–V, RQD-V and the porphyric quartz diorite lithological unit was conducted (e.g., RockWorks^{TM} 15, 2010; Fig. 4. 12). The theoretical variogram for RQD is as follow:

$$\gamma_{RQD}(h) = 135.71 + 190\ sph\ (20, 20, 20) + 499.88\ sph\ (120, 120, 270)$$

Equation 4-1
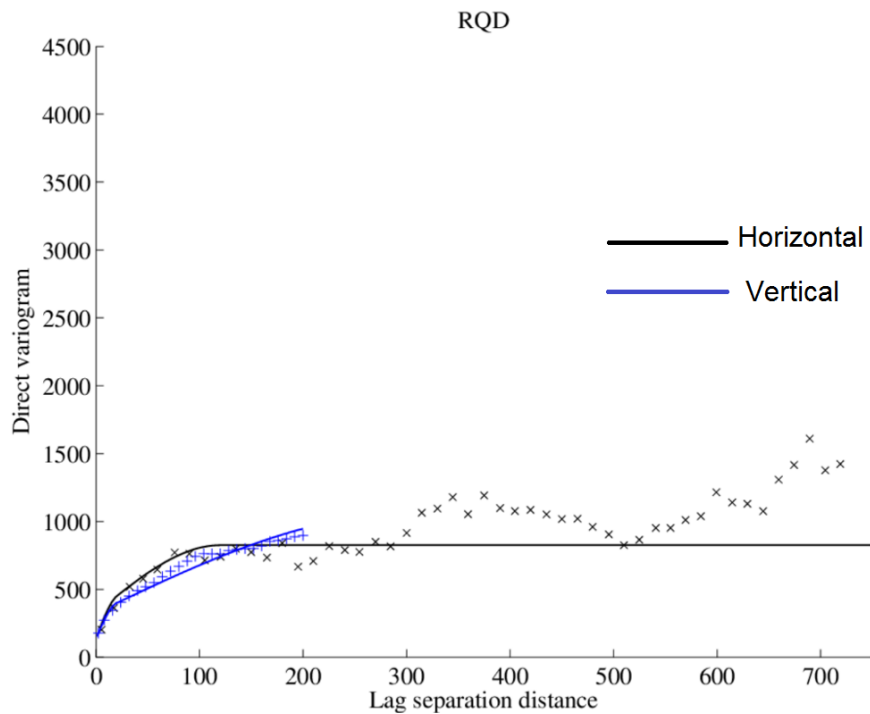
Fig. 4. 4. Experimental and theoretical variogram for RQD
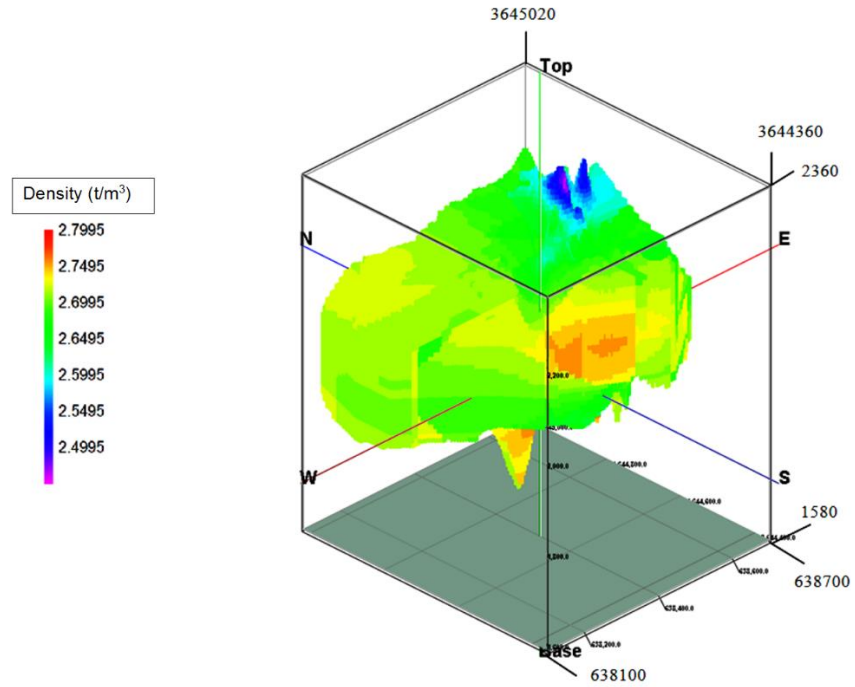
Fig. 4. 5. Density block model determined using estimated data
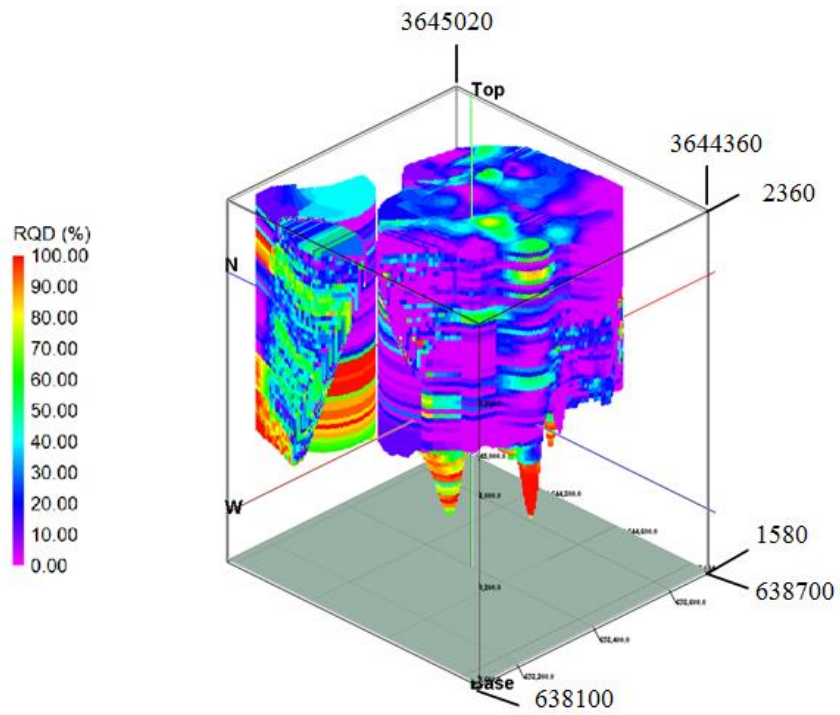
Fig. 4. 6. RQD block model in Kahang porphyry deposit determined using estimated data

4.3.1 D-V Fractal Model

Fractal and multifractal modelling was generated with respect to a partition function and a power-law relationship between parameters such as density and RQD (Evertz and Mandelbrot, 1992; Li et al., 2003; Carranza, 2008). The D-V fractal model was constructed based on a Concentration-Volume (C-A) fractal model, shown in Equation 4-2:

$$V(\rho \leq \upsilon) \propto \rho^{-a1} \; ; \; V(\rho \geq \upsilon) \propto \rho^{-a2}$$

Equation 4-2

Where $V(\rho \leq \upsilon)$ and $V(\rho \geq \upsilon)$ denote two volumes with density values less than, or equal to, and greater than, or equal to, the contour value ρ; υ which represents the threshold value of a population (or volume); and $a1$ and $a2$ which are characteristic exponents. Threshold values in this model indicate boundaries between different density populations within ore deposits. To calculate $V(\rho \leq \upsilon)$ and $V(\rho \geq \upsilon)$, which are the volumes enclosed by a contour level ρ in a 3D model, the drill core data of density values was interpolated by using a geo-statistical estimation. The density 3D model was evaluated by IDW, which can improve the interpolation of voxel values that lie between data point clusters and can be useful for modelling drill hole based data in different types of deposits (Lima et al., 2013). D–V fractal model reveals that there are two populations according to the log–log plot, one above and one below 2.7t/m^3 within the deposit (Fig. 4. 7), indicating that the rocks with correspondingly high density commence from this break point. Most parts of the

deposit have density values higher than 2.7t/m^3, especially in the central part of the deposit (Fig. 4. 5).
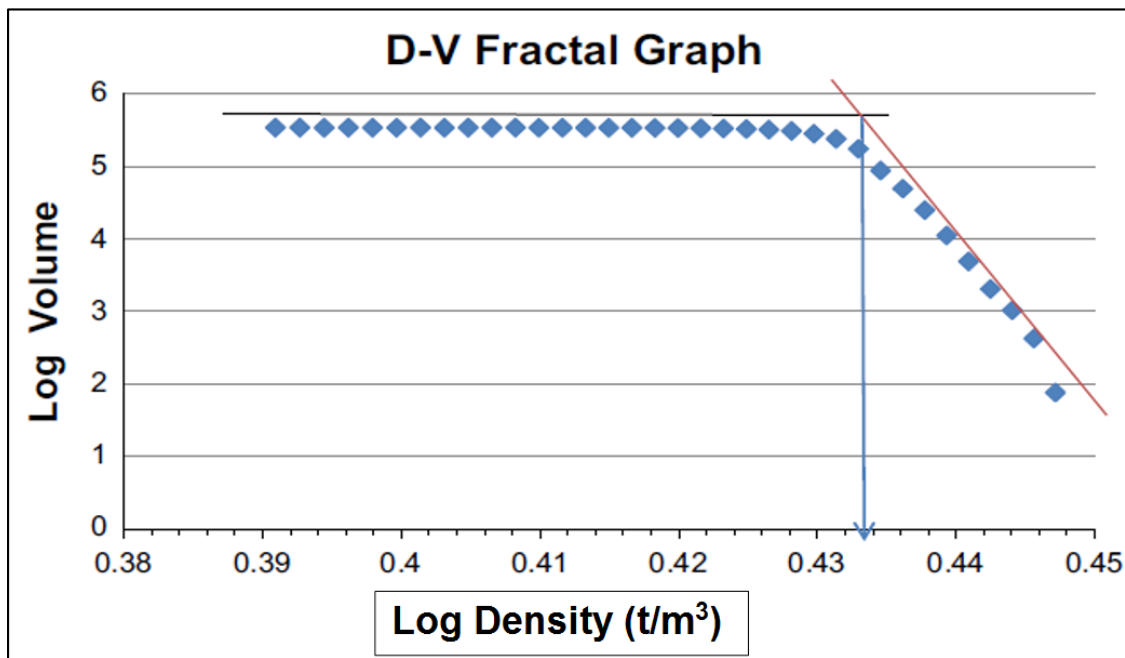
Fig. 4. 7. D–V log–log plot in the Kahang deposit

Results of the D–V model are correlated to the major lithological units of the deposit consisting of porphyritic quartz diorite (PQD), dacite and andesite. High density rocks (≥2.7 t/m^3) defined by means of the D–V modelling are clearly correlated with porphyritic quartz diorite defined by the 3D modelling of lithological drill core data (compare Fig. 4. 5 with Fig. 4. 8a). However, the high density rocks are also associated with andesite in the marginal parts of the deposits, as illustrated in Fig. 4. 8b. The high density is not present in the majority of dacitic rocks, as depicted in Fig. 4. 8c.
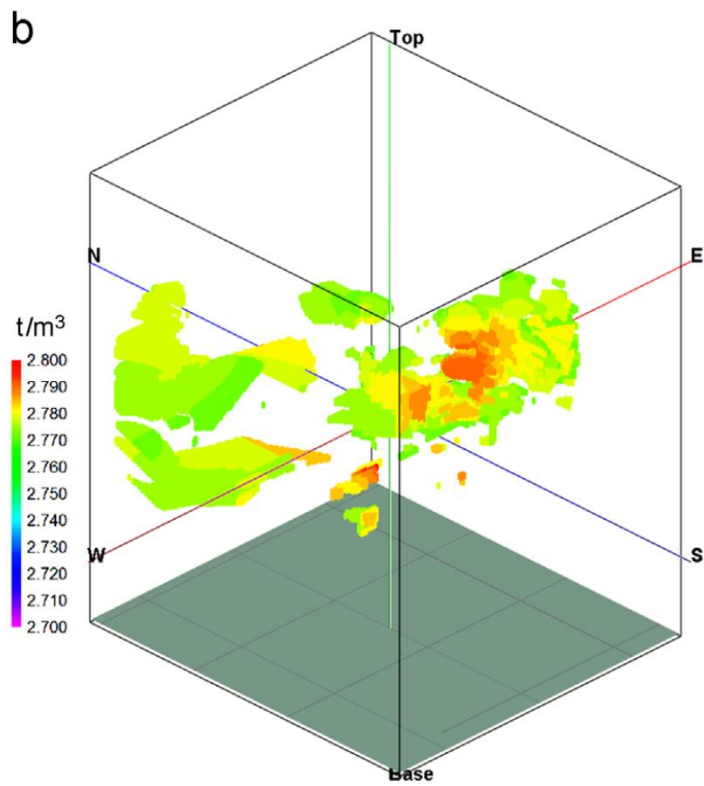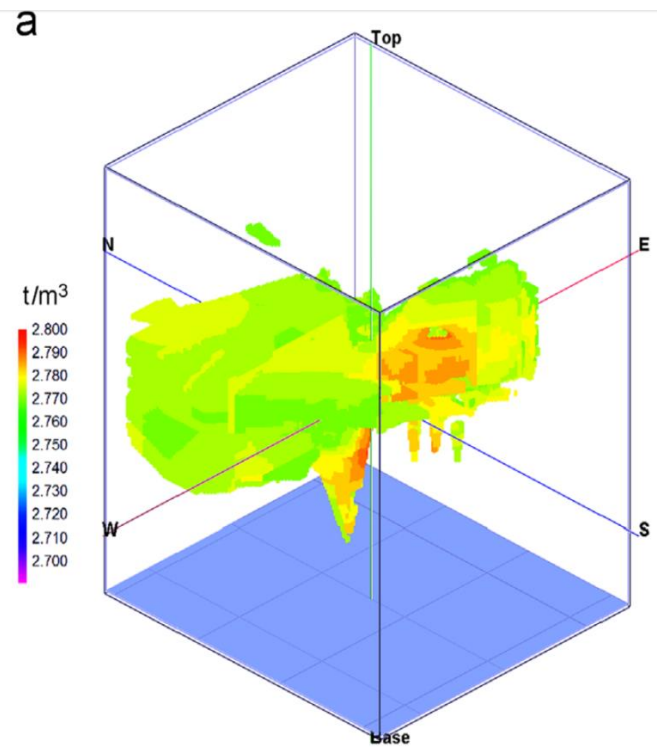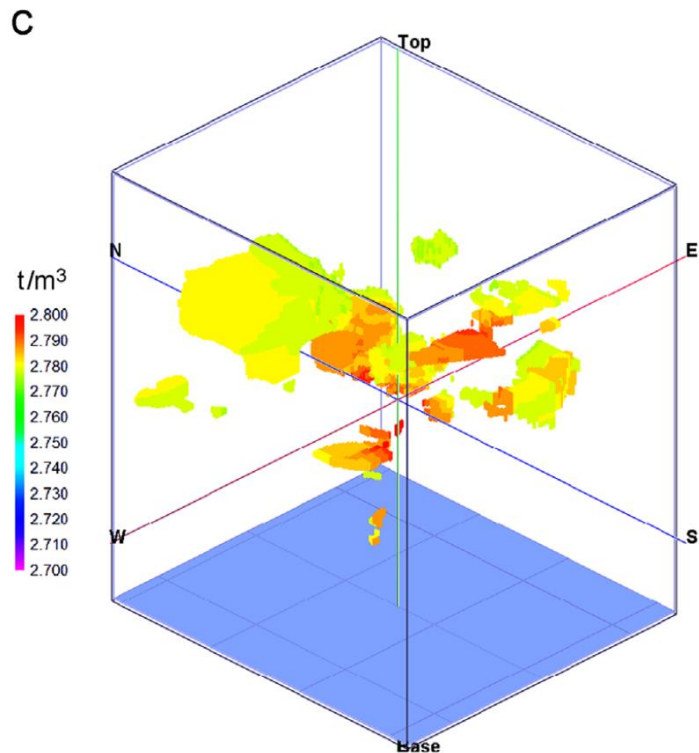
Fig. 4. 8. Voxels with density ≥2.7 t/m^3 within lithological units: a) porphyritic quartz diorite, b) andesite, and c) dacite

Carranza (2011) has provided a method for determining the overlap correlations between two binary models (See Chapter 3, section 3.8.1). An intersection operation between the results from the fractal model and major lithological units was performed to obtain the number of voxels corresponding to each of the four classes of overlap zones. Using the number of voxels, Type I error (T1E), Type II error (T2E) and overall accuracy (OA) of the fractal model were calculated with respect to the lithological model. Correlation between the high density rocks obtained via the D–V fractal model and the major lithological units show that the porphyritic quartz diorites have higher OA compared with andesitic and dacitic rocks (OA$_{PQD}$=0.65, as shown in Table. 4. 2). Moreover, overall accuracies of the

high density zones with andesite and dacite are 0.35 and 0.32, respectively, as depicted in Tables 4. 3 and 4. 4.

Table. 4. 2. Overall accuracy (OA), Type I and Type II errors (T1E and T2E, respectively) with respect to PQD rocks resulted from geological model and high density rocks obtained through D–V fractal modelling of density data (the obtained values are the overlap number of voxels between two binary geological and fractal models)

			PQD of geological model		
			Inside zones		Outside zones
D–V fractal model of high density rocks	Inside zones	A	164442	B	48382
	Outside zones	C	75258	D	60956
		T1E	0.314	T2E	0.442
			OA		0.646

Table. 4. 3. Overall accuracy (OA), Type I and Type II errors (T1E and T2E, respectively) with respect to andesite rocks resulted from geological model and high density rocks obtained through D–V fractal modelling of density data (the obtained values are the overlap number of voxels between two binary geological and fractal models)

			Andesite of geological model		
			Inside zones		Outside zones
D–V fractal model of high density rocks	Inside zones	A	31404	B	208296
	Outside zones	C	14314	D	88024
		T1E	0.313	T2E	0.7
			OA		0.349

Table. 4. 4. Overall accuracy (OA), Type I and Type II errors (T1E and T2E, respectively) with respect to dacite rocks resulted from geological model and high density rocks obtained through D–V fractal modelling of density data (the obtained values are the overlap number of voxels between two binary geological and fractal models)

		Dacite of geological model			
		Inside zones		Outside zones	
D–V fractal model of high density rocks	Inside zones	A	33932	B	205768
	Outside zones	C	26579	D	75759
		T1E	0.44	T2E	0.73
		OA		0.32	

4.3.2 RQD-Volume (RQD-V) Fractal Model

The RQD–V fractal model which is developed based on Concentration-Volume (C-V) fractal (Yasrebi et al., 2013b) for separation of rock populations based on RQD as an important parameter for the rock mass characterisation, can be shown in Equation 4-3:

$$V(\rho \leq \upsilon) \propto \rho^{-a1}; \; V(\rho \geq \upsilon) \propto \rho^{-a2}$$

Equation 4-3

Where $V(\rho \leq \upsilon)$ and $V(\rho \geq \upsilon)$ denote two volumes with RQD values less than or equal to and greater than or equal to the contour value ρ; υ which represents the threshold value of a volume; $a1$ and $a2$ which are characteristic exponents. Threshold values in this model represent boundaries between different rock mass populations of mineral deposits. To calculate $V(\rho \leq \upsilon)$ and $V(\rho \geq \upsilon)$, which are the volumes enclosed by a contour level ρ in a 3D model, the borehole data of RQD values were interpolated by using the IDW estimation. According to the RQD 3D block model, volumes corresponding to various

RQD values were calculated to derive a RQD-V fractal model. Threshold values of RQD were recognised in the RQD-V log–log plot (Fig. 4. 9) which reveals a power-law relationship between RQD values and volumes occupied. Depicted arrows in the log–log plot illustrate threshold values at three breakpoints corresponding to 3.55%, 25.12% and 89.12% for RQD. Based on the log–log plot, the excellent RQD populations are considered to have > 89.12%. The range of RQD values between 89.12% and 25.12% indicate a combination of good, fair and poor rock mass quality of which definition is in accordance with the Deere and Miller rock classification (Table. 4. 1 and 4. 5). However, very poor rock characterisation is for RQD < 25.12% containing of threshold value equal to 3.55% so therefore, there are two very poor RQD populations in this deposit considering RQD-V fractal modelling.
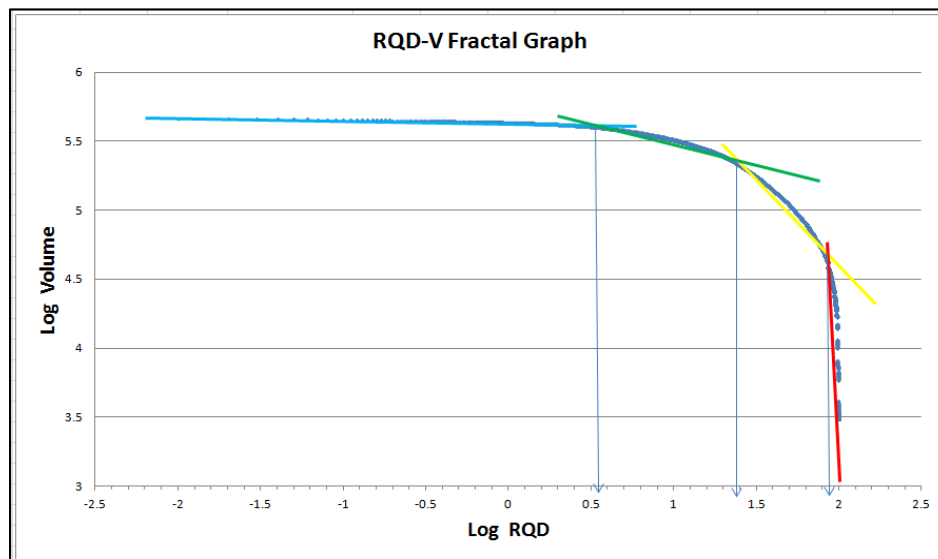
Fig. 4. 9. RQD-V log–log plot in the Kahang deposit

Table. 4. 5. RQD populations (zones) based on three thresholds defined from RQD-V fractal model

Deere and Miller RQD Classification	RQD Range Obtained by RQD-N Log-log Plot	The Amount of Voxels in Each RQD Range within the Whole Model
Very Poor	<3.55	111,697
Very poor	3.55 – 25.12	191,416
Poor, Fair & Good	25.12 – 89.12	180,524
Excellent	>89.12	30,254

Based on the RQD-V fractal model, the majority of the deposit consists of very poor zones which include 303,113 voxels (Fig. 4. 10 and Table. 4. 5). However, poor, fair and good zones are present along NE-NW trend. Excellent zones in terms of RQD occur in the central and NW parts of the deposit. As a result, for an RQD > 89.12%, the slope of the straight line fit is near to 90° based on the RQD-V log–log plot (Fig. 4. 9).

(a)

(b)

(c)

(d)
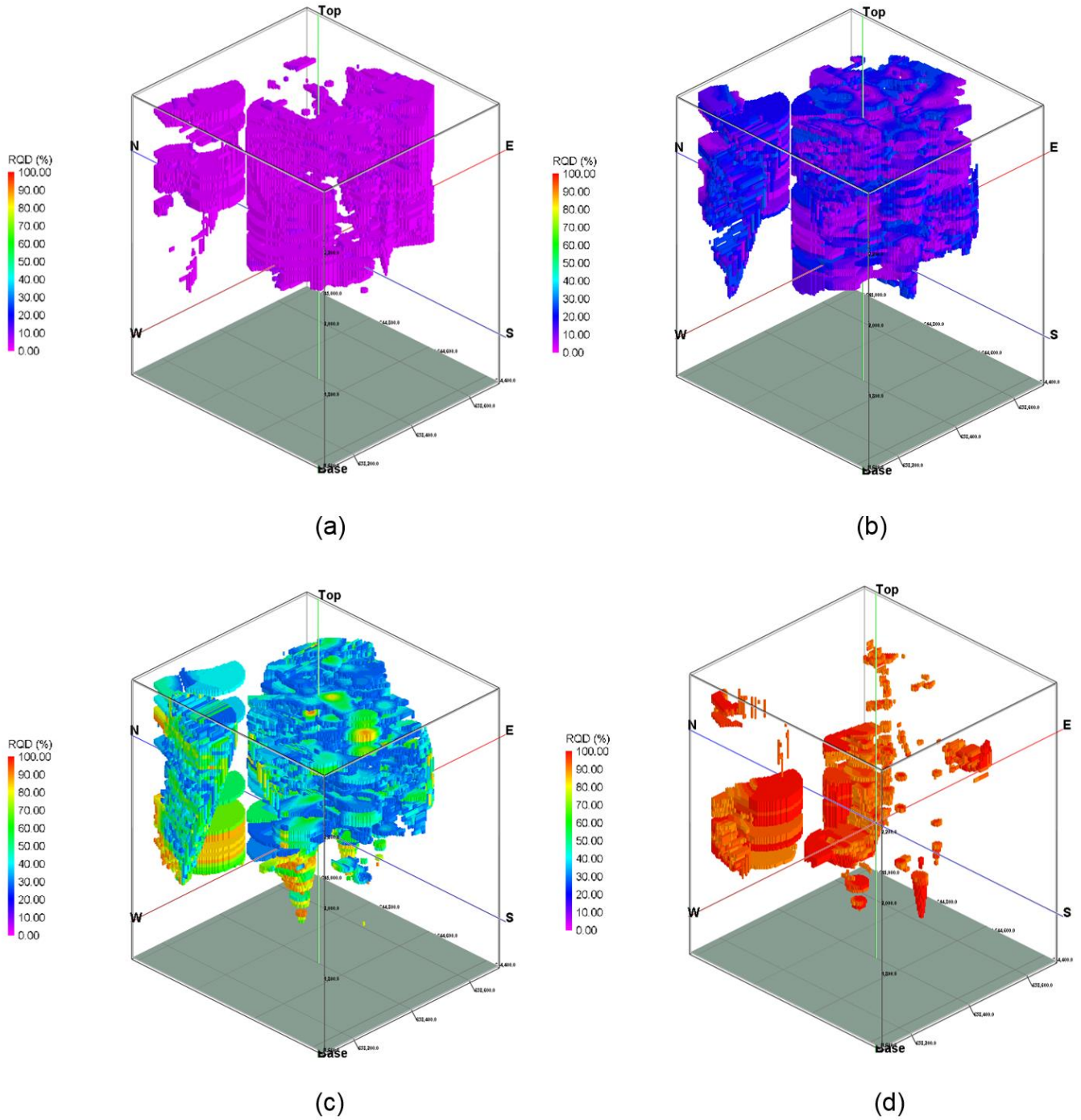
Fig. 4. 10. RQD populations within the Kahang deposit based on thresholds defined from the RQD-V fractal model: a) very poor zones, b) very poor zones, c) poor, fair and good zones, and d) excellent zones

Results from the RQD-V model were correlated to the major lithological units (e.g., porphyritic quartz diorite, andesite and dacite: Fig. 4. 11a, c and e) which were constructed using RockWorks™ v. 15 software and drill core data. Rocks with excellent RQD, defined using the RQD-V model, show a good spatial correlation with porphyritic quartz diorites, defined by the 3D modelling, in comparison with the andesite and dacite lithological units (Table. 4. 6), particularly in the central and NW parts of the deposit (Fig. 4. 11b). Therefore, it can be concluded that the porphyritic quartz diorite unit hosts excellent RQD values.

Table. 4. 6. Amount of the excellent RQD populations (voxels) defined from the RQD-V fractal model (RQD ≥ 89.12t/m^3) in each major lithological unit within the Kahang deposit

Lithological Units	The Amount of Voxels in Each Lithological Unit within the Whole Model	The Amount of Voxels in Each Major Lithological Unit Associated with RQD≥89.12t/m^3 (Excellent RQD)
Porphyritic Quartz Diorite	394,122	15,085
Andesite	142,802	3,742
Dacite	122,384	3,687

(a)

(b)

(c)

(d)

<div align="center">(e)   (f)</div>
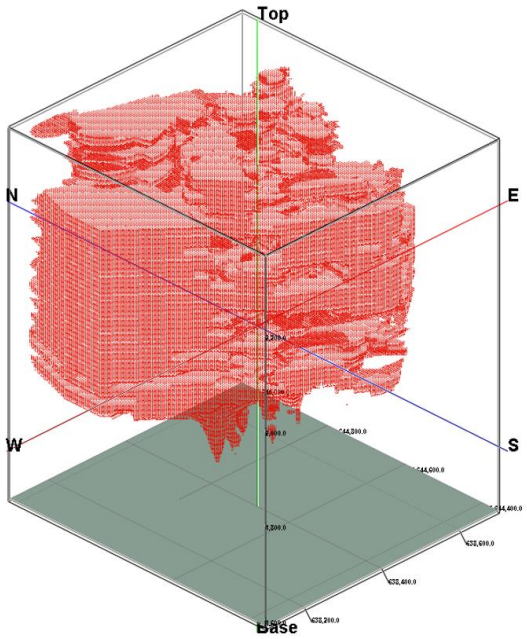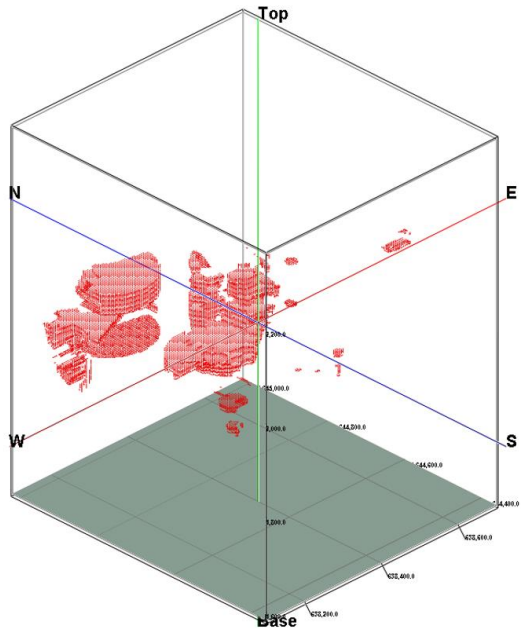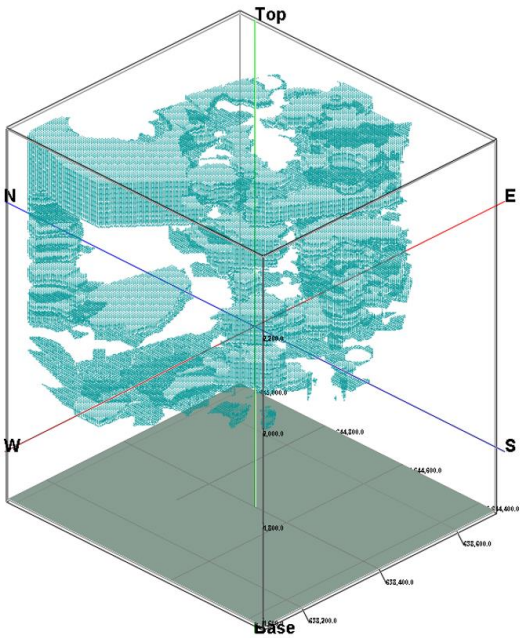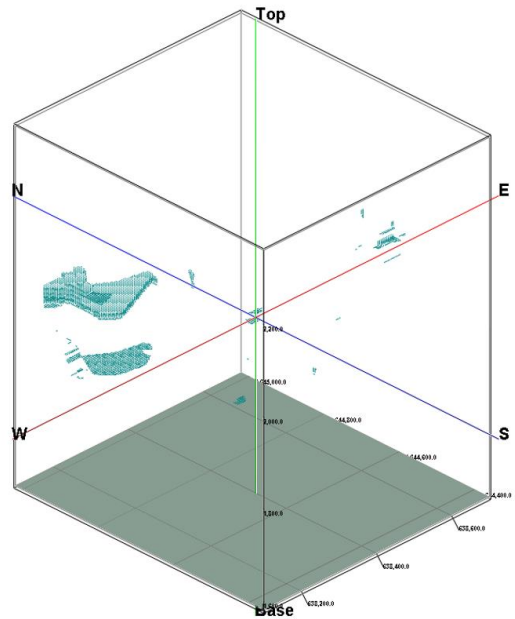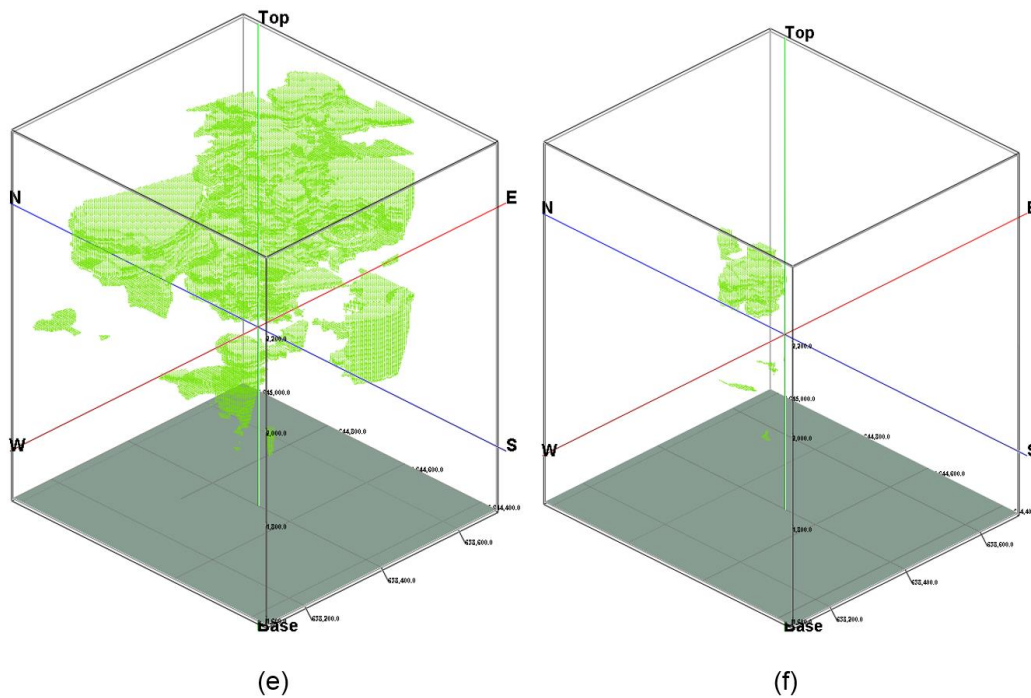
Fig. 4. 11. a) 3D lithology model for porphyritic quartz diorite , b) porphyritic quartz diorite unit based on the RQD-V model for RQD > 89.12%, c) 3D lithology model for andesite , d) andesite unit associated with RQD > 89.12%, e) 3D lithology model for dacite , and f) dacite unit associated with RQD > 89.12%

4.4   Comparison between D–V and RQD Models

The RQD parameter is an extremely useful indicator of rock mass quality, especially if used alongside density interpretation (Harrison, 1999; Zhang et al., 2012). This can lead to better understanding of rock quality in the study area because density variation within a rock mass has a direct relationship with changes in geomechanical properties such as porosity and permeability (Singh and Baliga, 1994). Demonstration and analysis of the correlation between RQD and density can be used in optimisation studies for the determination of the ultimate pit limit and mine planning. As can be seen in the RQD histogram (Fig. 4. 3) for all of the lithological units, the RQD average is around 48%

representing a "moderate" quality for the studied rock mass. However, use of the average RQD can be misleading for design purposes. The increased RQD in the porphyritic quartz diorite is accompanied by a corresponding increase in the density of the same rock type. As a result, there is a positive correlation between RQD > 70% with density > 2.7t/m^3, as depicted in Fig. 4. 12. Since RQD is a quality indicator for the rock mass and is associated with factors such as strength, modulus of elasticity, coefficient of permeability and different rock types, it can also be an indicator of potential slope stability. This suggests that the porphyritic quartz diorite, which is the main host rock in this deposit, with a RQD > 70% and a density > 2.7t/m^3, would be associated with competent areas for potential bench and slope stability which will ultimately influence the future pit slope design and ultimate pit limit.
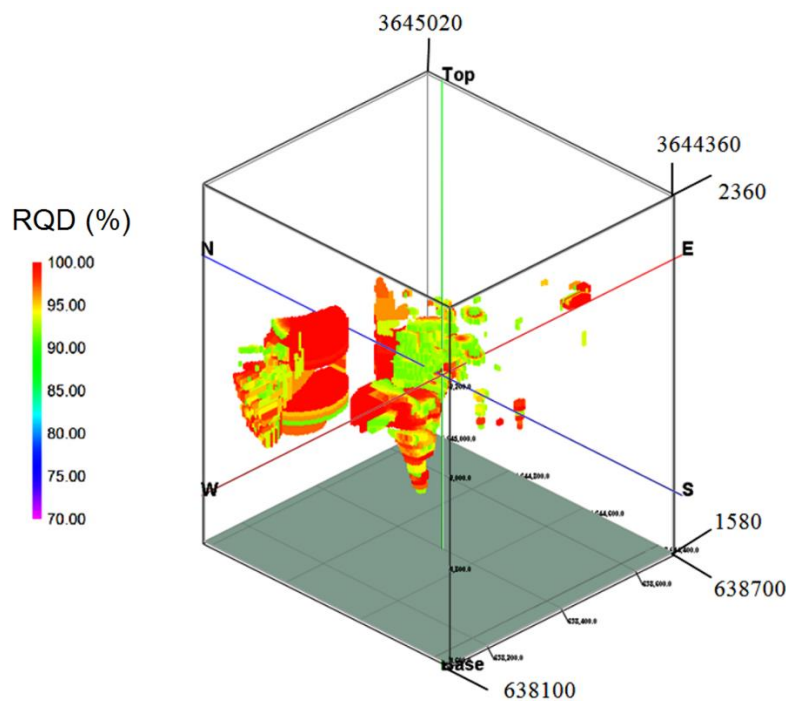
Fig. 4. 12. Correlation between RQD > 70% with density > 2.7t/m^3 block model within the porphyritic quartz diorite

4.5   Results

From the D–V log–log plot for the Kahang deposit, there is a mono-fractal model with a break point in density at 2.7 t/m^3. Correlation between the results of D–V and RQD models reveals that the rock units with a higher density (>2.7t/m^3) are associated with RQD values > 70%. The final pit slope geometry and ultimate pit limit will depend on the economic evaluation of the orebody. However, an awareness of the spatial variability of parameters such as RQD, density can be used to assess geotechnical characteristics of the rock mass[1]. This can then be used to evaluate potential slope stability and be incorporated into a geotechnical risk model for the final pit geometry. Regions of high RQD may be targeted as offering greater potential for increased slope angles or locations for siting of critical haul roads. Regions of lower RQD should, where possible, be avoided for final pit limits as they will require lower slope angles. As a result, it seems rather obvious that there are likely to be multiple populations, presumably related to geology, e.g. lithology. Certainly from a slope stability point of view it would be expected that anyone examining this data would consider at least multiple domains for slope stability assessments, hence two final pit slopes would be selected in determining an ultimate pit limit. Further geotechnical characterisation will, however, be necessary to establish any potential influence of the 3D fracture network and presence of any major discontinuity- controlled instability.

The threshold RQD value for excellent rocks is 89.12% based on the fractal model as situated in the central and NW parts of the deposit. Models of good and fair rocks in the

---

[1] *See Appendix. E for Density and RQD plans in different levels*

central, eastern and NW parts of the deposit contain 25.12%–89.12% RQD values according to the RQD-V model. According to the correlation between results derived by fractal modelling and the major lithological unit of PQD in the Kahang deposit, rocks with excellent RQD defined by the means of RQD-V model have a sensible correlation with porphyritic quartz diorites resulted from the 3D geological model.

CHAPTER FIVE. Mining Optimisation

5.1 Introduction

Pit limit optimisations form an integral part of open pit mine planning and combined with the other mine planning tools such as pit design and cut-off grade (COG) determination are used in open pit mine planning to define the final pit limit and open pit mining sequences (Johnson, 1968; Hustrulid and Kuchta, 2006). Various definitions and recognised techniques for the analysis of pit limit optimisation results have been introduced, developed and consequently improved by the mining industry. Following this, Armstrong (1990) said the Ultimate Pit Limit (UPL) is the maximum boundary of all materials certifying the criteria of:

1. A block of the material will not be mined unless it can cover all costs for its subsequent mining (ore and waste), processing (ore) and marketing (ore).
2. Any block meeting the first criterion will be included in the pit.

Whittle (1988) suggested that an ultimate pit meets the highest possible undiscounted cash flow without considering of scheduling target including pushbacks and consequent mine planning. Hustrulid (1995) proposed that the pit remaining at the end of mining (mine life) is called the final or ultimate pit. However, the destination of the material with different money values defined as cut-off grade must be identified meeting economic criteria. In total, an ultimate pit is the pit producing the highest value of NPV compared with the other potential pits. One of the best ways to recognise a final pit limit was suggested by Lerch and Grossman whose 3D graph theory is a practical computer-supported alternative (Dynamic programming) to the conventional manual approach for open pit design through a block model. They introduced a block model of a mine by a weighted directed graph

where each vertex represents the blocks and each arc represents the blocks interdependency from an excavation perspective. The direction of the arcs from a vertex to the other vertex reveals the excavation priority of the second block to the first block and so on by the weights (e.g. NPV of each block) which comes from the blocks' economic values (Caccetta and Giannini, 1988; Akbari et al., 2008; Yasrebi et al., 2011). They proposed that the aim of an ultimate pit limit is to find the maximum weight of the above-stated weighted directed graph. In other words, the most famous optimisation algorithm is the Lerch and Grossman algorithm which considers the influences of operating costs, product prices, slope geometry, etc. The Lerch and Grossman algorithm is utilised with varying revenue factors to develop a value mining-based sequence strategy which introduces pit shells from revenue factors. The actual design has to also address functional considerations such as haul road access, cut-off grades and processing, etc.

The determination of the final pit limit is one of the most significant aspects which must be frequently reviewed and correspondingly corrected in the early stages and throughout a mine life on the basis of deposit information and changes in economic parameters due to uncertainty of the relative metal's world commodity price and related mining costs (Dimitrakopoulos et al., 2002; Akbari et al., 2008; Yasrebi et al., 2011; Asad and Dimitrakopoulos, 2013). As a result, ultimate pit recognition in each period of time is a function of financial affairs, which is well defined by Break-Even Stripping Ratio (BESR). The calculation of economic elements of a deposit therefore has to be performed according to the final exploration information and economical regime of the country in which the project is being carried out (Johnson, 1968). In other words, identification of a

final pit limit can be examined at almost every stage of a project, from exploration program definitions to the preparation of feasibility studies, modifications of development options for an open pit mine and pit development sequence.

The determination of a final pit limit in an open pit mine in various implementation forms is one of the most fundamentally important aspects of mine design which can produce feasible optimum pit development geometries considering the geology, grade, slope and economic information. Nowadays, in optimisation of open pit mines, determination of the ultimate pit limit is just one of the many steps which are used in optimisation studies and following this, engineers continue to utilise software packages which can achieve yearly optimised mine plans or even selective mining designs. The goal of this chapter is to determine the ultimate pit limit of the Kahang deposit by employing 3D block models (for Cu and Mo) via the C-V fractal model and rock mass characterisation through D-V and RQD-V fractal models by which the achieved results can be comprehensively adjusted for all kinds of open pit mines in a way that can be used by mine planners.

One way to maximise the use of block modelling functions in order to optimise the pit design process is to fully integrate block modelling and slope stability analysis. This is because it is believed that optimised slope stability results in a lower amount of waste material removed which reduces mining cost and correspondingly raises the NPV of the whole project (Lerch and Grossmann, 1965; Koenigsberg, 1982; Hustrulid and Kuchta, 2006; Yasrebi et al., 2011 and 2014; Marcotte and Caron, 2013). In addition, there is a logical action where one identifies different rock types (ore or waste) in terms of the

grades of each block. This process can be further enhanced by defining at every block location an identified COG.

Before performing any of the computerised optimisation processes, a range of basic information was required for the study (Fig. 5. 1). Technical data and economic information are crucial within the optimisation process. These factors greatly influence pit design. A sensitivity analysis was carried out on the basis of technical and economic parametric changes for the mining strategy (See chapter 6). The Lerch and Grossman algorithm considers the influences of operating costs, product prices, slope geometry, etc.

(a)

(b)
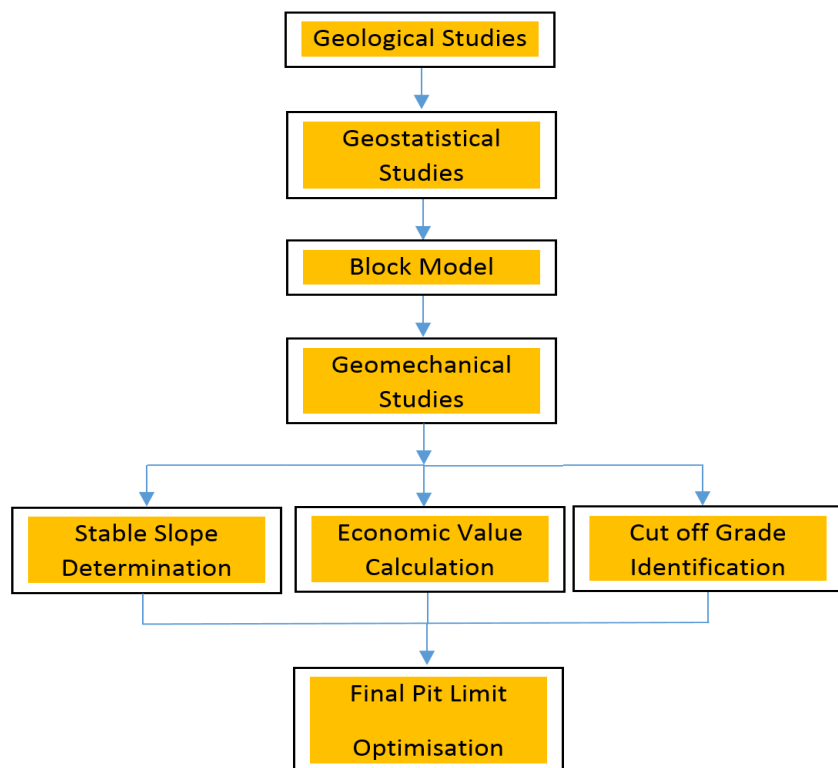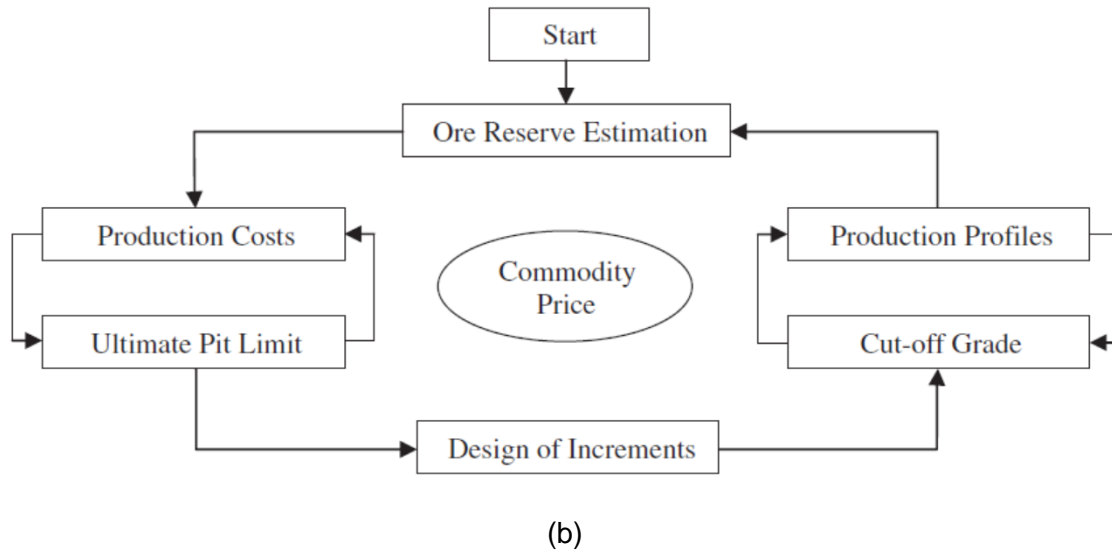
Fig. 5. 1. a) Design procedure in an open pit mine with regard to ultimate pit limit determination (Akbari et al., 2008) and b) steps in mining design and planning by circular and interdependent analysis (Osanloo et al., 2008b)

5.2 Methodology

Initially, the dataset obtained from a block model, via the C-V fractal model, was exported in the form of a table or Open Database Connectivity (ODBC) format which is compatible with optimisation software packages. Before this, careful validation of all data analysed from boreholes was conducted, which is an important preliminary action before generating a block model. The RockWorks^{TM} 15 enables us to generate a 3D geological and deposit block model which includes ore grade, rock density and rock type. The result of this was a deposit reserve estimation and the likely modification of existing geological maps matching the general observation of the region in question, and new cross sections. Following this, NPV Scheduler was used in order to establish the final pit limit in terms of the maximum Net Present Value (NPV) and associated ''Pushbacks'' to produce a best case mining scenario (Hustrulid and Kuchta, 2006; Elkington and Durham, 2011; Yasrebi

et al., 2011; Armstrong and Galli, 2012). To do this, all the required data such as grade, density and rock type (1 for ore and 0 for waste) and other similar data were entered as numerical values into each of the deposit's block models. Resulting 3D models were exported mathematically as 3D matrices into the optimisation programs in the following manner:

1-   Coordinates for the centre of sub cells in each plan were entered into an EXCEL spreadsheet;

2-   The layout of grade-based coordinates was adjusted using ACAD;

3-   Coordinates and grades for each block (in all plans) were input into an EXCEL spreadsheet;

4-   Contours were drawn for minerals and specified zones in each plan;

5-   Created blocks and the grade database were harmonised;

6-   Overlaps existing in the blocks were removed;

7-   Grades were allocated for each block and the geological 3D models were controlled with high accuracy.

5.3   Deposit Block Model via the C-V Fractal Model for Optimisation Study

Data from the C-V fractal model for the deposit (Fig. 5. 2) was entered into the optimisation algorithms. As discussed in chapters 1 and 3 (See chapter 1 section 1.3, chapter 3 section 3.7.2, Table. 3. 8 and Fig. 3. 23a), the C-V fractal model has provided a mathematic tool to delineate geochemical populations from 'barren' host rock, including

weakly mineralised zones, thus providing a cut-off grade. The mineralised zones with Cu less than 0.075 wt.%, apparent from the C-V log-log plot (Table. 3. 8 and Fig. 3. 23a), are assumed to be waste materials which decrease NPV by increasing stripping ratio (Hustrulid and Kuchta, 2006; Grenon and Hadjigeorgiou, 2010). From this, a Cu deposit block model was generated, at Cu ≥ 0.075, resulting in lower stripping, as shown in Fig. 5. 2. As can be seen, the weakly mineralised zones with less than 0.075 wt.% Cu occur within the marginal parts of the deposit (e.g., propylitic and argillic alteration zones; Lowell and Guilbert,1970: See also chapter 2, Fig. 2. 5).

(a)   (b)
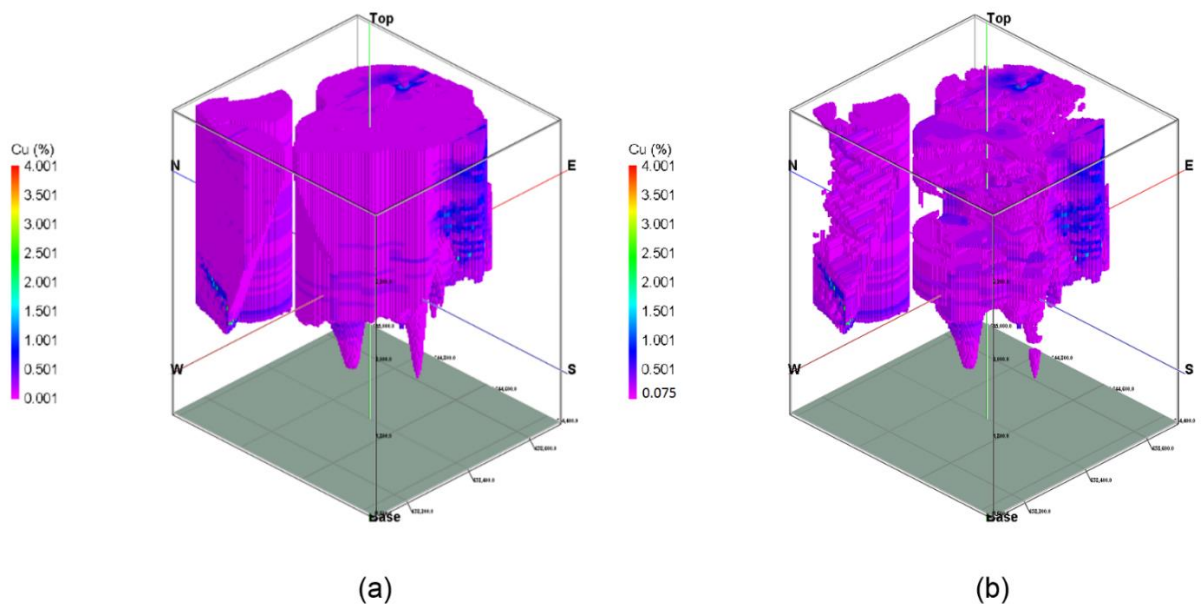
Fig. 5. 2. a) Estimated Cu block model and b) estimated Cu block model excluding Cu ≤ 0.075 wt.%, generated using the C-V fractal model

5.4 Mine Topographical Features of Land Surface

Topographical features of the deposit land surface (Fig. 5. 3), as well as other related data, are presented in a 3D block model entered in the optimisation software, prepared

using the most recent topographical maps. It is clear that blocks located between topographical surfaces and deposit surfaces are considered as waste blocks and are entered in the economic model as blocks of negative significance.
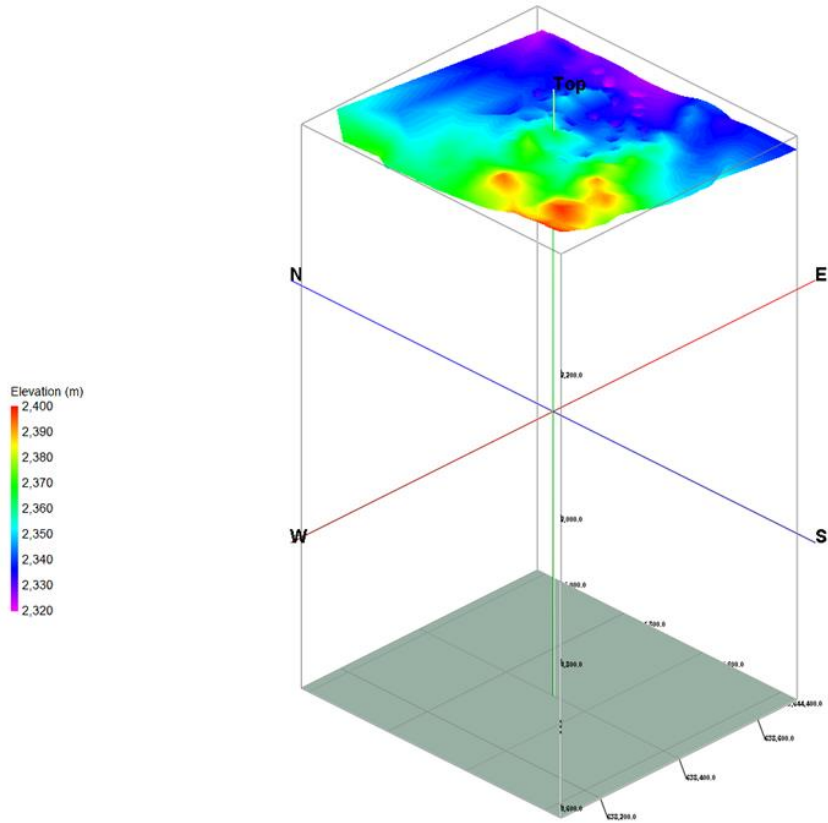
Fig. 5. 3. Land topographical surface of the deposit for optimisation study

5.5 Pit Geometrical Characteristics

The geometrical parameters used in the pit design will now be discussed. Some of these parameters are approximate. If they are changed then new optimisation studies have to be carried out. However, generally, the variance of the results obtained from changing these parameters are so insignificant that many of these parameters could be used reliably with current approximations. Final slope angles of the mine are considered to be

the most influential geometrical parameters in an optimisation study (Singh and Baliga, 1994; Wyllie and Mah, 2004; Hustrulid and Kuchta, 2006; Grenon and Hadjigeorgiou, 2010). Optimisation software algorithms have been designed in such a way that the blocks of different levels are extracted given this gradient (final pit slope). In NPV Scheduler, a slope region is a physical volume to which a particular group of overall slope angles and corresponding azimuths are defined (Fig. 5. 4).

As a general rule, slope stability studies for establishing an accurate final pit slope should be accomplished prior to optimisation studies. But to do such studies, some data is needed which are often obtained after completion of drilling operations and geotechnical studies (Little, 2006; Grenon and Hadjigeorgiou, 2010; Yasrebi et al., 2014). Therefore, calculation of a final slope for a mine is the most essential matter which should be studied carefully at the initial stages of design (See chapter 4). Unfortunately, due to the lack of systematic drilling and sub-surface data in the Kahang deposit, the possibility of studying slope stability is precluded. So, error percentage of any study performed using these kinds of observations in this regard will be very high and accordingly the accuracy of the determination of stable slopes could not be guaranteed. To determine the gradient, Density-Volume and RQD-Volume fractal models have been created. As a result, the mine's general gradient of 35° and 45° have been applied for performing optimisation calculations (Fig. 5. 4). However, the extracted benches are characterised according to the general features of the mine under consideration and more importantly on the basis of extraction capacity and the machines and equipment to be allocated during mining. In consideration of the current imposed constraints on the application of heavy machines as

well as harmonisation of the plan and executed plans, the heights of the benches have been constrained to 10 m.
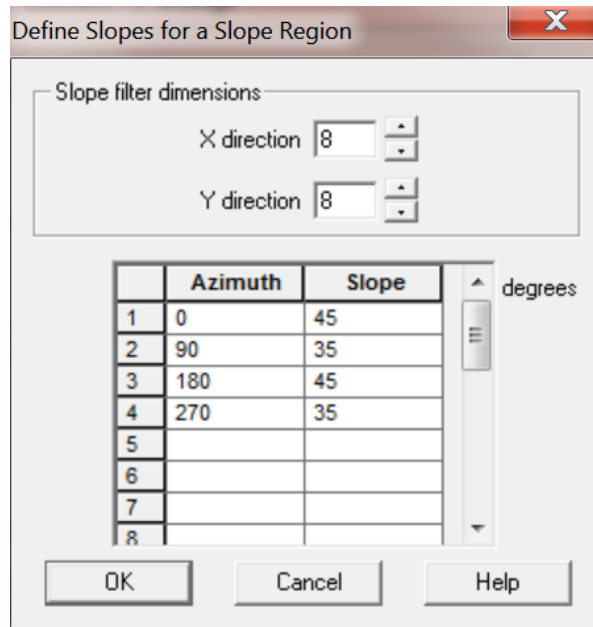
Fig. 5. 4. Stable pit slopes in the Kahang deposit, input into NPV Scheduler (See also chapter 4)

The results obtained from the optimisation software naturally have a 'blocky' nature so it is necessary to use the characteristics of the benches and the roads in detail for optimisation within the supplied ultimate pit surface. Given that, the phases and then pushbacks need to be designed at different working slope angles to the final overall slope angles. It makes more sense to use the working angles for internal phase and subsequent pushback development (NPV – Scheduler. 2001). Given the previous experiences of neighbouring deposits (e.g., Sharif Abad Cu porphyry deposit located in Isfahan province, central Iran; Dareh-Zereshk and Ali Abad Cu porphyry deposits in Yazd province and Dalli Cu porphyry deposit located in Markazi province), these characteristics have been determined as follows:

➢ Face angle of the extracted benches: 70°

➢ Width of interconnecting roads: 10m

➢ Gradient of interconnecting roads: 8% (Max)

The estimate of cut-off grade is not consistent with the corresponding values for other deposits in the region because it is dependent on ore grade distribution, deposit geometrical shape and especially economical parameters which are different from one deposit to another (Lerch and Grossmann, 1965; Lane, 1988; Osanloo and Ataei, 2003; Hustrulid and Kuchta, 2006; See Chapter 3, section 3.7.2 and Appendix. A).

5.6   Mine's Annual Production

The mine's annual production capacity is one of the factors determined using economic parameters and project profitability studies. Similarly, determination of production capacity in this research should be subject to various detailed and basic studies. Fortunately, optimisation software has useful capabilities that make it possible for designers to conduct such studies extensively. Since the annual production will be limited; i.e. around 1,000,000 tonnes (as the nominal capacity of the plant); this amount has been exactly included in the calculations.

5.7   Ore Density

The cost of mining each block has been calculated using the dimension and specific density of that block. It is clear that the tonnage of blocks located in each zone is determined on the basis of each zones' ore density. The average density of three major

lithological units of porphyritic quartz diorite (PQD), andesite (ANS) and dacite (DAC) within the Kahang deposit is shown in Table. 5. 1.

Table. 5. 1. Ore density average of the mineralisation zones within the deposit

Lithological Unit	Density Average (t/m^3)
Porphyritic Quartz Diorite	2.67
Andesite	2.69
Dacite	2.68

The density 3D model for the studied deposit, including all densities within the lithological units (three of which are illustrated in Fig. 5. 5), were generated using IDWAM. The aim was to generate the finalised block model (database) for the optimisation study (Yasrebi et al., 2014).
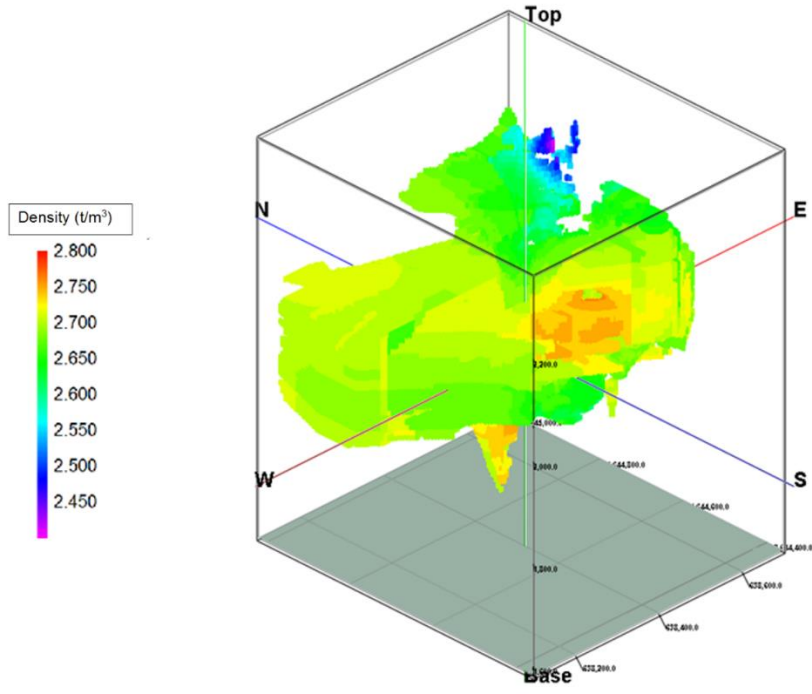
(a)
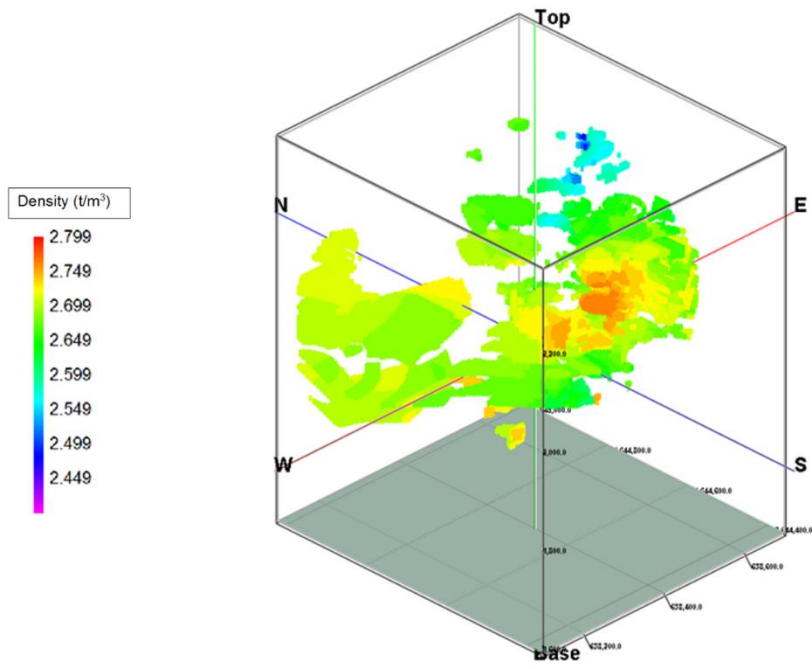
(b)
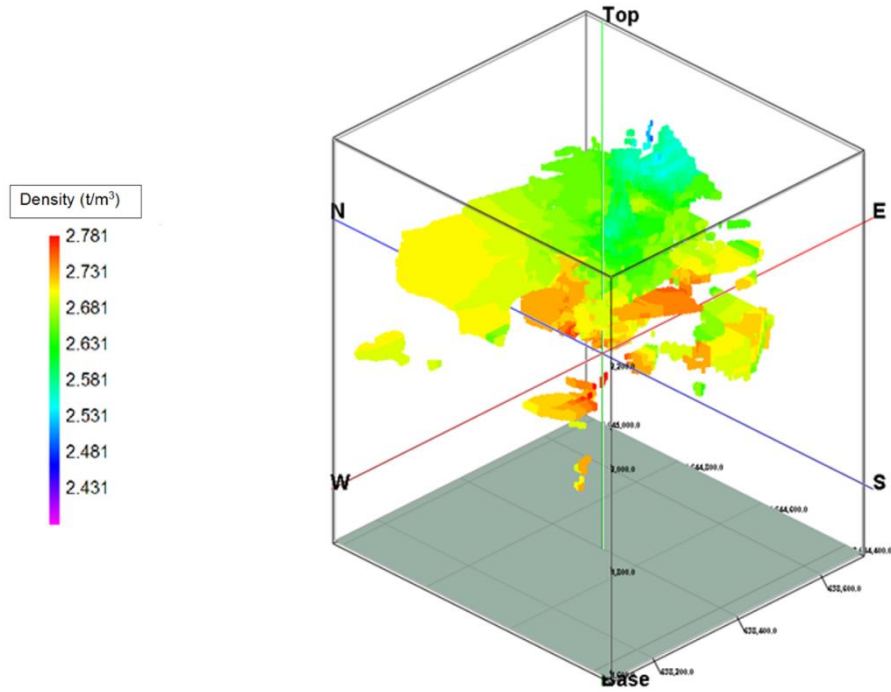
(c)

Fig. 5. 5. Density distribution for block models in the Kahang deposit for a) PQD, b) ANS, and c) DAC lithological units (See abbreviation table for lithological units)

5.8   Kahang's Exploitation Percentage

To determine the amount of exploitable Cu and Mo in each tonne of ore, and so calculate the value of each block, some factors such as processing efficiency within the different ore minerals must be calculated and applied in this study. By referring to the results of mineral processing tests, obtained by the laboratory, and the data sources (See Appendix. A) provided by the deposit owner, NICICO, the percentage of mining recovery, mining dilution and recovery fraction for concentrated Cu and Mo have been specified as follows:

- ➢ Mining recovery: 95%

- ➢ Mining dilution: 3%

- ➢ Recovery fraction for Cu and Mo: 80%

5.9   Economic Principles

5.9.1   Prices and Expenses

The results obtained from optimisation studies are significantly affected by the price of the product (Fig. 5. 6) and operational costs of production. These parameters must therefore be determined more precisely. However, due to the importance of economic principles, and the large influence they have on the results, the above-mentioned parameters are discussed in detail in the subsequent sections.

Determination of operational costs including ore and waste exploitation costs and milling costs for the Kahang deposit is a demanding task. However, after consideration of studies conducted previously and simulation of cost figures incorporated in the records of Iranian (as well as western authorities; See chapter 1, section 1.5 for political context of mining in Iran), these values were determined by the deputy of the Economic and Financial Department of NICICO (See Appendix. A for data sources) and then included in the NPV Scheduler software (Table. 5. 2).

(a)
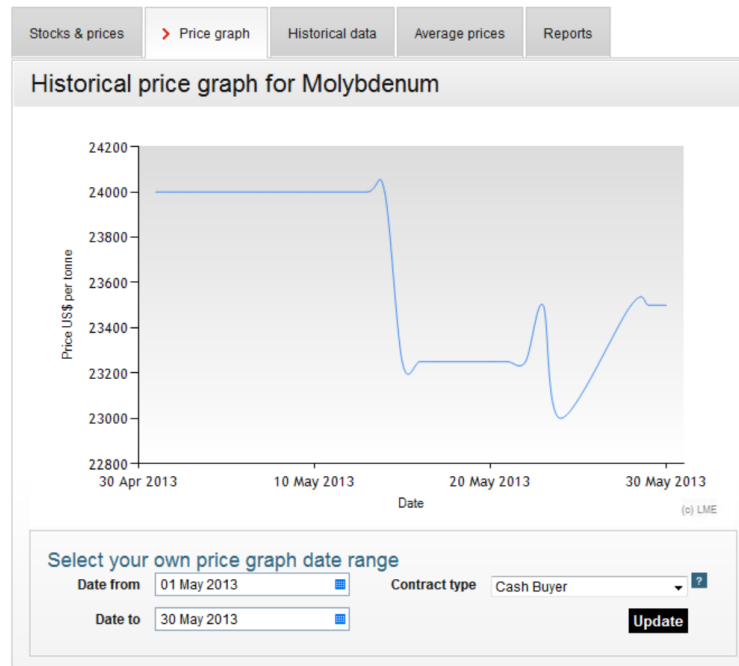
(b)

Fig. 5. 6. Metal commodity prices during the optimisation study: a) copper, and b) molybdenum
(London Metal Exchange, 2015a and b)

Table. 5. 2. Prices and mining costs for the Kahang optimisation study

	Price	Unit	Mining Cost	Unit	Mining CAF	Milling Cost	Unit	Additional Milling Cost (refinery) & Selling	Unit
Cu	7000	$/tonne	4	$/m^3	1.3	4	$/tonne	200	$/tonne
Mo	0.023	$/g	4	$/m^3	1.3	4	$/tonne	0.0002	$/g
Waste	-	-	4	$/m^3	1	-	-	-	-
Comments	*Rock type mining CAF (Cost Adjustment Factor) = Mining cost for rock type/ Reference waste mining cost **The metal commodity price was considered on the date when the optimisation study was conducted								

5.9.2 Annual Discount Rate

During strategic optimisation calculations, valuation of the blocks will be carried out on the basis of exploitation time. Indeed, this task was undertaken by consideration of an annual discount rate and updating the value of the blocks intended to be exploited in the coming years. By comparing the optimisation studies of different mining projects in Iran, it can be concluded that this annual rate varies slightly from project to project as this was defined by the Central Bank of Iran (CBI) from 10% to 18% for short-term and long-term projects, respectively (Fig. 5. 7a; Appendix. A. However, discount rate can be higher or less than the above-mentioned one for foreign investors in regard to their countries' economic principles (e.g., in the United Kingdom, rates were cut to 0.5% by the Monetary Policy Committee; Fig. 5. 7b). Iran has been a World Trade Organisation (WTO) observer

member since 2005 and policy of the Iranian government is to facilitate absorption and development of foreign investment for the country's mining projects as well as oil and gas development projects by providing a secure investment climate and creating free trade zones (See chapter 1, section 1.5). In addition, because of low labour and energy costs in Iran, mining projects and related minerals production, which consume huge volume of energy, are profitable for foreign fund managers and companies (e.g., British-based mining corporations, multinational-based mining companies and banks).
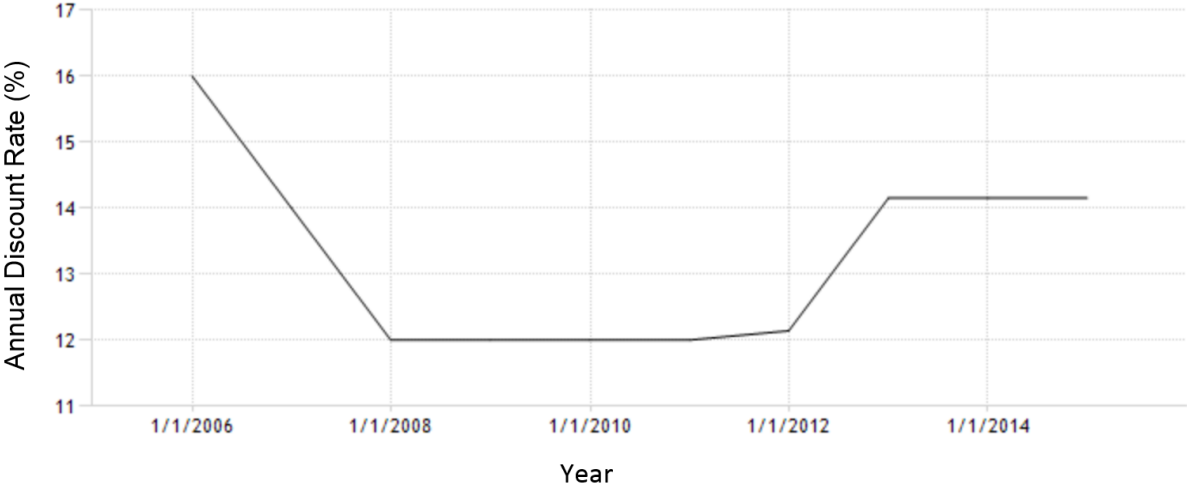
(a)
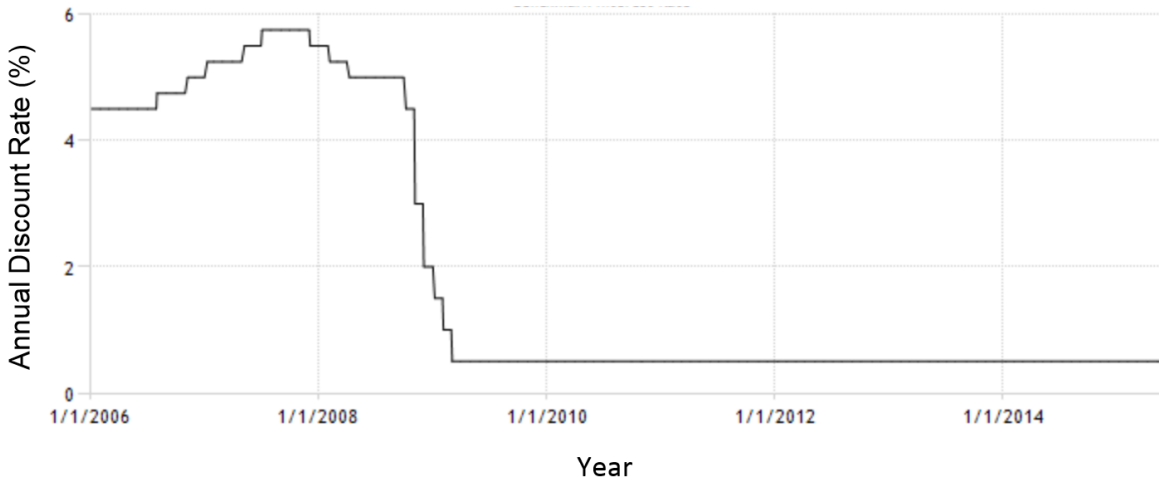
(b)

Fig. 5. 7. Annual discount rates for choice of parameters and model outputs for domestic and foreign decision makers, a) Iran b) United Kingdom (Trading Economics, 2015)

Given that the Kahang deposit is considered as a short-term project, a discount rate of 14% has been conservatively applied in optimisation calculations because the project belongs to an Iranian based-corporation (NICICO). The project owner, as well as other individual and governmental mining sectors in Iran, are seeking foreign investors, as revealed by the Minister of Industries, Mines and Commerce of Iran (See section 1.5). However, an extension of exploratory boreholes for the Kahang deposit is required, which is likely to increase the reserve due to better geological constraints. The discount rate of the project will be higher than 14% if the project expansion goes ahead which correspondingly will increase the mine life so that Kahang becomes a long-term project. The supplied discount rate is intended to determine the discounted cash flow (DCF). The sequence used for allocation of blocks with respect to time is determined so as to demonstrate the highest total DCF.

5.9.3 Cut-off Grade

Specifying the cut-off grade strategy is a matter which should be discussed before studying the results of optimisation. Cut-off grade is usually calculated taking consideration of the cost of mining, cost of processing as well as the price of the commodity (Cairns and Shinkuma, 2003; Osanloo and Ataei, 2003; He et al., 2009; Wang et al., 2010b). However, prior to performing such studies, it is necessary that a cut-off grade needs to be considered for separating the blocks containing ore and waste. In optimisation software, a grade is calculated similarly which is called the marginal limit grade. The COG for the optimisation study is calculated in order to identify the best course of action, either to mine or to leave, to mill or to dump. A COG of 0.07 wt.% Cu was calculated based on Equation 5-1 as follows:

$$NPV = (I_1 + I_2) - (MC + PC_1 + PC_2) \qquad \text{Equation 5-1}$$

$$I_1 = (G_1 \times D \times V \times P_{Cu} \times MR \times PR)/100 \qquad \text{Equation 5-2}$$

$$I_2 = G_2 \times D \times V \times P_{Mo} \times MR \times PR \qquad \text{Equation 5-3}$$

$$MC = D \times V \times MCPU \qquad \text{Equation 5-4}$$

$$PC_1 = (D \times V \times PCPU \times G_1 \times MR \times PR)/100 \qquad \text{Equation 5-5}$$

$$PC_2 = (D \times V \times MR \times PR \times PCPU \times G_2)/1000000 \qquad \text{Equation 5-6}$$

Where NPV, I_1, I_2, MC, MR, PC_1 and PC_2 are Net Present Value of each voxel, incomes of Cu and Mo, mining cost for a voxel, mining recovery and processing costs for Cu and Mo, respectively. Furthermore, P_{Cu}, P_{Mo} and PR are the metal commodity price for Cu and Mo and fraction recovery. In addition, D, V, $MCPU$, $PCPU$, G_1 and G_2 denote voxel density, voxel volume, mining cost per volume unit, processing cost per tonnage unit, Cu and Mo

concentration values, respectively. Economic cut-of grade was calculated using Equation 5-1, illustrated in Table. 5. 3. This indicates that the economic COG for Cu as the main target is equal to 0.07 wt.% which has almost equal to the first threshold obtained by the C-V fractal modelling (See Chapter 3, section 3.7.2).

Table. 5. 3. COG specification for optimisation study

Cu (wt.%)	Mo (ppm)	Density (t/m^3)	Volume (m^3)	Mining Cost ($/m^3)		Processing Cost ($/Tonne)		Cu Price ($/Tonne)
0.07	17.309	2.25	160	4		200		7000

Mo Price ($/g)	Mining Recovery	Processing Recovery	Income Cu ($/Tonne)	Income Mo ($/g)	Voxel Mining Cost ($/m^3)	Processing Cost Cu ($/Tonne)	Processing Cost Mo ($/g)	Voxel NPV ($)
0.023	0.97	0.8	1368.864	111.215	1440	39.110	0.967	0

5.10   Determination of the Kahang Deposit Ultimate Pit Limit

5.10.1   Ultimate Pit Limit

Specifying the ultimate pit limit is the first step in optimisation studies. This limit is typically specified by application of the Lerch & Grossman algorithm in the mine's economic model. Through this method, a pit with maximum cash flow is determined. If the magnitude of the pit is greater than this limit, it means that profitability will be low. Tables 5. 4 and 5. 5 depict the imported model data (the database obtained by the means of the C-V fractal model extended by topography) and economic model of the Kahang deposit (Yasrebi et al., 2011; Marcotte and Caron, 2013).

Table. 5. 4. Initial imported data into the optimisation software based on Fig. 3. 13 and Table. 5. 2

Imported Model Data Check							
kahang							
bm001bm.dm							
Model Definition							
Reblocked	No						
Density Multiplier	1.0000						
Cell Count	1,980,214						
Subcell Count	0						
	Block Count	Block Size	Origin				
X	151	4.0000	638,098				
Y	166	4.0000	3,644,358				
Z	79	10.0000	1,575				
Field Assignment							
Field	Assigned to	Unit	Data Type				
Density	Density	tonnes/cu.m					
RockType	Rock Type						
Cu	Product	tonnes	percentage				
Mo	Product	g	grade				
Global Stats							
	tonnes						
Ore	148,812,100						
Waste	586,122,518						
Rock	734,934,618						
Rock Type Stats							
	Tonnage	Cu	Cu Min	Cu Max	Mo	Mo Min	Mo Max
	tonnes	Percent	Percent	Percent	g/tonne	g/tonne	g/tonne
ore	148,812,100	0.1759%	0.0100%	4.0000%	35.2012	0.6600	785.4200
waste	586,122,518	0.0032%	0.0100%	0.0600%	0.4938	0.7600	12.9900

Table. 5. 5. Economic specification of the Kahang deposit driven by NPV Scheduler

Economic Model Data Check														
Economic Model 1														
Global Stats														
Cash	Revenue	Minimum	Maximum	Process Cost	Minimum	Maximum	Mining Cost	Minimum	Maximum	Net Value	Ore Value			
	$1,433,650,948	$1,475	$93,896	$536,892,565	$1,471	$4,395	$1,267,336,960	$640.00	$640.00	($370,578,576)	$701,092,464			
	Block Count	Mass												
ORE	305,728	124,521,903												
Waste	1,674,486	610,412,715												
Total Rock	1,980,214	734,934,618												
Strip Ratio	4.9021													
ORE Stats														
	Mass	Cu	Cu Min	Cu Max	Mo	Mo Min	Mo Max	Cu R	Cu R Min	Cu R Max	Mo R	Mo R Min	Mo R Max
	tonnes	tonnes	Percent	Percent	g	g/tonne	g/tonne	tonnes	Percent	Percent	g	g/tonne	g/tonne
ORE	124,521,903	248,105	0.0400%	4.0000%	4,815,385,183	0.6600	785.4200	192,529	0.0310%	3.1040%	3,736,738,904	0.5122	609.4859
Waste Stats														
Total	610,412,715													

The individual economic parameters of all sequences, before a finalised optimisation (1580 m<Elevation<2360 m), and some supporting 2D economic models in different section levels are given in Appendix. F.

As a general rule, nested pits which have the greatest cash flow are considered as the mine's ultimate pit limit. Tables 5. 6 and 5. 7 represent the specifications of the final pit and ultimate pit limit reserve report. As a result, the pit located at the elevation equal to 2225 m (Fig. 5. 8) is determined as the Kahang final pit limit in which the NPV value, ore and waste amount, strip ratio and mine lifetime are $3,032,862, 3,648,294 tonnes, 13,970,954 tonnes, 3.8, 3.65 years, respectively (See Appendix. G).
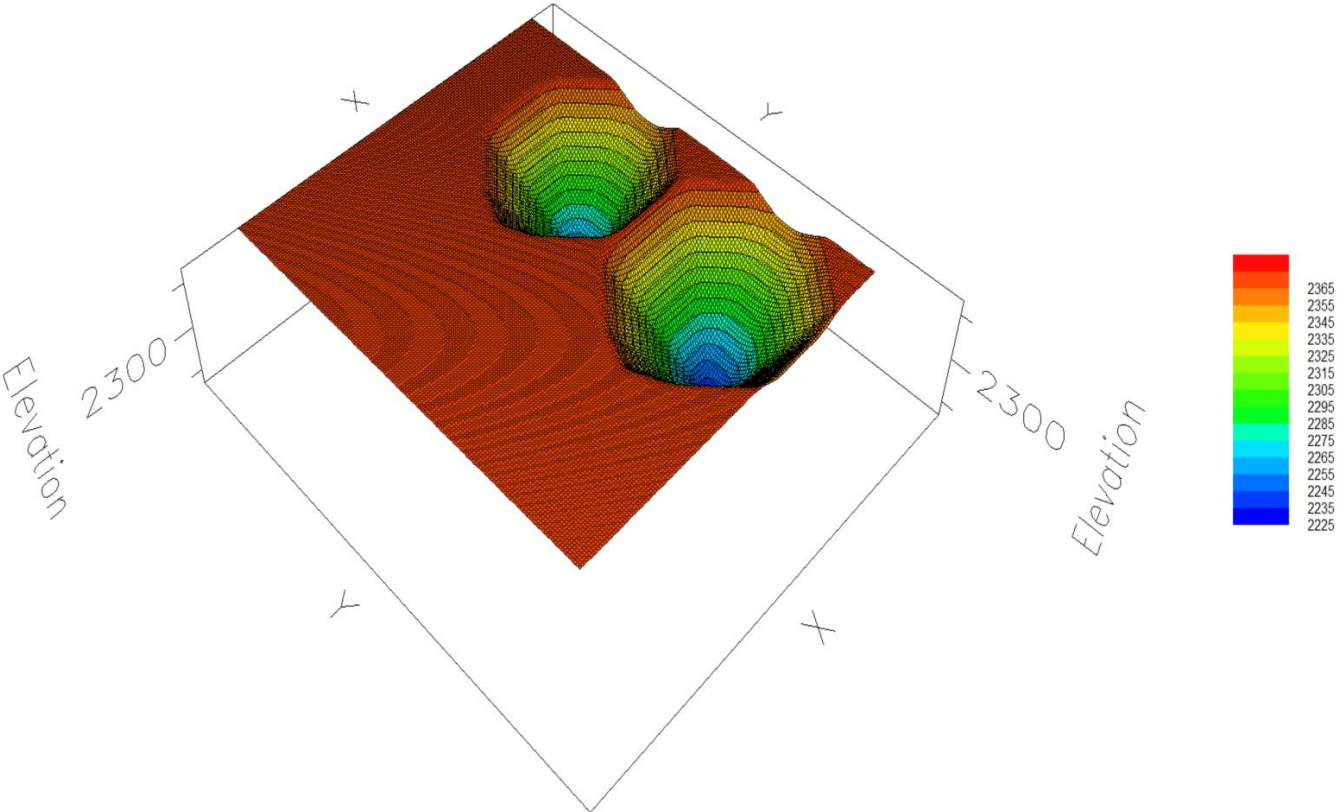
Fig. 5. 8. Kahang pit limit 3D view without consideration of ramps and safety berms

Table. 5. 6. Ultimate pit statistics determined by NPV Scheduler

Economic Model 1+Ultimate Pit 1														
Final Pit														
	Type	Lifetime	Shells generated											
	LG Max Cash	3.65	3											
Global Stats														
Cash	Revenue	Process Cost	Mining Cost	Net Value	NPV	Ore Value								
	$54,443,507	$16,115,534	$30,225,280	$8,102,693	$3,032,862	$32,401,573								
	Block Count	Mass												
ORE	9,260	3,648,294												
Waste	37,967	13,970,954												
Total Rock	47,227	17,619,248												
Strip Ratio	3.8294													
ORE Stats														
	Mass	Cu	Cu Min	Cu Max	Mo	Mo Min	Mo Max	Cu R	Cu R Min	Cu R Max	Mo R	Mo R Min	Mo R Max	
	tonnes	tonnes	Percent	Percent	g	g/tonne	g/tonne	tonnes	Percent	Percent	g	g/tonne	g/tonne	
ORE	3,648,294	9,837	0.07%	2.71%	56,487,225	0.66	246.05	7,634	0.05%	2.10%	43,834,086	0.5122	190.9348	
Waste Stats														
Total	13,970,954													

Table. 5. 7. Pit limit reserve in the Kahang deposit

Reserve report for UltPit								
Bench	Elevation	Profit	Revenue	Processing Cost	Mining Cost	Total Rock	Total Ore	Total Waste
		$	$	$	$	tonnes	tonnes	tonnes
0	2,355	(6,035,200)	0	0	6,035,200	3,394,800	0	3,394,800
1	2,345	(5,201,280)	0	0	5,201,280	2,925,720	0	2,925,720
2	2,335	(4,416,640)	0	0	4,416,640	2,490,926	0	2,490,926
3	2,325	(2,779,725)	1,834,573	956,698	3,657,600	2,135,390	226,483	1,908,907
4	2,315	3,498,563	9,894,173	3,390,170	3,005,440	1,841,843	778,400	1,063,443
5	2,305	(798,460)	3,574,235	1,988,055	2,384,640	1,461,627	472,632	988,995
6	2,295	(239,966)	3,361,934	1,738,219	1,863,680	1,141,152	411,392	729,760
7	2,285	2,854,095	6,895,524	2,660,949	1,380,480	842,965	617,427	225,538
8	2,275	5,579,821	8,460,982	1,888,521	992,640	603,200	412,534	190,666
9	2,265	4,482,414	6,686,578	1,558,403	645,760	392,166	342,488	49,678
10	2,255	7,810,850	9,406,906	1,205,656	390,400	237,651	235,131	2,520
11	2,245	2,602,454	3,320,706	535,852	182,400	110,669	110,669	0
12	2,235	673,841	909,464	173,543	62,080	36,966	36,966	0
13	2,225	71,926	98,433	19,466	7,040	4,171	4,171	0
Total	0	8,102,693	54,443,507	16,115,534	30,225,280	17,619,248	3,648,294	13,970,954

5.10.2 Internal Pit Shells (Phases)

The application of optimisation software will not be limited to determination of a pit's optimised limit, but after completion of this phase, a general scenario for exploitation of this pit and so-called exploitation sequences (Nested pits) will be discussed and optimised in the form of some smaller pits (Koenigsberg, 1982; Bond, 1995; Yamatomi et al., 1995;

Darwen, 2001; NPV – Scheduler, 2001; Goodwin et al., 2008; Marcotte and Caron, 2013). Occasionally, a mine is exploited at one stage and the ultimate pit is not divided into smaller pits. Indeed, this condition is considered as the worst mining scenario. To improve the economic and technical outcome, the ultimate pit will be designed in the form of mining sequences as nested pits. By increasing the number of mining phases, the best mining scenario will be achieved due to increase the number of working benches increasing production capacity. In a different definition, after generation of the ultimate pit, internal phases (pit shells) will be produced (Table. 5. 8 and Fig. 5. 9), each of which may be considered as an optimal pit corresponding to the 'worst-case' economic scenario compared with that derived using case-base parameters (economic principles).

The phase conducted for a supplied final pit is utilised as the basis for generation of a nested pit, which is a block by block extraction sequence, and consequent optimal extraction sequence (OES). However, each phase has been constructed to present the highest undiscounted cash flow based on economic principles. Accordingly, specifying the optimised number which ensures the project's profitability and does not impose restrictions executively is generally considered to be the most important fundamental of designing open pit mines (Akbari et al., 2008; Yasrebi et al., 2011).

Table. 5. 8. Pit optimisation phases of the Kahang deposit

Incremental Data								
Phase	Profit	Revenue	Processing Cost	Mining Cost	Total Rock	Total Ore	Total Waste	Strip Ratio
	$	$	$	$	tonnes	tonnes	tonnes	
1 (80.00%)	7,882,658	50,276,051	14,573,233	27,820,160	16,176,052	3,291,584	12,884,468	3.914
2 (90.00%)	138,203	1,538,750	573,666	826,880	497,296	132,726	364,569	2.747
3 (100.00%)	81,830	2,628,704	968,634	1,578,240	945,899	223,984	721,915	3.223
Cumulative Data								
	Profit	Revenue	Processing Cost	Mining Cost	Total Rock	Total Ore	Total Waste	Strip Ratio
	$	$	$	$	tonnes	tonnes	tonnes	
1 (80.00%)	7,882,658	50,276,051	14,573,233	27,820,160	16,176,052	3,291,584	12,884,468	3.914
2 (90.00%)	8,020,862	51,814,802	15,146,900	28,647,040	16,673,348	3,424,310	13,249,038	3.869
3 (100.00%)	8,102,692	54,443,507	16,115,534	30,225,280	17,619,248	3,648,294	13,970,953	3.829
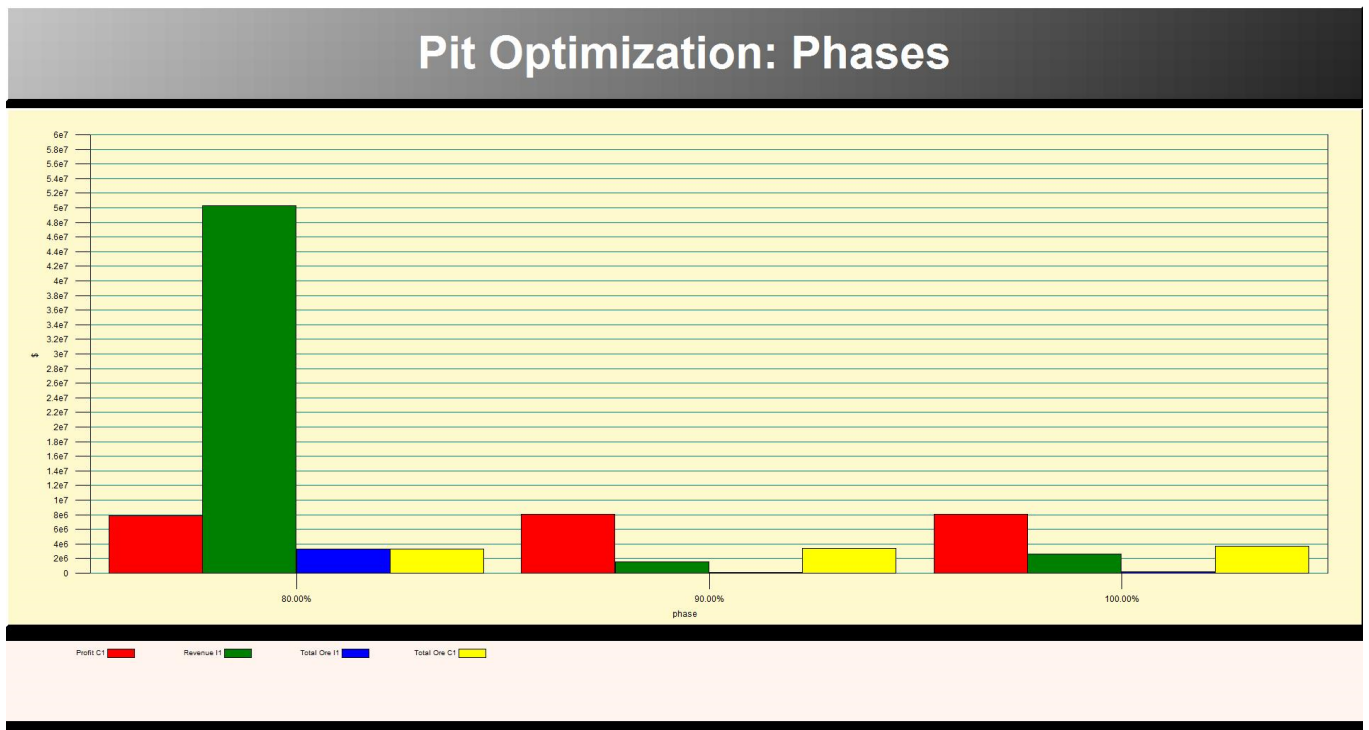
Fig. 5. 9. Pit optimisation within the internal pit shells, stages of 80%, 90% and 100%, driven by NPV Scheduler based on Table. 5. 8 (**Cumulative profit**, **Incremental revenue**, **Incremental total ore** and **Cumulative total ore**)

5.10.3 Nested Pits

Nested pits are a collection of optimised pits which are calculated on the basis of the Lerch & Grossman algorithm (Hustrulid and Kuchta, 2006). Indeed, constructing optimised nested pits is considered as an 'art' applied by design engineers to perform analyses such as specifying the ultimate optimised pit as well as determining the extraction sequence of the blocks.

The total number of extraction sequences existing in the Kahang deposit reaches 100. In other words, a maximum revenue factor of more than 100%, which is recommended in NPV Scheduler software, can be determined, in which case the largest ultimate pit produced is a pit 'past the peak', in terms of the base economic parameters (NPV – Scheduler, 2001; See Table. H. 1 for both incremental and cumulative NPVs). Tonnage of exploitable mineral, waste, waste ratio, cash flow and current value of the pits have been calculated individually as depicted in Appendix. H. With this useful data, one is able to perform the required analysis, detect a pit's optimised limit and design an exploitation schedule and timetable. In other words, the importance of nested pits is not always evident in the long-term open pit planning procedure. Usually a mining sequence is derived from a simple selection of pit shells based on optimum pit limits. The performance of the obtained mining sequence to the production constraints is generally not questioned prior to the detailed production stages of a project.

5.10.4 Identification of an Optimal Extraction Sequence (OES)

Identification of an optimal extraction sequence (OES) is significant for the selection of alternative optimal pits in order to generate the best mining sequences (Dincer, 2001;

Godoy and Dimitrakopoulos, 2004; Hustrulid and Kuchta, 2006; Osanloo et al., 2008a; Elkington and Durham, 2011). For all of the blocks inside the ultimate pit, an OES is also constructed. This aims to achieve the highest DCF based on the given discount rate and ore processing rate. The phase structure created for a supplied final pit is utilised as the basis for constructing the OES (a block by block extraction sequence). It may be that some blocks towards the end of the ultimate pit may not be added to the DCF, in which case a smaller pit than the ultimate pit could produce the highest DCF. In other words, the ultimate pit limit may have smaller magnitude than the recognised final pit when it indicates that the addition of higher sequences does not increase the pit NPV (See Appendix. H, rows 92 to 100 for cumulative NPV). By referring to Appendix. H, sequence No. 92 (specified as the Kahang ultimate pit limit due to the fact that the NPV cumulative trend becomes steady), the mining operation can be terminated at this point (Fig. 5. 10). The exploitable reserve existing (ore) at this point (from sequence 1 to 92) amounts to 3,291,944 tonnes with the total NPV of $2,884,968 and a strip ratio of 3.919. Furthermore, the cumulative profit value at the mentioned extraction sequence is equal to £7,853,825.

It is good to bear in mind that the data obtained from this pit should not be considered as a basis for the design during optimisation studies because mining orientation has not been yet recognised. However, after selecting and designing the extraction phases (pushbacks), an optimised pit will be derived.
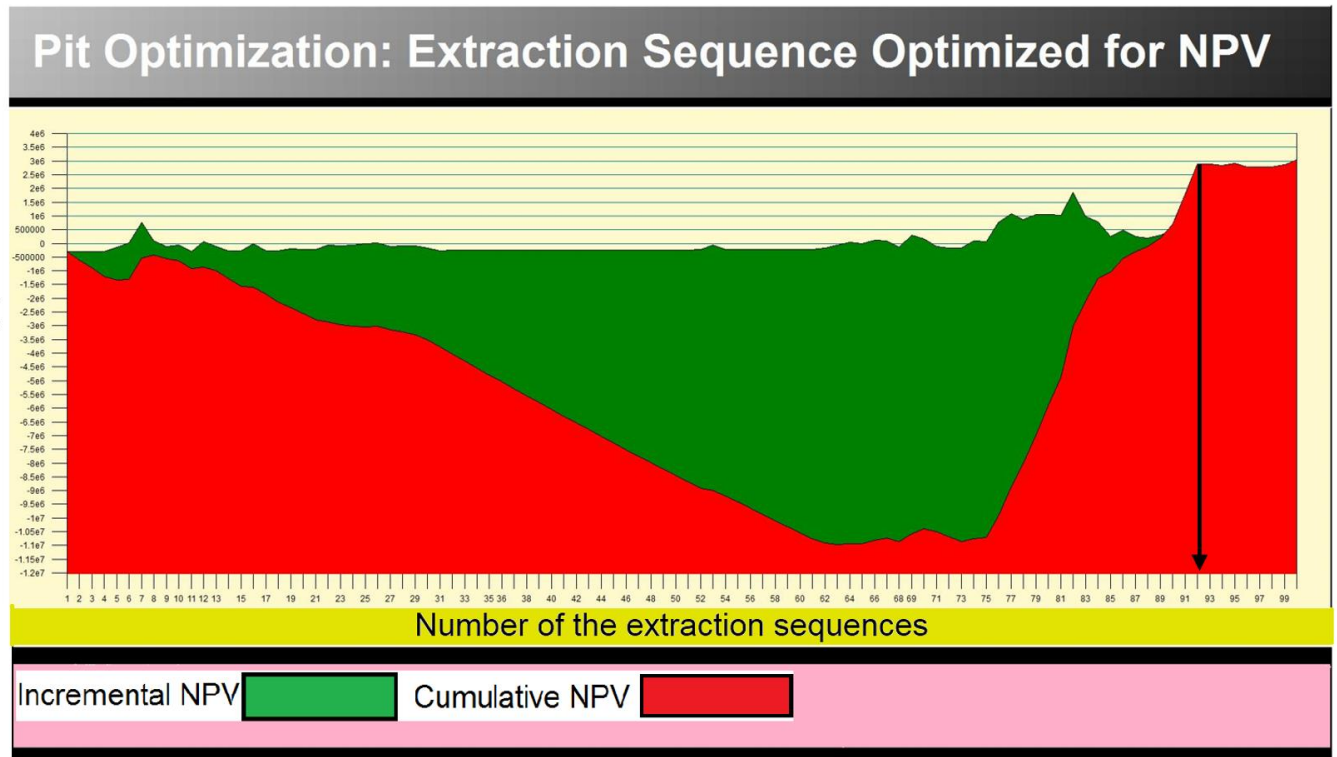
Fig. 5. 10. Comparison between incremental and cumulative NPV values for the Kahang deposit, driven by NPV Scheduler based on Table. H. 1 (the black arrow indicates sequence No. 92 which specifies the Kahang ultimate pit limit)

5.11 Comparative Case Study

The boreholes drilled in the Kahang deposit are not evenly distributed (anisotropic grid drilling), with a particularly large gap between the main cluster and the three drill holes (KAG-43, KAG-38 and KAG-30) located in the NW of the study area, as depicted in the Fig. 5. 11. The gap is due to the existence of a private garden that the National Iranian Copper Industries Co (NICICO), as the project holder, is not allowed to enter and conduct any drilling, even underneath. However, the aim of the comparative case study is to ignore the three isolated boreholes and to compare the relative changes in terms of reserve

estimation, Concentration-Volume (C-V) fractal log-log plot and finally the consequential variance to the NPV, with this mentioned scenario.
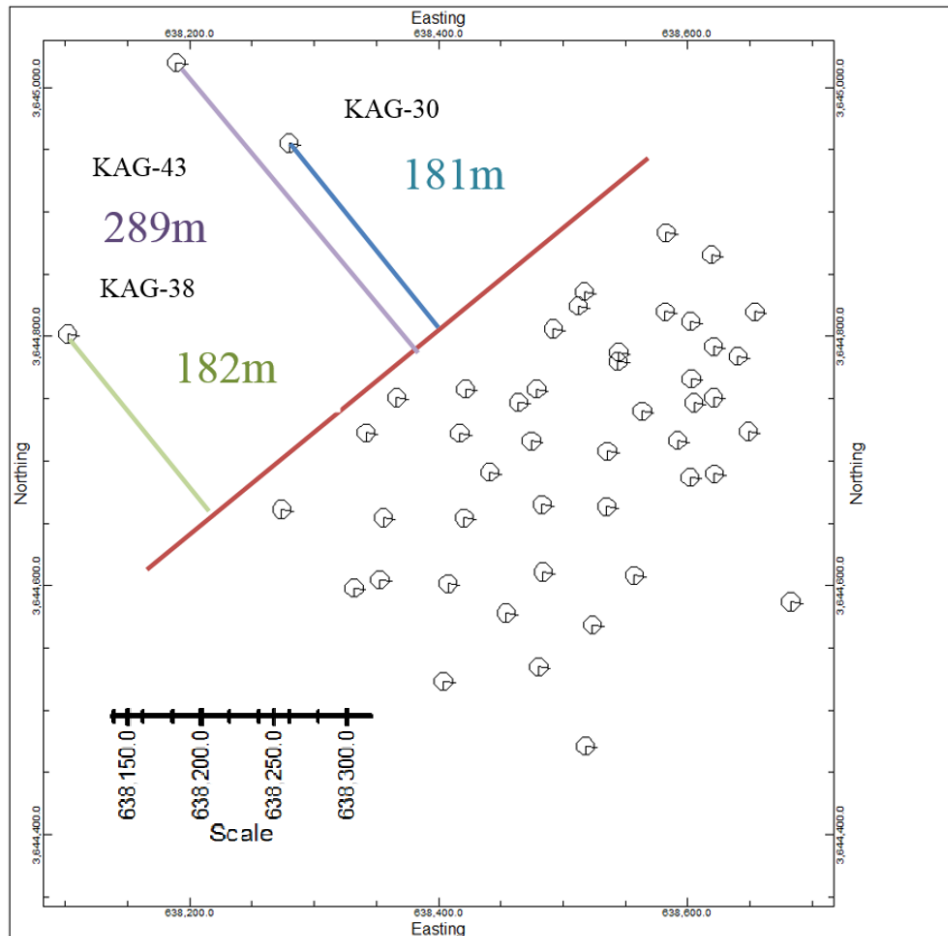
Fig. 5. 11. Disposition of boreholes in the Kahang deposit

As a result, the Kahang deposit was modelled with 263,410 voxels corresponding to 112,950,208 tonnes of sulphide ore (Fig. 5. 12) with an average grade of 0.166 wt.% based on a Cu distribution function which is not normal (Fig. 5. 13).
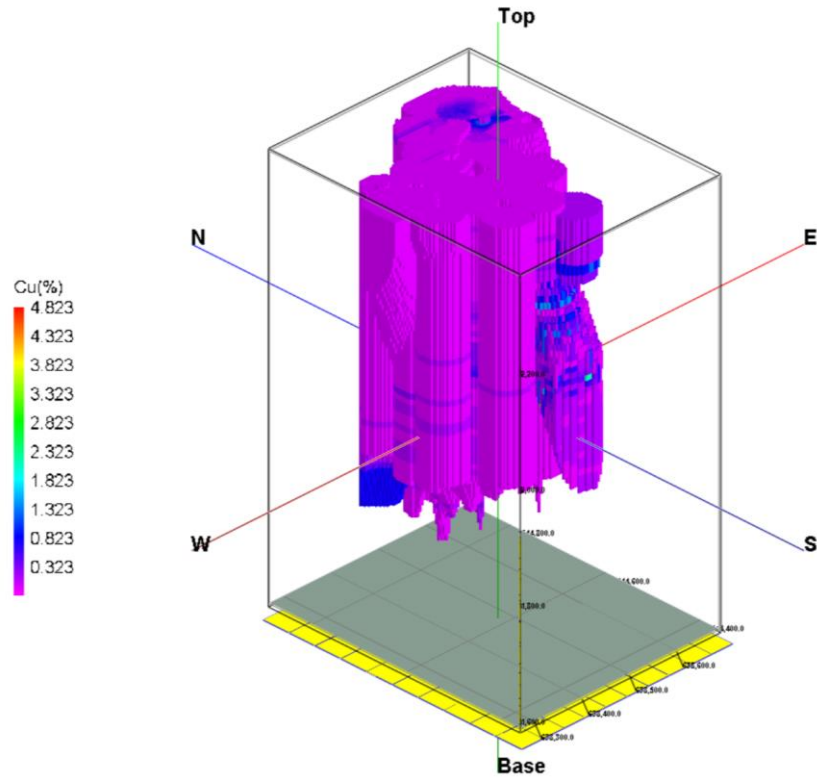
Fig. 5. 12. 3D Cu block model excluding the three isolated boreholes
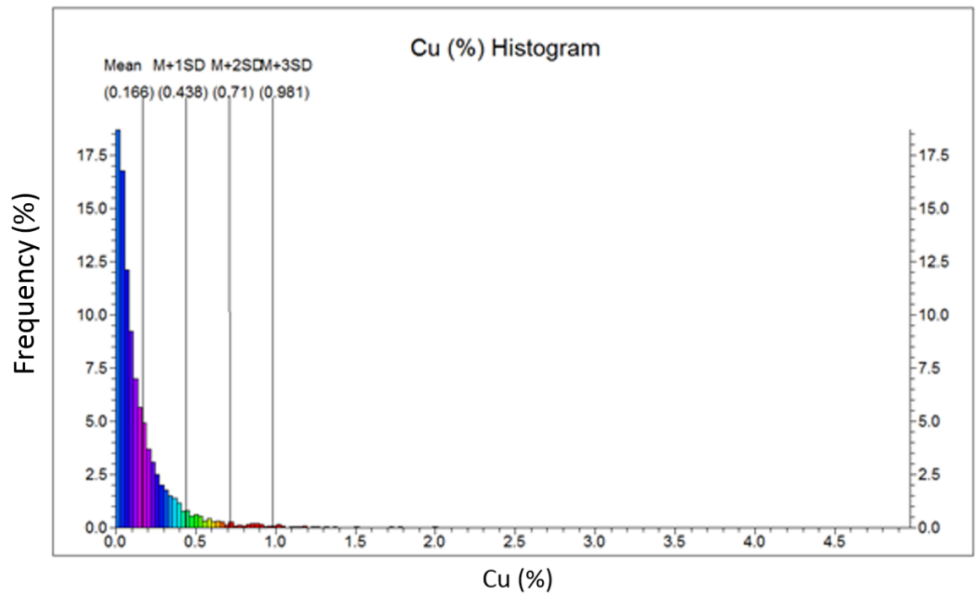
Fig. 5. 13. Cu histogram from original data in the Kahang deposit excluding the isolated

boreholes

The C-V log-log plot for the new Cu block model indicates that there are four Cu populations corresponding to 0.071 wt.%, 0.4 wt.% and 1.86 wt.% (Fig. 5. 14 and Table. 5. 9). Cu concentrations higher than 1.86 wt.% are from an enriched zone.
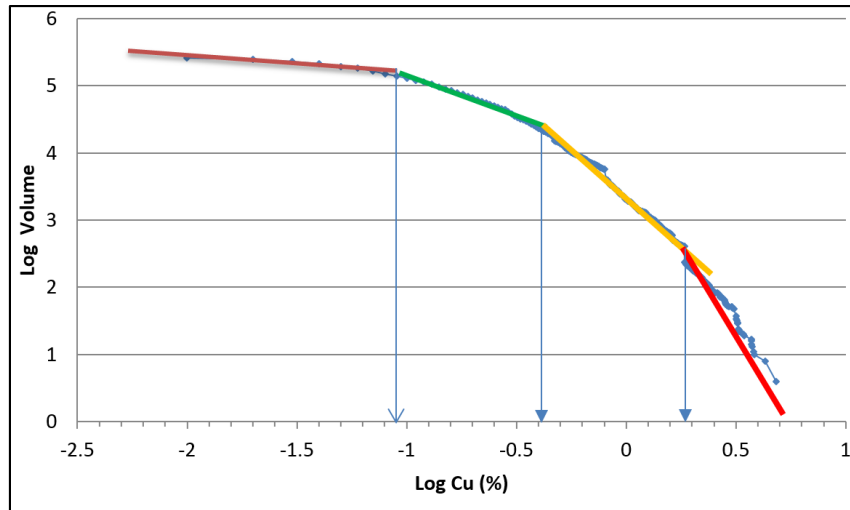
Fig. 5. 14. C-V log-log plot for Cu concentrations, excluding the three isolated boreholes

Table. 5. 9. Cu thresholds defined by the C-V model in the Kahang deposit, ignoring the three isolated boreholes

Geochemical population	Cu (wt.%) threshold value	Range Cu (wt.%)
First (Barren host rock)	-	<0.071
Second (Main mineralisation starting)	0.071	0.071-0.40
Third	0.40	0.40-1.86
Fourth	1.86 (Enriched zone for Cu)	>1.86

The Cu average values with and without the three boreholes are 0.164 wt.% and 0.166 wt.% respectively, and the Cu histograms are similar in the both scenarios. Moreover, the Cu estimated histogram in the new scenario (Fig. 5. 15) is similar to the Cu estimated from all of the bore holes (See chapter 3). The comparison between two block models is depicted in Table. 5. 10.
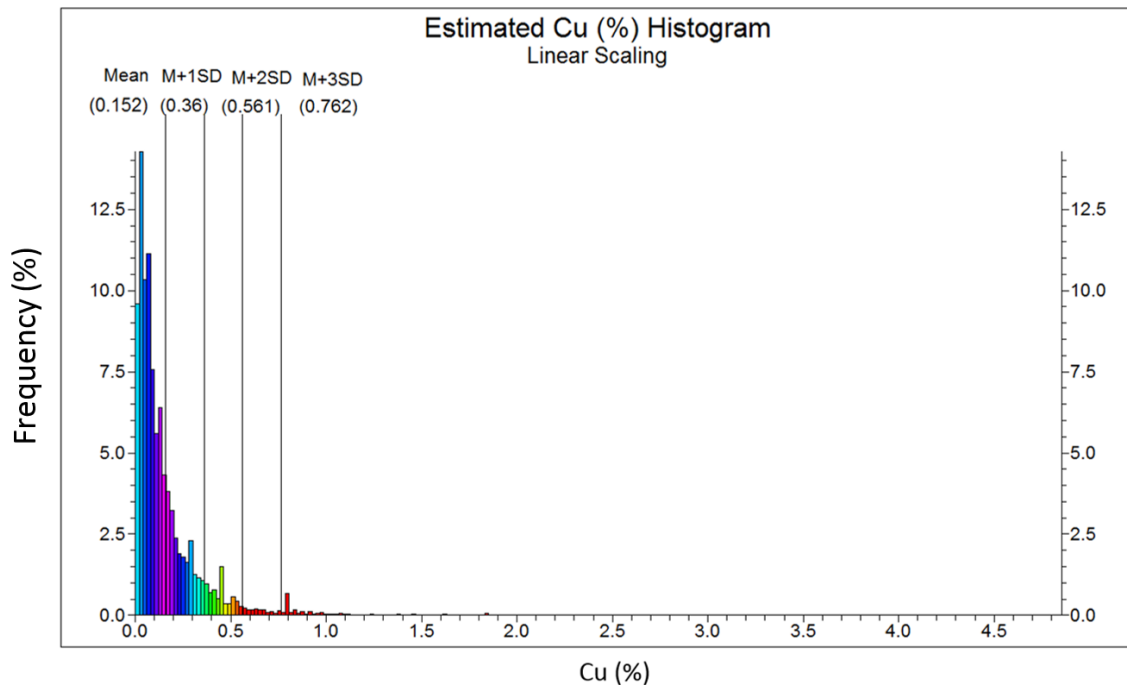
Fig. 5. 15. Estimated Cu histogram, ignoring the 3 boreholes located in the NW part of the deposit

Table. 5. 10. Comparison between results obtained from the two Cu block models

Cu Block Model	Ore Tonnage	Average Grade (wt.%), Raw Data	Average Grade (wt.%), Estimated	Total Voxel Amount	Cu Range for Enriched zone (wt.%)
48 Boreholes	210,080,697	0.164	0.14	489,927	1.86-3.24
45 Boreholes by Ignoring the Three Isolated Boreholes Located in the NW	112,950,208	0.166	0.152	263,410	>1.86

5.12 Determination of an Ultimate Pit Limit when Ignoring the Three Isolated Boreholes

The pit located with an elevation equal to 2210 m (Table. 5. 11) is determined as the new Kahang final pit limit in which the NPV value corresponds to $3,731,732. Furthermore, the ore and waste, strip ratio and mining lifetime report values of 1,475,582 tonnes, 4,713,207 tonnes, 3.19 and 1.48 years, respectively (Table. 5. 12).

Table. 5. 11. Pit limit reserve of the comparative case study

Reserve report for UltPit								
Bench	Elevation	Profit	Revenue	Processing Cost	Mining Cost	Total Rock	Total Ore	Total Waste
		$	$	$	$	tonnes	tonnes	tonnes
Surface 1								
0	2,360	(1,594,880)	0	0	1,594,880	897,120	0	897,120
1	2,350	(1,487,520)	0	0	1,487,520	836,730	0	836,730
2	2,340	(1,361,600)	0	0	1,361,600	767,770	0	767,770
3	2,330	(978,731)	487,333	259,984	1,206,080	702,378	61,630	640,748
4	2,320	727,520	2,847,882	1,065,962	1,054,400	642,291	246,748	395,543
5	2,310	(418,674)	1,183,676	702,830	899,520	547,652	167,891	379,762
6	2,300	(316,726)	1,007,794	563,241	761,280	462,940	134,032	328,908
7	2,290	592,244	2,089,175	877,411	619,520	376,314	205,026	171,288
8	2,280	1,376,886	2,547,005	670,599	499,520	303,324	149,896	153,428
9	2,270	1,288,644	2,315,418	644,054	382,720	232,478	144,808	87,671
10	2,260	2,461,441	3,358,317	609,035	287,840	174,816	128,700	46,116
11	2,250	2,107,424	2,832,878	528,814	196,640	119,432	112,478	6,954
12	2,240	1,249,737	1,726,617	350,479	126,400	76,750	75,580	1,170
13	2,230	492,112	718,956	166,205	60,640	36,504	36,504	0
14	2,220	138,784	201,685	45,461	17,440	9,951	9,951	0
15	2,210	24,612	39,223	10,451	4,160	2,340	2,340	0
Total	0	4,301,274	21,355,960	6,494,526	10,560,160	6,188,790	1,475,582	4,713,208

221

Table. 5. 12. Ultimate pit characteristic for the comparative case study

Cumulative Data								
Profit	Revenue	Processing Cost	Mining Cost	NPV	Total Rock	Total Ore	Total Waste	Strip Ratio
$	$	$	$	$	Tonnes	Tonnes	Tonnes	
4,301,274	21,355,959	6,494,525	10,560,160	3,731,732	6,188,790	1,475,582	4,713,207	3.194

The total number of nested pits existing in this scenario reaches 100 extraction sequences and five pit shells (Table. 5. 13). The sequence No. 90 is determined as the OES with NPV equal to $3,590,462. In addition, the total ore and waste and corresponding strip ratio at this point reports as 1,349,158 tonnes, 4,228,982 tonnes and 3.13, respectively (Fig. 5. 16).
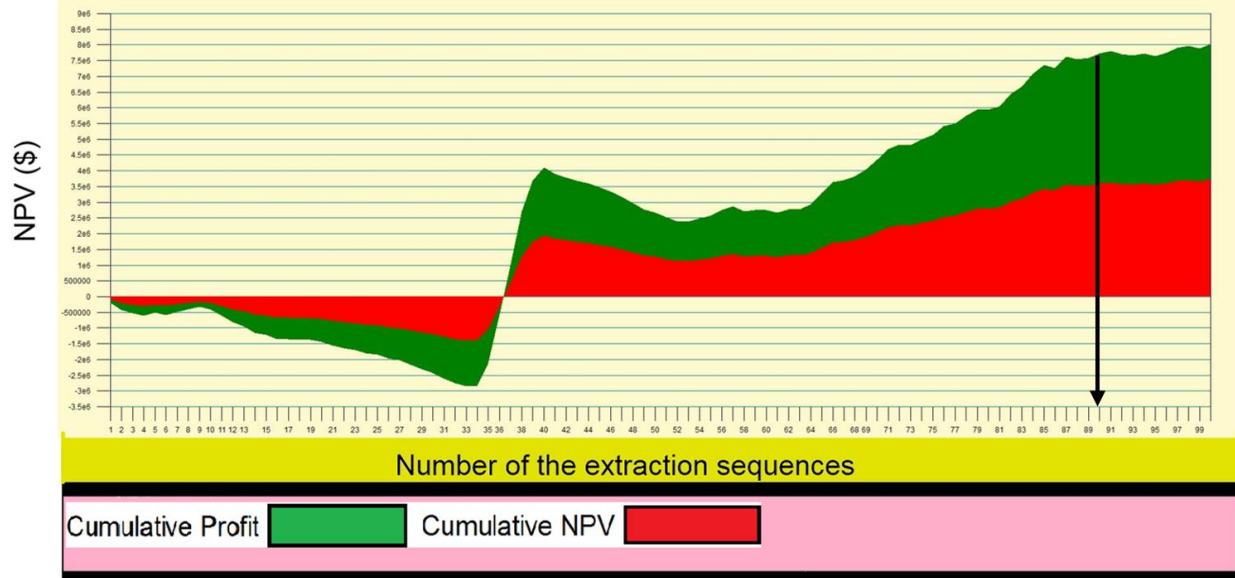
Fig. 5. 16. Cumulative NPV and profit values for the comparative case study driven by NPV Scheduler (the black arrow indicates sequence No. 90 which specifies the Kahang ultimate pit limit)

Table. 5. 13. Pit optimisation phases for the comparative case study

Incremental Data

Phase	Profit	Revenue	Processing Cost	Mining Cost	Total Rock	Total Ore	Total Wast	Strip Ratio
	$	$	$	$	tonnes	tonnes	tonnes	
1 (60.00%)	2,193,484	9,693,603	3,303,959	4,196,160	2,503,043	759,812	1,743,230	2.294
2 (70.00%)	1,909,760	9,397,022	2,463,421	5,023,840	2,895,965	549,750	2,346,215	4.268
3 (80.00%)	103,299	775,938	246,399	426,240	252,098	56,198	195,900	3.486
4 (90.00%)	82,347	1,053,073	327,526	643,200	376,137	74,562	301,574	4.045
5 (100.00%	12,382	436,321	153,219	270,720	161,545	35,258	126,286	3.582

Cumulative Data

	Profit	Revenue	Processing Cost	Mining Cost	Total Rock	Total Ore	Total Wast	Strip Ratio
	$	$	$	$	tonnes	tonnes	tonnes	
1 (60.00%)	2,193,484	9,693,603	3,303,959	4,196,160	2,503,043	759,812	1,743,230	2.294
2 (70.00%)	4,103,244	19,090,625	5,767,380	9,220,000	5,399,008	1,309,562	4,089,446	3.123
3 (80.00%)	4,206,544	19,866,564	6,013,780	9,646,240	5,651,107	1,365,761	4,285,346	3.138
4 (90.00%)	4,288,891	20,919,637	6,341,306	10,289,440	6,027,244	1,440,323	4,586,921	3.185
5 (100.00%	4,301,274	21,355,959	6,494,525	10,560,160	6,188,790	1,475,582	4,713,207	3.194

5.13 Results

One of the most crucial parameters in mining is the cut-off grade (COG) which defines the grade for discriminating between ore and waste in an orebody over a mine life. The results of this study show that the economic COG of the Kahang for Cu is 0.07 wt.% which is almost equal to the commencement of Cu mineralisation resulted by the C-V fractal model (See chapter 3, section 3.7.2).

Determination and analysis of the complete dataset, and the run without the three remote drill holes, indicates that this deposit shows a positive NPV meaning that it is financially feasible to produce Cu (as the main target) and Mo (by-product) for decision makers. The pits located at elevations equal to 2225 m and 2210 m were determined as the Kahang final pit limit for the complete dataset and dataset without the remote drill holes, respectively (Tables. 5. 7 and 5. 11). The differences between the two scenarios mentioned above in terms of the ultimate pit characteristics are shown in Table. 5. 14.

Table. 5. 14. Differences between ultimate pit limits characteristics of the complete dataset and without the three remote drill holes

	NPV ($)	Ore (Tonne)	Waste (Tonne)	Strip Ratio	Mine Lifetime (Year)
Complete Dataset	3,032,862	3,648,294	13,970,954	3.8	3.65
Dataset without the Three Remote Drill Holes	3,731,732	1,475,582	4,713,207	3.19	1.48

The NPV value of the pit without the three isolated drill holes is higher than the pit generated with the complete dataset, although the productivity of the first scenario is higher than the pit without three remote drill holes.

From a comparison of the two ultimate pit limit scenarios the sequence No. 92 was determined as the Kahang optimal extraction sequence (OES) with respect to the complete dataset. However, for the run without the three remote drill holes, sequence No. 90 was identified as the OES (Table. 5. 15).

Table. 5. 15. Differences between optimal extraction sequences characteristics of the complete dataset (sequence No. 92) and without the three remote drill holes (sequence No. 90)

	NPV ($)	Ore (Tonne)	Waste (Tonne)	Strip Ratio	Cumulative Profit Value ($)
Complete Dataset	2,884,968	3,291,944	12,901,028	3.91	7,853,825
Dataset without the Three remote Drill Holes	3,590,462	1,349,158	4,228,982	3.13	4,128,521

From the optimisation models run for the two scenarios, the cumulative profit value for the Kahang deposit is lower when ignoring the three remote drill holes which may be due to lower productivity (e.g., ore tonnage). From this, completion of more comprehensive and systematic drilling in the deposit, especially to overcome the gap between boreholes shown in Fig. 5. 11, seems sensible as it will likely increase the reserve due to better geological constraints.

CHAPTER SIX. Present Value-Volume (PV-V) Fractal Modelling for Mining Strategy Selection

6.1 Introduction

The definition of optimal pit limits and profit is a fundamental part of prefeasibility and feasibility studies in open pit mines (Koenigsberg, 1982; Dowd and Onur, 1993; Whittle, 1998b; Bernabe, 2001; Dincer, 2001; Dimitrakopoulos et al., 2007; Osanloo et al., 2008a; Armstrong and Galli, 2012). The pit limit defines the ore and waste tonnages and the ore values. The OES of the optimal pit represents a maximised Net Present Value (NPV). The classical problem of pit optimisation is solvable using well-known and efficient algorithms like the Lerch and Grossmann (1965) in order to reach the highest value of DCF (Picard, 1976; Bond, 1995; Seymour, 1995; Hustrulid and Kuchta, 2006; Yasrebi et al., 2011; Mart and Markey, 2013). In practice, pit optimisation is performed on voxels whose true grades are unknown and can only be estimated or simulated using the available information. However, future metals' commodity prices are uncertain (Dowd, 1994; Marcotte and Caron, 2013). One of the key pieces of information required is an optimal determination of the COG which depends on all of the salient technological features of mining, such as the capacity of extraction and of milling, the geometry and geology of the orebody and the optimal grade of ore to send for processing (Dagdelen and Mohammed, 1997; Cairns and Shinkuma, 2003). Following this, Krautkraemer (1988) found that the COG changing rate depends on the difference between the price and the rate of interest. As a result, an increase in the metal's commodity price reduces the COG (Cairns and Shinkuma, 2003). Alternatively, when the metal price drops producers attempt to mine ores with higher grades. Consequently, it is often necessary to design a mining scenario (excavation orientation) to optimise pay-back in order to overcome the problems of unpredictability of commodity price and variable mining expenses because

of maturity time, geological factors, engineering parameters, economic conditions and political issues which can all influence the economic regime (Costa Lima and Suslick, 2006; King, 2011).

The project value is a linear function with respect to commodity price (e.g., Costa Lima and Suslick, 2006; Asad and Dimitrakopoulos, 2013; Fig. 6. 1). However, in real cases, project value is a nonlinear function due to the effects of grade distributions, fixed and variable costs due to the spatial location of mineable voxels (Dimitrakopoulos et al., 2002; Costa Lima and Suslick, 2006; Elkington and Durham, 2011; Marcotte and Caron, 2013).

Open pit mine design and long-term sequencing is an intricate and critically important part of mining ventures. It provides the technical plan to be followed from mine development to mine closure which has a profound effect on the economic value of the mine. Therefore, the aim of this chapter is to propose a Present Value-Volume (PV-V) fractal model to identify an accurate excavation orientation with respect to the economic principals of all voxels within the Cu-Mo block model. This is obtained using the C-V fractal model and voxels located within the determined ultimate pit limit which will take into account best mining strategy.
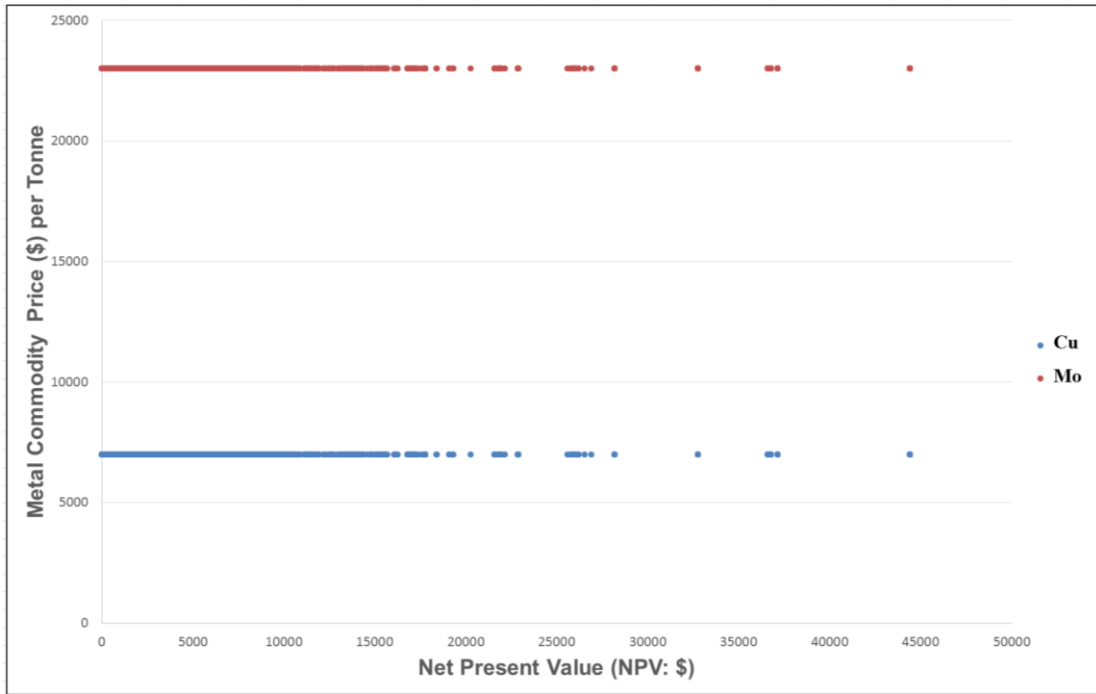
Fig. 6. 1. Linear relationship between the NPV and metal prices

6.2　Methodology

Based on the Cu-Mo block model of the Kahang deposit obtained by means of the C-V fractal model (See chapter 3), a dataset was created for economic modelling including the voxel's coordination, density (See chapter 4), Cu and Mo values and metal prices, rock type, mining and processing costs, recoveries and revenue (economic principals) with respect to the each voxel. The PV values were calculated for each voxel. Subsequently, a PV-V fractal model was generated for classification of the voxels' values in terms of profitability regarding positive values, as depicted in Fig. 6. 2. The proposed PV–V fractal model can be expressed as follow:

$$V(\rho_{PV} \leq \upsilon) \propto \rho_{NPV}^{-a1}; \quad V(\rho_{PV} \geq \upsilon) \propto \rho_{PV}^{-a2}$$

Equation 6-1

Where $V(\rho_{PV}\leq\upsilon)$ and $V(\rho_{PV}\geq\upsilon)$ denote volumes (V) with PV values (ρ_{PV}) that are, respectively, smaller and greater than PV threshold values υ. $a1$ and $a2$ are characteristic exponents as fractal dimensions.
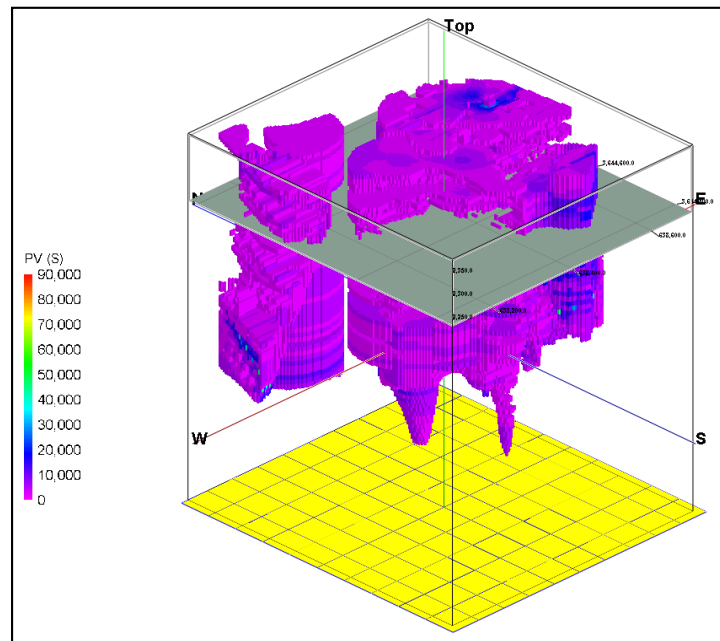
Fig. 6. 2. Present Value (PV) block model for the Kahang Cu-Mo porphyry deposit (the grey platform distinguishes the boundary between open pit and underground mining surfaces based on chapter 5, section 5.10.1 and Table. 5. 7)

Secondly, the excavation orientation (pushbacks) were defined based on the results obtained from the fractal modelling. In addition, a NPV-Cumulative Total Ore (NPV-CTO) fractal model, in line with mining sequences (Nested pits: See Appendix. H), was proposed in order to validate an optimal extraction sequences (OES). The fractal model is expressed in the following form:

$$CTO(\rho_{NPV} \leq v) \propto \rho_{NPV}^{-a1}; \quad CTO(\rho_{NPV} \geq v) \propto \rho_{NPV}^{-a2}$$

Equation 6-2

Where $CTO(\rho_{NPV} \leq v)$ and $CTO(\rho_{NPV} \geq v)$ reveal cumulative total ore (CTO) with NPV values (ρ_{NPV}) that are, respectively, smaller and greater than NPV threshold values. v defines those CTO and $a1$ and $a2$ are characteristic exponents as fractal dimensions. For calculation of $CTO(\rho_{NPV} \leq v)$ and $CTO(\rho_{NPV} \geq v)$, mining sequences with their corresponding NPV values were used.

6.3 Statistical Characteristics

According to the PV calculation for each voxel of the Kahang block model, 86,650 voxels consisting of the positive PV values were used. The PV histogram generated based on its positive values (Fig. 6. 3) shows a PV mean equal to $2,933. Furthermore, a PV median was found to be $1,668 which reveals that the majority of voxels with positive PVs have values lower than the mean. Moreover, most of the voxels contain PV values lower than $10,000 and also a few voxels (1,253 voxels) have a PV value higher than $20,000. Finally, a histogram of cumulative NPV was generated based on the mining sequences derived via the optimisation operation considering the positive NPV values, as depicted in Fig. 6. 3. Twelve out of 100 nested pits have positive cumulative NPV values (See Appendix. H). There is a multimodal distribution for this variable. The main population has high values of cumulative NPVs which are greater than its mean ($2,370,497).
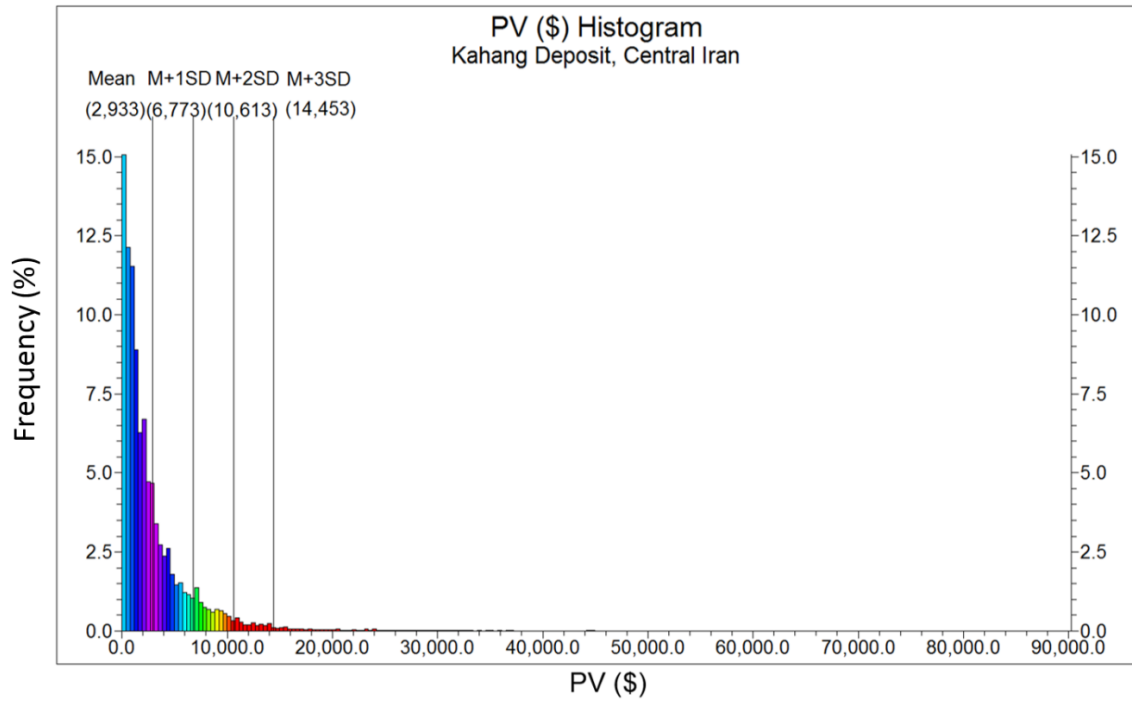
(a)
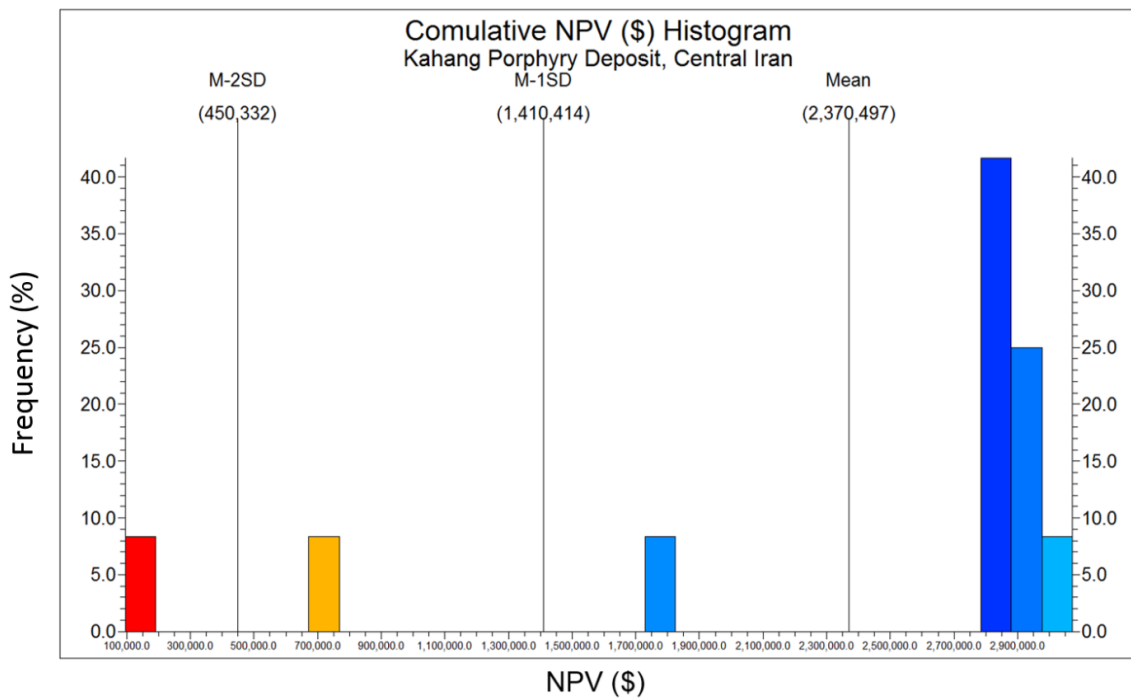
(b)

Fig. 6. 3. a) Profit value histogram based on PV block model, and b) NPV histogram based on the mining sequences for the Kahang deposit

6.4 Application of PV-V Model

According to the 3D PV block model, a PV-V fractal model has been created which, from log-log plot, shows that there are four populations corresponding to $501, $1,995, $19,054 and $31,623 (Fig. 6. 4). This indicates that there is a multifractal nature in terms of the PV values within the deposit. The voxels with high and extreme values of PV commence from $19,054 and $31,623, respectively, which exist in the NE and central parts of the area (Fig. 6. 5). The majority of voxels have PV values between $1,995 and $19,054 in the deposit (third population in the log-log plot) entitled moderate population of PV, as depicted in Fig. 6. 5. The number of voxels is around 112,000 and 134,000 in the weak and moderate populations based on the PV-V model, as depicted in Table. 6. 1. Low amounts of voxels (<2600) contain the high and extreme populations with high values of PV. Most of the voxels with high and extreme PV values exist at depth, in the NW and especially in the central parts, as depicted in Fig. 6. 5.
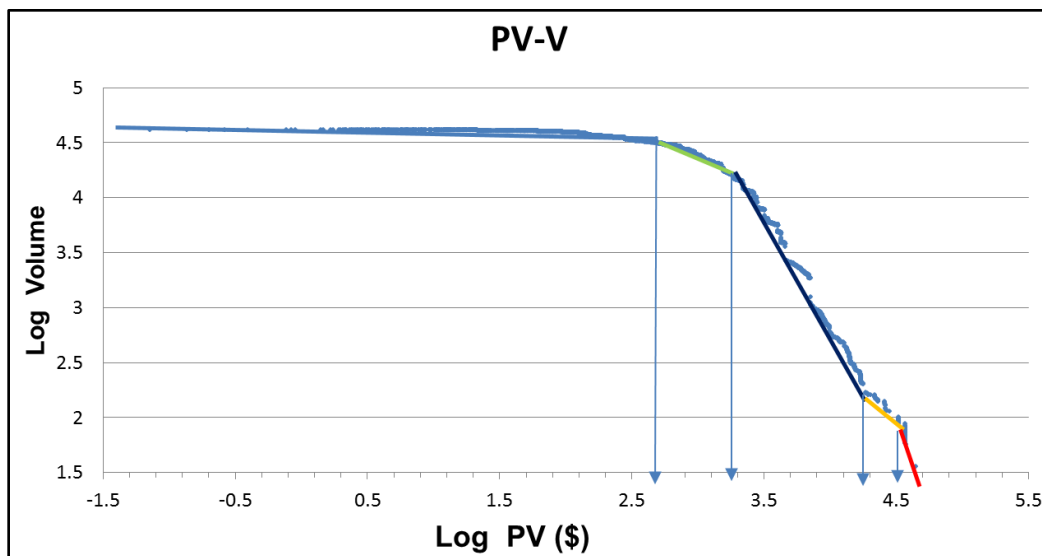
Fig. 6. 4. PV log-log plot
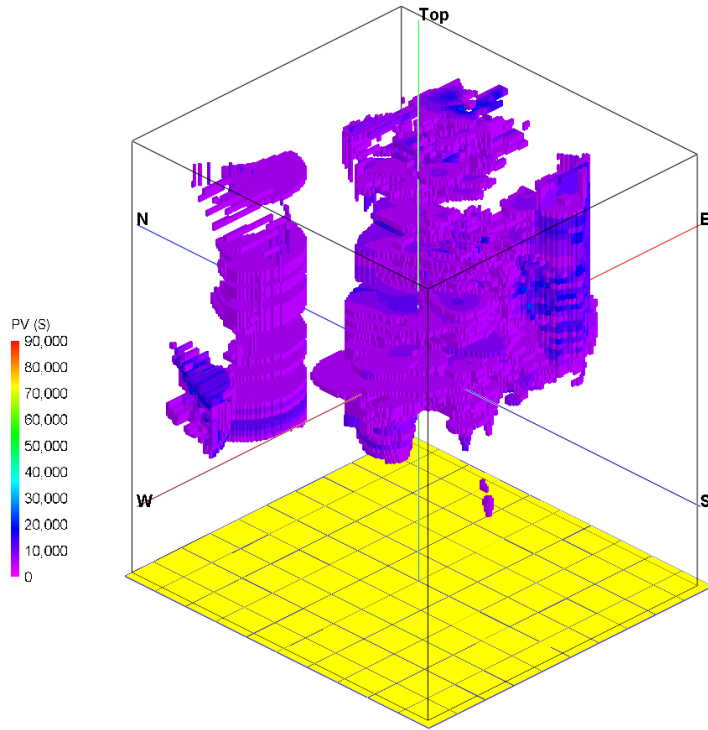
(a)
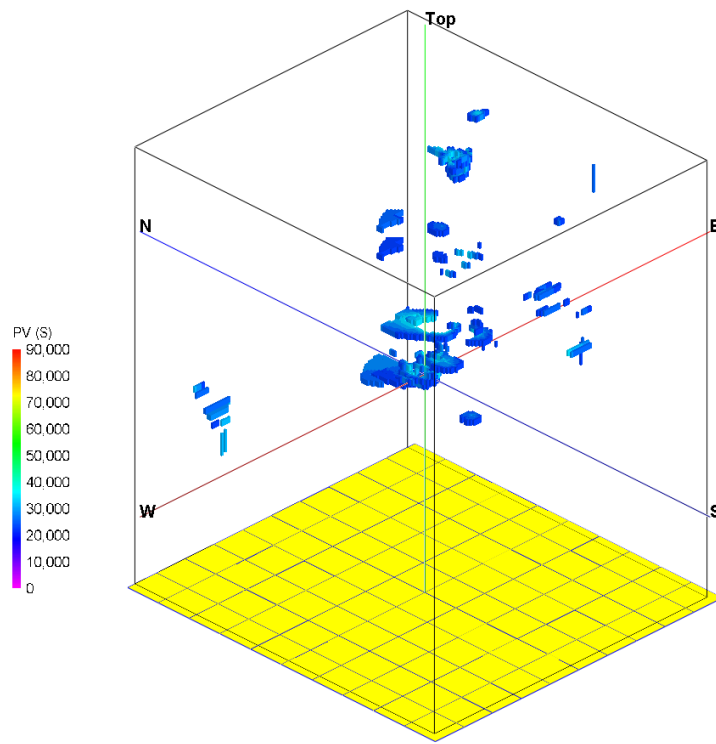
(b)
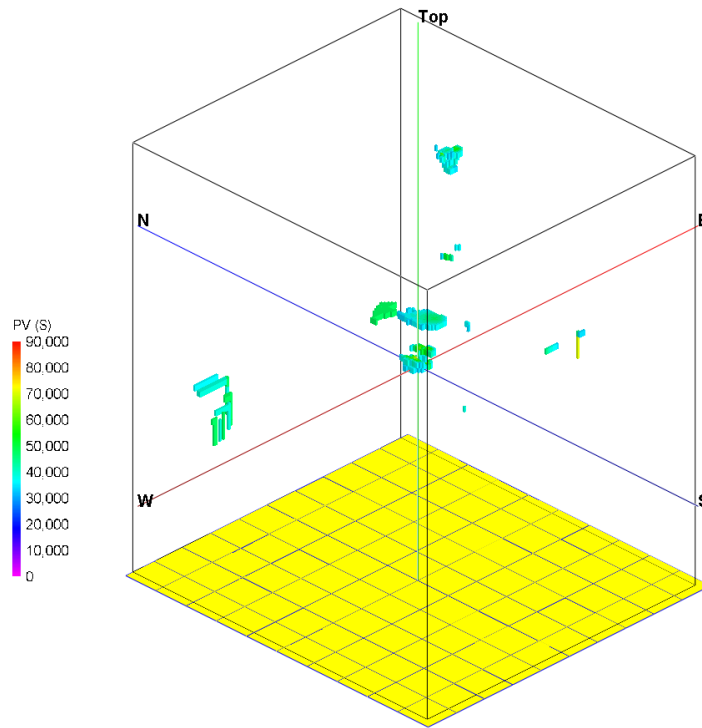
(c)

Fig. 6. 5. PV distribution within the deposit based on the PV-V fractal modelling consisting of a) moderate population, b) high PVs, and c) extreme population

Table. 6. 1. PV thresholds defined by PV-V model in the Kahang deposit

PV Population	PV ($) Range	Number of Voxels
Very weak	<501	57305
Weak	501-1995	111994
Moderate	1995-19054	133757
High	19054-31623	1925
Extreme	≥31623	604

Based on the ultimate pit limit (See chapter 5), most of the voxels with high and extreme PV values are situated in the deeper parts of the mine, as depicted in Fig. 6. 6. The majority of these voxels are close to the open pit limit, especially in the central part, which

means that an ultimate pit limit can be moved deeper if detailed grid drilling can be carried out. The PV plans in the different excavation levels were derived via a PV block model and classified on the basis of PV-V fractal modelling to propose an accurate mining orientation in order to achieve an earlier pay-back period (Fig. 6. 7). As a result, the PV values increase from the north of the deposit to the south which is defined as the excavation orientation.
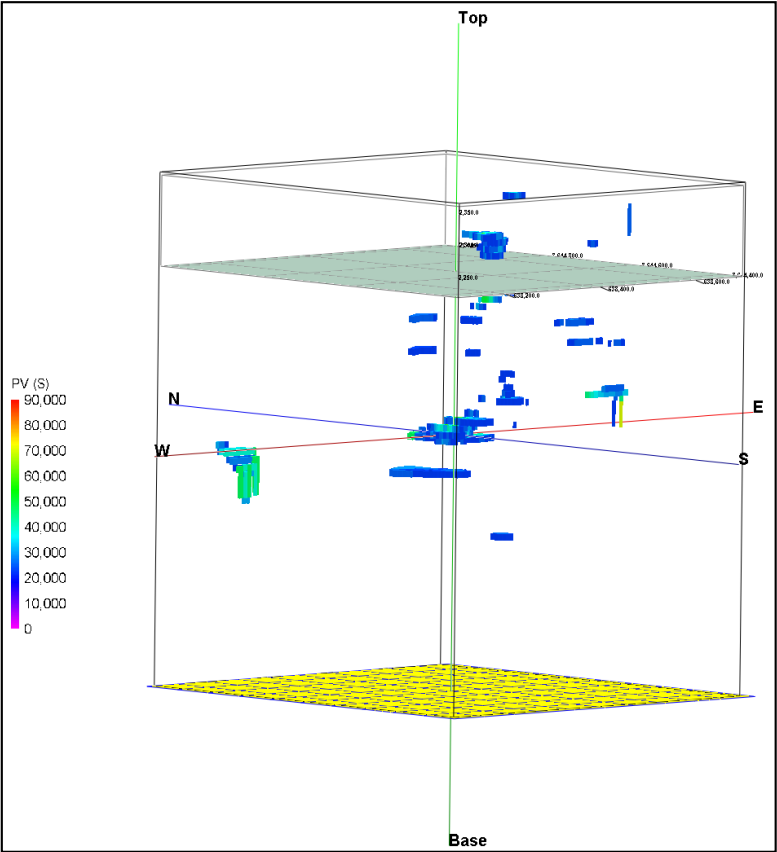
Fig. 6. 6. Voxels with high and extreme PV values within the deposit (the grey platform distinguishes the boundary between open pit and underground mining surfaces based on chapter 5, section 5.10.1 and Table. 5. 7)
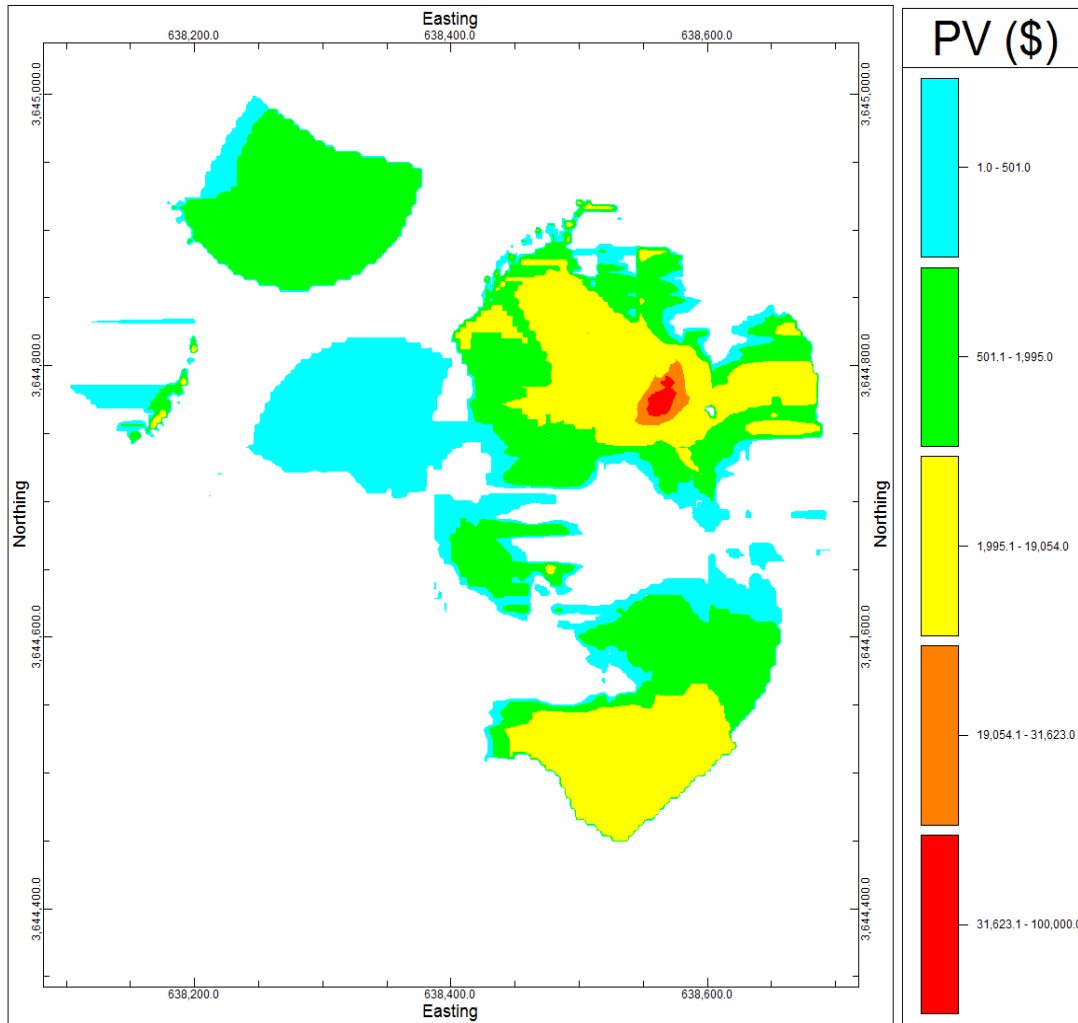
(a)
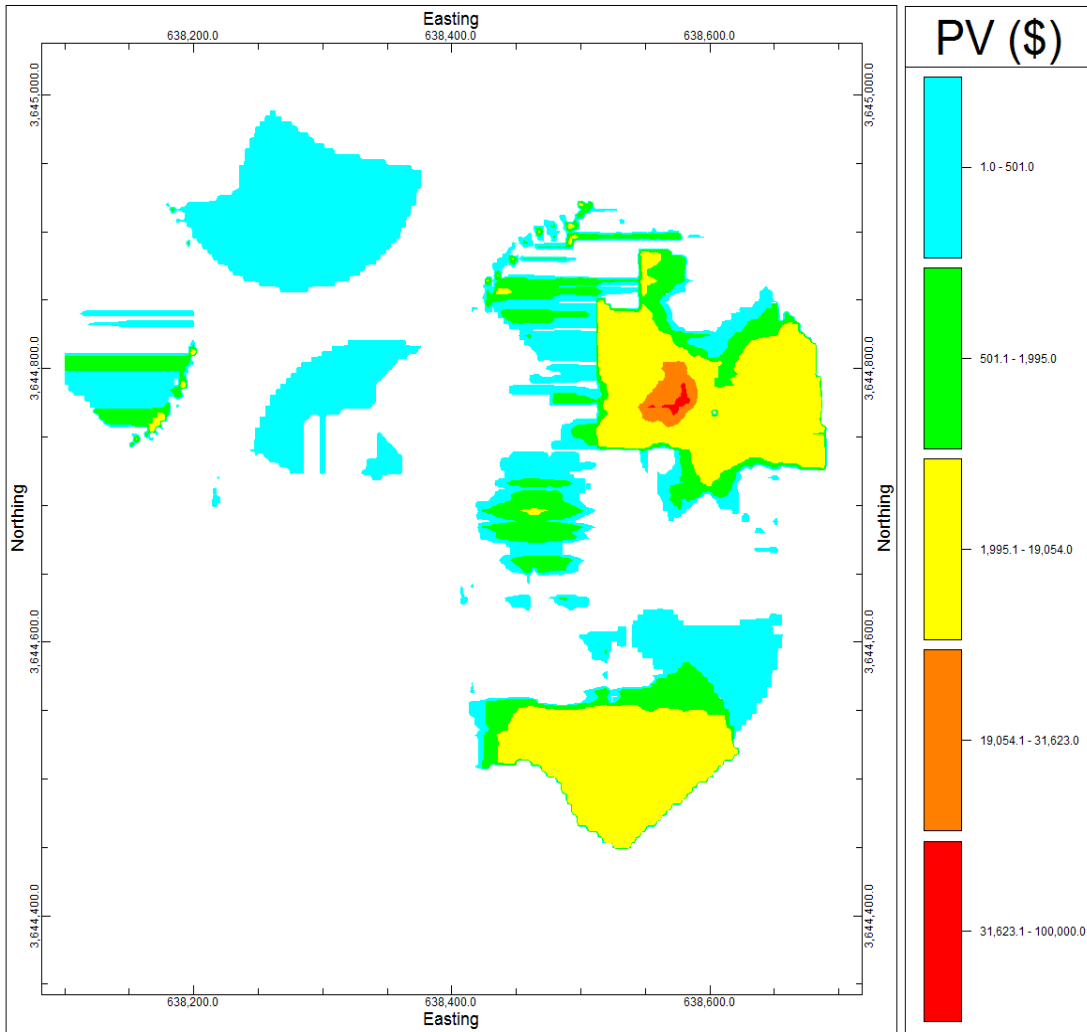
(b)
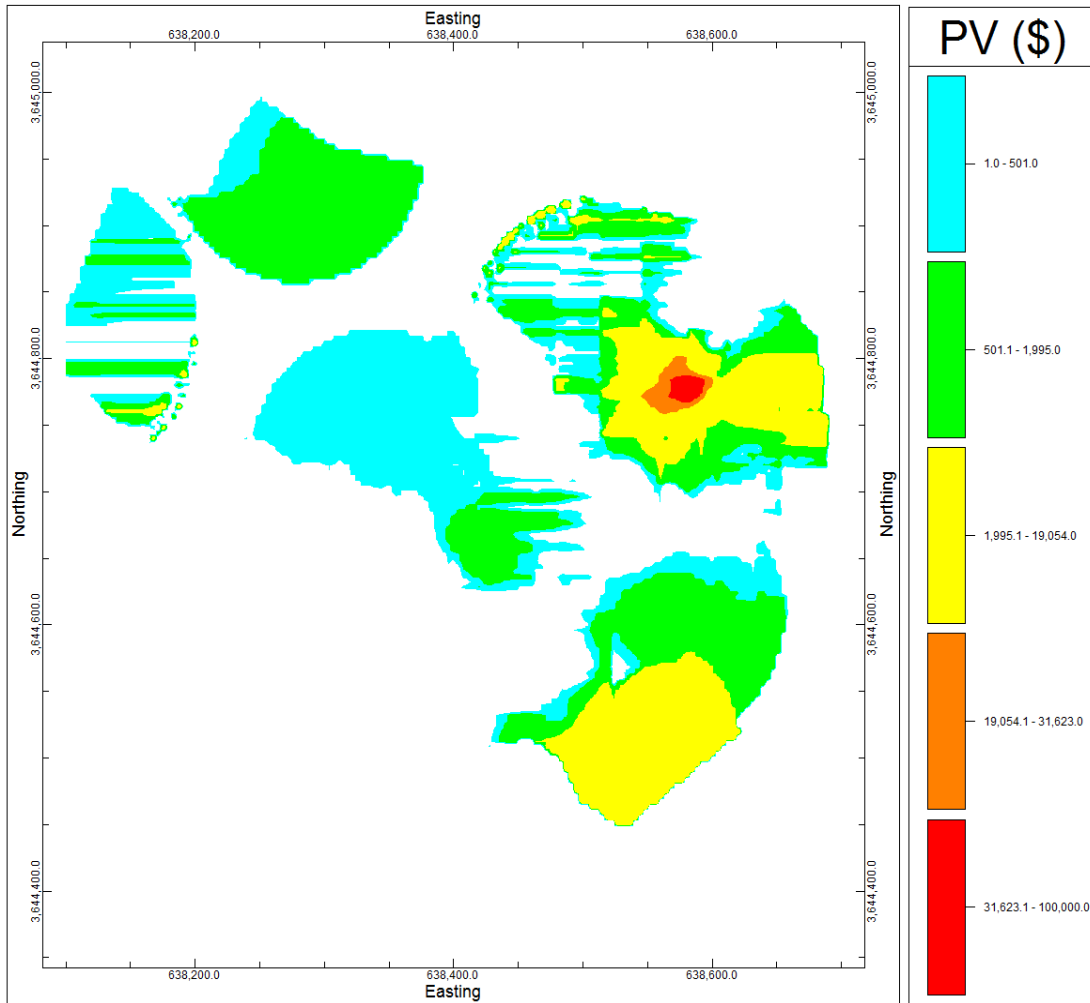
(c)
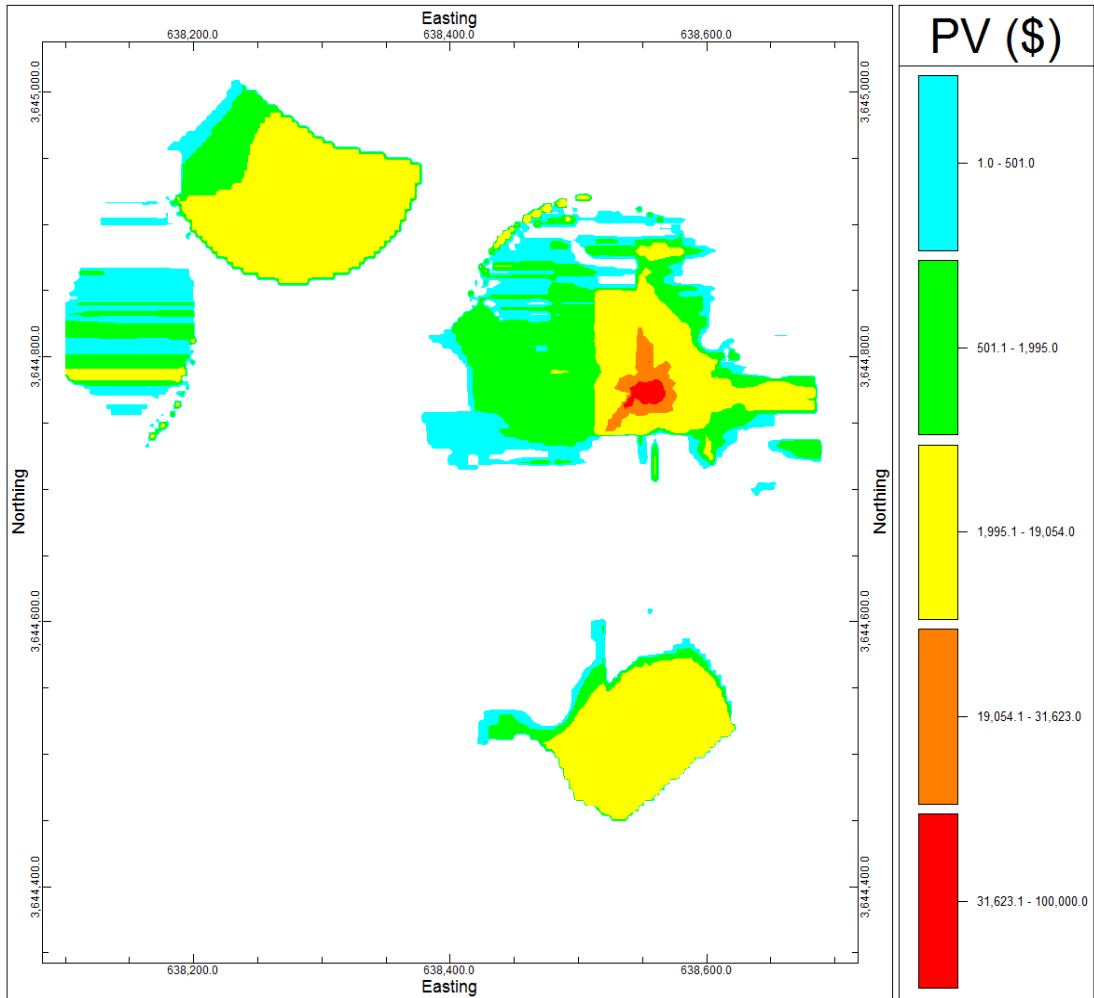
(d)
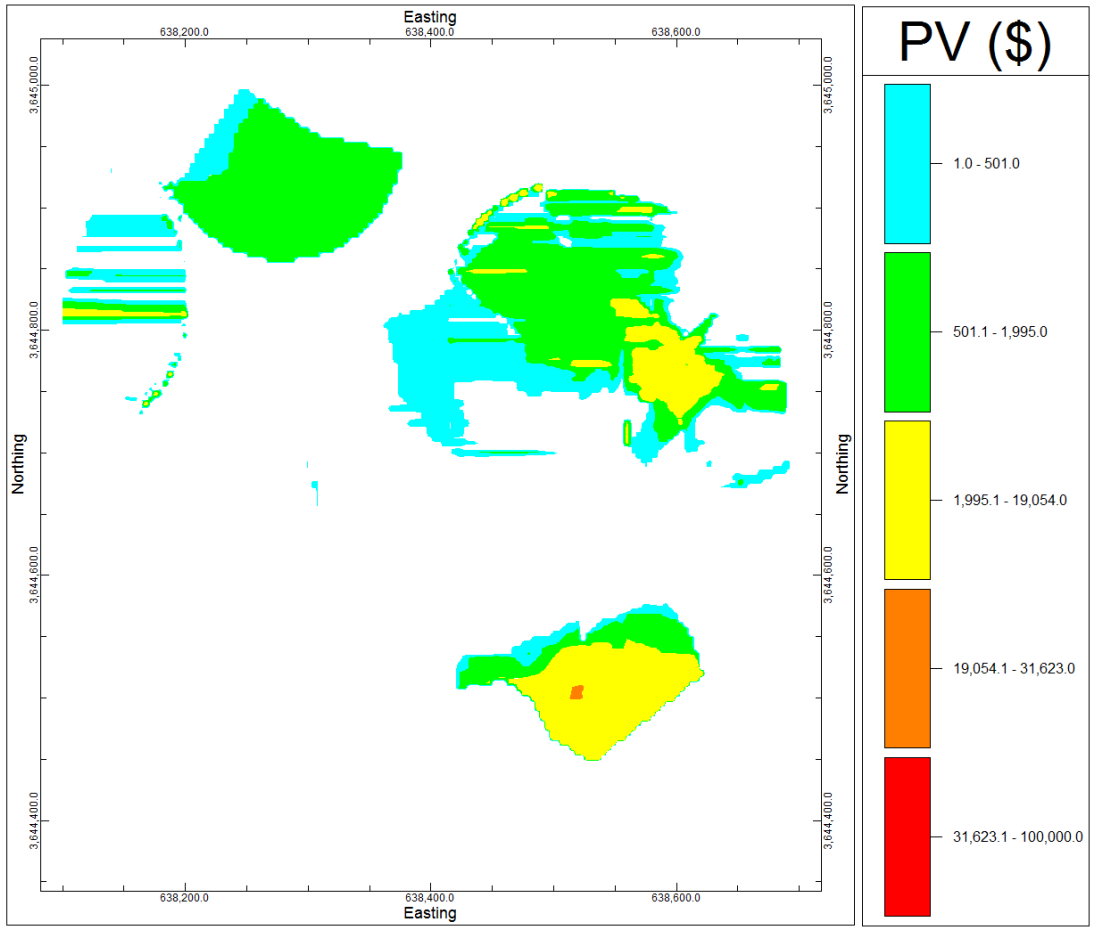
(e)
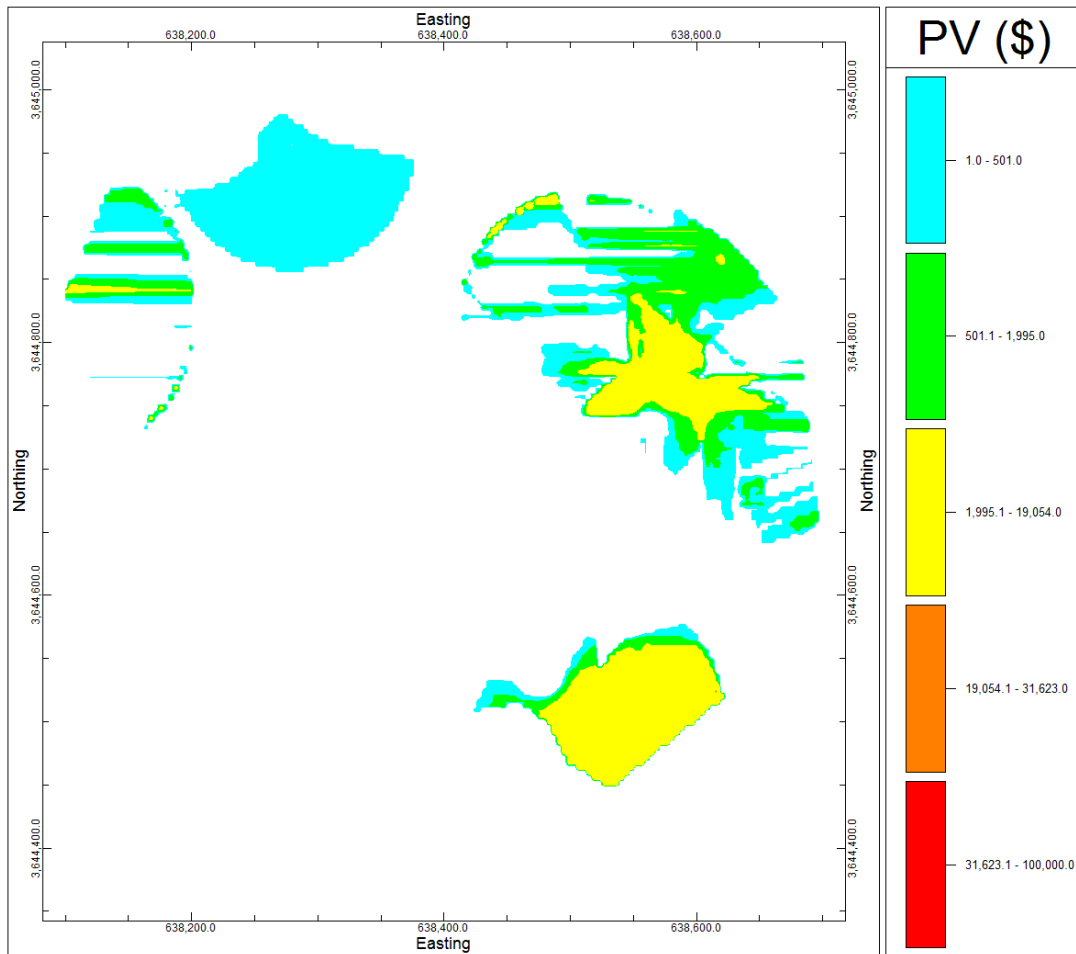
(f)
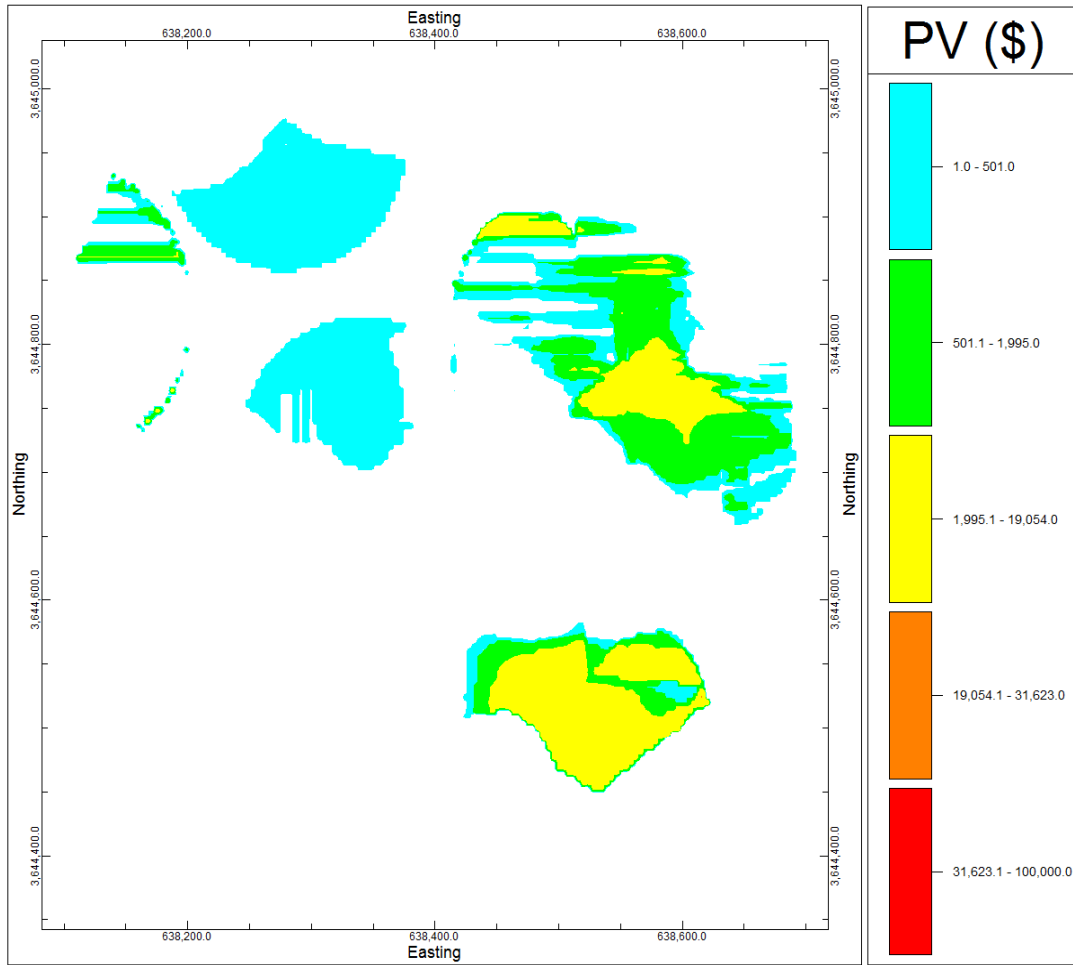
(g)
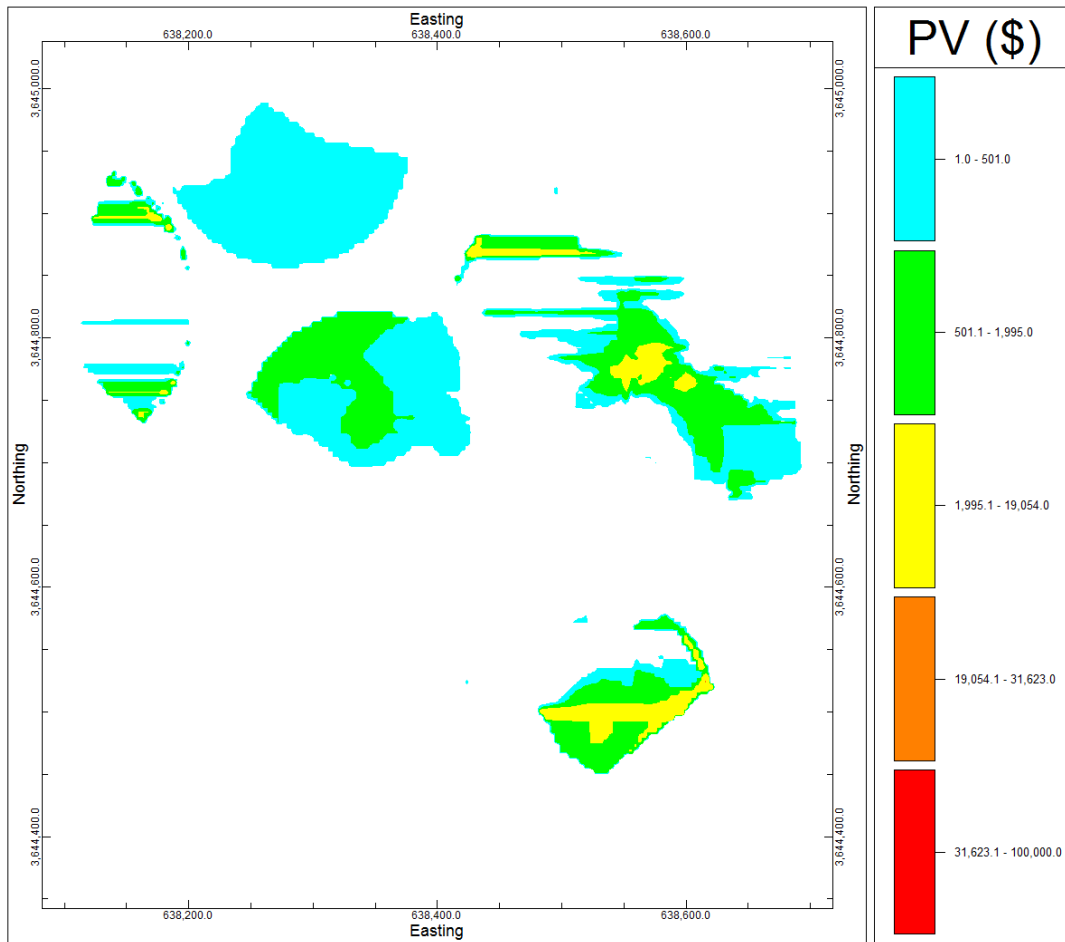
(h)

Fig. 6. 7. PV plan views based on the PV-V fractal model in elevations of: a) 2230 m, b) 2240 m,

c) 2250 m, d) 2260 m, e) 2270 m, f) 2280 m, g) 2290 m, and h) 2300 m

6.5 Application of NPV-CTO Model

The criteria used to determine an OES is subjective in the sense that the chosen sequence is the one that has the NPV nearest to the highest NPV calculated via NPV Scheduler. The proposed NPV-CTO fractal model is a reward of developing a new method to reduce the number of required mining sequences and practical time to obtain an optimal solution to determine an OES, especially in an absence of computer-based optimisation software (i.e., NPV Scheduler). In addition, this model reduces the number of analyses and data transfer processes that are often necessary in standard computer-based practice for open pit optimisation. This is necessary to overcome probable mining risks due to uncertainty resulting from e.g. any sudden economic changes or a decrease in the commodity metal price especially if this happens at the end of mine life (Godoy and Dimitrakopoulos, 2004; Montiel and Dimitrakopoulos, 2013). However, the best selection of mining sequence is determined when the NPV cumulative trend becomes steady (See chapter 5, Fig. 5. 10). This selection for identification of an OES is controlled manually, typically from a nested pit shell methodology based on the experience of the engineer, and consequently an optimum solution for this problematic issue cannot be developed and it may lead to suboptimal results (Lerch and Grossmann, 1965; Bond, 1995; Hustrulid and Kuchta, 2006; Elkington and Durham, 2011; Mart and Markey, 2013). As a result, a mathematical method to provide an analytical practice, which intends to prevent manual identification of an OES, seems to be inevitable.

In the author's view, a proposed model should be rigorously tested against those already available, and the possible errors discussed. Therefore, results of the proposed fractal

model were compared with the results of the OES, generated from NPV Scheduler (See chapter 5 and Appendix. H). The NPV-CTO log-log plot indicates a mono-fractal nature meaning that there is only one threshold value which corresponds to $2,754,229 and 3,288,516 tonnes of minable ore (Fig. 6. 8). The result of an obtained OES (from Chapter 5), which is the point that mining will be suspended due to a steady trend in the cumulative NPV, is close to the result achieved through the NPV-CTO model. Possible errors for this are shown in Table. 6. 2.

Table. 6. 2. Comparison between OESs regarding cumulative NPV and ore, calculated from NPV Scheduler and NPV-CTO fractal model

Identification of an Optimal Extraction Sequence (OES)					
Extraction Sequence Chart via NPV Scheduler		*Extraction Sequence Chart via NPV-CTO model*		*Errors*	
NPV ($)	Ore (Tonne)	NPV ($)	Ore (Tonne)	NPV (%)	Ore (%)
2,884,968	3,291,944	2,754,229	3,288,516	4	0.1
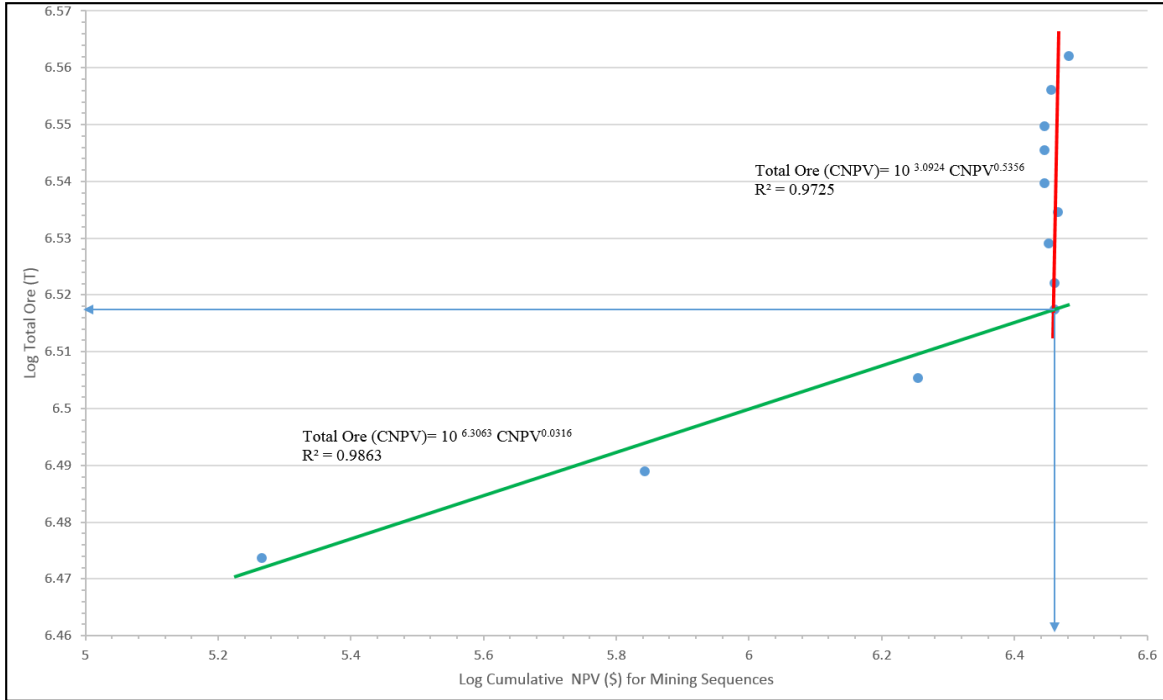
Fig. 6. 8. The NPV-CTO log-log plot in the Kahang deposit

6.6 Results

From the PV-V log–log plot from Kahang, there is a multifractal PV distribution within the deposit. In addition, there are five threshold values meaning four PV populations for the deposit. The threshold value of $1995 is the commencement of the moderate population which occurs in the majority of voxels within the deposit. The high PV values are present in the NE and central parts of the deposit. The extreme values are situated at the depth and NW parts, around the three remote drill holes. The 2D and 3D maps for PV distribution show that the profitability increases from the north to south of the deposit proposing an open pit excavation orientation to achieve an earlier pay-back.

The NPV-Cumulative Total Ore (NPV-CTO) fractal model was proposed in order to find an OES. The NPV-CTO log–log plot from the Kahang deposit shows that there is a mono-fractal model which has a threshold value for cumulative NPV and enclosing ore equal to $2,754,229 and 3,288,516 tonnes, respectively. This indicates that the mining operation can be terminated when reaching this point to reduce the number of required mining sequences. This overcomes probable mining risks due to uncertainty of the relative metal's world commodity price and sudden mining costs.

The comparison between the results for OES calculated from NPV Scheduler and NPV-CTO fractal model shows that the errors for NPV and minable ore are 4% and 0.1%, respectively. This may suggest that the developed model is reliable and can be used beyond the Kahang deposit in determination of an OES for open pit mines.

CHAPTER SEVEN. Conclusions and Recommendation for Future Work

Conventional methods including calculation of mean and standard derivation (SD), probability graphs, explorational data analysis (EDA) and multivariate data analysis have been widely used in geochemical exploration. However, these methods do not consider spatial variations in geochemical patterns. In the past decades, a number of complex structures and phenomena have been quantitatively characterised by fractal/multifractal modelling (the most commonly used fractal models have been introduced in this thesis). The utility of fractal/multifractal models for geochemical data is to delineate geochemical populations and quantify the spatial distribution of geochemical data. A variety of fractal/multifractal models for this purpose have been introduced and used in different kinds of deposits (e.g., Qulong copper deposit, Tibet, western China; Sungun porphyry copper deposit, Iran; Mitchell Sulphurets precious metal district, British Columbia, Canada; Cambrian Hellyer volcanic-hosted massive sulphide deposit, Australia; undiscovered mineral deposits in Gejiu, Yunnan province, China; Zaghia iron ore deposit, central Iran; Tangedezan Pb–Zn carbonate hosted deposits, central Iran; bauxite orebodies in the Guangxi province, China). The fractal/multifractal modelling has been shown to be a useful tool for mineral exploration, rock mechanics and economical evaluation of the Kahang porphyry deposit due to ore elements, rock mass and economical parameter variation. The advantages of the fractal modelling, using C-V, D-V, RQD-V, PV-V and NPV-CTO, is its simplicity and easy computational implementation, as well as the possibility to compute numerical values for variables, e.g., geochemical data, density, RQD and present value (PV) thresholds, which are deemed to be the most useful criteria for cross examination of data.

Evaluation of ore element distribution via the C-V fractal model was carried out to separate 'barren' host rock, below the cut-off grade in an open pit optimisation, from mineralised zones, especially for the cases in which element concentrations occur in the various geological zones. Such complexity can be efficiently recognised by fractal/multifractal analysis such as C-V fractal model using log–log plots.

A comparison between the resulting 3D models from multifractal analysis and traditional statistical methods indicates that the statistical methods can only consider the elemental concentration and they ignore the spatial variability in the block models of the deposits which may appear within the model. In fractal models, the spatial correlation of data is of interest such as Cu and Mo grades, density, RQD and PV. Statistical analysis applied to the data has shown non-normal distribution for Cu, Mo, density, RQD and PV. Accordingly, in statistics, only one threshold can be extracted for each element which is the mean value. The multifractal model provides several thresholds separating various stages of the regional variables.

The Kahang Cu-Mo porphyry deposit in this case study consists of Eocene volcanic–pyroclastic rocks which were intruded by Oligo-Miocene porphyric granitoids rocks, quartz monzonite, monzodiorite-monzogranites and diorites. The geological results from lithology, alteration and zonation and also subsurface geochemical data including Cu and Mo values in this study have shown a porphyry deposit in this area. The main host rock is porphyritic quartz diorite for Cu-Mo mineralisation. The alteration map in Fig. 2. 5a shows four major types of hydrothermal alterations in the Kahang deposit: potassic,

phyllic, argillic and propylitic. The most extensive hydrothermal alteration zone in the Kahang is phyllic. Minor amounts of chalcopyrite and molybdenite are seen in this zone, but the major sulphide mineral is pyrite. The Cu mean value within this zone is equal to 0.14 wt.% based on raw data from drill holes. This zone has occupied a large part of the deposit from depth to surface (Fig. 2. 13). Potassic alteration is observable in the NW and deep parts of the deposit. The common potassic alteration zone in Kahang was distinguished from the presence of mineral assemblages (e.g., KF, secondary biotite, quartz veins and veinlets, magnetite and chlorite). Moreover, there is evidence of potassic alteration to the west, especially around the three remote drill holes located in the NW part, which can suggest that mineralisation within this zone may continue to the west (See Cu distribution with different thresholds in the NW drillholes in Fig. 3. 20). In addition, the Cu mean value within the potassic zone is 0.12 wt.% based on the raw data. Argillic alteration is seen on surface. Main products of this alteration is kaolinite which was produced from alteration of plagioclase phenocrysts and groundmass. Jarosite, as the second major alteration mineral in this zone is present (Fig. 2. 8c). The propylitic alteration zone is developed in marginal parts of the deposit. The most important products of this alteration in order of abundance are chlorite, calcite and minor epidote (Fig. 2. 9). Based on abundance of chlorite and calcite, this alteration zone is divided into two main chloritic and calcitic parts. Hypogene-type mineralisation hosts most Cu ore in the Eastern part of the Kahang deposit but the supergene enrichment zone is relatively small and occurs in the central part of the area which approaches the surface.

According to the C-V fractal model, the main threshold values for Cu and Mo are 0.42 wt.% and 100 ppm, respectively. Enriched Cu-Mo mineralised zones with Cu ≥ 1.8 wt.% and Mo ≥645 ppm are located in the central, NW and NE parts within the hypogene zone. The supergene enrichment zone occurs in small areas within the deposit, especially in the central and eastern parts close to the surface. The hypogene and supergene enrichment zones outlined by the C-V model correlate well with the alterations and mineralogical data shown in the 3D geological models. The C-V log-log plots from the Kahang deposit show that there is a multifractal model for Cu and Mo. Correlation between the results of the C-V model and the chosen geological particulars show that the supergene enrichment zone has a high correlation within the chalcocite accumulations within the Kahang deposit. The main hypogene zone has an association with the chalcopyrite distribution model having Cu ≥ 0.42 wt.%. According to the correlation between results driven by fractal modelling and geological models by a logratio matrix, the main Cu and Mo mineralised zones generated by the C-V fractal model have a strong correlation with the potassic alteration zone with respect to the overall accuracy.

In this research, the D–V (Density–Volume) fractal model has been proposed to delineate rock mass characteristics. The results from the D–V fractal model have been correlated with the major rock types and validated against an RQD model. The D–V model has been successfully applied to model relationships between density values and volumes in the Kahang Cu–Mo porphyry deposit. The D–V log–log plot from the Kahang deposit indicates that there is a mono-fractal model which has a breakpoint in density of 2.7t/m^3.

Correlation between the results of D–V and RQD models reveals that the rock units with a higher density (>2.7t/m^3) are associated with RQD values > 70%. The final pit slope geometry and ultimate pit limit will depend on the economic evaluation of the ore body. An awareness of the spatial variability of parameters such as RQD and density can be used to assess the geotechnical characteristics of the rock mass. This can then be used to evaluate potential slope stability and be incorporated into a geotechnical risk model for the final pit geometry. Regions of high RQD may be targeted as offering greater potential for increased slope angles or locations for siting of critical haul roads. Regions of lower RQD should, where possible, be avoided for final pit limits. Further geotechnical characterisation will, however, be necessary to establish any potential influence of the 3D fracture network and presence of any major discontinuity-controlled instability.

The RQD-Volume (RQD-V) fractal model was used to investigate and delineate various RQD populations in the Kahang Cu-Mo porphyry deposit (Central Iran). The RQD-V fractal model illustrates four RQD populations in the deposit. The RQD threshold value for excellent rocks is 89.1% based on the fractal model as situated in the central and NW parts of the deposit. Models of good and fair rocks in the central, eastern and NW parts of the deposit contain 25.1–89.1% RQD according to the RQD-V model. Furthermore, the correlation between results driven by the fractal modelling and major lithological unit (PQD) in the Kahang deposit, rocks with excellent RQD defined by the means of the RQD-V model have a strong correlation with porphyritic quartz diorite shown by the 3D geological model.

The numbers of mining sequences (nested pits) were determined during optimisation studies using an exported dataset of the Cu-Mo block model shown by the means of the C-V fractal model. Furthermore, various combinations of nested pits (pit No.1 to pit No. 100) have been discussed and finally pit No. 92 was selected as the closure of the open pit mining of the Kahang deposit.

The need for copper especially in developing countries like Iran is of paramount importance therefore, the first choice of Cu block model considering all 48 boreholes is recommended due to the higher level of productivity in comparison to the second scenario, however the NPV of the second scenario is higher than the NPV of the deposit including all 48 boreholes. Therefore, a minable reserve exists in the pit consisting of all completed boreholes of 3,648,294 tonnes of sulphide ore which indicates the range of greater productivity compared to the final pit, ignoring the three isolated boreholes in the NW section of the studied deposit.

With respect to the C-V fractal model histograms, there is no major difference in terms of Cu average grades for either of the Cu block models however; there are remarkable differences between ore tonnage and the total voxel count considering the two block models as depicted in Table. 5. 10.

The PV-V and NPV-CTO fractal models have been proposed to delineate economic parameters. The voxels' values were classified according to the PV-V fractal model in the deposit which reveal that the open pit limit can be deeper if grid drilling can be developed.

Supporting that, the deposit sections in terms of elemental concentrations (Cu as the main target) is low within the initial years of excavation and it will be gradually upgraded at depth especially at plan level 2225 m in terms of Z direction (elevation) as depicted in the Fig. G. 2 of Appendix. G and Fig. 6. 6 of the Chapter 6. Consequently, the results obtained by the PV-V fractal model show that the majority of the orebody can be extracted by an underground mining operation. The threshold values obtained by the means of the PV-V fractal modelling suggest that the PV values have an increase from the north of the deposit to the south which can be used as an indicator for determination of the excavation orientation.

Open pit mine design and determination of mining orientation are a critically important part of a mining venture from mine development to mine closure and have a profound effect on the economic value of the mine. The most established and frequently employed practice to mine closure since the 1980s is based on the Lerch and Grossman three dimensional graph theory to determine the best mining sequence by which the mining operation (ore and waste excavation within the pit) will be terminated. However, the proposed NPV-CTO fractal model provided an analytical tool which can be used for determination of an OES for an open pit mine. The OES results via NPV Scheduler is much the same with the results obtained by the suggested model (Table. 6. 2) meaning that the NPV-CTO fractal can be implemented in the absence of optimisation software packages.

Since hydrological and geotechnical studies have not been undertaken in the study area, one is really forced to do such tests and experiments to calculate and evaluate the total gradient of the open pit mine's slope walls.

The necessity of reviewing the cut-off grade throughout the project lifetime and specifying the grade limit using optimisation models to increase the project NPV is highly recommended simultaneously with variations in the world metal commodity price.

Furthermore, the general geological observation and careful consideration of geological features of the Kahang deposit suggests that the mineralisation continues to the west and east and even also towards the Kahang village. As such a more comprehensive and systematic drilling programme is recommended in order to better characterise the Kahang deposit, which may correspondingly increase its estimated resource.

Mineral resource classification is important in uncertainty assessment and risk analysis. The Joint Ore Reserves Committee (JORC) is widely utilised for this purpose which classifies mineral resources as measured, indicated and inferred, depending on the degrees of confidence. Ore reserves are classified as proven and probable from either measured or indicated mineral resource. However; it is recommended for those who are interested in the area of this research to establish an innovative application based on the combination of geostatistical simulation (e.g., turning bands simulation) and fractal modelling for mineral resource classification.

An accurate description for geological domains which discriminates types of mineralogy, alteration and lithology is an important task in mineral resource and reserve evaluation. Deterministic models, based on drill hole data, define just one layout of these domains and do not consider uncertainty in a study area so they cannot measure uncertainty in the domain boundaries. However, stochastic models with respect to geostatistical simulation (especially plurigaussian) have distinctive power to assess uncertainty in the spatial layout of the domains which contribute to enhanced geological control for the quantitative variables of interest (e.g., porosity, permeability and concentration). Therefore, the use of a plurigaussian simulation is recommended to determine geological domains that control the grade distribution to obtain a final grade model for the Kahang deposit.

References

Afshooni, S.Z., Asadi Harooni, H., Esmaili, D., 2011. The microthermometry study of fluid inclusions in quartz veins of Kahang deposit (north eastern of Isfahan). 2nd National Symposium of Iranian Society of Economic Geology. Lorestan University, p. 144 (In Persian with English abstract).

Afshooni, S.Z., Esmaili, D., Asadi Harooni, H., 2010. The study of mineralography in Kahang exploration area (NE Isfahan). Geophysical Research Abstracts: EGU General Assembly, 13, p. 318.

Afshooni, S.Z., Mirnejad, H., Esmaeily, D., Asadi Haroni, H., 2013. Mineral chemistry of hydrothermal biotite from the Kahang porphyry copper deposit (NE Isfahan), Central Province of Iran. Ore Geology Reviews 54, 214–232.

Afzal, P., Ahari, H.D., Omran, N.R., Aliyari, F., 2013c. Delineation of gold mineralized zones using concentration–volume fractal model in Qolqoleh gold deposit, NW Iran. Ore Geology Reviews 55, 125–133.

Afzal, P., Alhoseini, S.H., Tokhmechi, B., Kaveh Ahangarana, D., Yasrebi A.B., Madani, N., Wetherelt, A., 2014. Outlining of high quality coking coal by concentration–volume fractal model and turning bands simulation in East-Parvadeh coal deposit, Central Iran. International Journal of Coal Geology 127, 88-99.

Afzal, P., Dadashzadeh Ahari, H., Rashidnejad Omran, N., Aliyari, F., 2013a. Delineation of gold mineralized zones using concentration–volume fractal model in Qolqoleh gold deposit, NW Iran. Ore Geology Reviews 55, pp. 125–133.

Afzal, P., Fadakar Alghalandis, Y., Khakzad, A., Moarefvand, P., Rashidnejad Omran, N., 2011. Delineation of mineralization zones in porphyry Cu deposits by fractal

concentration–volume modeling. Journal of Geochemical Exploration 108, 220–232.

Afzal, P., Fadakar Alghalandis, Y., Moarefvand, P., Rashidnejad Omran, N., Asadi Haroni, H., 2012. Application of power-spectrum–volume fractal method for detecting hypogene, supergene enrichment, leached and barren zones in Kahang Cu porphyry deposit, Central Iran. Journal of Geochemical Exploration 112, 131–138.

Afzal, P., Harati, H., Fadakar Alghalandis, Y., Yasrebi, A.B., 2013b. Application of spectrum–area fractal model to identify of geochemical anomalies based on soil data in Kahang porphyry-type Cu deposit, Iran. Chemie der Erde - Geochemistry 739 (4), 533-543.

Afzal, P., Khakzad, A., Moarefvand, P., Rashidnejad Omran, N., Esfandiari, B., Fadakar Alghalandis, Y., 2010. Geochemical anomaly separation by multifractal modeling in Kahang (Gor Gor) porphyry system. Central Iran. Journal of Geochemical Exploration 104, 34–46.

Agard, P., Omrani, J., Jolivet, L., Mouthereau, F., 2005. Convergence history across Zagros, Iran: constraints from collisional and earlier deformation. International Journal of Earth Sciences 94, 401–419.

Aghanabati, A., 2004. Geology of Iran. Geological Survey of Iran, 587 pp (In Persian).

Aghazadeh, M., Hou, Z., Badrzadeh, Z., Zhou, L., 2015. Temporal–spatial distribution and tectonic setting of porphyry copper deposits in Iran: Constraints from zircon U–Pb and Molybdenite Re–Os geochronology. Ore Geology Reviews 70, 385–406.

Agterberg, F.P., 2007. Mixtures of multiplicative cascade models in geochemistry. Nonlinear Processes in Geophysics 14, 201–209.

Agterberg, F.P., 2012. Multifractals and geostatistics. Journal of Geochemical Exploration 122, 113–122.

Agterberg, F.P., Cheng, Q., Brown, A., Good, D., 1996. Multifractal modeling of fractures in the Lac du Bonnet batholith, Manitoba. Computers and Geosciences 22 (5), 497–507.

Agterberg, F.P., Cheng, Q., Wright, D.F., 1993. Fractal modeling of mineral deposits. In: Elbrond, J., Tang, X. (Eds.), 24th APCOM symposium proceeding, Montreal, Canada, pp. 43–53.

Ahmadian, J., Haschke, M., McDonald, I., Regelous, M., Ghorbani, M., Emami, M., Murata, M., 2009. High magmatic flux during Alpine–Himalayan collision: constraints from the Kal-e-Kafi complex, central Iran. Geological Society of America Bulletin 121, 857–868.

Ahrens, L.H., 1954. The lognormal distribution of elements (a fundamental law of geochemistry and its subsidiary). Geochimica et Cosmochimica Acta 5, 49–73.

Ahrens, L.H., 1957. Lognormal-type distributions-III. Geochimica et Cosmochimica Acta 11, 205–212.

Akaike A., Dagdelen K., 1999. A strategic production scheduling method for an open pit mine. In: Proceedings of the 28th APCOM, Golden Colorado, USA, pp. 729-738.

Akbari, A.D., Osanloo, M., Shirazi, M.A., 2008. Determination of ultimate pit Limits in open Mines Using Real Option Approach. IUST International Journal of Engineering Science 19, 23–38.

Alavi, M., 1994. Tectonic of Zagros orogenic belt of Iran: new data and interpretations. Tectonophysics 229, 211-238.

Alavi, M., 2004. Regional stratigraphy of the Zagros folded-thrust belt of Iran and its proforeland evolution. American Journal of Science 304, 1-20.

Albanese, S., De Vivo, B., Lima, A., Cicchella, D., 2007. Geochemical background and baseline values of toxic elements in stream sediments of Campania region (Italy). Journal of Geochemical Exploration 93, 21–34.

Ali, K., Cheng, Q., Zhijun, C., 2007. Multifractal power spectrum and singularity analysis for modelling stream sediment geochemical distribution patterns to identify anomalies related to gold mineralization in Yunnan Province, South China. Geochemistry: Exploration, Environment, Analysis 7 (4), 293–301.

Alpers, C.N., Brimhall, G.H., 1989. Paleohydrologic evolution and geochemical dynamics of cumulative supergene metal enrichment at La Escondida, Atacama Desert, Northern Chile. Economic Geology 84, 229–255.

Amit, K., Chatterjee, D., Jacks, G., 2014. Shallow hydrostratigraphy in an arsenic affected region of Bengal Basin: Implication for targeting safe aquifers for drinking water supply. Science of the Total Environment 485–486, 12–22.

Armstrong, D., 1990. Definition of Mining Parameters. In Surface Mining, 2nd Edition (Ed. B.A. Kennedy), Littleton: Society for Mining, Metallurgy and Exploration, Inc. pp. 459–464.

Armstrong, M., Boufassa, A., 1988. Comparing the robustness of ordinary kriging and lognormal kriging: outlier resistance. Mathematical Geology 20 (4), 447–457.

Armstrong, M., Galli, A., 2012. New approach to flexible open pit optimisation and scheduling. Mining Technology 121 (3), 132-138.

Asad, M.W.A., Dimitrakopoulos, R., 2013. Implementing a parametric maximum flow algorithm for optimal open pit mine design under uncertain supply and demand. Journal of the Operational Research Society 64, 185-197.

Asadi, H., Kianpouryan, S., Lu, Y., McCuaig, T.C., 2014. Exploratory data analysis and C-A fractal model applied in mapping multi-element soil anomalies for drilling: A case study from the Sari Gunay epithermal gold deposit, NW Iran. Journal of Geochemical Exploration 145, 233–241.

Asadi, H., Porwal, A., Fatehi, M., Kianpouryan, S., Lua, Y.J., 2015. Exploration feature selection applied to hybrid data integration modeling: Targeting copper-gold potential in central Iran. Ore Geology Reviews (In Press, Corrected Proof).

Asadi, S., Moore, F., Zarasvandi, A., 2014. Discriminating productive and barren porphyry copper deposits in the southeastern part of the central Iranian volcano-plutonic belt, Kerman region, Iran: A review. Earth-Science Reviews 138, 25–46.

Asghari, O., Hezarkhani, A., 2008. Applying discriminant analysis to separate the alteration zones within the Sungun porphyry copper deposit. Asian Journal of Applied Sciences 8 (24), 4472—4486.

Asghari, O., Hezarkhani, A., Soltani, F., 2009. The comparison of alteration zones in the Sungun porphyry copper deposit, Iran (based on fluid inclusion studies). Acta Geologica Polonica 59 (1), 93–109.

Asghari, O., Madani Esfahani, N., 2013. A new approach for the geological risk evaluation of coal resources through a geostatistical simulation Case study: Parvadeh III coal deposit. Arabian Journal of Geosciences 6, 957-970.

Askari-Nasab, H., Pourrahimian, Y., Ben-Awuah, E., Kalantari, S., 2011. Mixed integer linear programming formulations for open pit production scheduling. Journal of Mining Science 47, 338-359.

Ataei, M., Osanloo, M., 2003. Methods for Calculation of Optimal Cutoff Grades in Complex Ore Deposits. Journal of Mining Science 39 (5), 499-507.

Atapour, H., Aftabi, A., 2007. The geochemistry of gossans associated with Sarcheshmeh porphyry copper deposit, Rafsanjan, Kerman, Iran: Implications for exploration and the environment. Journal of Geochemical Exploration 93 (1), 47–65.

Awadelseid, S.F., Xie, S., Bao, Z., Lei, L., Pan, F., Xu, D., Abdel Rahman, A.A., 2015. Multifractal distribution of geochemical elements in Dexing porphyry copper deposit, Jiangxi Province, China. Journal of Geochemical Exploration 149, 30–42.

Ayati, F., Yavuz, F., Noghreyan, M., Asadi Haroni, H., Yavuz, R., 2008. Chemical characteristics and composition of hydrothermal biotite from the Dalli porphyry copper prospect, Arak, central province of Iran. Mineralogy and Petrology 94, 107–122.

Azadi, M., Mirmohammadi, M., Hezarkhani, A., 2014. Aspects of magmatic–hydrothermal evolution of Kahang porphyry copper deposit, Central Iran. Arabian Journal of Geosciences, DOI 10.1007/s12517-014-1528-2.

Baecher, G.B., Lanney, N.A., Einstein, H.H., 1977. Statistical description of rock properties and samples. In: Proceedings of 18th US Symposium on Rock Mechanics, Colorado, USA, pp. 5c1-5c8.

Bastante, F.G., Taboada, J., Alejano, L., Alonso, E., 2008. Optimization tools and simulation methods for designing and evaluating a mining operation .Stochastic Environmental Research and Risk Assessment 22, 727–735.

Beane, R.E., 1982. Hydrothermal alteration in silicate rocks. In: Titley, S.R. (Ed.), Advances in Geology of the Porphyry Copper Deposits, Southwestern North America. The University of Arizona Press, Tucson, pp. 117–137.

Beane, R.E., Titley, S.R., 1981. Porphyry copper deposits, Part II: Hydrothermal alteration and mineralization. Economic Geology 75, 235-269.

Behrens, J.T., 1997. Principles and Procedures of Exploratory Data Analysis. Psychological Methods 2, 131–160.

Berberian, M., King, G.C.P., 1981. Towards a palaeogeography and tectonic evolution of Iran. Canadian Journal of Earth Sciences 18, 210-265.

Berberian, F., Muir, I.D., Pankhurst, R.J., Berberian, M., 1982. Late Cretaceous and Early Miocene Andean-type plutonic activity in northern Makran and Central Iran. Journal of the Geological Society of London 139, 605-614.

Berger, B., Ayuso, R., Wynn, J., Seal, R., 2008. Preliminary Model of Porphyry Copper Deposits. U.S. Geological Survey Open-File Report 2008, Reston, Virginia, 20–55.

Bernabe, D., 2001. Comparative analysis of open pit mine scheduling techniques for strategic mine planning of a copper mine in Southern Peru. M.Sc. Thesis, Colorado School of Mines, Golden CO.

Bieniawski, Z.T., 1984. Rock Mechanics Design in Mining and Tunnelling, Balkema publisher, Rotterdam, 272 pp.

Boadu, F.K., Long, LT., 1994. The fractal character of fracture spacing and RQD. International Journal of Rock Mechanics and Mineral Science- Geomechanics Abstracts 31, 127–134.

Bölviken, B., Stokke, P.R., Feder, J., Jössang, T., 1992. The fractal nature of geochemical landscapes. Journal of Geochemical Exploration 43 (2), 91–109.

Bond, G., 1995. A mathematical analysis of the Lerchs and Grossmann algorithm and the nested Lerch and Grossmann algorithm, Ph.D. Dissertation, Colorado School of Mines, Golden, USA.

Bondy, J.A., Murty, U.S.R., 1976. Graph Theory with Applications. Macmillan, The University of California.

Boomeri, M., Nakashima, K., Lentz, D.R., 2009. The Miduk porphyry Cu deposit, Kerman, Iran: A geochemical analysis of the potassic zone including halogen element systematics related to Cu mineralization processes. Journal of Geochemical Exploration 103 (1), 17-19.

Caccetta, L., Giannini, L., 1986. Optimisation Techniques for the Open Pit Limit Problem. In: Proceedings of Australian Institute of Mining and Metallurgy 291 (8), pp. 57-63.

Caccetta, L., Giannini, L.M., 1988. An application of discrete mathematics in the design of an open pit mine. Discrete Applied Mathematics 21 (1), 1–19.

Cairns, R.D., Shinkuma, T., 2003. The choice of the cut-off grade in mining. Resources Policy 29, 75–81.

Carranza, E.J.M., 2008. Geochemical anomaly and mineral prospectivity mapping in GIS. Handbook of Exploration and Environmental Geochemistry, Vol. 11. Elsevier, Amsterdam. 351 pp.

Carranza, E.J.M., 2009. Controls on mineral deposit occurrence inferred from analysis of their spatial pattern and spatial association with geological features. Ore Geology Reviews 35, 383–400.

Carranza, E.J.M., 2011. Analysis and mapping of geochemical anomalies using logratio-transformed stream sediment data with censored values. Journal of Geochemical Exploration 110, 167—185.

Carranza, E.J.M., Owusu, E., Hale, M., 2009. Mapping of prospectivity and estimation of number of undiscovered prospects for lode-gold, south western Ashanti Belt, Ghana. Mineralium Deposita 44 (8), 915–938.

Carranza, E.J.M., Sadeghi, M., 2010. Predictive mapping of prospectively and quantitative estimation of undiscovered VMS deposits in Skellefte district (Sweden). Ore Geology Reviews 38, 219–241.

Carrasco, P., Carrasco, P., Jara, E., 2004. The economic impact of correct sampling and analysis practices in the copper mining industry. Chemometrics Intelligent Laboratory Systems 74, 209–213.

Carvalho, J.L., Carter, T.G., Diederichs, M.S., 2007. An approach for prediction of strength and post yield behaviour for rock masses of low intact strength. Rock Mechanics: Meeting Society's Challenges and Demands, In: Proceedings of the 1st Canada-US Rock Mechanics Symposium, Vancouver, Canada, pp. 277-285.

Cheng, Q., 1999. Spatial and scaling modelling for geochemical anomaly separation. Journal of Geochemical Exploration 65 (3), 175–194.

Cheng, Q., 2007. Mapping singularities with stream sediment geochemical data for prediction of undiscovered mineral deposits in Gejiu, Yunnan Province, China. Ore Geology Review 32, 314–324.

Cheng, Q., 2012. Singularity theory and methods for mapping geochemical anomalies caused by buried sources and for predicting undiscovered mineral deposits in covered areas. Journal of Geochemical Exploration 122, 55–70.

Cheng, Q., Agterberg, F.P., 1996. Multifractal modeling and spatial statistics. Mathematical Geology 28 (1), 1–16.

Cheng, Q., Agterberg, F.P., 2009. Singularity analysis of ore-mineral and toxic trace elements in stream sediments. Computers and Geosciences 35 (2), 234–244.

Cheng, Q., Agterberg, F.P., Ballantyne, S.B., 1994. The separation of geochemical anomalies from background by fractal methods. Journal of Geochemical Exploration 51, 109–130.

Clark, I., 1999. A case study in the application of geostatistics to lognormal and quasi-lognormal problems. 28th International Symposium on Application of Computers and Operations Research in the Mineral Industry. Colorado School of Mines, CSM, 407–416.

Coghill, P., Miljak, D., Williams, E., 2014. Consequences of fractal grade distribution for bulk sorting of a copper porphyry deposit. Geoscience Frontiers (In Press, Corrected Proof).

Costa Lima, G.A., Suslick, S.B., 2006. Estimating the volatility of mining projects considering price and operating cost uncertainties. Resources Policy 31, 86–94.

Cox, D., Singer, D., 1986. Mineral deposits models. U.S. geological survey bulletin. 1693 pp.

Cressie, N., 1993. Statistics for spatial data, John Wiley & Sons, New York, 900 pp.

Dagdelen, K., Mohammed, W.A.A., 1997. Multi mineral cutoff grade optimization with option to stockpile. In: Proceedings of the SME Annual Meeting, Society for Mining, Metallurgy and Exploration Inc., Littleton, CO, pp. 1–12.

Dargahi, S., Arvin, M., Pan, Y., Babaei, A., 2010. Petrogenesis of Post-Collisional A-type granitoid from the Urumieh-Dokhtar magmatic assemblage, Southwestern Kerman, Iran: Constraints on the Arabian- Eurasian continental collision. Lithos 115, 190-204.

Darnley, A.G., Bjorklund, B., Gustavsson, N., Koval, P.V., Plant, J., Steenfelt, A., Tauchid, T.M., Xie, X.J., 1995. A global geochemical database for environmental and resource management. Recommendations for international geochemical mapping. Earth Sciences Report 19. UNESCO Publishing, Paris.

Darwen, P.J., 2001. Genetic algorithms and risk assessment to maximize NPV with robust open-pit scheduling. Fourth biennial conference on strategic mine planning, pp. 29–34.

Das, M., Edgar, G.A., 2005. Separation properties for graph-directed self-similar fractals. Topology and its Applications 152 (1–2), 138–156.

David. M., 1970. Geostatistical Ore Reserve Estimation, Elsevier, Amsterdam, 283 pp.

Davies, T.C., Mundalamo H.R., 2010. Environmental health impacts of dispersed mineralisation in South Africa, Journal of African Earth Sciences 58, 652–666.

Davis. B., 1987. Uses and abuses of cross validation in geostatistics. Mathematical Geology 19 (3), 241-48.

Davis. J.C., 2002. Statistics and Data Analysis in Geology, 3th ed. John Wiley & Sons Inc, New York.

Deere, D.U., Deere, D.W., 1989. Rock Quality Designation (RQD) After Twenty Years. U.S. Army Engineer Waterways Experiment Station Publisher, 34 pp.

Deere, D.U., Miller, R.P., 1966. Engineering classification and index properties for intact rock. Air Force Weapons Laboratory Technical Report AFWL-TR-65-116, 277 pp.

Demetriades, A., 2014. Basic Considerations: Sampling, the Key for a Successful Applied Geochemical Survey for Mineral Exploration and Environmental Purposes. Reference Module in Earth Systems and Environmental Sciences 15: Analytical Geochemistry/Inorganic INSTR. Analysis, 1–31.

Dershowitz, W.S., Einstein, H.H., 1988. Characterizing rock joint geometry with joint system models. Rock Mechanics and Rock Engineering 21, 21–51.

Deutsch, C., Journel, A.G., 1998. GSLIB: Geostatistical Software Library and User's Guide Second Edition. Oxford University Press, New York.

Dewey, J.F., Pitman, W.C., Ryan, W.B., Bonnin, J., 1973. Plate tectonics and the evolution of the Alpine system. Geological Society of America Bulletin 84, 3137–3180.

Dimitrakopoulos, R., Farrelly, C.T., Godoy, M., 2002. Moving forward from traditional optimization: grade uncertainty and risk effects in open-pit design. Mining Technology 111 (A), 82–8.

Dimitrakopoulos, R., Martinez, L., Ramazan, S., 2007. A maximum upside/minimum downside approach to the traditional optimization of open pit mine design. Journal of Mining Science 43, 73–82.

Dincer, T., 2001. Application of Pit Optimisation Algorithms beyond Open Pit Limits. 17th International Mining Congress and Exhibition of Turkey- IMCET 2001, ISBN 975-395, 417–4.

Dowd, P., 1994. Risk assessment in reserve estimation and open pit planning. Transactions of the Institution of Mining and Metallurgy 103, A148–A154.

Dowd, P.A., Onur, A.H., 1992. Optimizing open pit design and scheduling. 23rd APCOM symposium, 411-422.

Dowd, P., Onur, A., 1993. Open pit optimisation: I. Optimal open pit design. Transactions of the American Institute of Mining and Metallurgical Engineers, A94–A104.

Efron, B., 1982. The Jackknife, the Bootstrap, and other Resampling Plans. Society for Industrial and Applied Math, Philadelphia.

Ehlen, J., 2000. Fractal analysis of joint patterns in granite. International Journal of Rock Mechanics and Mining Sciences 37, 909-922.

Elkington, T., Durham, R., 2011. Integrated open pit pushback selection and production capacity optimization. Journal of Mining Science 47 (2), 177-190.

Emery, X., 2012. Análisis estadístico de datos. FACULTAD DE CIENCIAS, FISICAS Y MATEMATICAS, UNIVERSIDAD DE CHILE, 30 pp (In Spanish).

Emery, X., Ortiz, J.M., 2005. Histogram and variogram inference in the multi Gaussian model. Stochastic Environmental Research and Risk Assessment 19 (1), 48–58.

Emery, X., Ortiz, J.M., 2011. Two approaches to direct block-support conditional co-simulation. Computers & Geosciences 37 (8), 1015–1025.

Englund, E.J., Weber, D.D., Leviant, N., 1992. The effects of sampling design parameters on block selection. Mathematical Geology 24, 29–343.

Eslamian, S., 2014. Handbook of Engineering Hydrology: Fundamentals and Applications. CRC Press, 218 pp.

Evertz, C.J.G., Mandelbrot, B.B., 1992. Multifractal measures (appendix B). In: Peitgen, H. O., Jurgens, H., Saupe, D. (Eds.), Chaos and Fractals. Springer, New York.

Falconer, K., 1991. Fractals. Non-Integral Dimensions and Applications, G. Gherbit (Ed.), John Wiley, New York, 249. Endeavour 15 (2), 95 pp.

Falconer, K., Hu, J., 2001. Nonlinear Diffusion Equations on Unbounded Fractal Domains. Journal of Mathematical Analysis and Applications 256 (2), 606–624.

Fisher, R. A., Tippett, L. H. C., 1928. Limiting forms of the frequency distribution of the largest or smallest member of a sample. In: Mathematical Proceedings of the Cambridge Philosophical Society 24(2), pp. 180-190.

Fletcher, W.K., 1981. Analytical methods in geochemical exploration. G.J.S. Govett (Editor), Handbook of Exploration Geochemistry 1, Elsevier, Amsterdam, 25-46.

Frangois-Bongarcon, D., Guidal, D., 1982. Algorithms for parametrizing reserves under different geometrical constraints. In: T.B. Johnson and R.J. Barnes (Eds.), Proceedings of 17th APCOM Symposium, Society of Mining and Engineering. AIME, New York, NY, pp. 297-309.

Franke, R., 1982. Scattered data interpolation: tests of some methods. Mathematics of Computation 38, 181–200.

Gałuszka, A., 2007. A review of geochemical background concepts and an example using data from Poland. Environmental Geology, 52, 861–870.

Godoy, M.C., Dimitrakopoulos, R., 2004. Managing risk and waste mining in long-term production scheduling. SME Transactions, 316 pp.

Goncalves, M.A., Mateus, A., Oliveira, V., 2001. Geochemical anomaly separation by multifractal modeling. Journal of Geochemical Exploration 72, 91–114.

Goodwin, G.C., Seron, M.M., Mayne, D.Q., 2008. Optimization opportunities in mining, metal and mineral processing. Annual Reviews in Control 32, 17–32.

Goovaerts, P., 1997. Geostatistics for Natural Resources Evaluation. Oxford University Press, New York, 496 pp.

Grenon, M., Hadjigeorgiou, J., 2010. Integrated structural stability analysis for preliminary open pit design. International Journal of Rock Mechanics and Mining Sciences 47 (3), 450–460.

Gu, X.W., Wang, Q., Chu, D.Z., Zhang, B., 2010. Dynamic optimization of cutoff grade in underground metal mining. Journal of Central South University of Technology 17 (3), 492-497.

Halsey, T.C., Jensen, M.H., Kadanoff, L.P., Procaccia, I., Shraiman, B.I., 1986. Fractal measures and their singularities: the characterization of strange sets. Physical Review, A 33 (2), 1141–1151.

Hamdi, E., Mouza, JD., 2005. A methodology for rock mass characterisation and classification to improve blast results. International Journal of Rock Mechanics and Mining Sciences 42, 177–94.

Harati, H., Khakzad, A., Rashidnejad Omran, N., Afzal, P., Hosseini, M., Harati, S., 2013. Identifying Hydrothermal Alteration: Geochemical Particulars based on Lithogeochemical Data from the Kahang Cu Porphyry Deposit, Central Iran. Iranian Journal of Earth Sciences 5, 1-12.

Harrison, J.P., 1999. Selection of the threshold value in RQD assessments. International Journal of Rock Mechanics and Mining Sciences 36, 673-685.

Hartley, A.J., Rice, C.M., 2005. Controls on supergene enrichment of porphyry copper deposits in the Central Andes—A review and discussion: Mineralium Deposita 40, 515–525.

Hassanpour, S., Afzal, P., 2013. Application of concentration–number (C–N) multifractal modeling for geochemical anomaly separation in Haftcheshmeh porphyry system, NW Iran. Arabian Journal of Geosciences 6 (3), 957–970.

Hawkes, H.E., Webb, J.S., 1962. Geochemistry in Mineral Exploration. Harper and Row, New York.

He, Y., Zhu, K., Gao, S., Liu, T., Li, Y., 2009. Theory and method of genetic-neural optimizing cut-off grade and grade of crude ore. Expert Systems with Applications 36 (4), 7617–7623.

Heidari, S.M., Ghaderi, M., Afzal, P., 2013. Delineating mineralized phases based on lithogeochemical data using multifractal model in Touzlar epithermal Au–Ag (Cu) deposit, NW Iran. Applied Geochemistry 31, 119–132.

Hejazi, M., 2005. Geometry in nature and Persian architecture. Building and Environment 40, 1413–1427.

Hitzman, M.W., Oreskes, N., Einaudi, M.T., 1992. Geological characteristics and tectonic setting of Proterozoic iron oxide (Cu-U-Au-REE) deposits. Precambrian Research 58, 241-287.

Hochbaum, D.S., Chen, A., 2000. Performance analysis and best implementations of old and new algorithms for the open-pit mining problem. Operations Research 48, 894–913.

Homayoon, SR., Keshavarzi, A., Gazni, R., 2010. JSEA Application of artificial neural network, kriging, and inverse distance weighting models for estimation of scour depth around bridge pier with bed sill. Journal of Software Engineering and Applications 3, 944–964.

Howarth, R.J., Thompson, M., 1976. Duplicate analysis in geochemical practice, Part II. Analyst 101, 699-709.

Hustrulid, W., Kuchta, M., 2006. Open Pit Mine Planning and Design. Taylor & Francis.

Isaaks, E., Srivastava. R., 1989. An Introduction to Applied Geostatistics. Oxford University Press, New York.

Jinga, L., Hudson, J.A., 2002. Numerical methods in rock mechanics. International Journal of Rock Mechanics and Mining Sciences 39, 409–427.

Johnson, T B., 1968. Optimum open pit mine production scheduling in mining engineering, University of California: Berkley, 120 pp.

Juan, P., Mateu, J., Jordan, M.M., Mataix-Solera, J., Meléndez-Pastor, I., Navarro-Pedreño, J., 2011. Geostatistical methods to identify and map spatial variations of soil salinity. Journal of Geochemical Exploration 108, 62–72.

Julia, G., 1959. Éléments d'algèbre. Gauthier-Villars, Paris, 1-207 (In French).

Journel, A., 1993. Geostatistics: roadblocks and challenges, In A. Soares, (Ed.), Geostatistics-Troia, pp. 213-224.

Journel, A.G., Huijbregts, Ch. J., 1978. Mining Geostatistics, Virginia, Academic Press, 600 pp.

Kalenchuk, K.S., Diederichs, M.S., McKinnon, S., 2006. Characterizing block geometry in jointed rock masses. International Journal of Rock Mechanics and Mining Sciences 43, 1212–25.

Kazi, A., Sen, Z., 1985. Volumetric RQD: an index of rock quality, in Fundamentals of rock joints. In Stephansson (Ed.), Centek Publisher, Sweden. pp. 95-101.

Khayrollahi, H., 2003. The Investigation of Mass Transfer and Element Mobility within the Sar-Cheshmeh Copper Mine Alteration Zones. (MSc Thesis) Amirkabir University of Technology, 145 pp.

King, B., 2011. Optimal mining practice in strategic planning. Journal of Mining Science 47 (2), 247-253.

Kirkham, R.V., Dunne, K.P., 2000. World distribution of porphyry, porphyry-associated skarn, and bulk-tonnage epithermal deposits and occurrences. Geological Survey of Canada 3792, 1–26.

Koenigsberg, E., 1982. The optimum contours of an open pit mine: an application of dynamic programming. In: T.B. Johnson and R.J. Barnes (Eds.), Proceedings of 17th

APCOM Symposium, Society of Mining and Engineering. AIME, New York, NY, pp. 274-287.

Krautkraemer, J.A., 1988. The cut-off grade and the theory of extraction. Canadian Journal of Economics 21 (1), 146–160.

Krige, D.G., 1966. A study of gold and uranium distribution patterns in the Klerksdorp goldfield. Geoexploration 4, 43–53.

Lam, N.S., 1983. Spatial interpolation methods: A review. American Cartographer 10, 129–149.

Lane, K.F., 1964. Choosing the optimum cut-off grade. Quarterly of the Colorado School of Mines, Golden, USA, pp. 811–829.

Lauwerier, H., 1991. Fractals: Images of Chaos. Princeton University Press, New Jersey. 240 pp.

Laznicka, P., 2005. Giant Metallic Deposits Future Sources of Industrial Metals. Springer-Verlag. 732 pp.

Lerch, H., Grossmann, I.F., 1965. Optimum design of open-pit mines. Canadian Institute of Mining and Metallurgy 58, 47–54.

Li, C., Ma, T., Shi, J., 2003. Application of a fractal method relating concentrations and distances for separation of geochemical anomalies from background. Journal of Geochemical Exploration 77, 167–175.

Lima, A., Albanese, S., Cicchella, D., 2005. Geochemical baselines for the radioelements K, U, and Th in the Campania region, Italy: a comparison of stream–sediment geochemistry and gamma-ray surveys. Journal of Geochemical Exploration 20, 611–625.

Lima, A., De Vivo, B., Cicchella, D., Cortini, M., Albanese, S., 2003. Multifractal IDW interpolation and fractal filtering method in environmental studies: an application on regional stream sediments of (Italy), Campania region. Applied Geochemistry 18, 53–65.

Lima, A., Plant, J.A., Vivo, B.D., Tarvainen, T., Albanese, S., Cicchella, D., 2008. Interpolation methods for geochemical maps: a comparative study using arsenic data from European stream waters. Geochemistry: Exploration, Environment, Analysis 8, 41–48.

Limpert, E., Stahel,W.A., Abbt,M., 2001. Lognormal distributions across the sciences: keys and clues. Bioscience 51 (5), 341–352.

Lina, J.S., Kub, C.Y., 2006. Two-scale modeling of jointed rock masses. International Journal of Rock Mechanics and Mining Sciences 43, 426-436.

Little, M., 2006. The benefit to open pit rock slope design of geotechnical databases. In: Proceedings of international symposium on stability of rock slopes in open pit mining and civil engineering. SAIMM, pp. 97–116.

London Metal Exchange, 2015a. LME Copper. https://www.lme.com/metals/non-ferrous/copper/.

London Metal Exchange, 2015b. LME Molybdenum. https://www.lme.com/metals/minor-metals/molybdenum/.

Lowell, J.D., 1968. Geology of the Kalamazoo orebody, San Manuel district, Arizona. Economic Geology 63, 645—654.

Lowell, J.D., Guilbert, J.M., 1970. Lateral and vertical alteration-mineralization zoning in porphyry ore deposits. Economic Geology 65, 373–408.

Luz, F., Mateus, A., Matos, J.X., Gonçalves,M.A., 2014. Cu- and Zn-Soil Anomalies in the NE Border of the South Portuguese Zone (Iberian Variscides, Portugal) Identified by Multifractal and Geostatistical Analyses. Natural Resources Research 23, 195–215.

Madani Esfahani, N., Asghari, O., 2013. Fault detection in 3D by sequential Gaussian simulation of Rock Quality Designation (RQD), Arabian Journal of Geosciences 6, 3737–3747.

Makkonen, H., Mäkinen, J., Kontoniemi, O., 2008. Geochemical discrimination between barren and mineralized intrusions in the Svecofennian (1.9 Ga) Kotalahti Nickel Belt, Finland. Ore Geology Reviews 33, 101–114.

Mandelbrot, B.B., 1983. The Fractal Geometry of Nature. W.H. Freeman, San Francisco, CA. Updated and Augmented Edition.

Marcotte, D., Caron, J., 2013. Ultimate open pit stochastic optimization. Computers & Geosciences 51, 238–246.

Mart, W.S., Markey, G., 2013. Intelligent Mining Software "Solutions" IMS - Lerch-Grossman Pit Optimization. MineMap Pty Ltd.

McInnes, B.I.A., Evans, N.J., Fu, F.Q., Garwin, S., Belousova, E., Griffin, W.L., Bertens, A., Sukama, D., Permanadewi, S., Andrew, R.L., Deckart, K., 2005. Thermal history analysis of selected Chilean, Indonesian, and Iranian porphyry Cu–Mo–Au deposits. In: Porter, T.M. (Ed.), Super Porphyry Copper and Gold Deposits: A Global Perspective. PGC publishing, Adelaide. pp 1–16.

Meagher, C., Avis, D., Dimitrakopoulos, R., 2010. The Direct Cut Polytope, Integrality and Triangular Elimination: Theoretical developments for mining optimization problems, COSMO Research Report no. 5, 64-88.

Melfos, V., Vavelidis, M., Christo des, G., Seidel, E., 2002. Origin and evolution of the Tertiary Maronia porphyry copper-molybdenum deposit, Thrace, Greece. Mineralium Deposita 37, 648—668.

Meyer, C., Hemley, J. J., 1967. Wall rock alteration in barnes. H. L. (Ed.) Geochemistry of hydrothermal ore deposits, Holt, Reinhart and winston, New York. pp. 166-235.

Meyer, T., Einstein, H.H., 2002. Geologic stochastic modelling and connectivity assessment of fracture systems in the Boston area. Rock Mechanics and Rock Engineering 35, 23–44.

Mihalasky, M.J., Bookstrom, A.A., Frost, T.P., Ludington, S., with contributions from Logan, J.M., Panteleyev, A., Abbot, G., 2011, revised 2013. Porphyry copper assessment of British Columbia and Yukon Territory, Canada: U.S. Geological Survey Scientific Investigations Report 2010-5090-C, v. 1.1, 128 pp.

Milne, D., 2007. Rock mass classification challenges. Rock Mechanics: Meeting Society's Challenges and Demands, In: Proceedings of the 1st Canada-US Rock Mechanics Symposium, Vancouver, Canada, pp. 191-197.

Mirnejad, H., Mathur, R., Einali, M., Dendas, M., Alirezaei, S., 2010. A comparative copper isotope study of porphyry copper deposits in Iran. Geochemistry: Exploration, Environment, Analysis 10, 413–418.

Monecke, T., Gemmell, J.B., Monecke, J., 2001. Fractal distributions of veins in drill core from the Hellyer VHMS deposit, Australia: constraints on the origin and evolution of the mineralising system. Mineralium Deposita 36 (5), 406-415.

Monecke, T., Monecke, J., Herzig, P.M., Gemmell, J.B., Monch, W., 2005. Truncated fractal frequency distribution of element abundance data: a dynamic model for the metasomatic enrichment of base and precious metals. Earth and Planetary Science Letters 232, 363–378.

Montiel, L., Dimitrakopoulos, R., 2013. Stochastic mine production scheduling with multiple processes: Application at Escondida Norte, Chile. Journal of Mining Science 49 (4), 583-597.

Nash, J.T., 1976. Fluid inclusion petrology-data from porphyry copper deposits and applications to exploration. Geological Survey Professional Paper 907-D, 1—16.

Neimark, J.I., 2003. Mathematical Models in Natural Science and Engineering: An Example-Based Approach. Springer Science & Business Media Publisher, Berlin-Germany.

Nematzadeh, M.R., 2015. Speech of minister of Industries, Mines and Commerce of Iran at the Parliament. www.dolat.ir/NSite/FullStory/Cabine/?Serv=0&Id=208570 (Government Information Centre: In Persian).

NPV – Scheduler. 2001. Tutorial of Earthworks NPV-Scheduler software version 3.4. Copyright @ 2001 Mineral Industries Computing Ltd.

Olea, R.A., 2007. Declustering of clustered preferential sampling for global histogram and semi variogram inference. Mathematical Geology 39(5), 453–467.

Oliveira Neto, M., 2006. Pythagoras' celestial spheres in the context of a simple model for quantization of planetary orbits. Chaos, Solitons and Fractals 30, 399–406.

Ortega, O.J., Marrett, R., Laubach, S.E., 2006. A scale-independent approach to fracture intensity and average fracture spacing. American Association of Petroleum Geologists Bulletin 90 (2), 193–208.

Osanloo, M., Ataei, M., 2003. Using equivalent grade factors to find the optimum cut-off grades of multiple metal deposits. Minerals Engineering 16, 771–776.

Osanloo, M., Gholamnejad, J., Karimi, B., 2008a. Long-term open pit mine production planning: a review of models and algorithms. International Journal of Mining, Reclamation and Environment 22, 3–35.

Osanloo, M., Rashidinejad, F., Rezai, B., 2008b. Incorporating environmental issues into optimum cut-off grades modeling at porphyry copper deposits. Resources Policy 33, 222–229.

Palmstrom, A. 1985. Application of the volumetric joint count as a measure of rock mass jointing, in Fundamentals of rock joints. In Stephansson (Ed.), Centek Publisher, Sweden. pp. 103-109.

Palmstrom, A., 2005. Measurements of and Correlations between Block Size and Rock Quality Designation (RQD). Tunnels and Underground Space Technology 20, 362-377.

Panahi, A., Cheng, Q., Bonham-Carter, G.F., 2004. Modelling lake sediment geochemical distribution using principal component, indicator kriging and multifractal power spectrum analysis: a case study from Gowanda, Ontario. Exploration, Environment, Analysis 4, 59–70.

Parhizkar, A., Ataei, M., Moarefvand, P., Rasouli, V., 2011. Grade uncertainty and its impact on ore grade reconciliation between the resource model and the mine. Archives of Mining Sciences 56119–134.

Parhizkar, A., Ataei, M., Moarefvand, P., Rasouli, V., 2012. A probabilistic model to improve reconciliation of estimated and actual grade in open-pit mining. Arabian Journal of Geosciences 5 (6), 1279-1288.

Picard, J. C., 1976. Maximal closure of a graph and applications to combinatorial problems. Management Science 22, 1268–1272.

Pirajno, F., 2009. Hydrothermal processes and mineral system: Vol. 1, Springer, 1250 pp.

Priest, S.D., Hudson, J.A., 1976. Discontinuity spacing in rock. International Journal of Rock Mechanics and Mining Sciences- Geomechanics Abstracts 13, 135-148.

Plant, J., Smith, D., Smith, B., Williams, L., 2001. Environmental geochemistry at the global scale. Applied Geochemistry 16, 1291–1308.

Popov, K.P., Ruskov, K.I., Georgiev, G.I., 2003. 3D Geostatistical model of the ore body in Elatsite porphyry copper deposit, Panagyurishte ore region. 50 years University of Mining and Geology "St. Ivan Rilski" Annual 46 (I), Geology and Geophysics, Sofia, 113-118.

Rafiee, A., Vinches, M., 2008. Application of geostatistical characteristics of rock mass fracture systems in 3D model generation. International Journal of Rock Mechanics and Mining Sciences 45, 644–52.

Ramazan, S., 2007. The new Fundamental Tree Algorithm for production scheduling of open pit mines, European Journal of Operational Research 177, 1153–1166.

Razique, A., Lo Grasso, G., Livesey, T., 2007. Porphyry Copper–Gold Deposits at Reko
    Diq Complex, Chagai Hills Pakistan. In: Proceedings of Ninth Biennial SGA Meeting,
    Dublin, pp. 1–7.

Reimann, C., Filzmoser, P., 2000. Normal and lognormal data distribution in
    geochemistry: death of a myth. Consequences for the statistical treatment of
    geochemical and environmental data. Environmental Geology 39, 1001–1014.

Richards, J.P., Spell, T., Rameh, E., Razique, A., Fletcher, T., 2012. High Sr/Y magmas
    reflect arc maturity, high magmatic water content, and porphyry Cu ± Mo ± Au
    potential: examples from the Tethyan arcs of Central and Eastern Iran and Western
    Pakistan. Economic Geology 107, 295–332.

Richmond, A., 2002. Two-point declustering for weighting data pairs in experimental
    variogram calculations. Computers & Geosciences 28,231–241.

Robb, L., 2005. Introduction to Ore-forming processes, Blackwell Science Ltd, 325 pp.

RockWorks 15 by RockWare®, Inc. 2010. Tutorial of RockWorks 15™, Third edition.

Roedder, E., 1971. Fluid inclusion studies on the porphyry-type ore deposits at Bingham,
    Utah, Butte, Montana, and Climax, Colorado. Economic Geology 66, 98—120.

Rouleau, A., Gale, J.E., 1985. Statistical characterisation of fracture system in the Stripa
    Granite, Sweden. International Journal of Rock Mechanics and Mining Sciences-
    Geomechanics Abstracts 22(6), 353-367.

Sadeghi, B., Madani, N., Carranza, E.J., 2015. Combination of geostatistical simulation
    and fractal modeling for mineral resource classification. Journal of Geochemical
    Exploration 149, 59–73.

Sadeghi, B., Moarefvand, P., Afzal, P, Yasrebi, A.B., Daneshvar Saein, L., 2012. Application of fractal models to outline mineralized zones in the Zaghia iron ore deposit, Central Iran. Journal of Geochemical Exploration 122, 9–19.

Sameni Keivani, F., Khalili Sourkouhi, Z., 2014. A Survey on Supply Side of Mines: a Case Study of Iran. European Online Journal of Natural and Social Sciences 3, 589-596.

Schroder, J.W., 1944. Essaisur la structure de l'Iran. Ecologae Geologicae Helvetiae 37, 37-81 (In French).

Schwab, R., Ruff, V., 2013. On the nature of the yield point phenomenon. Acta Materialia 61, 1798–1808.

Schwartz, G.M., 1947. Hydrothermal alteration in the "porphyry copper" deposits. Economic Geology 42, 319–352.

Şen, Z., Eissa, E.A., 1991. Volumetric rock quality designation. Journal of Geotechnical Engineering (ASCE) 117, 1331–1348.

Şen, Z., Eissa, E.A., 1992. Rock quality charts for log-normally distributed block sizes. International Journal of Rock Mechanics and Mining Sciences- Geomechanics Abstracts 29 (1), 1–12.

Seymour, F., 1995. Pit limit parameterisation for modified 3D Lerch-Grossmann Algorithm. SME Transactions 298, 1860-1864.

Shafiei, B., Haschke, M., Shahabpour, J., 2009. Recycling of orogenic arc crust triggers porphyry Cu mineralization in Kerman Cenozoic arc rocks, southeastern Iran. Mineralium Deposita 44, 265–283.

Shahabpour, J., 1982. Aspects of Alteration and Mineralization at the Sar-Cheshmeh Copper Molybdenum Deposit, Kerman, Iran. (PhD Thesis) Leeds University, 342 pp.

Shahabpour, J., 1994. Post-mineral breccia dyke from the Sar-Cheshmeh porphyry copper deposit, Kerman, Iran. Exploration and Mining Geology 3, 39-43.

Shahbeik, Sh., Afzal, P., Moarefvand, P., Qumarsy, M., 2014. Comparison between ordinary kriging (OK) and inverse distance weighted (IDW) based on estimation error. Case study: Dardevey iron ore deposit, NE Iran. Arabian Journal of Geosciences 7 (9), 3693–3704.

Shen, W., Zhao, P., 2002. Theoretical study of statistical fractal model with applications to mineral resource prediction. Computers & Geosciences 28, 369–376.

Shepard, D., 1968. A two-dimensional interpolation function for irregularly-spaced data. In: Proceedings of the 1968 ACM National Conference. pp. 517–524.

Sillitoe, R.H., 1997. Characteristics and controls of the largest porphyry copper–gold and epithermal gold deposits in the circum-Pacific region. Australian Journal of Earth Science 44, 373–388.

Sillitoe, R.H., 2005. Supergene oxidized and enriched porphyry copper and related deposits: Society of Economic Geologists, Economic Geology 100th Anniversary Volume, 723–768.

Sim, B.L., Agterberg, F.P., Beaudry, C., 1999. Determining the cut-off between background and relative base metal contamination levels using multifractal methods. Computers & Geosciences 25, 1023–1041.

Singh, V.K., Baliga, B.D., 1994. Slope design of an open pit copper mine. International Journal of Rock Mechanics and Mineral Science- Geomechanics Abstracts 31, 55–69.

Slob, S., 2010. Automated Rock Mass Characterisation Using 3-D Terrestrial Laser Scanning. ITC Publisher, 38 pp.

Soleymani Shishvan, M., Sattarvand, J., 2015. Long term production planning of open pit mines by ant colony optimization, European Journal of Operational Research 240, 825–836.

Soltani, F., Afzal, P., Asghari, O., 2014. Delineation of alteration zones based on Sequential Gaussian Simulation and concentration–volume fractal modeling in the hypogene zone of Sungun copper deposit, NW Iran. Journal of Geochemical Exploration 140, 64–76.

Soltani Mohammadi, S., Hezarkhan, A., Tercan, E., 2012. Optimally Locating Additional Drill Holes in Three Dimensions Using Grade and Simulated Annealing. Journal of Geological Society of India 80, 700-706.

Spalla, M.I., Morotta, A.M., Gosso, G., 2010. Advances in interpretation of geological processes: refinement of multi-scale data and integration in numerical modelling. Geological Society, London, 240 pp.

Stermole, F., Stermole, J., 2012. Economic Evaluation and Investment Decisions Methods Textbook; 13th Ed, Graphic Designer, USA, 159 pp.

Sun, T., Liu, L., 2014. Delineating the complexity of Cu-Mo mineralization in a porphyry intrusion by computational and fractal modeling: A case study of the Chehugou

deposit in the Chifeng district, Inner Mongolia, China. Journal of Geochemical Exploration 144, 128–143.

Sweetkind, D.S., Drake, R.M. II, 2007, Geologic characterization of young alluvial basin-fill deposits from drill-hole data in Yucca Flat, Nye County, Nevada: U.S. Geological Survey Scientific Investigations Report 2007–5062, 17 pp.

Tabatabaei, S. H., Asadi Haroni, H., 2006. Geochemical characteristics of Gor Gor Cu-Mo porphyry system, 25th Iranian symposium on geosciences, Geological survey of Iran, 60 pp.

Tahmasebi, P., Hezarkhani, A., 2010. Application of Adaptive Neuro-Fuzzy Inference System for Grade Estimation; Case Study, Sarcheshmeh Porphyry Copper Deposit, Kerman, Iran. Australian Journal of Basic and Applied Sciences 4, 408-420.

Takayasu, H., 1990. Fractals in the Physical Sciences. Manchester University Press, Manchester and New York. 176 pp.

Thompson, M., Howarth, S.R., 1978. A new approach to the estimation of analytical precision. Journal of Geochemical Exploration 9, 23-30.

Todorov, J., Popov, K., Shanov, S., Boykova, A. 2002. Geological Conditions for a Correct Geostatistical Evaluation: Example from the Elatsite Copper Deposit in Bulgaria. In: Geostatistics Rio 2000, Kluwer Academic Publishers, 177-189.

Trading Economics, 2015a. Iran Interest Rate 1973-2015 Data Chart. http://www.tradingeconomics.com/iran/interest-rate.

Trading Economics, 2015b. United Kingdom Interest Rate 1971-2015 Data Chart. http://www.tradingeconomics.com/united-kingdom/interest-rate.

Tukey, J.W., 1977. Exploratory data analysis. Addison-Wesley, Reading, USA.

Turcotte, D.L., 1986. A fractal approach to the relationship between ore grade and tonnage. Economic Geology 18, 1525–1532.

Turcotte, D.L., 1997. Fractals and Chaos in Geology and Geophysics. Cambridge University Press, Cambridge.

Ulrich, T., Gunther, D., Heinrich, C.A., 2001. The evolution of a porphyry Cu—Au deposit, based on La-ICP-MS analysis of fluid inclusions, Bajo de la Alumbrera, Argentina. Economic Geology 96, 1743—1774.

Verly, G., 1984. Estimation of Spatial Point and Block Distributions: The Multi-Gaussian Model, PhD thesis, Stanford University, Stanford, CA.

Villaescusa, E., Brown, E.T., 1990. Characterising joint spatial correlation using geostatistical methods, in Rock Joints. In Barton & Stephansson (Eds.), Balkema publisher, Rotterdam. pp. 115-122.

Wang, Q., Deng, J., Liu, H., Wang, Y., Sun, X., Wan, L., 2011. Fractal models for estimating local reserves with different mineralization qualities and spatial variations. Journal of Geochemical Exploration 108, 196–208.

Wang, Q.F., Deng, J., Liu, H., Yang, L.Q., Wan, L., Zhang, R.Z., 2010a. Fractal models for ore reserve estimation. Ore Geology Reviews 37, 2–14.

Wang, Q., Deng, J., Zhao, J., Li, N., Wan, L., 2012. The fractal relationship between orebody tonnage and thickness. Journal of Geochemical Exploration 122, 4–8.

Wang, Q., Deng, J., Zhao, J., Liu, H., Wan, L., Yang, L., 2010b. Tonnage-cut-off model and average grade-cut-off model for a single ore deposit. Ore Geology Reviews 38 (1–2), 113–120.

Wang, G., Pang, Z., Boisvert, J.B., Hao, Y., Cao, Y., Qu, J., 2013. Quantitative assessment of mineral resources by combining geostatistics and fractal methods in the Tongshan porphyry Cu deposit (China). Journal of Geochemical Exploration 134, 85–98.

Weber, D.D., Englund, E.J., 1992. Evaluation and comparison of spatial interpolators. Mathematical Geosciences 24, 381–391.

Weber, D.D., Englund, E.J., 1994. Evaluation and comparison of spatial interpolators, II. Mathematical Geology 26, 589–603.

Whittle, J., 1988. Beyond Optimization in Open Pit Design, Proc. 1st Canadian Conference on Computer Applications in the Mineral Industry, Quebec City, pp. 331-337.

Whittle, J., 1989. The Facts and fallacies of open pit optimization. Whittle Programming Pty Ltd.

Whittle Programming, 1998a. Four-X, Reference Manual, Whittle Programming, Melbourne, 385 pp.

Whittle, J., 1998b. Beyond optimization in open pit design. In: Proceedings of the Canadian Conference on Computer Applications in the Mineral Industries, pp. 331-337.

Whittle, J., 1990. Surface Mining Society for Mining Metallurgy and Exploration (Open Pit Optimization), Colorado, pp. 470– 475.

Whittle, J., 1999. A decade of open pit mine planning and optimisation - the craft of turning algorithms into packages. In: Proceedings of the 28th International Symposium on Application of Computers and Operations Research in the Mineral Industry, pp. 15-24.

Wilson, A.J., Cooke David, R., Harper, B.J., Deyell, C.L., 2007. Sulfur isotopic zonation in the Cadia district, southeastern Australia: exploration significance and implications for the genesis of alkalic porphyry gold-copper deposits. Mineralium Deposita 42, 465—487.

Wyllie, D.C., Mah, C.W., 2004. Rock slope engineering. London, Taylor & Francis.

Xiao, F., Chen, j., Agterberg, F., Wang, C., 2014. Element behavior analysis and its implications for geochemical anomaly identification: A case study for porphyry Cu–Mo deposits in Eastern Tianshan, China. Journal of Geochemical Exploration 145, 1–11.

Xu, Y., Cheng, Q., 2001. A fractal filtering technique for processing regional geochemical maps for mineral exploration. Geochemistry: Exploration, Environment, Analysis 1, 147–156.

Yamatomi, J., Mogi, G., Akaike, A., Yamaguchi, U., 1995. Selective extraction dynamic cone algorithm for three dimensional open pit designs. 25th APCOM Conference, pp. 267-274.

Yang, L., Wang, Q., Liu, X., 2015. Correlation between mineralization intensity and fluid–rock reaction in the Xinli gold deposit, Jiaodong Peninsula, China: Constraints from petrographic and statistical approaches. Ore Geology Reviews 71, 29–39.

Yasrebi, A.B., Afzal, P., Wetherelt, A., Foster, P., Esfahanipour, R., 2013a. Correlation between geology and concentration-volume fractal models: significance for Cu and Mo mineralized zones separation in the Kahang porphyry deposit (Central Iran). Geologica Carpathica 64, 153–163.

Yasrebi, A.B., Afzal, P., Wetherelt, A., Foster, P., Esfahanipour, R., Parvaz, D., 2012. 3D Lithology, Alteration and Zonation Modelling of the Eastern Part of Kahang Cu-Mo-Au Porphyry Deposit in Central Iran. 12th International Multidisciplinary Scientific GeoConference SGEM, Varna, pp. 417-424.

Yasrebi, J., Saffari, M., Fathi, H., Karimian, N., Moazallahi, M., Gazni, R., 2009. Evaluation and comparison of ordinary kriging and inverse distance weighting methods for prediction of spatial variability of some chemical parameters. Research Journal of Biological Sciences 4, 93–102.

Yasrebi, A.B., Wetherelt, A., Foster, P., Afzal, P., 2011. Determination and analysis of final pit limit of Esfordi phosphate open pit mine. 22th World Mining Congress, Turkey, pp. 513–522.

Yasrebi, A.B., Wetherelt, A., Foster, P., Afzal, P., Coggan, J., Kaveh Ahangaran, D., 2013b. Application of RQD-Number and RQD-Volume Multifractal Modeling to delineate rock mass characterisation in Kahang Cu-Mo Porphyry Deposit, Central Iran. Archives of Mining Sciences 58 (4), 1023–1035.

Yasrebi, A.B., Wetherelt, A., Foster, P., Coggan, J., Afzal, P., Agterberg, F., Kaveh Ahangaran, D., 2014. Application of a density–volume fractal model for rock characterisation of the Kahang porphyry deposit. International Journal of Rock Mechanics and Mining Sciences 66, 188-193.

Young, K.C., 1978. Ultimate pit design methodologies using computer models-the state of the art. AIME Transactions (264), 1454-1459.

Yousefi, M., Kamkar-Rouhani, A., Carranza, E.J.M., 2012. Geochemical mineralization probability index (GMPI): A new approach to generate enhanced stream sediment

geochemical evidential map for increasing probability of success in mineral potential mapping. Journal of Geochemical Exploration 115, 24–35.

Yousefi, M., Kamkar-Rouhani, A., Carranza, E.J.M., 2014. Application of staged factor analysis and logistic function to create a fuzzy stream sediment geochemical evidence layer for mineral prospectivity. Geochem. Geochemistry: Exploration, Environment, Analysis 14, 45–58.

Zarasvandi, A., Liaghat, S., Zentilli, M., 2005. Geology of the Darreh–Zerreshk and Ali-Abad porphyry copper deposit, central Iran. International Geology Review 47, 620–646.

Zeng, Q., Liu, J., Zhang, Z., Chen, W., Qin, F., Zhang, R., Yu, W., Zhang, X., Zhai, M., 2009. Mineralizing type, geological characteristics and geodynamic background of molybdenum deposit in Xilamulun molybdenum polymetal metallogenic belt on northern margin of North China Craton. Acta Petrolei Sinica 25 (5), 1225–1238 (in Chinese with English abstract).

Zhang, C., Jordan, G., Higgins, A., 2007. Using neighbourhood statistics and GIS to quantify and visualize spatial variation in geochemical variables: an example using Ni concentrations in the topsoils of Northern Ireland. Geoderma 137, 466–476.

Zhang, L., Einstein, H.H., 2000. Estimating the intensity of rock discontinuities. International Journal of Rock Mechanics and Mining Sciences 37, 819–37.

Zhang, W., Wang, Q., Chen, J.P., Tan, C., Yuan, X.Q., Zhou, F.J., 2012. Determination of the optimal threshold and length measurements for RQD calculations, International Journal of Rock Mechanics and Mining Sciences 51, 1–12.

Zhao, Y., Kim, Y.C., 1992. A New Ultimate Pit Limit Design Algorithm. 23rd APCOM, 423-434.

Zhmud, L., 1989. Pythagoras as a mathematician. Historia Mathematica 16, 249-268.

Zhu, Z., Jia, B., Zhou, Z., 2003. The lower bound of the Hausdorff measure of Koch Curve, Acta Mathematica Sinica, English series 19, 106–112.

Zimmerman, D., Pavlik, C., Ruggles, A., Armstrong, M.P., 1999. An Experimental comparison of ordinary and universal kriging and inverse distance weighting. Mathematical Geology 31, 375–390.

Zuo, R., 2014. Identification of weak geochemical anomalies using robust neighborhood statistics coupled with GIS in covered areas. Journal of Geochemical Exploration 136, 93–101.

Zuo, R., Carranza, E.J.M., Cheng, Q., 2012. Fractal/multifractal modelling of geochemical exploration data. Journal of Geochemical Exploration 122, 1–3.

Zuo, R., Cheng, Q., Agterberg, F.P., Xia, Q., 2009b. Application of singularity mapping technique to identify local anomalies using stream sediment geochemical data, a case study from Gangdese, Tibet, western China. Journal of Geochemical Exploration 101, 225–235.

Zuo, R., Cheng, Q., Xia, Q., 2009a. Application of fractal models to characterization of vertical distribution of geochemical element concentration. Journal of Geochemical Exploration 102, 1, 37—43.

Zuo, R., Wang, J., 2015. Fractal/multifractal modeling of geochemical data: A review. Journal of Geochemical Exploration (In Press, Corrected Proof).

Zuo, R., Wang, J., Chen, G., Yang, M., 2015. Identification of weak anomalies: A multifractal perspective. Journal of Geochemical Exploration 148, 12–24.

Appendices

Appendix. A: Certificate of Data Sources

Dated: 18/Feb/2015

Our Ref: Amir Bijan Yasrebi research entitled" Determination of an Ultimate Pit Limit Utilising Fractal Modelling to Optimise NPV in Kahang Porphyry Deposit".

To Whom It May Concern

This is to certify that Mr. Amir Bijan Yasrebi informed National Iranian Copper Industries Co (NICICO) in January 2011 that he decided to conduct research on copper as a target material because mining of copper ore and the related industries play an important role in Iran's economy which accounts for 75% of the total production in the Middle East. Consequently, we had some very productive meetings in a very friendly environment and Bijan succeeded in convincing the NICICO of the benefits of working on the mentioned project to be delivered for both parties under the supervision of Dr. Andrew Wetherelt, Dr. Patrick Foster and Dr. Peyman Afzal. As a result, the NICICO provided him with subsurface data including collar coordinates of drillcores, azimuth and dip (orientation), logging of the boreholes, samples were analysed for density and RQD and chemical analyses carried out by ALS Chemex (ALS Canada Ltd.) and Zarazma Mineral Studies Company certified by Geostats Pty Ltd (Australia).

It is good to bear in mind that the choice of input parameters to the pit optimisation study including mining recovery and dilution, recovery fraction for Cu and Mo, mining and milling costs, processing and marketing costs are determined by the deputy of the Economic and Financial Department of the NICICO with careful consideration of neighbouring deposits and in line with Iranian standards (economic regime of the country) as well as the western standards for mining projects held by the NICICO. The mentioned parameters were officially introduced to Bijan for the intended optimisation study for identification of the Kahang porphyry deposit ultimate pit limit.

In Iran, Discount Rate is defined by the Central Bank of Iran (CBI) and varies from 10% to 18% for short-term and long-term projects (for local investors) and it would be higher or lower for foreign investors considering their countries economic principles (e.g. in the United Kingdom, rates were cut to 0.5% with respect to the decision set by the England's Monetary Policy Committee) subject to the case that the foreign investors aim to transfer their project income out of Iran.

18.02.2015   No: M-9300415   Attach: —

The discount rate intended in the optimisation study would be better chosen a little higher than the official announced value (14% for instance) due to the conservative calculations used.

The Cut-off Grade (COG) used is not consistent for other neighbouring deposits and so differs and is case-sensitive from one project to another due to the various deposits' geometries, different densities and consequent block models. Therefore, this parameter is not given or suggested by the NICICO and this then becomes the investigators responsibility to calculate the COG based on the provided database information.

I am sure that Bijan's research is just at the beginning of his academic contribution between us, and I strongly believe in our future collaboration.

Yours faithfully,

Reza Esfahani Pour

Kahang Copper Project Manager

National Iranian Copper Industries Company
NICICO

Reza Esfahani Pour
Kahang Copper Project Manager

No.21, No.12 Alley, Freiburg St. Isfahan-Iran
Tel: +98 31 36696329 - 36681967 Mobile: +98 912 2190226
Fax: +98 31 36681862
e-mail: r_esfahani@nicico.com   aesfahanipour@yahoo.com
www.nicico.com

Add : No 2161 Valiasr Ave, Tehran - Iran P.C. 1511813311   P.O.Box : 15875 - 8198
FAX : (+9821)88713477 - 88717965   TEL : (+9821)88711101 - 7
Website : http://www.nicico.com   E-mail: office@nicico.com

Fig. A. 1. Letter issued by the Kahang deposit project manager authorising the use of data and choice of input parameters to the pit optimisation study

Appendix. B: Cu Re-Analysed or Duplicated Samples in the Kahang Deposit

Table. B. 1. 399 randomised samples for Cu selected and analysed for assay quality assurance and quality control

BHID	Drill Core No	Cu(%)	control sample	Cu(%)
KAG-01	C01539	0.0841	C01539D	0.0897
KAG-01	C01565	0.0286	C01565D	0.0314
KAG-01	C01601	0.0457	C01601D	0.0471
KAG-01	C01629	0.057	C01629D	0.0599
KAG-01	C01663	0.0997	C01663D	0.1
KAG-01	C01691	0.0781	C01691D	0.0802
KAG-01	C01712	0.0388	C01712D	0.0388
KAG-01	C01735	0.0936	C01735D	0.0946
KAG-02	C02044	0.0294	C02044D	0.0316
KAG-02	C02068	0.089	C02068D	0.0863
KAG-02	C02094	0.0462	C02094D	0.0498
KAG-02	C02116	0.0643	C02116D	0.0691
KAG-02	C02144	0.0696	C02144D	0.0706
KAG-02	C02162	0.1607	C02162D	0.1605
KAG-03	C02189	0.0494	C02189D	0.0483
KAG-03	C02227	0.0276	C02227D	0.0273
KAG-03	C02239	0.0142	C02239D	0.0118
KAG-03	C02266	0.0214	C02266D	0.0211
KAG-03	C02294	0.0524	C02294D	0.0573
KAG-03	C02339	0.2459	C02339D	0.2531
KAG-03	C02363	0.0082	C02363D	0.009
KAG-03	C02373	1.2507	C02373D	1.2499
KAG-03	C02414	0.1201	C02414D	0.125
KAG-03	C02437	0.1137	C02437D	0.1155
KAG-04	C02767	0.084	C02767D	0.0807
KAG-04	C02796	0.0222	C02796D	0.0235
KAG-04	C02819	0.0687	C02819D	0.0644
KAG-04	C02852	0.0388	C02852D	0.0376
KAG-04	C02896	0.5206	C02896D	0.5335
KAG-04	C02907	0.2127	C02907D	0.2365
KAG-04	C02946	0.4417	C02946D	0.466
KAG-04	C02963	0.7886	C02963D	0.8131
KAG-07	C03008	0.0122	C03008D	0.0127
KAG-07	C03029	0.0033	C03029D	0.0031
KAG-07	C03060	0.2891	C03060D	0.3148
KAG-07	C03086	1.1535	C03086D	1.2074
KAG-07	C03128	0.1067	C03128D	0.1008
KAG-07	C03160	0.1209	C03160D	0.1226
KAG-07	C03194	0.195	C03194D	0.2083
KAG-07	C03213	0.2365	C03213D	0.2525
KAG-07	C03248	0.2187	C03248D	0.2205
KAG-07	C03262	0.053	C03262D	0.0581
KAG-08	C03604	0.0252	C03604D	0.0265
KAG-08	C03625	0.0334	C03625D	0.0369
KAG-08	C03648	0.0054	C03648D	0.0055
KAG-08	C03677	0.108	C03677D	0.1035
KAG-08	C03712	0.0065	C03712D	0.0064
KAG-08	C03752	0.2473	C03752D	0.2452
KAG-08	C03770	0.3379	C03770D	0.32
KAG-08	C03807	0.2558	C03807D	0.2587
KAG-08	C03835	0.1982	C03835D	0.2001
KAG-08	C03864	0.175	C03864D	0.1754

BHID	Drill Core No	Cu(%)	control sample	Cu(%)
KAG-09	C03881	0.0726	C03881D	0.0707
KAG-09	C03900	0.029	C03900D	0.0282
KAG-09	C03957	0.0906	C03957D	0.0878
KAG-09	C03971	0.2536	C03971D	0.2521
KAG-09	C03999	0.4216	C03999D	0.4184
KAG-09	C04039	0.1414	C04039D	0.1424
KAG-09	C04073	0.3169	C04073D	0.3138
KAG-09	C04092	0.1096	C04092D	0.1133
KAG-09	C04139	0.151	C04139D	0.1482
KAG-09	C04160	0.131	C04160D	0.1345
KAG-10	C05739	0.0036	C05739D	0.0036
KAG-10	C05767	0.0068	C05767D	0.0069
KAG-10	C05802	0.0219	C05802D	0.0211
KAG-10	C05829	0.0042	C05829D	0.0043
KAG-10	C05848	0.001	C05848D	0.001
KAG-10	C05887	0.008	C05887D	0.0086
KAG-10	C05923	0.0537	C05923D	0.0587
KAG-10	C05953	0.0978	C05953D	0.1024
KAG-10	C05972	0.1195	C05972D	0.1194
KAG-05	C05993	0.3604	C05993D	0.3873
KAG-05	C06024	0.0009	C06024D	0.001
KAG-05	C06052	0.0417	C06052D	0.0422
KAG-05	C06089	0.0051	C06089D	0.0058
KAG-05	C06111	0.0495	C06111D	0.0522
KAG-11	C06148	0.0453	C06148D	0.0452
KAG-11	C06169	0.0827	C06169D	0.0821
KAG-11	C06200	0.0991	C06200D	0.0955
KAG-11	C06236	0.0658	C06236D	0.0717
KAG-11	C06261	0.4359	C06261D	0.4139
KAG-11	C06292	0.1273	C06292D	0.1225
KAG-11	C06326	0.1383	C06326D	0.1406
KAG-11	C06361	0.1248	C06361D	0.1321
KAG-11	C06381	0.1149	C06381D	0.1262
KAG-11	C06402	0.0947	C06402D	0.0972
KAG-06	C06422	0.1027	C06422D	0.1058
KAG-06	C06440	0.1223	C06440D	0.1235
KAG-06	C06476	0.0903	C06476D	0.0874
KAG-06	C06501	0.2237	C06501D	0.2337
KAG-06	C06543	0.1907	C06543D	0.1979
KAG-06	C06578	0.1671	C06578D	0.166
KAG-06	C06604	0.0771	C06604D	0.0785
KAG-12	C07075	0.031	C07075D	0.0345
KAG-12	C07113	0.0302	C07113D	0.0301
KAG-12	C07130	0.0076	C07130D	0.0081
KAG-12	C07163	0.091	C07163D	0.0883
KAG-12	C07192	0.0505	C07192D	0.0586
KAG-12	C07228	0.0354	C07228D	0.0357
KAG-12	C07256	0.1708	C07256D	0.1688
KAG-12	C07286	0.0043	C07286D	0.0048
KAG-12	C07307	0.002	C07307D	0.0022
KAG-15	C08996	0.059	C08996D	0.0554
KAG-15	C09010	1.1887	C09010D	1.2521
KAG-15	C09056	0.1553	C09056D	0.159
KAG-15	C09106	0.1845	C09106D	0.1832

BHID	Drill Core No	Cu(%)	control sample	Cu(%)
KAG-15	C09136	0.309	C09136D	0.2975
KAG-15	C09163	2.4318	C09163D	2.3048
KAG-15	C09190	0.199	C09190D	0.1904
KAG-15	C09218	0.1716	C09218D	0.1664
KAG-13	C09236	0.0445	C09236D	0.0442
KAG-13	C09263	0.0602	C09263D	0.0615
KAG-13	C09309	0.0156	C09309D	0.0152
KAG-13	C09329	0.0268	C09329D	0.0254
KAG-13	C09356	0.0376	C09356D	0.0392
KAG-13	C09390	0.1155	C09390D	0.1166
KAG-13	C09426	0.0223	C09426D	0.0209
KAG-13	C09450	0.0059	C09450D	0.0057
KAG-16	C09757	4.635	C09757D	4.772
KAG-16	C09784	0.0132	C09784D	0.0133
KAG-16	C09819	0.0182	C09819D	0.0187
KAG-16	C09849	0.0292	C09849D	0.0278
KAG-16	C09880	0.0253	C09880D	0.0244
KAG-16	C09903	0.0088	C09903D	0.0088
KAG-14	C09935	0.2964	C09935D	0.2865
KAG-14	C09968	0.0127	C09968D	0.0112
KAG-14	C10005	0.069	C10005D	0.0719
KAG-14	C10032	0.118	C10032D	0.1143
KAG-14	C10066	0.1452	C10066D	0.1471
KAG-14	C10095	0.2298	C10095D	0.2024
KAG-14	C10124	0.1013	C10124D	0.097
KAG-14	C10159	0.0902	C10159D	0.0784
KAG-17	C11996	0.0628	C11996D	0.0612
KAG-17	C12031	0.1118	C12031D	0.1093
KAG-17	C12063	0.0407	C12063D	0.0397
KAG-17	C12094	0.1458	C12094D	0.1438
KAG-17	C12115	0.0163	C12115D	0.0172
KAG-17	C12156	0.842	C12156D	0.8189
KAG-17	C12172	0.3451	C12172D	0.3464
KAG-19	C12203	0.0458	C12203D	0.0512
KAG-19	C12246	0.0202	C12246D	0.0206
KAG-19	C12274	0.051	C12274D	0.0532
KAG-19	C12295	0.0232	C12295D	0.0207
KAG-19	C12327	0.0482	C12327D	0.0463
KAG-19	C12360	0.2056	C12360D	0.2203
KAG-19	C12389	0.0675	C12389D	0.0626
KAG-19	C12422	0.0087	C12422D	0.0082
KAG-20	C12671	0.0475	C12671D	0.0449
KAG-20	C12702	0.0054	C12702D	0.005
KAG-20	C12732	0.0245	C12732D	0.0255
KAG-20	C12764	0.0504	C12764D	0.0516
KAG-20	C12786	0.1067	C12786D	0.1079
KAG-20	C12819	0.0828	C12819D	0.0833
KAG-20	C12854	0.1885	C12854D	0.1849
KAG-20	C12879	0.1968	C12879D	0.2076
KAG-22	C12906	0.1218	C12906D	0.127
KAG-22	C12933	0.0916	C12933D	0.0898
KAG-22	C12961	0.0442	C12961D	0.0459
KAG-22	C12985	0.0698	C12985D	0.0712
KAG-21	C14293	0.0389	C14293D	0.0392

BHID	Drill Core No	Cu(%)	control sample	Cu(%)
KAG-21	C14319	0.0021	C14319D	0.0022
KAG-21	C14348	0.0223	C14348D	0.0237
KAG-21	C14378	0.0792	C14378D	0.082
KAG-25	C14401	0.0577	C14401D	0.0591
KAG-25	C14438	0.0034	C14438D	0.0033
KAG-25	C14464	0.0206	C14464D	0.0225
KAG-25	C14491	0.011	C14491D	0.0112
KAG-24	C14530	0.8897	C14530D	0.8575
KAG-24	C14552	0.0455	C14552D	0.0453
KAG-24	C14580	0.0501	C14580D	0.0496
KAG-24	C14616	0.0348	C14616D	0.0326
KAG-23	C14640	0.0855	C14640D	0.0886
KAG-23	C14683	0.023	C14683D	0.0225
KAG-23	C14716	0.005	C14716D	0.0056
KAG-26	C14753	0.0917	C14753D	0.0915
KAG-26	C14779	0.0355	C14779D	0.0367
KAG-26	C14820	0.0282	C14820D	0.029
KAG-26	C14848	0.0812	C14848D	0.0791
KAG-26	C14864	0.1513	C14864D	0.1495
KAG-28	C14892	0.0317	C14892D	0.0363
KAG-28	C14917	0.0365	C14917D	0.0317
KAG-28	C14947	0.0912	C14947D	0.0947
KAG-28	C14982	0.0807	C14982D	0.0826
KAG-28	C15002	0.0716	C15002D	0.0734
KAG-28	C15030	0.1217	C15030D	0.1254
KAG-27	C15061	0.0595	C15061D	0.0593
KAG-27	C15077	0.0738	C15077D	0.0742
KAG-27	C15113	0.04	C15113D	0.0385
KAG-27	C15144	0.1142	C15144D	0.1133
KAG-27	C15172	0.2497	C15172D	0.242
KAG-27	C15203	0.2722	C15203D	0.2735
KAG-27	C15228	0.5221	C15228D	0.5345
KAG-29	C15263	0.0511	C15263D	0.0492
KAG-29	C15290	0.0617	C15290D	0.0628
KAG-30	C15309	0.0129	C15309D	0.0128
KAG-30	C15343	0.1104	C15343D	0.1137
KAG-30	C15380	0.0937	C15380D	0.0976
KAG-30	C15400	0.0044	C15400D	0.0043
KAG-30	C15432	0.2183	C15432D	0.2159
KAG-27	C16006	0.8334	C16006D	0.8228
KAG-27	C16032	0.4257	C16032D	0.4295
KAG-27	C16057	0.103	C16057D	0.1059
KAG-28	C16112	0.0176	C16112D	0.0181
KAG-28	C16146	0.2869	C16146D	0.2884
KAG-28	C16177	0.0725	C16177D	0.077
KAG-28	C16211	0.0984	C16211D	0.0979
KAG-28	C16251	0.1573	C16251D	0.1666
KAG-52	C26363	0.3074	C16363D	0.3142
KAG-30	C16661	0.2238	C16661D	0.2258
KAG-30	C16713	0.2606	C16713D	0.2664
KAG-30	C16747	0.0878	C16747D	0.0842
KAG-29	C16781	0.0317	C16781D	0.0325
KAG-34	C16800	1.3208	C16800D	1.3925
KAG-34	C16832	1.0247	C16832D	1.0263

BHID	Drill Core No	Cu(%)	control sample	Cu(%)
KAG-34	C16872	0.0632	C16872D	0.0619
KAG-34	C16901	0.0099	C16901D	0.0102
KAG-34	C16925	0.0017	C16925D	0.0015
KAG-34	C16971	0.3657	C16971D	0.3622
KAG-34	C16994	0.8403	C16994D	0.8234
KAG-34	C17030	0.9713	C17030D	0.9774
KAG-35	C17765	0.116	C17765D	0.1169
KAG-35	C17788	0.0118	C17788D	0.0119
KAG-31	C17815	0.0858	C17815D	0.0836
KAG-31	C17846	0.6059	C17846D	0.5751
KAG-31	C17887	0.1366	C17887D	0.1373
KAG-31	C17922	0.137	C17922D	0.1277
KAG-31	C17968	0.0703	C17968D	0.0684
KAG-31	C18003	0.123	C18003D	0.127
KAG-31	C18059	0.0971	C18059D	0.0981
KAG-33	C18073	0.0485	C18073D	0.0474
KAG-33	C18124	0.0319	C18124D	0.03
KAG-33	C18156	0.0789	C18156D	0.0781
KAG-33	C18207	0.0982	C18207D	0.1015
KAG-33	C18237	0.9325	C18237D	0.9178
KAG-32	C18267	0.0113	C18267D	0.0114
KAG-32	C18277	0.0134	C18277D	0.0137
KAG-36	C18309	0.3793	C18309D	0.3659
KAG-36	C18341	0.0315	C18341D	0.0318
KAG-36	C18376	0.3167	C18376D	0.3352
KAG-36	C18407	0.7294	C18407D	0.7329
KAG-36	C18432	0.4269	C18432D	0.4193
KAG-39	C18901	6.7749	C18901D	6.7958
KAG-36	C19169	0.0181	C19169D	0.0185
KAG-36	C19203	0.1461	C19203D	0.149
KAG-36	C19232	0.3503	C19232D	0.3225
KAG-36	C19258	0.4591	C19258D	0.4471
KAG-37	C19315	0.2168	C19315D	0.2139
KAG-37	C19361	0.3692	C19361D	0.3849
KAG-37	C19391	0.0764	C19391D	0.0776
KAG-38	C19431	0.0492	C19431D	0.0482
KAG-38	C19458	0.0568	C19458D	0.0538
KAG-38	C19488	0.0186	C19488D	0.019
KAG-38	C19513	0.0861	C19513D	0.081
KAG-38	C19544	0.0356	C19544D	0.037
KAG-38	C19576	0.0378	C19576D	0.0376
KAG-38	C19601	0.0404	C19601D	0.0415
KAG-38	C19889	0.0865	C19889D	0.0871
KAG-40	C19947	0.1087	C19947D	0.102
KAG-40	C19964	0.0081	C19964D	0.0092
KAG-41	C20603	0.0324	C20603D	0.0332
KAG-41	C20625	0.2359	C20625D	0.2363
KAG-41	C20657	0.0552	C20657D	0.0555
KAG-41	C20702	0.2494	C20702D	0.229
KAG-41	C20739	0.3778	C20739D	0.4089
KAG-42	C21675	0.0099	C21675D	0.0098
KAG-42	C21712	0.0581	C21712D	0.0576
KAG-42	C21737	0.0705	C21737D	0.0722
KAG-42	C21764	0.1635	C21764D	0.1695

BHID	Drill Core No	Cu(%)	control sample	Cu(%)
KAG-43	C21792	0.0196	C21792D	0.0199
KAG-43	C21817	0.0263	C21817D	0.0258
KAG-43	C21847	0.0402	C21847D	0.0388
KAG-43	C21876	0.0586	C21876D	0.0626
KAG-44	C21914	0.0919	C21914D	0.0897
KAG-41	C22322	0.3408	C22322D	0.3448
KAG-41	C22380	0.0887	C22380D	0.0941
KAG-42	C22423	0.1839	C22423D	0.1779
KAG-42	C22455	0.0003	C22455D	0.0003
KAG-43	C22510	0.0224	C22510D	0.0236
KAG-43	C22529	0.0746	C22529D	0.0752
KAG-43	C22557	0.0442	C22557D	0.0511
KAG-44	C23018	0.0085	C23018D	0.0087
KAG-45	C23471	0.3469	C23471D	0.3537
KAG-45	C23502	0.0249	C23502D	0.0244
KAG-47	C23841	0.1201	C23841D	0.1188
KAG-47	C23869	0.0937	C23869D	0.0932
KAG-47	C23894	0.0993	C23894D	0.1028
KAG-47	C23930	0.1493	C23930D	0.1434
KAG-47	C23943	0.102	C23943D	0.1045
KAG-47	C23964	0.0025	C23964D	0.0027
KAG-47	C23990	0.7987	C23990D	0.8002
KAG-47	C24023	0.1588	C24023D	0.1558
KAG-47	C24060	0.2129	C24060D	0.1977
KAG-47	C24082	0.0706	C24082D	0.0715
KAG-47	C24104	0.1749	C24104D	0.1729
KAG-47	C24140	0.2617	C24140D	0.2519
KAG-47	C24164	0.1841	C24164D	0.1881
KAG-46	C24448	0.0047	C24448D	0.0047
KAG-46	C24488	0.0015	C24488D	0.0016
KAG-46	C24520	0.0023	C24520D	0.0021
KAG-46	C24548	0.146	C24548D	0.1348
KAG-46	C24585	0.066	C24585D	0.0735
KAG-46	C24611	0.3624	C24611D	0.3752
KAG-46	C24664	0.1747	C24664D	0.1742
KAG-46	C24688	0.1588	C24688D	0.1647
KAG-46	C24721	0.0603	C24721D	0.0584
KAG-48	C24752	0.0788	C24752D	0.0794
KAG-48	C24788	0.036	C24788D	0.0382
KAG-48	C24832	0.0969	C24832D	0.0973
KAG-48	C24873	0.06	C24873D	0.0609
KAG-48	C24899	0.3349	C24899D	0.3575
KAG-49	C24931	0.0194	C24931D	0.0192
KAG-49	C24954	0.0177	C24954D	0.0173
KAG-49	C24993	0.018	C24993D	0.5443
KAG-49	C25017	0.0495	C25017D	0.0485
KAG-49	C25051	0.0622	C25051D	0.0655
KAG-49	C25103	0.1372	C25103D	0.1294
KAG-49	C25123	0.0789	C25123D	0.0812
KAG-49	C25150	0.0391	C25150D	0.0407
KAG-49	C25201	0.0201	C25201D	0.0202
KAG-51	C25270	0.0124	C25270D	0.0117
KAG-51	C25317	0.0839	C25317D	0.0894
KAG-51	C25347	0.1558	C25347D	0.1555

BHID	Drill Core No	Cu(%)	control sample	Cu(%)
KAG-51	C25379	0.0977	C25379D	0.0985
KAG-51	C25426	0.1404	C25426D	0.1467
KAG-51	C25445	0.5634	C25445D	0.5717
KAG-51	C25484	0.722	C25484D	0.7041
KAG-51	C25526	0.0836	C25526D	0.0811
KAG-50	C25561	0.167	C25561D	0.1641
KAG-50	C25600	0.2114	C25600D	0.2207
KAG-50	C25651	0.0025	C25651D	0.0026
KAG-50	C25677	0.2446	C25677D	0.2451
KAG-50	C25709	0.9208	C25709D	0.8852
KAG-50	C25740	1.0918	C25740D	1.0861
KAG-50	C25761	0.4718	C25761D	0.5105
KAG-48	C25781	0.263	C25781D	0.2625
KAG-50	C25809	0.25	C25809D	0.2297
KAG-50	C25848	0.3286	C25848D	0.3116
KAG-50	C25877	0.5866	C25877D	0.5771
KAG-50	C25899	0.2789	C25899D	0.281
KAG-51	C25932	0.1282	C25932D	0.1334
KAG-51	C25976	0.2292	C25976D	0.2339
KAG-53	C25988	0.0306	C25988D	0.0321
KAG-53	C26017	0.1282	C26017D	0.1284
KAG-52	C26043	0.0083	C26043D	0.008
KAG-52	C26089	0.0208	C26089D	0.0211
KAG-52	C26130	0.0991	C26130D	0.1019
KAG-54	C26165	0.0914	C26165D	0.094
KAG-54	C26196	0.0526	C26196D	0.0532
KAG-54	C26219	0.0027	C26219D	0.0025
KAG-52	C26247	0.1622	C26247D	0.1635
KAG-52	C26273	0.5265	C26273D	0.5299
KAG-52	C26308	0.2025	C26308D	0.2112
KAG-52	C26335	0.3538	C26335D	0.3607
KAG-52	C26399	0.1	C26399D	0.0975
KAG-52	C26416	0.0894	C26416D	0.0906
KAG-52	C26446	0.0905	C26446D	0.0931
KAG-52	C26481	0.0826	C26481D	0.0822
KAG-56	C26510	1.223	C26510D	1.2358
KAG-56	C26535	0.3578	C26535D	0.3592
KAG-54	C26741	0.0012	C26741D	0.0011
KAG-54	C26766	0.209	C26766D	0.2164
KAG-54	C26808	0.0008	C26808D	0.0007
KAG-55	C26838	0.1816	C26838D	0.1754
KAG-55	C26874	0.0596	C26874D	0.0549
KAG-55	C26902	0.6302	C26902D	0.6321
KAG-55	C26939	0.3691	C26939D	0.3655
KAG-55	C26975	0.2065	C26975D	0.2035
KAG-55	C26994	0.1444	C26994D	0.1412
KAG-55	C27034	0.1112	C27034D	0.1196
KAG-55	C27063	0.0742	C27063D	0.0727
KAG-55	C27114	0.0708	C27114D	0.0691
KAG-55	C27138	0.2256	C27138D	0.2343
KAG-54	C27236	0.2387	C27236D	0.2304
KAG-54	C27265	0.0164	C27265D	0.0162
KAG-59	C27295	0.0439	C27295D	0.044
KAG-59	C27338	0.0256	C27338D	0.0256

BHID	Drill Core No	Cu(%)	control sample	Cu(%)
KAG-59	C27366	0.1176	C27366D	0.1163
KAG-59	C27395	0.0213	C27395D	0.0223
KAG-59	C27430	0.0859	C27430D	0.0866
KAG-59	C27457	0.3287	C27457D	0.3315
KAG-59	C27482	0.7023	C27482D	0.6851
KAG-59	C27517	0.3137	C27517D	0.316
KAG-59	C27553	0.1037	C27553D	0.1052
KAG-59	C27585	0.2692	C27585D	0.2544
KAG-59	C27625	0.1719	C27625D	0.1761
KAG-58	C27659	0.0504	C27659D	0.0523
KAG-58	C27682	0.013	C27682D	0.0132
KAG-58	C27716	0.0236	C27716D	0.021
KAG-58	C27743	0.0494	C27743D	0.0447
KAG-58	C27780	0.0507	C27780D	0.0555
KAG-58	C27818	0.0794	C27818D	0.0803
KAG-57	C27866	0.1472	C27866D	0.1478
KAG-57	C27906	0.0719	C27906D	0.0725
KAG-57	C27932	0.4161	C27932D	0.4147
KAG-57	C27957	0.1064	C27957D	0.1071
KAG-63	C28100	0.1087	C28100D	0.108
KAG-63	C28125	0.2347	C28125D	0.2285
KAG-63	C28164	0.4189	C28164D	0.4216
KAG-63	C28201	0.2729	C28201D	0.2752

Appendix. C: Geochemical Data Variances via F-Distribution

Table. C. 1. Fisher distribution $F(n_1, n_2)$ with n_1 and n_2 degrees of freedom, $\alpha = 0.025$ and 97. 5% of confidence level (Emery, 2012)

n_2 \ n_1	1	2	3	4	5	6	7	8	9	10	11	12	13	14	16	20	24	30	40	50	75	100	200	500	∞
1	647.79	799.50	864.16	899.58	921.85	937.11	948.22	956.66	963.28	968.63	973.03	976.71	979.84	982.53	986.92	993.10	997.25	1001.4	1005.6	1008.1	1011.5	1013.2	1015.7	1017.2	1018.3
2	38.51	39.00	39.17	39.25	39.30	39.33	39.36	39.37	39.39	39.40	39.41	39.41	39.42	39.43	39.44	39.45	39.46	39.46	39.47	39.48	39.48	39.49	39.49	39.50	39.50
3	17.44	16.04	15.44	15.10	14.88	14.73	14.62	14.54	14.47	14.42	14.37	14.34	14.30	14.28	14.23	14.17	14.12	14.08	14.04	14.01	13.97	13.96	13.93	13.91	13.90
4	12.22	10.65	9.98	9.60	9.36	9.20	9.07	8.98	8.90	8.84	8.79	8.75	8.71	8.68	8.63	8.56	8.51	8.46	8.41	8.38	8.34	8.32	8.29	8.27	8.26
5	10.01	8.43	7.76	7.39	7.15	6.98	6.85	6.76	6.68	6.62	6.57	6.52	6.49	6.46	6.40	6.33	6.28	6.23	6.18	6.14	6.10	6.08	6.05	6.03	6.02
6	8.81	7.26	6.60	6.23	5.99	5.82	5.70	5.60	5.52	5.46	5.41	5.37	5.33	5.30	5.24	5.17	5.12	5.07	5.01	4.98	4.94	4.92	4.88	4.86	4.85
7	8.07	6.54	5.89	5.52	5.29	5.12	4.99	4.90	4.82	4.76	4.71	4.67	4.63	4.60	4.54	4.47	4.41	4.36	4.31	4.28	4.23	4.21	4.18	4.16	4.14
8	7.57	6.06	5.42	5.05	4.82	4.65	4.53	4.43	4.36	4.30	4.24	4.20	4.16	4.13	4.08	4.00	3.95	3.89	3.84	3.81	3.76	3.74	3.70	3.68	3.67
9	7.21	5.71	5.08	4.72	4.48	4.32	4.20	4.10	4.03	3.96	3.91	3.87	3.83	3.80	3.74	3.67	3.61	3.56	3.51	3.47	3.43	3.40	3.37	3.35	3.33
10	6.94	5.46	4.83	4.47	4.24	4.07	3.95	3.85	3.78	3.72	3.66	3.62	3.58	3.55	3.50	3.42	3.37	3.31	3.26	3.22	3.18	3.15	3.12	3.09	3.08
11	6.72	5.26	4.63	4.28	4.04	3.88	3.76	3.66	3.59	3.53	3.47	3.43	3.39	3.36	3.30	3.23	3.17	3.12	3.06	3.03	2.98	2.96	2.92	2.90	2.88
12	6.55	5.10	4.47	4.12	3.89	3.73	3.61	3.51	3.44	3.37	3.32	3.28	3.24	3.21	3.15	3.07	3.02	2.96	2.91	2.87	2.82	2.80	2.76	2.74	2.72
13	6.41	4.97	4.35	4.00	3.77	3.60	3.48	3.39	3.31	3.25	3.20	3.15	3.12	3.08	3.03	2.95	2.89	2.84	2.78	2.74	2.70	2.67	2.63	2.61	2.60
14	6.30	4.86	4.24	3.89	3.66	3.50	3.38	3.29	3.21	3.15	3.09	3.05	3.01	2.98	2.92	2.84	2.79	2.73	2.67	2.64	2.59	2.56	2.53	2.50	2.49
16	6.12	4.69	4.08	3.73	3.50	3.34	3.22	3.12	3.05	2.99	2.93	2.89	2.85	2.82	2.76	2.68	2.63	2.57	2.51	2.47	2.42	2.40	2.36	2.33	2.32
20	5.87	4.46	3.86	3.51	3.29	3.13	3.01	2.91	2.84	2.77	2.72	2.68	2.64	2.60	2.55	2.46	2.41	2.35	2.29	2.25	2.20	2.17	2.13	2.10	2.09
24	5.72	4.32	3.72	3.38	3.15	2.99	2.87	2.78	2.70	2.64	2.59	2.54	2.50	2.47	2.41	2.33	2.27	2.21	2.15	2.11	2.05	2.02	1.98	1.95	1.94
30	5.57	4.18	3.59	3.25	3.03	2.87	2.75	2.65	2.57	2.51	2.46	2.41	2.37	2.34	2.28	2.20	2.14	2.07	2.01	1.97	1.91	1.88	1.84	1.81	1.79
40	5.42	4.05	3.46	3.13	2.90	2.74	2.62	2.53	2.45	2.39	2.33	2.29	2.25	2.21	2.15	2.07	2.01	1.94	1.88	1.83	1.77	1.74	1.69	1.66	1.64
50	5.34	3.97	3.39	3.05	2.83	2.67	2.55	2.46	2.38	2.32	2.26	2.22	2.18	2.14	2.08	1.99	1.93	1.87	1.80	1.75	1.69	1.66	1.60	1.57	1.55
75	5.23	3.88	3.30	2.96	2.74	2.58	2.46	2.37	2.29	2.22	2.17	2.12	2.08	2.05	1.99	1.90	1.83	1.76	1.69	1.65	1.58	1.54	1.48	1.44	1.42
100	5.18	3.83	3.25	2.92	2.70	2.54	2.42	2.32	2.24	2.18	2.12	2.08	2.04	2.00	1.94	1.85	1.78	1.71	1.64	1.59	1.52	1.48	1.42	1.38	1.35
200	5.10	3.76	3.18	2.85	2.63	2.47	2.35	2.26	2.18	2.11	2.06	2.01	1.97	1.93	1.87	1.78	1.71	1.64	1.56	1.51	1.44	1.39	1.32	1.27	1.23
500	5.05	3.72	3.14	2.81	2.59	2.43	2.31	2.22	2.14	2.07	2.02	1.97	1.93	1.89	1.83	1.74	1.67	1.60	1.52	1.46	1.38	1.34	1.25	1.19	1.14
∞	4.93	3.67	3.11	2.78	2.56	2.41	2.29	2.19	2.11	2.05	1.99	1.94	1.90	1.87	1.80	1.71	1.64	1.57	1.48	1.43	1.34	1.30	1.21	1.13	1.00

Appendix. D: Distribution of Student (T) with n Degrees of Freedom

Table. D. 1. Critical values for student's T distributions (column headings denote probabilities' α above tabulated values: Emery, 2012)

α n	0.25	0.2	0.15	0.1	0.05	0.025	0.01	0.005	0.0005
1	1.000	1.376	1.963	3.078	6.314	12.71	31.82	63.66	636.6
2	0.816	1.061	1.386	1.886	2.920	4.303	6.965	9.925	31.599
3	0.765	0.978	1.250	1.638	2.353	3.182	4.541	5.841	12.924
4	0.741	0.941	1.190	1.533	2.132	2.776	3.747	4.604	8.610
5	0.727	0.920	1.156	1.476	2.015	2.571	3.365	4.032	6.869
6	0.718	0.906	1.134	1.440	1.943	2.447	3.143	3.707	5.959
7	0.711	0.896	1.119	1.415	1.895	2.365	2.998	3.499	5.408
8	0.706	0.889	1.108	1.397	1.860	2.306	2.896	3.355	5.041
9	0.703	0.883	1.100	1.383	1.833	2.262	2.821	3.250	4.781
10	0.700	0.879	1.093	1.372	1.812	2.228	2.764	3.169	4.587
11	0.697	0.876	1.088	1.363	1.796	2.201	2.718	3.106	4.437
12	0.695	0.873	1.083	1.356	1.782	2.179	2.681	3.055	4.318
13	0.694	0.870	1.079	1.350	1.771	2.160	2.650	3.012	4.221
14	0.692	0.868	1.076	1.345	1.761	2.145	2.624	2.977	4.140
15	0.691	0.866	1.074	1.341	1.753	2.131	2.602	2.947	4.073
16	0.690	0.865	1.071	1.337	1.746	2.120	2.583	2.921	4.015
17	0.689	0.863	1.069	1.333	1.740	2.110	2.567	2.898	3.965
18	0.688	0.862	1.067	1.330	1.734	2.101	2.552	2.878	3.922
19	0.688	0.861	1.066	1.328	1.729	2.093	2.539	2.861	3.883
20	0.687	0.860	1.064	1.325	1.725	2.086	2.528	2.845	3.850
21	0.686	0.859	1.063	1.323	1.721	2.080	2.518	2.831	3.819
22	0.686	0.858	1.061	1.321	1.717	2.074	2.508	2.819	3.792
23	0.685	0.858	1.060	1.319	1.714	2.069	2.500	2.807	3.768
24	0.685	0.857	1.059	1.318	1.711	2.064	2.492	2.797	3.745
25	0.684	0.856	1.058	1.316	1.708	2.060	2.485	2.787	3.725
26	0.684	0.856	1.058	1.315	1.706	2.056	2.479	2.779	3.707
27	0.684	0.855	1.057	1.314	1.703	2.052	2.473	2.771	3.690
28	0.683	0.855	1.056	1.313	1.701	2.048	2.467	2.763	3.674
29	0.683	0.854	1.055	1.311	1.699	2.045	2.462	2.756	3.659
30	0.683	0.854	1.055	1.310	1.697	2.042	2.457	2.750	3.646
40	0.681	0.851	1.050	1.303	1.684	2.021	2.423	2.704	3.551
60	0.679	0.848	1.045	1.296	1.671	2.000	2.390	2.660	3.460
120	0.677	0.845	1.041	1.289	1.658	1.980	2.358	2.617	3.373
∞	0.674	0.842	1.036	1.282	1.645	1.960	2.326	2.576	3.291

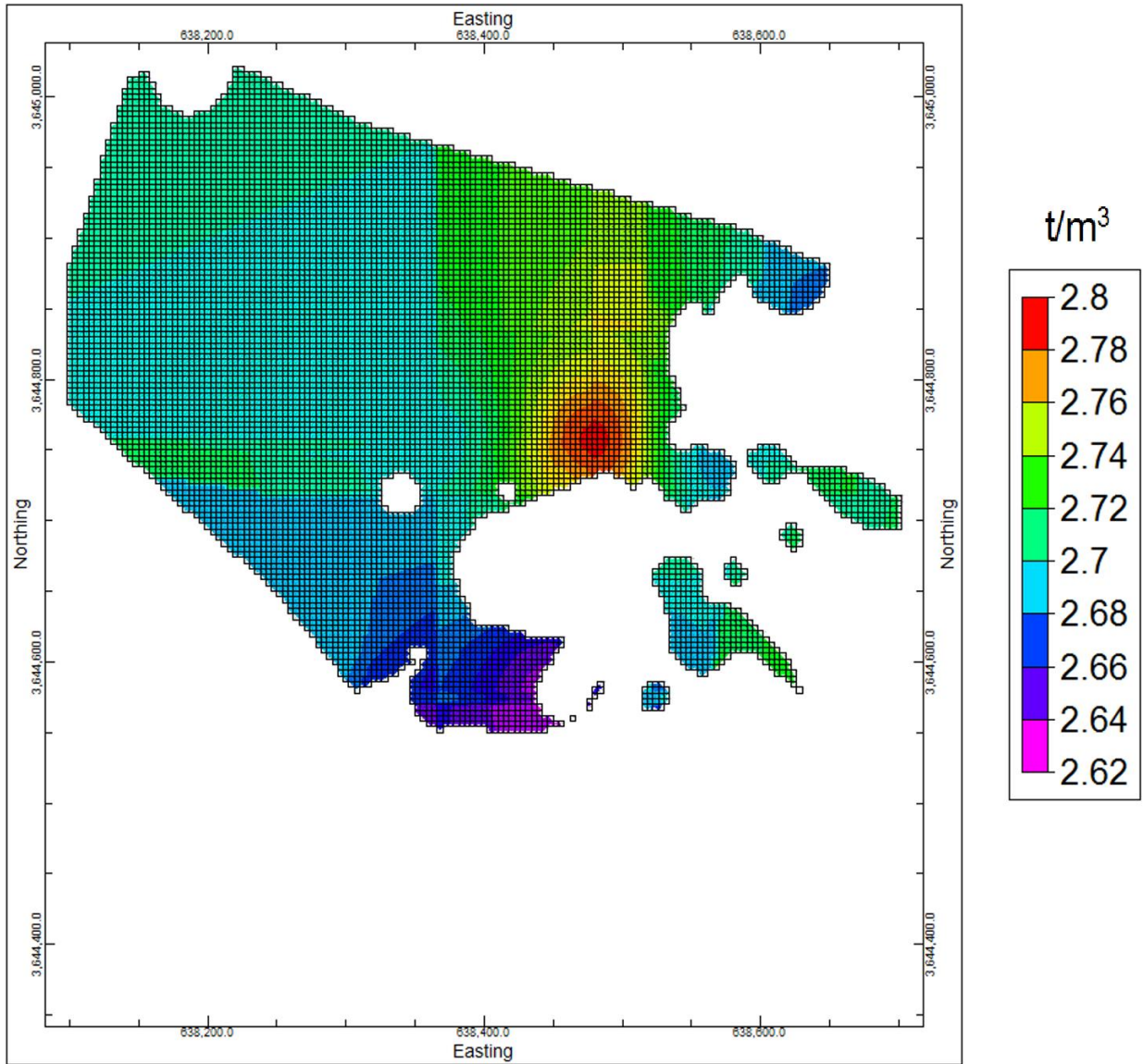# Appendix. E: Density and RQD Plans in Different Levels

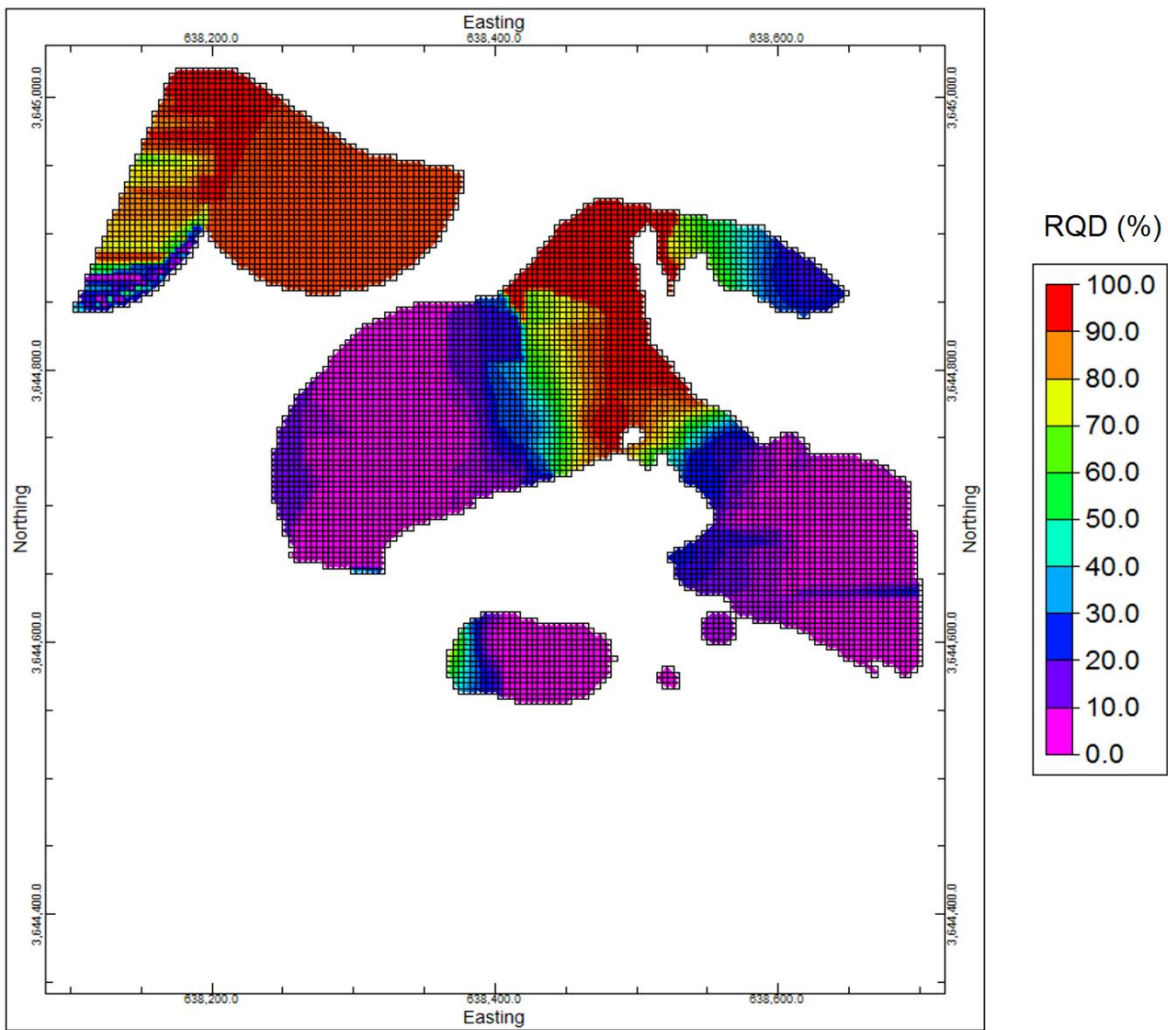
Fig. E. 1. Density plan view for layer # 32 (Z =1900 m)

Fig. E. 2. RQD plan view for layer # 32 (Z =1900 m)
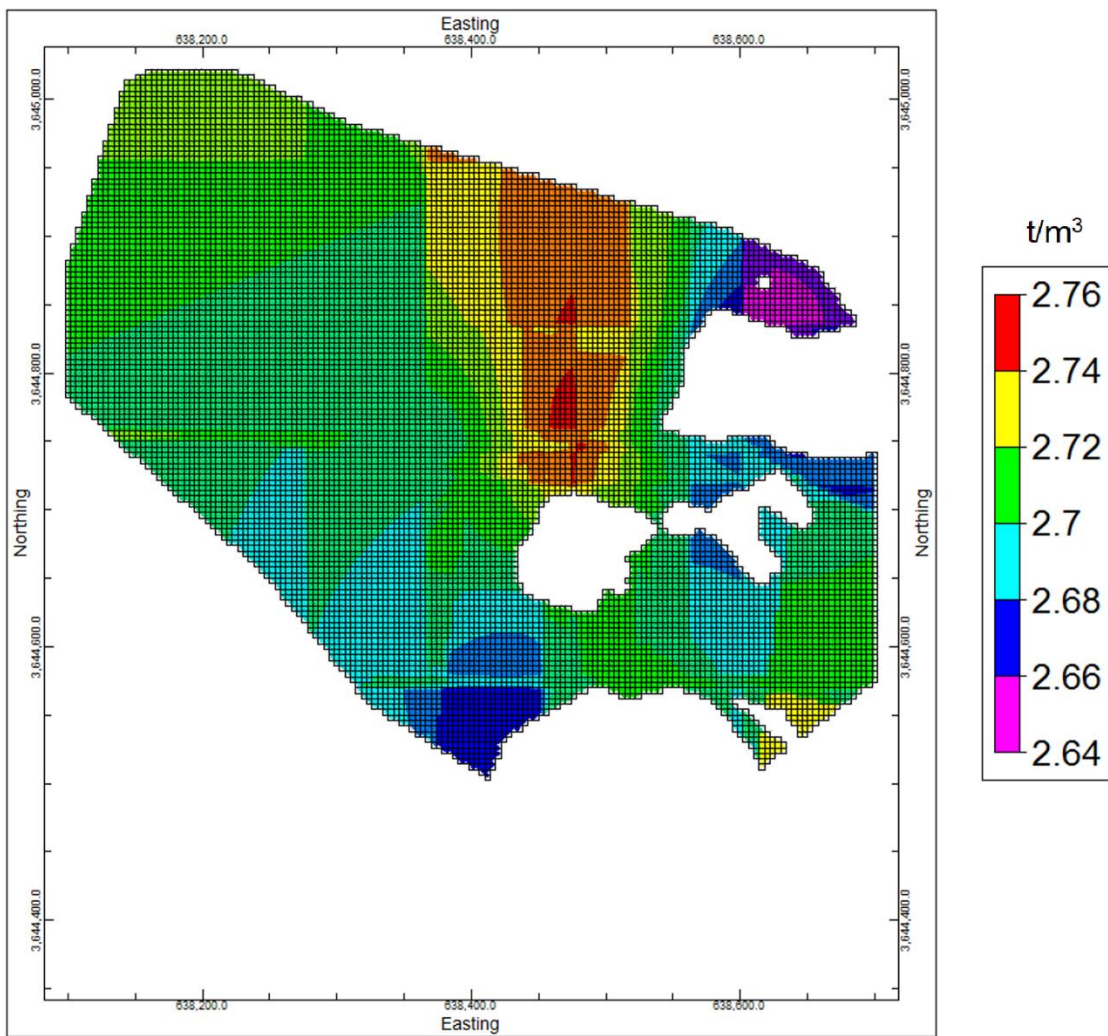
Fig. E. 3. Density plan view for layer # 37 (Z =1950 m)
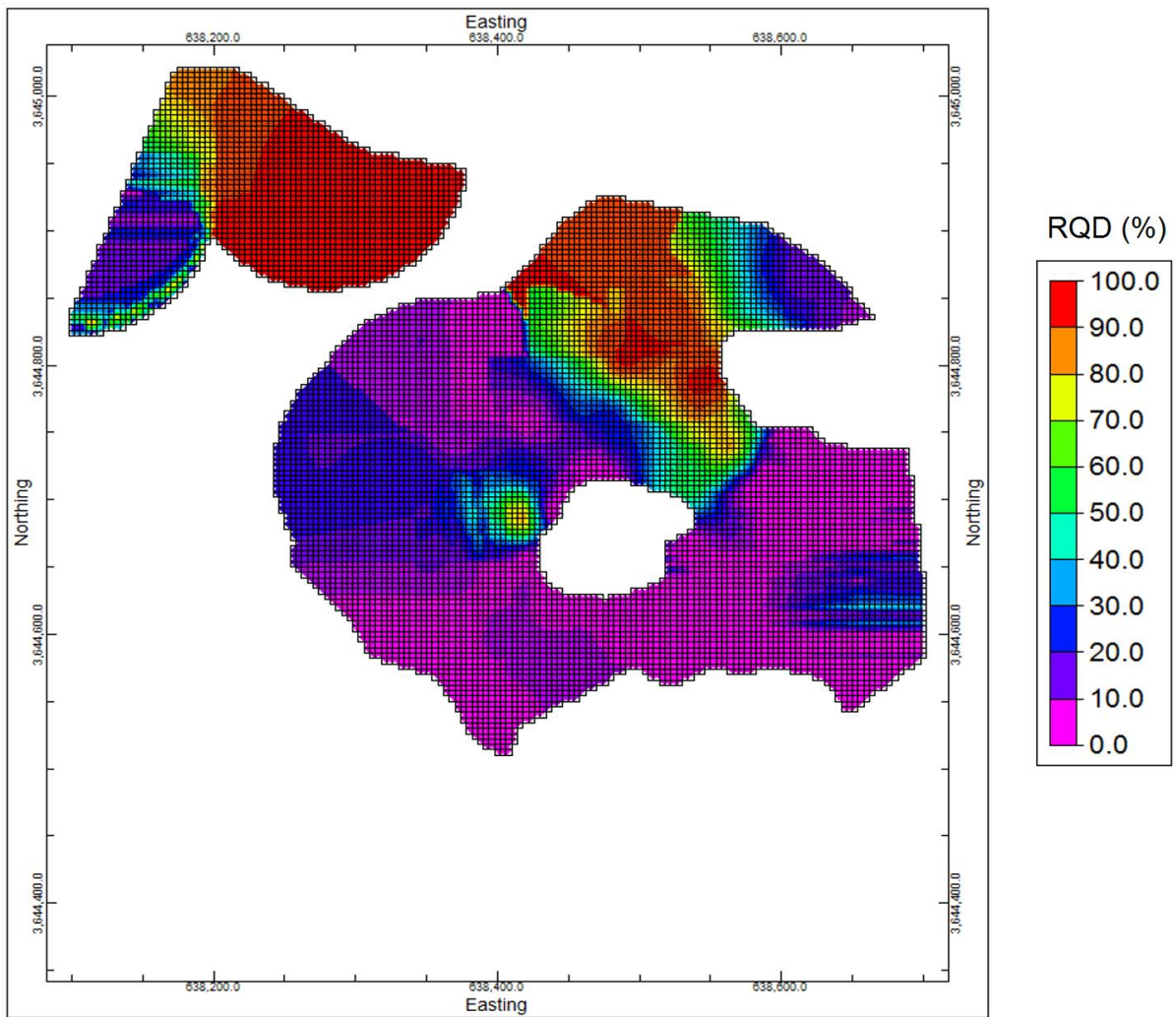
Fig. E. 4. RQD plan view for layer # 37 (Z =1950 m)
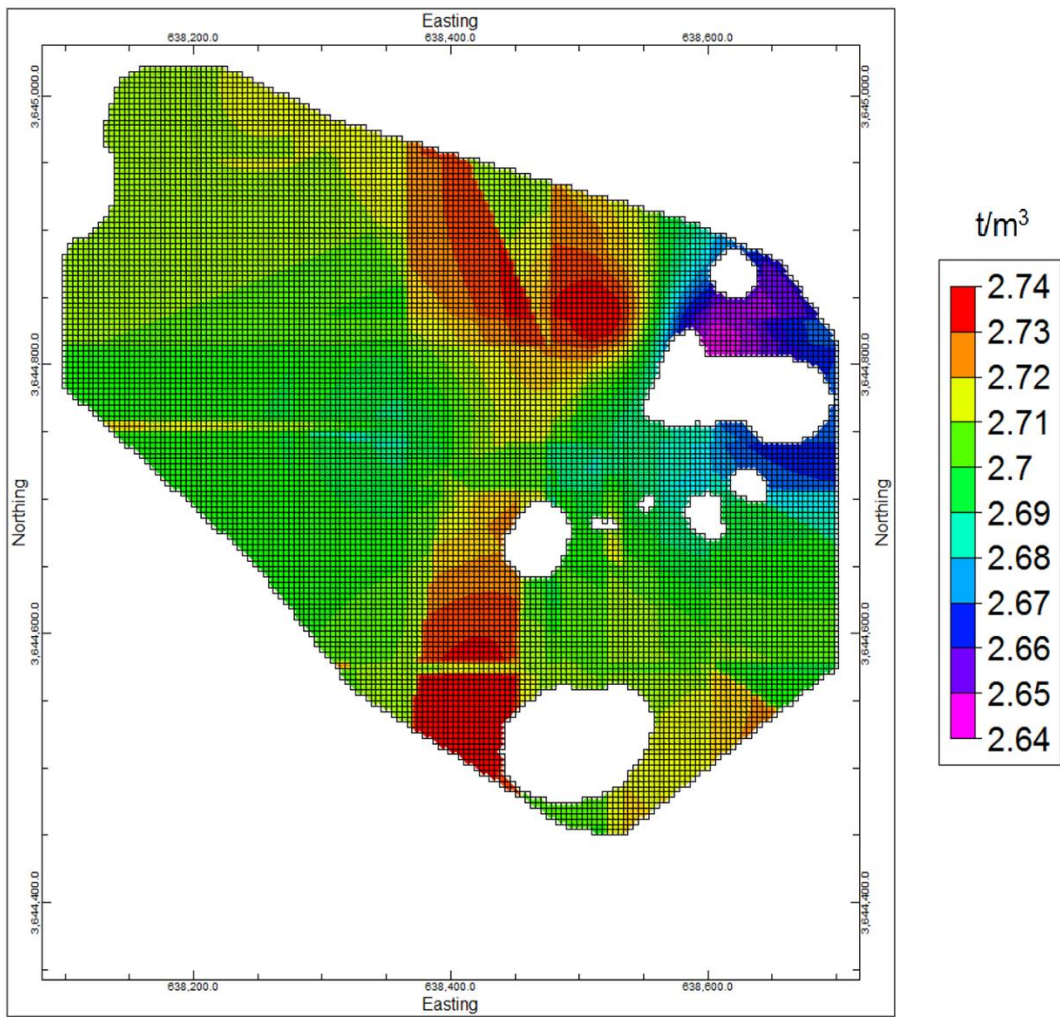
Fig. E. 5. Density plan view for layer # 42 (Z =2000 m)
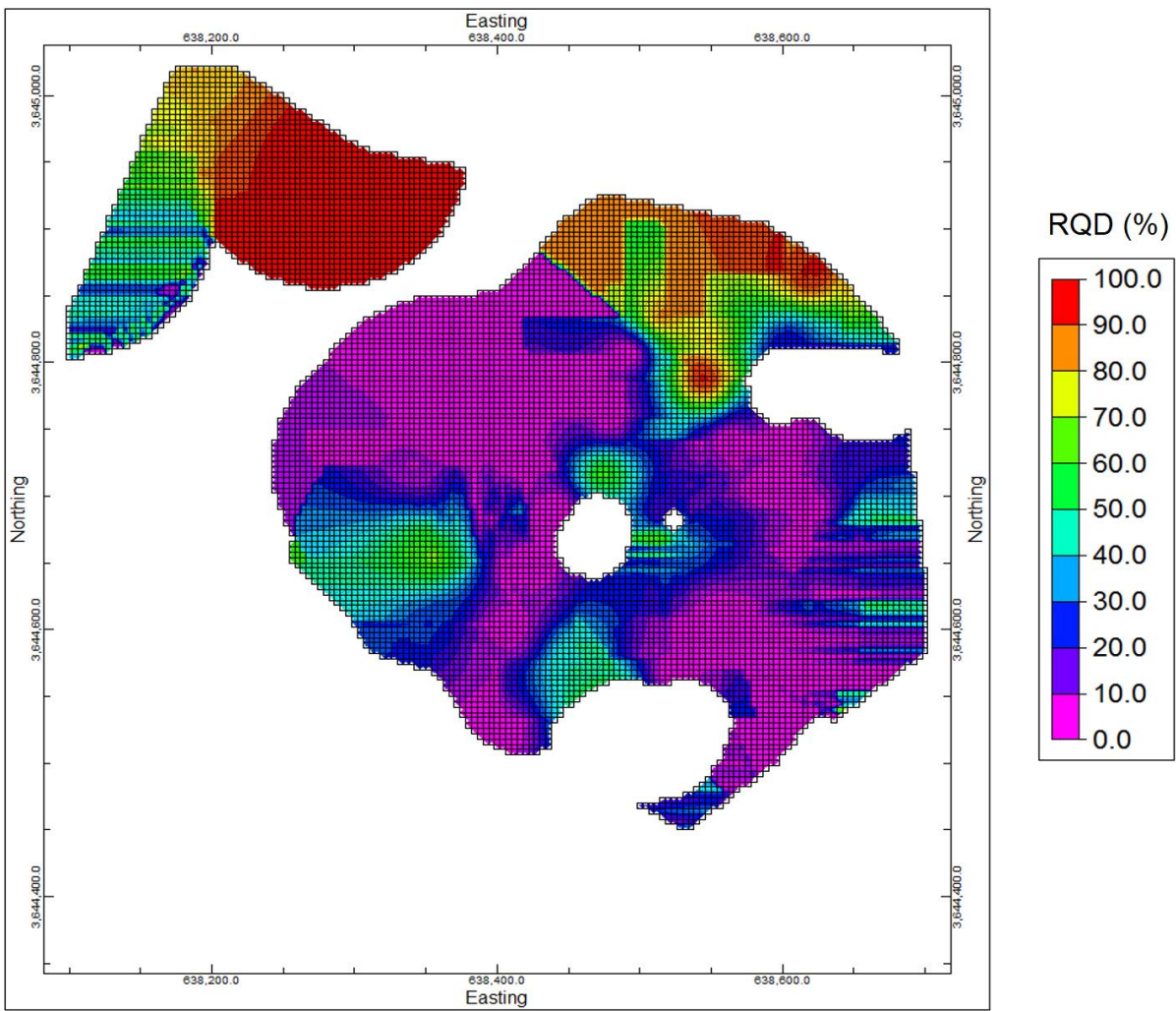
Fig. E. 6. RQD plan view for layer # 42 (Z = 2000m)

Appendix. F: Economic Models in the Kahang Deposit

Table. F. 1. The individual economic properties at all elevations (generated by NPV Scheduler software)

	Rock	Revenue	Processing Cost	Mining Cost	ORE	Cu	Mo	Cu R	Mo R
	tonnes	$	$	$	tonnes	tonnes	g	tonnes	g
Elevation 2360.00	9,023,760	0	0	36,095,040	0	0	0	0	0
Elevation 2350.00	9,023,760	0	0	36,095,040	0	0	0	0	0
Elevation 2340.00	9,032,698	352,689	235,197	36,543,325	56,520	57.924	2,131,657	44.949	1,654,166
Elevation 2330.00	9,181,637	3,933,008	2,573,962	38,051,538	616,757	694.2483	9,068,299	538.7367	7,037,000
Elevation 2320.00	9,330,494	22,333,601	11,305,510	41,238,636	2,673,549	3,953	48,381,836	3,067	37,544,305
Elevation 2310.00	9,331,390	9,282,607	6,258,133	40,457,095	1,502,934	1,585	37,806,669	1,230	29,337,975
Elevation 2300.00	9,331,123	8,806,450	5,894,721	39,925,122	1,414,317	1,537	25,560,388	1,193	19,834,861
Elevation 2290.00	9,330,651	13,233,657	7,228,669	40,267,129	1,717,344	2,319	35,601,503	1,800	27,626,766
Elevation 2280.00	9,421,616	15,084,434	6,338,199	40,311,682	1,481,192	2,664	34,448,430	2,067	26,731,982
Elevation 2270.00	9,448,712	17,154,578	8,066,531	41,150,138	1,899,480	3,022	41,388,101	2,345	32,117,166
Elevation 2260.00	9,481,392	25,883,725	8,681,095	41,081,036	1,991,168	4,617	44,945,946	3,583	34,878,054
Elevation 2250.00	9,482,797	26,068,428	11,226,408	41,806,517	2,629,322	4,556	73,927,805	3,536	57,367,977
Elevation 2240.00	9,482,554	22,353,675	9,052,246	41,639,910	2,109,890	3,945	51,849,770	3,061	40,235,421
Elevation 2230.00	9,489,563	25,217,308	11,182,161	41,957,644	2,622,562	4,465	53,952,212	3,465	41,866,917
Elevation 2220.00	9,490,387	15,271,558	6,967,022	41,207,374	1,636,674	2,718	28,500,705	2,109	22,116,547
Elevation 2210.00	9,490,979	16,565,029	7,602,964	41,138,049	1,788,267	2,893	47,790,545	2,245	37,085,463
Elevation 2200.00	9,488,928	16,645,859	8,915,088	41,210,997	2,117,070	2,868	59,672,108	2,226	46,305,555
Elevation 2190.00	9,489,166	19,906,548	8,808,052	41,476,358	2,066,827	3,474	57,998,104	2,696	45,006,528
Elevation 2180.00	9,574,547	18,599,586	8,613,910	41,454,441	2,030,506	3,126	90,824,624	2,426	70,479,908
Elevation 2170.00	9,601,150	18,312,328	8,689,065	42,000,570	2,047,771	3,206	50,338,290	2,488	39,062,513
Elevation 2160.00	9,602,128	21,369,488	10,784,993	42,268,380	2,551,000	3,745	57,452,098	2,906	44,582,828
Elevation 2150.00	9,621,101	25,711,762	12,955,453	43,077,426	3,066,822	4,405	99,842,612	3,419	77,477,868
Elevation 2140.00	9,621,848	27,341,372	12,076,400	42,485,149	2,831,880	4,829	62,320,722	3,747	48,360,880
Elevation 2130.00	9,622,366	37,335,117	12,732,713	42,447,296	2,925,688	6,630	73,925,020	5,145	57,365,816
Elevation 2120.00	9,625,715	31,523,737	13,695,741	43,015,405	3,210,568	5,473	100,500,011	4,247	77,988,008
Elevation 2110.00	9,624,093	32,208,151	12,806,872	42,465,159	2,980,376	5,706	68,037,942	4,428	52,797,443
Elevation 2100.00	9,622,622	34,179,284	13,324,379	42,667,702	3,096,834	6,030	79,940,457	4,679	62,033,795
Elevation 2090.00	9,619,555	28,624,330	12,140,447	42,441,936	2,838,426	5,076	58,845,125	3,939	45,663,817
Elevation 2080.00	9,628,918	35,090,334	12,474,049	42,905,364	2,877,643	6,194	81,031,058	4,806	62,880,101
Elevation 2070.00	9,624,630	28,993,026	12,941,047	42,857,911	3,038,491	5,056	85,560,266	3,924	66,394,767
Elevation 2060.00	9,621,541	28,384,376	9,916,674	42,385,513	2,283,789	5,029	59,880,729	3,902	46,467,445
Elevation 2050.00	9,662,571	31,925,895	13,218,188	43,153,065	3,086,480	5,611	81,156,842	4,354	62,977,709
Elevation 2040.00	9,654,058	29,830,005	12,213,544	42,428,700	2,849,336	5,252	72,809,496	4,076	56,500,169
Elevation 2030.00	9,641,288	35,746,696	13,418,225	42,540,906	3,112,821	6,181	121,739,848	4,796	94,470,122
Elevation 2020.00	9,536,663	34,600,255	13,879,150	42,197,072	3,232,736	6,104	81,002,611	4,736	62,858,026
Elevation 2010.00	9,528,478	31,923,163	13,393,076	42,227,111	3,129,136	5,652	68,483,387	4,386	53,143,108
Elevation 2000.00	9,522,661	39,475,263	15,488,844	42,564,472	3,602,915	6,918	106,307,095	5,368	82,494,306
Elevation 1990.00	9,457,766	46,406,926	14,266,289	41,829,155	3,245,968	8,249	89,671,195	6,401	69,584,848
Elevation 1980.00	9,445,909	51,162,105	15,682,269	42,139,121	3,572,942	8,878	164,663,453	6,889	127,778,840
Elevation 1970.00	9,435,226	47,174,842	15,105,093	41,960,335	3,453,978	8,256	130,337,038	6,407	101,141,542
Elevation 1960.00	9,429,946	37,106,416	14,217,274	41,880,778	3,296,890	6,659	52,430,757	5,167	40,686,267
Elevation 1950.00	9,446,502	59,257,392	15,041,979	41,943,059	3,355,443	10,346	171,342,763	8,028	132,961,984
Elevation 1940.00	9,433,090	43,164,730	14,330,607	41,741,437	3,288,949	7,515	131,437,446	5,831	101,995,459
Elevation 1930.00	9,415,318	33,261,814	12,630,563	41,510,774	2,931,694	5,790	101,476,235	4,493	78,745,558
Elevation 1920.00	9,356,635	36,287,687	10,835,532	41,065,834	2,467,573	6,100	176,655,762	4,734	137,084,872
Elevation 1910.00	9,334,368	42,349,766	11,805,429	40,835,705	2,675,339	6,904	271,436,265	5,358	210,634,541
Elevation 1900.00	9,267,184	38,443,692	9,756,401	40,006,008	2,192,710	6,105	295,815,803	4,738	229,553,064
Elevation 1890.00	9,242,189	30,992,846	8,230,910	39,504,916	1,862,798	4,788	279,321,626	3,715	216,753,582
Elevation 1880.00	9,215,891	22,904,176	6,850,172	39,060,596	1,567,299	3,589	191,090,043	2,785	148,285,873
Elevation 1870.00	9,181,584	18,006,565	5,545,494	38,514,810	1,269,906	2,907	124,119,545	2,256	96,316,767
Elevation 1860.00	9,147,789	15,757,662	4,898,402	37,961,342	1,121,509	2,588	95,320,754	2,008	73,968,905
Elevation 1850.00	9,123,883	21,915,101	4,500,830	37,727,449	978,819	3,691	104,494,575	2,864	81,087,790

Elevation 1840.00	9,106,318	17,010,375	3,941,386	37,493,496	872,562	2,838	89,443,509	2,202	69,408,163
Elevation 1830.00	9,090,488	12,593,760	3,422,890	37,303,833	773,824	2,046	82,995,508	1,587	64,404,514
Elevation 1820.00	9,078,981	7,194,576	2,678,609	37,060,244	619,413	1,303	6,684,634	1,011	5,187,276
Elevation 1810.00	9,071,219	6,688,723	2,205,226	36,894,177	504,733	1,204	8,440,405	934.0113	6,549,754
Elevation 1800.00	9,062,357	7,245,690	1,560,840	36,690,390	342,550	1,194	42,702,893	926.2184	33,137,445
Elevation 1790.00	9,056,654	2,567,146	1,098,557	36,539,766	257,866	423.285	15,007,978	328.4691	11,646,191
Elevation 1780.00	9,051,291	2,219,637	679,185	36,391,130	154,971	375.6501	10,035,073	291.5045	7,787,217
Elevation 1770.00	9,046,488	1,163,588	571,277	36,348,010	135,048	198.6992	4,720,615	154.1906	3,663,197
Elevation 1760.00	9,043,013	954,156	470,781	36,305,747	111,413	159.6237	4,879,002	123.868	3,786,105
Elevation 1750.00	9,039,635	684,504	367,443	36,263,473	87,443	111.4461	4,433,501	86.4822	3,440,397
Elevation 1740.00	9,036,195	533,661	295,403	36,229,341	70,467	84.729	4,113,223	65.7497	3,191,861
Elevation 1730.00	9,033,666	413,750	236,153	36,202,364	56,418	65.6459	3,202,658	50.9412	2,485,262
Elevation 1720.00	9,031,310	304,077	184,805	36,178,366	44,270	48.5246	2,268,665	37.6551	1,760,484
Elevation 1710.00	9,029,592	235,018	146,046	36,160,358	34,992	38.5344	1,439,899	29.9027	1,117,362
Elevation 1700.00	9,028,008	171,248	106,376	36,142,618	25,488	28.0368	1,061,847	21.7566	823,994
Elevation 1690.00	9,027,216	139,337	86,544	36,133,747	20,736	22.8096	864,816	17.7002	671,098
Elevation 1680.00	9,023,760	72,660	45,076	36,108,000	10,800	11.88	455,386	9.2189	353,379
Elevation 1670.00	9,023,760	0	0	36,095,040	0	0	0	0	0
Elevation 1660.00	9,023,760	0	0	36,095,040	0	0	0	0	0
Elevation 1650.00	9,023,760	0	0	36,095,040	0	0	0	0	0
Elevation 1640.00	9,023,760	0	0	36,095,040	0	0	0	0	0
Elevation 1630.00	9,023,760	0	0	36,095,040	0	0	0	0	0
Elevation 1620.00	9,023,760	0	0	36,095,040	0	0	0	0	0
Elevation 1610.00	9,023,760	0	0	36,095,040	0	0	0	0	0
Elevation 1600.00	9,023,760	0	0	36,095,040	0	0	0	0	0
Elevation 1590.00	9,023,760	0	0	36,095,040	0	0	0	0	0
Elevation 1580.00	9,023,760	0	0	36,095,040	0	0	0	0	0
Total	734,934,618	1,433,650,948	536,892,565	3,118,312,984	124,521,903	248,105	4,815,385,183	192,529	3,736,738,904
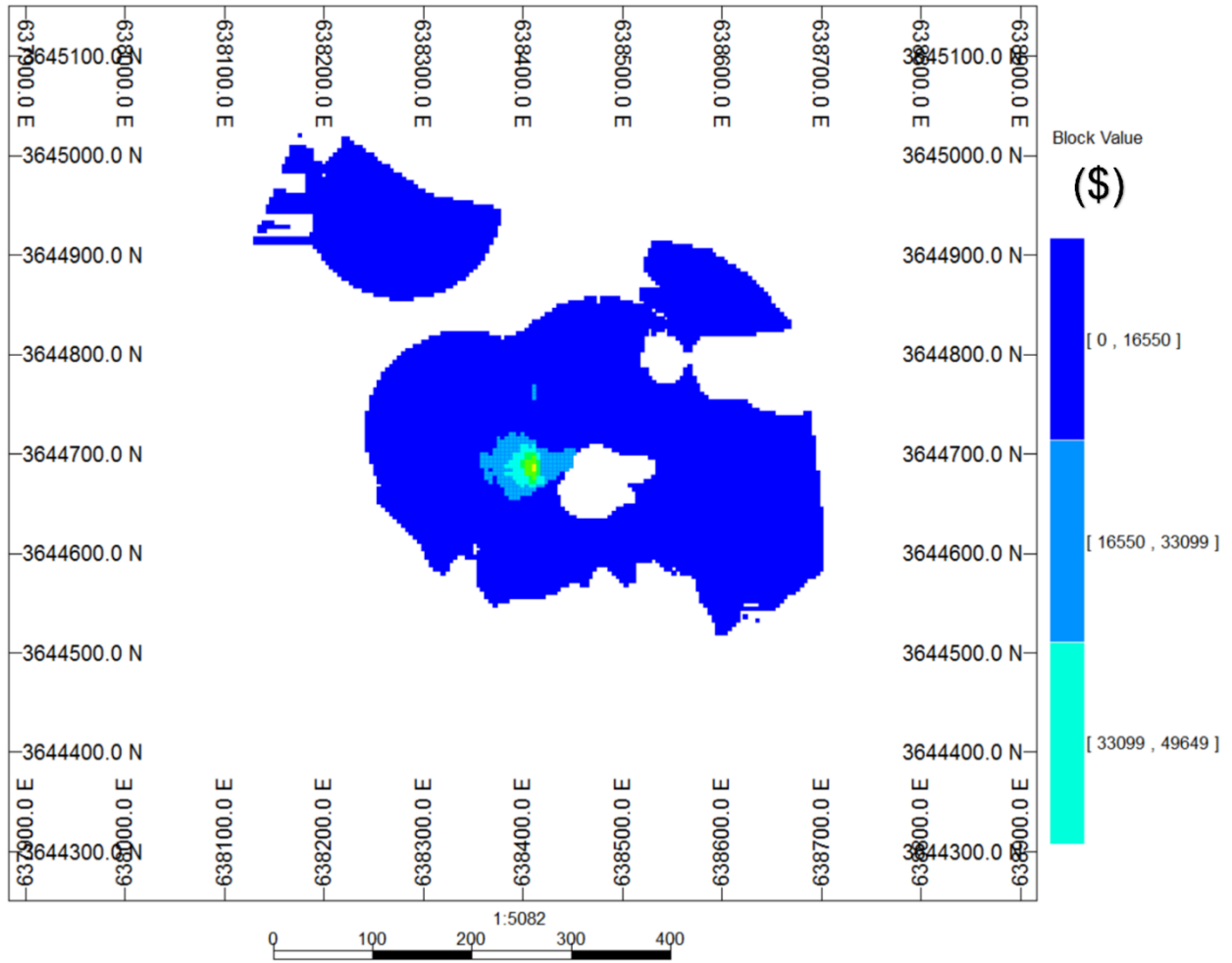
Fig. F. 1. 2D economic model (Section level 1970 m, Plan view)
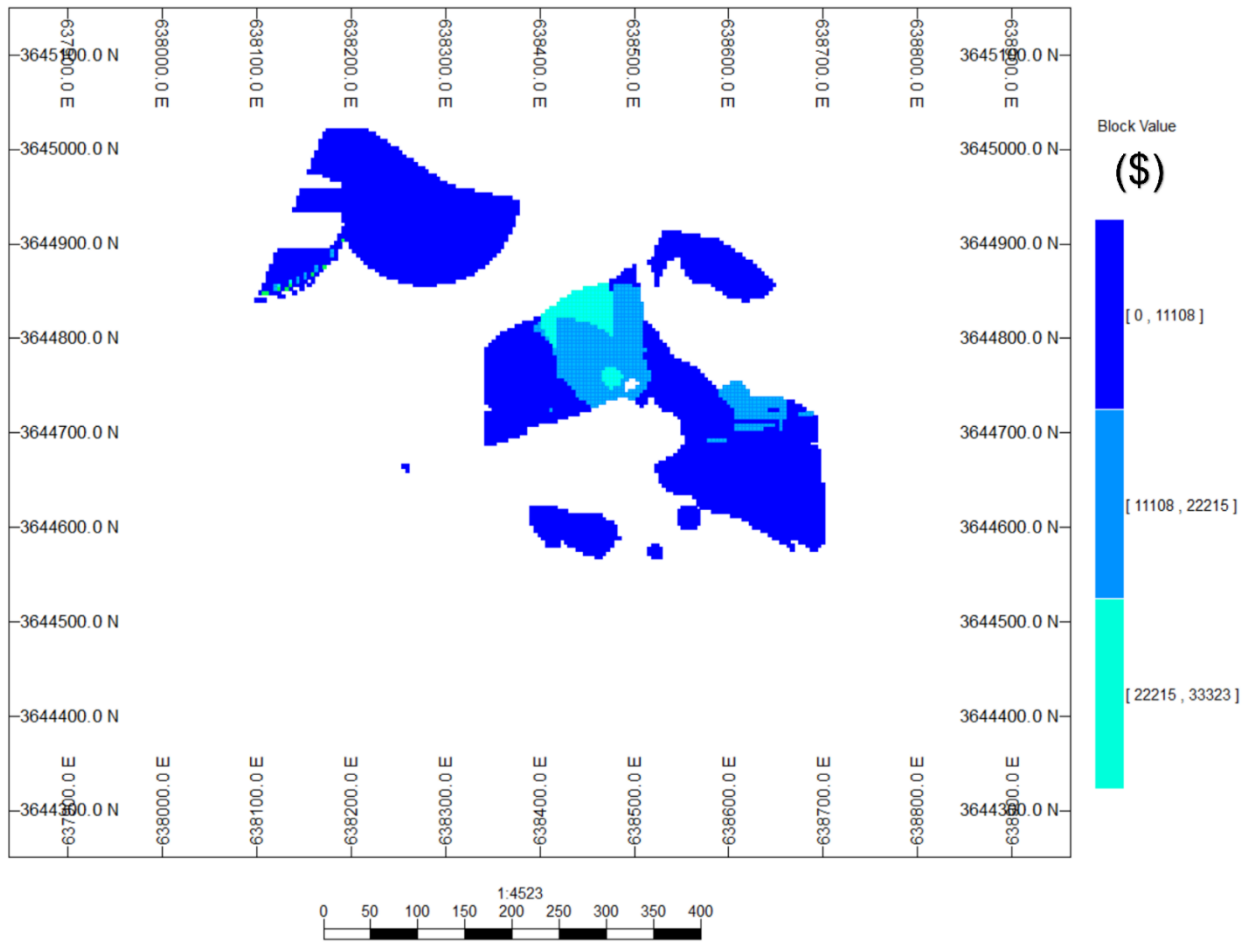
Fig. F. 2. 2D economic model (Section level 1900 m, Plan View)
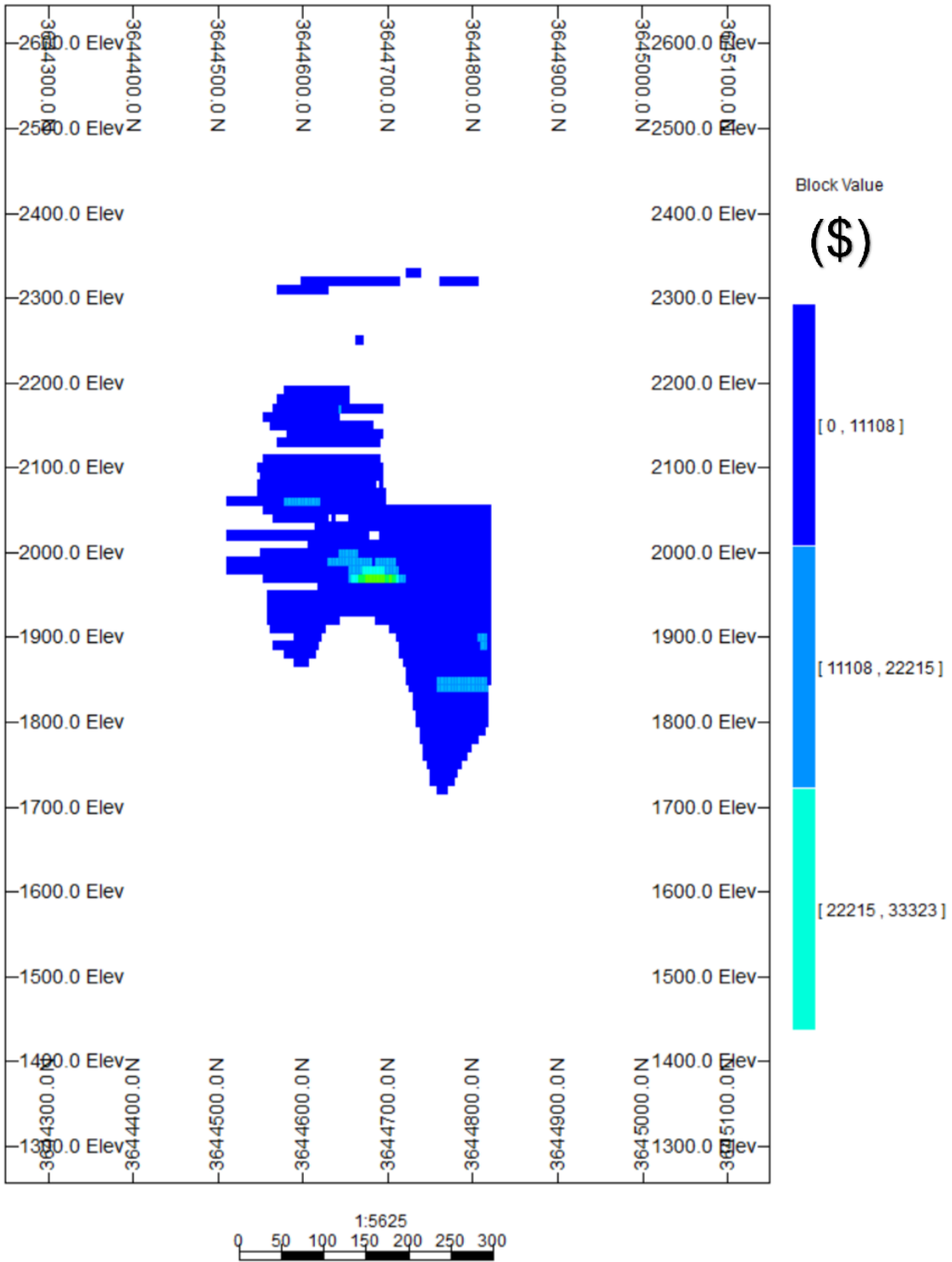
Fig. F. 3. 2D economic model (Section 638400 E North-South View)
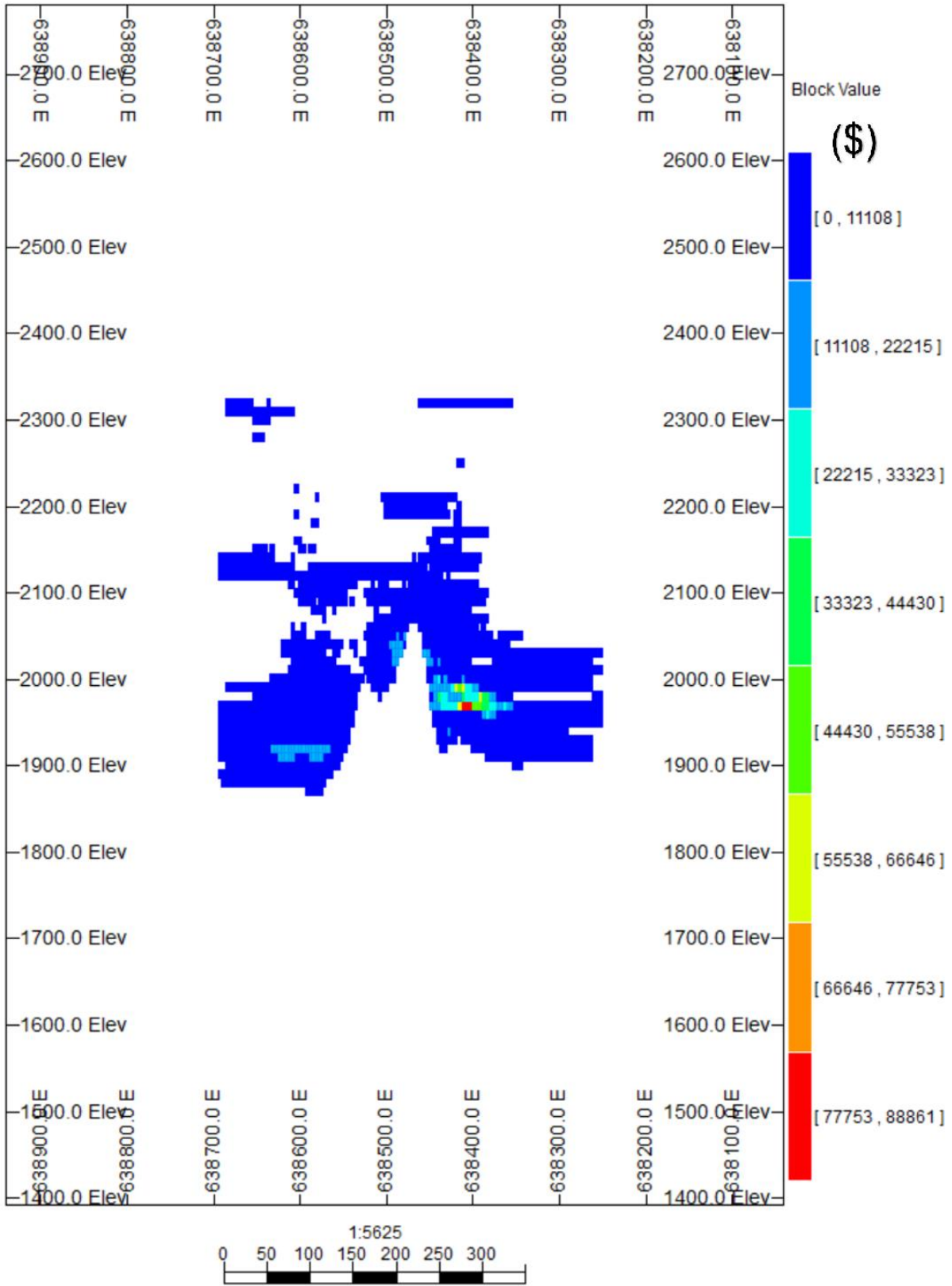
Fig. F. 4. 2D economic model (Section 3644688.00 N East-West View)

Appendix. G: The Kahang Ultimate Pit Limit
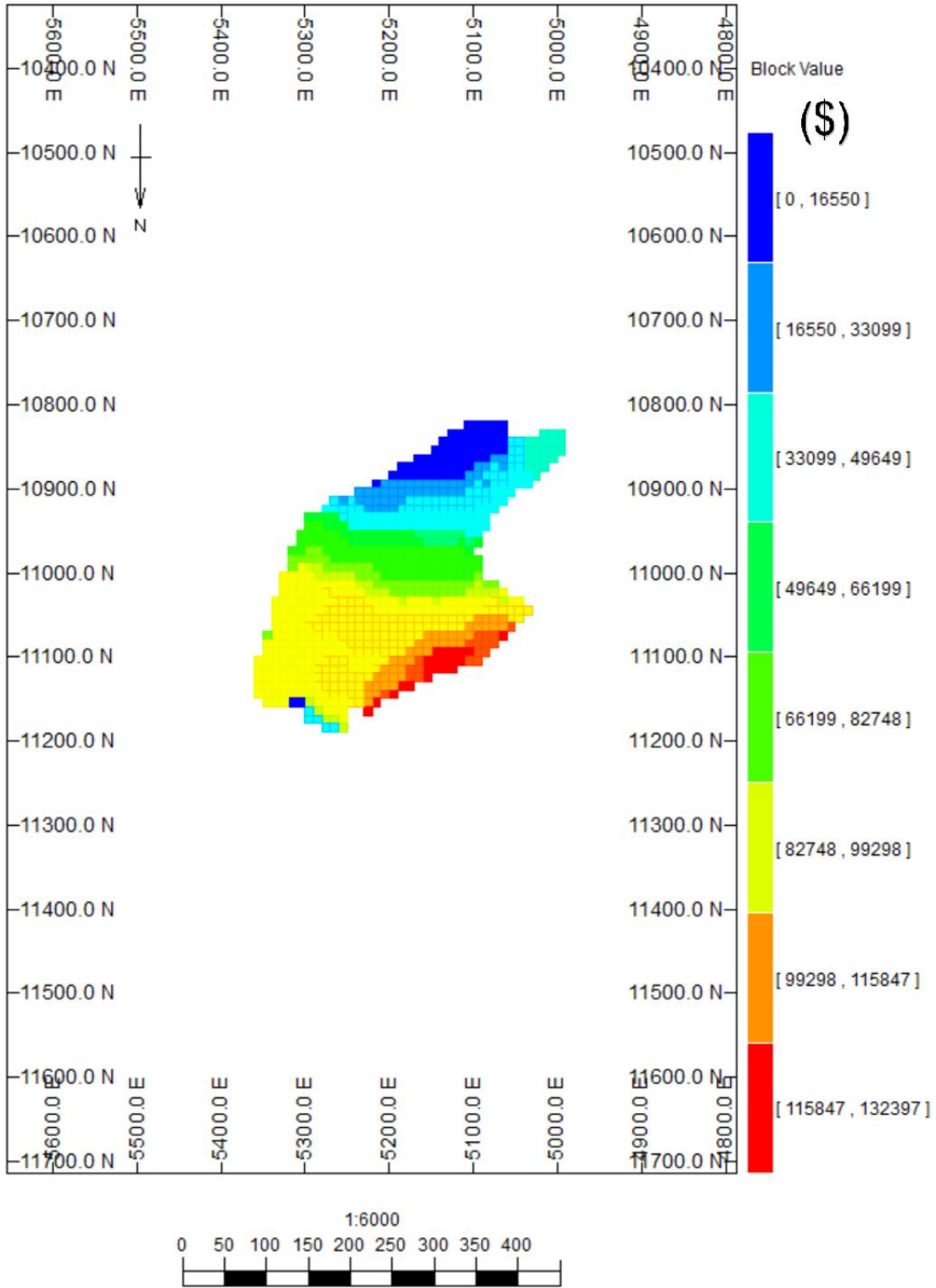
Fig. G. 1. 2D pit limit (Section level 2225 m, Plan View)
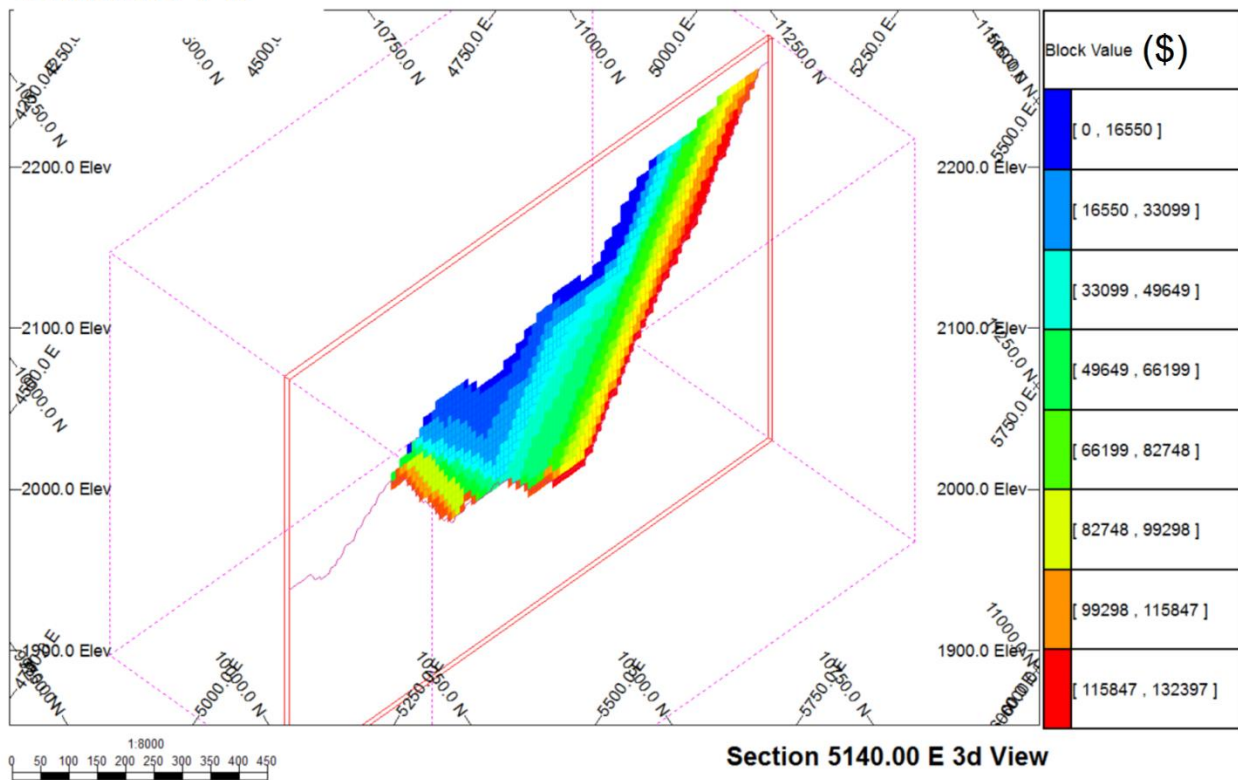
Fig. G. 2. 3D Ultimate pit limit view of the Kahang deposit including all boreholes (Section 5140.00 E)

Appendix. H: Extraction Sequences (Nested Pits)

Table. H. 1. Pit optimisation: Extraction sequences for incremental and cumulative NPV generated by NPV Scheduler software (sequence No. 92 specifies OES)

Incremental Data									
Point	Profit	Revenue	Processing Cost	Mining Cost	NPV	Total Rock	Total Ore	Total Waste	Strip Ratio
	$	$	$	$	$	Tonnes	Tonnes	Tonnes	
1	-302,720	0	0	302,720	-301,976	170,280	0	170,280	0
2	-302,720	0	0	302,720	-300,489	170,280	0	170,280	0
3	-302,720	0	0	302,720	-299,010	170,280	0	170,280	0
4	-302,720	0	0	302,720	-297,537	170,280	0	170,280	0
5	-137,860	202,453	37,593	302,720	-134,990	171,420	7,980	163,440	20.479
6	26,464	412,809	83,624	302,720	25,506	172,867	18,009	154,857	8.599
7	793,812	1,268,154	171,621	302,720	769,741	174,971	33,969	141,001	4.151
8	105,371	499,501	91,410	302,720	101,672	175,492	19,329	156,163	8.079
9	-134,013	213,817	45,109	302,720	-128,436	172,222	9,772	162,449	16.623
10	-73,933	298,893	70,106	302,720	-70,094	173,537	15,427	158,110	10.249
11	-302,720	0	0	302,720	-287,275	170,280	0	170,280	0
12	64,932	467,785	100,133	302,720	61,523	177,492	21,734	155,758	7.166
13	-137,780	214,213	49,272	302,720	-129,308	173,390	10,812	162,577	15.036
14	-302,720	0	0	302,720	-282,968	170,280	0	170,280	0
15	-302,720	0	0	302,720	-281,574	170,280	0	170,280	0
16	-26,561	435,028	158,868	302,720	-24,522	177,174	36,691	140,483	3.829
17	-302,720	0	0	302,720	-278,752	170,280	0	170,280	0
18	-302,720	0	0	302,720	-277,380	170,280	0	170,280	0
19	-214,493	183,810	95,583	302,720	-195,599	172,751	22,631	150,120	6.633
20	-252,914	132,560	82,753	302,720	-229,454	174,083	19,784	154,299	7.799
21	-257,887	112,450	67,617	302,720	-232,801	173,248	16,134	157,113	9.738
22	-85,507	439,206	221,992	302,720	-77,039	192,001	52,473	139,528	2.659
23	-96,224	304,941	98,445	302,720	-86,066	174,462	22,491	151,971	6.757
24	-66,359	390,875	154,514	302,720	-59,158	178,339	35,945	142,393	3.961
25	-19,790	483,914	200,984	302,720	-17,443	179,244	46,889	132,355	2.823
26	21,957	567,760	243,083	302,720	19,451	184,651	56,820	127,830	2.25
27	-147,140	483,294	327,714	302,720	-128,609	186,587	78,619	107,968	1.373
28	-98,236	463,734	259,250	302,720	-85,557	182,576	61,686	120,889	1.96
29	-115,813	455,952	269,045	302,720	-100,337	179,969	64,195	115,774	1.803
30	-210,706	186,391	94,377	302,720	-181,214	177,382	22,313	155,068	6.95
31	-302,720	0	0	302,720	-259,296	170,280	0	170,280	0
32	-302,720	0	0	302,720	-258,020	170,280	0	170,280	0
33	-302,720	0	0	302,720	-256,749	170,280	0	170,280	0
34	-302,720	0	0	302,720	-255,484	170,584	0	170,584	0

35	-302,720	0	0	302,720	-254,225	170,280	0	170,280	0
36	-302,720	0	0	302,720	-252,973	170,280	0	170,280	0
37	-302,720	0	0	302,720	-251,727	170,280	0	170,280	0
38	-302,720	0	0	302,720	-250,488	170,280	0	170,280	0
39	-302,720	0	0	302,720	-249,254	170,280	0	170,280	0
40	-302,720	0	0	302,720	-248,027	170,280	0	170,280	0
41	-302,720	0	0	302,720	-246,806	170,280	0	170,280	0
42	-302,720	0	0	302,720	-245,590	170,280	0	170,280	0
43	-302,720	0	0	302,720	-244,381	170,280	0	170,280	0
44	-302,720	0	0	302,720	-243,177	170,705	0	170,705	0
45	-302,720	0	0	302,720	-241,974	170,948	0	170,948	0
46	-302,720	0	0	302,720	-240,781	170,280	0	170,280	0
47	-302,720	0	0	302,720	-239,595	170,280	0	170,280	0
48	-302,720	0	0	302,720	-238,416	170,280	0	170,280	0
49	-302,720	0	0	302,720	-237,242	170,280	0	170,280	0
50	-302,720	0	0	302,720	-236,074	170,280	0	170,280	0
51	-302,720	0	0	302,720	-234,911	170,280	0	170,280	0
52	-291,811	12,710	1,801	302,720	-225,335	170,280	360	169,920	472
53	-90,719	310,050	98,048	302,720	-69,561	170,280	22,320	147,960	6.629
54	-294,195	14,699	6,174	302,720	-224,927	170,280	1,440	168,840	117.25
55	-274,259	50,029	21,568	302,720	-208,641	170,280	5,040	165,240	32.786
56	-302,720	0	0	302,720	-229,169	177,332	0	177,332	0
57	-302,720	0	0	302,720	-228,008	170,401	0	170,401	0
58	-291,174	23,728	12,182	302,720	-218,235	170,523	2,880	167,643	58.209
59	-302,427	2,029	1,735	302,720	-225,540	176,907	420	176,486	419.407
60	-290,988	117,539	105,806	302,720	-215,870	183,144	25,688	157,456	6.13
61	-283,584	38,944	19,807	302,720	-209,301	170,462	4,680	165,782	35.424
62	-222,790	105,973	26,043	302,720	-163,611	170,888	5,760	165,128	28.668
63	-78,237	336,201	111,717	302,720	-57,438	176,603	25,560	151,043	5.909
64	58,983	558,886	197,182	302,720	43,221	170,948	45,360	125,588	2.769
65	-3,251	510,359	210,889	302,720	-2,364	175,132	49,145	125,987	2.564
66	177,601	853,272	372,951	302,720	127,686	175,630	87,265	88,364	1.013
67	113,192	776,331	360,418	302,720	81,061	179,400	84,694	94,705	1.118
68	-209,846	168,892	76,018	302,720	-149,388	180,129	17,832	162,297	9.101
69	406,831	1,080,798	371,247	302,720	288,339	176,116	85,246	90,870	1.066
70	251,995	721,505	166,789	302,720	178,042	177,089	36,608	140,481	3.837
71	-150,600	223,021	70,900	302,720	-105,686	187,547	16,163	171,384	10.603
72	-243,195	87,166	27,640	302,720	-169,701	188,144	6,300	181,843	28.86
73	-247,876	169,045	114,200	302,720	-172,022	176,707	27,430	149,276	5.442
74	129,464	629,298	197,114	302,720	89,151	178,622	44,865	133,756	2.981
75	92,462	621,500	226,317	302,720	63,619	175,950	52,219	123,731	2.369
76	1,112,962	1,882,716	467,033	302,720	760,176	176,907	103,460	73,446	0.71
77	1,589,793	2,450,295	557,781	302,720	1,080,859	173,441	122,120	51,321	0.42

78	1,263,254	2,087,980	522,005	302,720	854,637	180,251	115,748	64,502	0.557
79	1,541,488	2,339,445	495,237	302,720	1,036,973	172,772	107,238	65,534	0.611
80	1,578,076	2,398,261	517,465	302,720	1,055,895	180,731	112,385	68,345	0.608
81	1,528,337	2,422,321	591,264	302,720	1,017,190	185,284	130,700	54,584	0.418
82	2,781,670	3,698,135	613,744	302,720	1,842,401	182,654	127,238	55,416	0.436
83	1,465,090	2,214,107	446,296	302,720	965,308	181,782	95,931	85,851	0.895
84	1,210,660	2,057,535	544,154	302,720	793,814	186,803	121,572	65,230	0.537
85	388,737	1,214,670	523,213	302,720	253,478	187,854	122,406	65,447	0.535
86	737,539	1,691,310	651,051	302,720	477,955	190,339	151,100	39,238	0.26
87	391,134	1,261,510	567,655	302,720	252,373	191,819	133,255	58,563	0.439
88	296,330	1,010,935	411,885	302,720	189,996	186,951	96,048	90,903	0.946
89	474,331	1,278,375	501,323	302,720	301,919	190,363	116,561	73,801	0.633
90	808,655	1,580,718	469,343	302,720	512,737	191,439	106,399	85,039	0.799
91	1,747,427	2,596,472	546,324	302,720	1,101,455	190,678	118,568	72,110	0.608
92	1,732,457	2,464,485	429,308	302,720	1,086,318	190,430	90,212	100,217	1.111
93	3,810	460,839	154,308	302,720	2,278	179,721	35,340	144,380	4.085
94	-99,673	431,512	228,464	302,720	-61,923	182,126	54,153	127,972	2.363
95	151,539	643,635	189,376	302,720	93,866	181,168	42,872	138,296	3.226
96	-219,275	250,807	167,361	302,720	-134,725	178,635	40,136	138,499	3.451
97	10,026	517,422	204,675	302,720	6,124	188,830	47,606	141,224	2.966
98	-7,950	443,913	149,143	302,720	-4,579	184,275	34,216	150,059	4.386
99	114,108	642,500	225,672	302,720	68,995	181,112	51,915	129,196	2.489
100	296,279	774,060	221,780	256,000	177,855	150,406	50,110	100,296	2.002
Cumulative Data									
Point	Profit	Revenue	Processing Cost	Mining Cost	NPV	Total Rock	Total Ore	Total Waste	Strip Ratio
	$	$	$	$	$	tonnes	tonnes	tonnes	
1	-302,720	0	0	302,720	-301,976	170,280	0	170,280	0
2	-605,440	0	0	605,440	-602,465	340,560	0	340,560	0
3	-908,160	0	0	908,160	-901,474	510,840	0	510,840	0
4	-1,210,880	0	0	1,210,880	-1,199,011	681,120	0	681,120	0
5	-1,348,740	202,453	37,593	1,513,600	-1,334,000	852,540	7,980	844,560	105.824
6	-1,322,276	615,262	121,218	1,816,320	-1,308,493	1,025,408	25,990	999,417	38.453
7	-528,463	1,883,417	292,839	2,119,040	-538,752	1,200,379	59,959	1,140,419	19.02
8	-423,092	2,382,918	384,250	2,421,760	-437,079	1,375,871	79,289	1,296,582	16.352
9	-557,105	2,596,735	429,359	2,724,480	-565,515	1,548,094	89,062	1,459,031	16.382
10	-631,037	2,895,629	499,466	3,027,200	-635,609	1,721,631	104,489	1,617,142	15.477
11	-933,757	2,895,629	499,466	3,329,920	-922,883	1,891,911	104,489	1,787,422	17.106
12	-868,825	3,363,415	599,599	3,632,640	-861,360	2,069,404	126,223	1,943,180	15.395
13	-1,006,604	3,577,628	648,872	3,935,360	-990,667	2,242,795	137,036	2,105,758	15.366
14	-1,309,324	3,577,628	648,872	4,238,080	-1,273,634	2,413,075	137,036	2,276,038	16.609
15	-1,612,044	3,577,628	648,872	4,540,800	-1,555,208	2,583,355	137,036	2,446,318	17.852

16	-1,638,605	4,012,656	807,740	4,843,520	-1,579,729	2,760,529	173,727	2,586,801	14.89
17	-1,941,325	4,012,656	807,740	5,146,240	-1,858,481	2,930,809	173,727	2,757,081	15.87
18	-2,244,045	4,012,656	807,740	5,448,960	-2,135,860	3,101,089	173,727	2,927,361	16.85
19	-2,458,538	4,196,467	903,324	5,751,680	-2,331,459	3,273,841	196,359	3,077,481	15.673
20	-2,711,451	4,329,027	986,077	6,054,400	-2,560,913	3,447,924	216,143	3,231,780	14.952
21	-2,969,337	4,441,478	1,053,694	6,357,120	-2,793,714	3,621,172	232,278	3,388,894	14.59
22	-3,054,844	4,880,684	1,275,687	6,659,840	-2,870,752	3,813,174	284,751	3,528,422	12.391
23	-3,151,067	5,185,625	1,374,132	6,962,560	-2,956,817	3,987,636	307,243	3,680,393	11.979
24	-3,217,426	5,576,501	1,528,646	7,265,280	-3,015,975	4,165,976	343,188	3,822,787	11.139
25	-3,237,216	6,060,415	1,729,631	7,568,000	-3,033,417	4,345,220	390,078	3,955,142	10.139
26	-3,215,259	6,628,176	1,972,714	7,870,720	-3,013,965	4,529,872	446,899	4,082,972	9.136
27	-3,362,398	7,111,471	2,300,429	8,173,440	-3,142,574	4,716,459	525,518	4,190,940	7.975
28	-3,460,634	7,575,206	2,559,679	8,476,160	-3,228,131	4,899,035	587,204	4,311,830	7.343
29	-3,576,446	8,031,158	2,828,724	8,778,880	-3,328,467	5,079,004	651,400	4,427,604	6.797
30	-3,787,152	8,217,550	2,923,102	9,081,600	-3,509,681	5,256,387	673,713	4,582,673	6.802
31	-4,089,872	8,217,550	2,923,102	9,384,320	-3,768,976	5,426,667	673,713	4,752,953	7.055
32	-4,392,592	8,217,550	2,923,102	9,687,040	-4,026,996	5,596,947	673,713	4,923,233	7.308
33	-4,695,312	8,217,550	2,923,102	9,989,760	-4,283,744	5,767,227	673,713	5,093,513	7.56
34	-4,998,032	8,217,550	2,923,102	10,292,480	-4,539,228	5,937,811	673,713	5,264,097	7.814
35	-5,300,752	8,217,550	2,923,102	10,595,200	-4,793,452	6,108,091	673,713	5,434,377	8.066
36	-5,603,472	8,217,550	2,923,102	10,897,920	-5,046,424	6,278,371	673,713	5,604,657	8.319
37	-5,906,192	8,217,550	2,923,102	11,200,640	-5,298,151	6,448,651	673,713	5,774,937	8.572
38	-6,208,912	8,217,550	2,923,102	11,503,360	-5,548,638	6,618,931	673,713	5,945,217	8.825
39	-6,511,632	8,217,550	2,923,102	11,806,080	-5,797,892	6,789,211	673,713	6,115,497	9.077
40	-6,814,352	8,217,550	2,923,102	12,108,800	-6,045,918	6,959,491	673,713	6,285,777	9.33
41	-7,117,072	8,217,550	2,923,102	12,411,520	-6,292,723	7,129,771	673,713	6,456,057	9.583
42	-7,419,792	8,217,550	2,923,102	12,714,240	-6,538,313	7,300,051	673,713	6,626,337	9.836
43	-7,722,512	8,217,550	2,923,102	13,016,960	-6,782,694	7,470,331	673,713	6,796,617	10.088
44	-8,025,232	8,217,550	2,923,102	13,319,680	-7,025,870	7,641,036	673,713	6,967,323	10.342
45	-8,327,952	8,217,550	2,923,102	13,622,400	-7,267,843	7,811,985	673,713	7,138,272	10.595
46	-8,630,672	8,217,550	2,923,102	13,925,120	-7,508,623	7,982,265	673,713	7,308,552	10.848
47	-8,933,392	8,217,550	2,923,102	14,227,840	-7,748,218	8,152,545	673,713	7,478,832	11.101
48	-9,236,112	8,217,550	2,923,102	14,530,560	-7,986,634	8,322,825	673,713	7,649,112	11.354
49	-9,538,832	8,217,550	2,923,102	14,833,280	-8,223,875	8,493,105	673,713	7,819,392	11.606
50	-9,841,552	8,217,550	2,923,102	15,136,000	-8,459,948	8,663,385	673,713	7,989,672	11.859
51	-10,144,272	8,217,550	2,923,102	15,438,720	-8,694,858	8,833,665	673,713	8,159,952	12.112
52	-10,436,083	8,230,261	2,924,903	15,741,440	-8,920,193	9,003,945	674,073	8,329,872	12.358
53	-10,526,801	8,540,311	3,022,952	16,044,160	-8,989,753	9,174,225	696,393	8,477,832	12.174
54	-10,820,996	8,555,010	3,029,126	16,346,880	-9,214,680	9,344,505	697,833	8,646,672	12.391
55	-11,095,255	8,605,040	3,050,694	16,649,600	-9,423,320	9,514,785	702,873	8,811,912	12.537
56	-11,397,975	8,605,040	3,050,694	16,952,320	-9,652,489	9,692,118	702,873	8,989,244	12.789
57	-11,700,695	8,605,040	3,050,694	17,255,040	-9,880,497	9,862,520	702,873	9,159,646	13.032
58	-11,991,868	8,628,768	3,062,876	17,557,760	-10,098,731	10,033,043	705,753	9,327,289	13.216

59	-12,294,295	8,630,798	3,064,612	17,860,480	-10,324,271	10,209,950	706,174	9,503,776	13.458
60	-12,585,282	8,748,337	3,170,418	18,163,200	-10,540,140	10,393,094	731,862	9,661,232	13.201
61	-12,868,865	8,787,281	3,190,226	18,465,920	-10,749,441	10,563,556	736,542	9,827,014	13.342
62	-13,091,655	8,893,255	3,216,269	18,768,640	-10,913,051	10,734,444	742,302	9,992,142	13.461
63	-13,169,891	9,229,456	3,327,987	19,071,360	-10,970,489	10,911,048	767,862	10,143,185	13.21
64	-13,110,908	9,788,343	3,525,170	19,374,080	-10,927,267	11,081,996	813,222	10,268,774	12.627
65	-13,114,158	10,298,702	3,736,059	19,676,800	-10,929,631	11,257,129	862,368	10,394,761	12.054
66	-12,936,557	11,151,975	4,109,011	19,979,520	-10,801,944	11,432,760	949,633	10,483,126	11.039
67	-12,823,364	11,928,307	4,469,430	20,282,240	-10,720,883	11,612,160	1,034,328	10,577,832	10.227
68	-13,033,209	12,097,199	4,545,448	20,584,960	-10,870,270	11,792,289	1,052,160	10,740,129	10.208
69	-12,626,378	13,177,998	4,916,696	20,887,680	-10,581,930	11,968,406	1,137,406	10,831,000	9.523
70	-12,374,382	13,899,504	5,083,486	21,190,400	-10,403,888	12,145,496	1,174,014	10,971,481	9.345
71	-12,524,982	14,122,525	5,154,386	21,493,120	-10,509,573	12,333,043	1,190,177	11,142,865	9.362
72	-12,768,176	14,209,692	5,182,027	21,795,840	-10,679,274	12,521,187	1,196,478	11,324,708	9.465
73	-13,016,051	14,378,738	5,296,228	22,098,560	-10,851,295	12,697,894	1,223,908	11,473,985	9.375
74	-12,886,587	15,008,036	5,493,342	22,401,280	-10,762,144	12,876,516	1,268,774	11,607,742	9.149
75	-12,794,124	15,629,537	5,719,660	22,704,000	-10,698,524	13,052,467	1,320,993	11,731,473	8.881
76	-11,681,161	17,512,253	6,186,694	23,006,720	-9,938,348	13,229,374	1,424,454	11,804,920	8.287
77	-10,091,368	19,962,549	6,744,476	23,309,440	-8,857,489	13,402,816	1,546,574	11,856,241	7.666
78	-8,828,113	22,050,529	7,266,481	23,612,160	-8,002,851	13,583,067	1,662,323	11,920,744	7.171
79	-7,286,625	24,389,974	7,761,718	23,914,880	-6,965,878	13,755,840	1,769,561	11,986,278	6.774
80	-5,708,548	26,788,236	8,279,184	24,217,600	-5,909,983	13,936,571	1,881,947	12,054,624	6.405
81	-4,180,211	29,210,558	8,870,448	24,520,320	-4,892,792	14,121,856	2,012,648	12,109,208	6.017
82	-1,398,540	32,908,693	9,484,193	24,823,040	-3,050,390	14,304,510	2,139,886	12,164,624	5.685
83	66,550	35,122,800	9,930,489	25,125,760	-2,085,082	14,486,292	2,235,817	12,250,475	5.479
84	1,277,211	37,180,336	10,474,644	25,428,480	-1,291,268	14,673,096	2,357,390	12,315,705	5.224
85	1,665,948	38,395,007	10,997,858	25,731,200	-1,037,789	14,860,950	2,479,796	12,381,153	4.993
86	2,403,488	40,086,317	11,648,909	26,033,920	-559,834	15,051,289	2,630,897	12,420,392	4.721
87	2,794,623	41,347,827	12,216,564	26,336,640	-307,461	15,243,108	2,764,153	12,478,955	4.515
88	3,090,953	42,358,763	12,628,450	26,639,360	-117,464	15,430,060	2,860,201	12,569,859	4.395
89	3,565,284	43,637,138	13,129,773	26,942,080	184,456	15,620,424	2,976,763	12,643,660	4.247
90	4,373,939	45,217,857	13,599,117	27,244,800	697,194	15,811,864	3,083,163	12,728,700	4.128
91	6,121,367	47,814,330	14,145,442	27,547,520	1,798,650	16,002,542	3,201,731	12,800,811	3.998
92	7,853,825	50,278,816	14,574,750	27,850,240	2,884,968	16,192,972	3,291,944	12,901,028	3.919
93	7,857,636	50,739,655	14,729,058	28,152,960	2,887,246	16,372,694	3,327,284	13,045,409	3.921
94	7,757,963	51,171,167	14,957,523	28,455,680	2,825,323	16,554,820	3,381,438	13,173,382	3.896
95	7,909,502	51,814,802	15,146,900	28,758,400	2,919,189	16,735,988	3,424,310	13,311,678	3.887
96	7,690,228	52,065,610	15,314,261	29,061,120	2,784,465	16,914,624	3,464,446	13,450,177	3.882
97	7,700,255	52,583,032	15,518,937	29,363,840	2,790,590	17,103,454	3,512,052	13,591,401	3.87
98	7,692,305	53,026,946	15,668,080	29,666,560	2,786,011	17,287,729	3,546,268	13,741,460	3.875
99	7,806,413	53,669,446	15,893,753	29,969,280	2,855,007	17,468,841	3,598,184	13,870,657	3.855
100	8,102,692	54,443,507	16,115,534	30,225,280	3,032,862	17,619,248	3,648,294	13,970,953	3.829